AD_____

Award Number: W81XWH-07-2-0121

TITLE: Proton Therapy Dose Characterization and Verification

PRINCIPAL INVESTIGATOR: Zelig Tochner, M.D.

CONTRACTING ORGANIZATION: """""""University of Pennsylvania
                                                      Philadelphia PA 19104-6205

REPORT DATE: October 2013

TYPE OF REPORT: Final

PREPARED FOR: U.S. Army Medical Research and Materiel Command
                            Fort Detrick, Maryland 21702-5012

DISTRIBUTION STATEMENT:

    """""""'Approved for public release; distribution unlimited

The views, opinions and/or findings contained in this report are those of the author(s) and should
not be construed as an official Department of the Army position, policy or decision unless so
designated by other documentation.

REPORT DOCUMENTATION PAGE

Form Approved
OMB No. 0704-0188

Public reporting burden for this collection of information is estimated to average 1 hour per response, including the time for reviewing instructions, searching existing data sources, gathering and maintaining the data needed, and completing and reviewing this collection of information. Send comments regarding this burden estimate or any other aspect of this collection of information, including suggestions for reducing this burden to Department of Defense, Washington Headquarters Services, Directorate for Information Operations and Reports (0704-0188), 1215 Jefferson Davis Highway, Suite 1204, Arlington, VA 22202-4302. Respondents should be aware that notwithstanding any other provision of law, no person shall be subject to any penalty for failing to comply with a collection of information if it does not display a currently valid OMB control number. **PLEASE DO NOT RETURN YOUR FORM TO THE ABOVE ADDRESS.**

1. REPORT DATE *(DD-MM-YYYY)*	2. REPORT TYPE	3. DATES COVERED *(From - To)*
October 2013	Final	48 October 2007 – 30 September 2013

4. TITLE AND SUBTITLE	5a. CONTRACT NUMBER
Proton Therapy Dose Characterization and Verification (Phase 4) Development of Technology for Image-Guided Proton Therapy (Phase 5)	
	5b. GRANT NUMBER W81XWH-07-2-0121
6. AUTHOR(S) Keith Cengel MD PhD, Eric Diffenderfer PhD, Derek Dolney PhD, Simon Hastings, Joel Karp PhD, Alexander Lin MD, Rulon Mayer, Sergei Savin, Jessica Sheehan PhD, Zelig Tochner MD Arnaud Belard, LTC John O'Connell MD	**5d. PROJECT NUMBER**
	5e. TASK NUMBER
Email: tochner@uphs.upenn.edu	**5f. WORK UNIT NUMBER**

7. PERFORMING ORGANIZATION NAME(S) AND ADDRESS(ES)	8. PERFORMING ORGANIZATION REPORT
Trustees of the University of Pennsylvania Philadelphia PA 19104-6205	

9. SPONSORING / MONITORING AGENCY NAME(S) AND ADDRESS(ES)	10. SPONSOR/MONITOR'S ACRONYM(S)
U.S. Army Medical Research and Materiel Command Fort Detrick, Maryland 21702-5012	
	11. SPONSOR/MONITOR'S NUMBER(S)

12. DISTRIBUTION / AVAILABILITY STATEMENT

Approved for public release; distribution unlimited

13. SUPPLEMENTARY NOTES

14. ABSTRACT

This report describes the final report of work on the award "Proton Therapy Dose Characterization and Verification" which includes investigation in the following areas: (A) the use of positron emission tomography (PET) to determine the dose deposited by a therapeutic proton beam, (B) studies of the radiobiological effect of proton therapy, and (C) support for matching patients to clinical trials. This report also covers a continuation award "Development of Technology for Image-Guided Proton Therapy" that focuses on transferring technology currently in conventional radiotherapy systems to the proton treatment rooms, especially that technology related to daily patient localization. A component of both of these awards also supports the work done by the Walter Reed Army Medical Center scientists.

15. SUBJECT TERMS
Radiation Oncology, Proton Therapy, Image-Guided Radiotherapy, PET

16. SECURITY CLASSIFICATION OF:			17. LIMITATION OF ABSTRACT	18. NUMBER OF PAGES	19a. NAME OF RESPONSIBLE PERSON USAMRMC
a. REPORT U	**b. ABSTRACT** U	**c. THIS PAGE** U	UU	159	**19b. TELEPHONE NUMBER** *(include area code)*

Standard Form 298 (Rev. 8-98)

Table of Contents

INTRODUCTION

The overall goal of this multi-year research project in collaboration with the Walter Reed Army Medical Center is to develop the necessary technology to make the Roberts Proton Therapy Center in Philadelphia the most advanced proton radiotherapy center. Award # W81XWH-07-2-0121 comprises phases 4 and 5 of this endeavor and consists of the following projects:

Phase 4

A. Positron Emission Tomography (PET) of proton beams to verify dose deposition

1. PET Detector Development: Design a PET scanner optimized for the application of verifying the dose distribution deposited by proton therapy beams. This includes detector selection, electronic and mechanical engineering, data acquisition, and reconstruction software.

2. Cross-section measurements: Measure positron-emitting isotope production from the primary elements found in tissue and compare to the GEANT4 Monte Carlo simulation program.

3. Determination of elemental composition: The verification of the dose distribution cannot be done directly because the production of isotopes is not easily related to the dose deposited. Instead a Monte Carlo simulation program is used to calculate both dose deposited and isotopes produced and the latter is compared to the measured value. It is critical that the correct elemental composition be used in the simulation for this comparison to work. We are investigating how additional imaging methods, such as dual-energy CT, can help determine the composition.

B. Radiobiology and microdosimetry of proton beams

1. Radiobiology studies in the proton beam: Develop techniques to measure the radiobiological effectiveness of the proton beam.

2. Microdosimetry studies in the proton beam: Build proportional chambers to measure the linear energy transfer in a proton therapy field.

Phase 5

A. Apply state-of-the-art localization methods, including cone-beam CT and

B. implanted radiofrequency beacons, currently used in conventional radiotherapy to proton radiotherapy.

C. Develop a computer program to maximize the efficiency of the proton facility.

BODY

### *Tissue Heterogeneity*

INTRODUCTION:

Megavoltage protons can deliver radiation therapy with great spatial precision. However, planning the radiation dose depends on knowing the electronic density of the materials (Schneider et al 1996, Schaffner et al.1998, Moyers et al. 2010) exposed to radiation as well as being able to accurately treatment plan based on measuring a variety of materials (Pflugfelder et al. 2007, Szymanowski et al. 2002), Sawakuchi et al. 2008). Actual empirical testing has mostly been limited despite a number of issues regarding tissue heterogeneity and proton treatment plan. Specifically, the distal edge of the Bragg peak (Chevstov et al. 2010) can be affected by inability to account for tissue heterogeneities. In addition, the Linear Energy Transfer (LET) due to protons depositing energy within heterogeneous materials has been confined to Monte Carlo calculation without experimental verification. This research effort compares the measured and expected doses over areas using radiochromic film. The technology developed by this research is leveraged for measuring radiation dose and LET within heterogeneous materials within a phantom. These measured doses will be compared to the dose distribution from the x-ray and proton treatment planner. The LET distribution within heterogeneous materials will be compared to Monte Carlo calculations.

1. Experimental exposure of heterogeneous phantom to protons
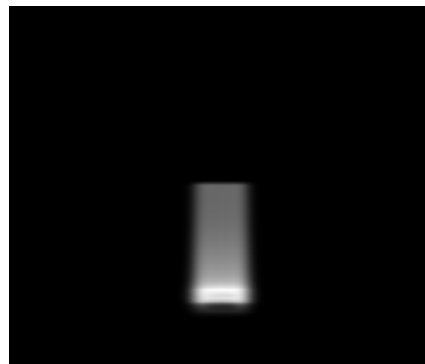
A phantom was constructed to examine the dose distribution of protons in heterogeneous materials. Specifically acrylic plates were drilled and delrin (to simulate bone) and cork (to simulate lung) plugs and unplugged (air cavity) were press fitted into the acrylic (see below). The goals were to experimentally test the predicted and distal edges for proton beams bombarding heterogeneous materials and also examine the predicted and measured LET distributions within heterogeneous materials. Anthropomorphic material phantoms have been built and tested for proton therapy (Grant et al. 2009) and found shifts in Bragg peaks and small differences in proton stopping power.

Delrin   Cork   Air
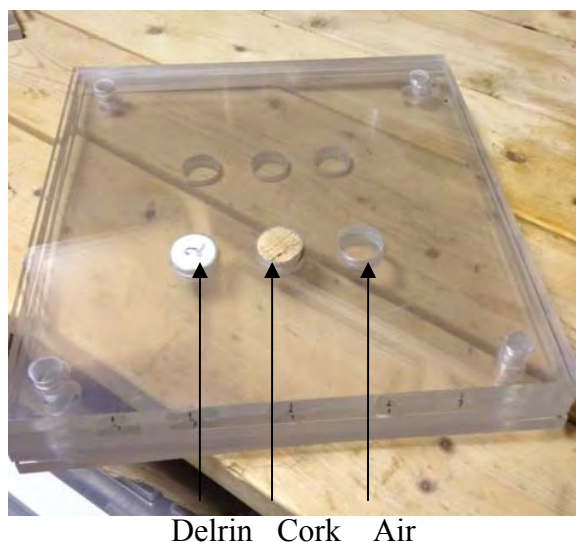
Proton treatment plans were remotely planned from Walter Reed that deposited the Bragg peaks beyond inserted materials (to test position of distal edge)and also deposited the beams within the heterogeneous materials (to test LET within the materials). Examples of plans for protons exposing Delrin for both long and short range are shown below.
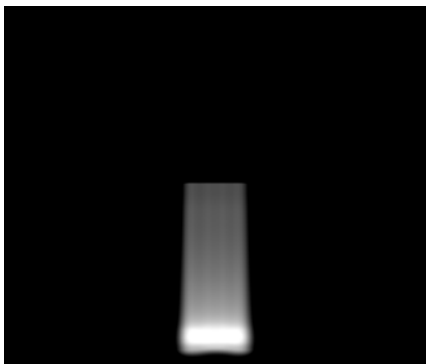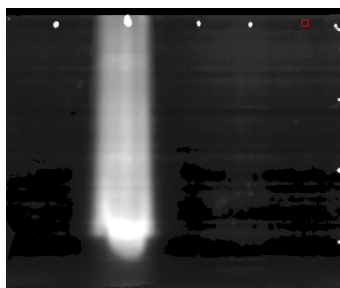

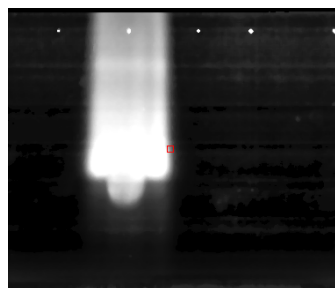Delrin Long Range (Bragg Peak beyond Delrin plug)   Delrin Short Range (Bragg peak inside plug)

Note the Bragg peaks but also the bowing and distortion at the end of the proton range that shortens the distal edge distance. In the case of cork and air, the bowing will be displaced in the opposite direction toward a longer proton range. Similar plans were generated for cork, air gap and pure acrylic.

The University of Pennsylvania Proton Pencil Beam exposed the radiochromic film sandwiched between slabs of the heterogeneous phantom. The radiocrhomic film darkening was converted to dose using the procedures outlined previously.

Cork Long Range (Bragg Peak beyond Delrin plug)   Cork Short Range (Bragg peak inside plug)

Radiochromic film was exposed to protons imposing on the cork, delrin, air plugs. The measure dose distribution and treatment plans will be compared at the pixel level as described earlier. The LET from MC calculations (from U of Pennsylvania) will also be generated and compared to the measured dose distribution, as described earlier.

2. CT Hounsfield distribution from inorganic materials and its affect on proton plans and measurements,

Proton telemedicine has not addressed the issue of compatible CT scanners for patients scanned at one institution but treated elsewhere. Compatible scanners will eliminate the need to scan the patient multiple times and reduce the patient's radiation exposure. Proton treatment planning requires correctly associating CT Hounsfield numbers with proton stopping power. A general procedure was developed by Schneider (Schneider et al 1996, Schaffner et al 1998,

Moyers et al. 2010) to calibrate CT imagers for proton treatment planning systems. It was noted by Schneider and verified by others that an appropriate look up table for synthetic materials (such as acrylic, delrin, cork) differs from tissues. The phantoms described above an exposed to protons are synthetic. So an appropriate look up table may need to be generated.

In addition, remote proton plans generated at Walter Reed used Walter Reed CT scans, not those from University of Pennsylvania. Currently the University of Pennsylvania treatment planning system uses the calibration taken from University of Pennsylvania CT scanners. To help evaluate the possible differences in look up tables, the Walter Reed CT scanner imaged a set of standard phantoms with plugs having known compositions using a common procedure (i.e. 120 keV energy used for U of Pennsylvania and Walter Reed). The average CT number within each plug (with known composition) was determined using the CT images. These plugs have a well defined density, average electronic number, parameters that govern the x-ray scattering from Compton scattering, photoelectric effect, and coherent scattering within the CT scanner. From numerical fitting, it is found that the A, B, C parameters (associated with photoelectric effect, coherent scattering, and Compton Scattering are:

A(WR) =0.000281 +/- 0.000974   vs   A(Penn)=0.00034 +/- 0.0016
B(WR)=3.96 +/- 0.199   vs.   B(Penn)=3.84 +/- 0.21
C(WR)=859.3 +/- 5.09   vs.   C(Penn)=862.5 +/- 5.09

These parameters can be applied to tissues with known compositions to generate a calculated CT Hounsfield numbers. In turn, the relative proton stopping power for a given proton energy can be computed using the Bethe-Bloch equation for each of these materials and the average ionization energies. The Walter Reed and University of Pennsylvania look up tables Proton stopping power (at 115 MeV) and CT Hounsfield numbers) are compared below (at various degrees of magnification).
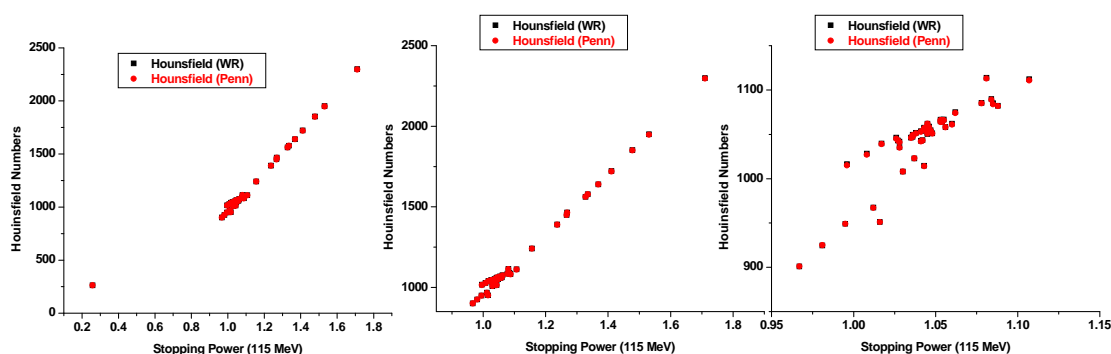
The agreement is so close between Walter Reed and Penn that it is difficult to discern a difference based on observing the graphs, even after magnifying the graphs. Small differences may be anticipated because the fitted parameters agree with each within the error bars.

Such a calculation will hopefully avoid the need for multiple CT scans of the patient (at Walter Reed and University of Pennsylvania). In addition, the machinery and analysis will be applied to synthetic materials and help validate the treatment planning procedure for these useful materials.

Linear Energy Transfer

INTRODUCTION:

Effective treatment of tumors depends on preferentially delivering radiation to the targets and minimizing the dose to sensitive organs. Due to the Bragg peak (Bragg 1904), high energy (mega electron volts) protons more selectively deliver maximal doses into desired areas with reduced radiation at the distal and proximal regions relative to photons. The high dose regions are attributed to protons slowing down near the end of the range. These slowing protons deliver doses within a short distance that yield a high Linear Energy Transfer (LET). The high rate of energy deposition within short distances has been correlated with high biological lethality (Paganetti 2003, Grassberger et al 2011a, Grassberger et al 2011b). Until recently, direct measurement of LET is accomplished only using point dosimeters through specially designed and configured ionization chambers. Specifically, current techniques measure LET use tissue-equivalent proportional counters (Kohno et al 2000), solid-state spectrometers (Borak et al 2004)), and other methods (Sawakuchi et al 2010, Spurny et al. 2004). Preliminary proof of principle studies (Gustavsson et al. 2004, Lopatiuk-Tirpak et al. 2012) used a BANG gel to explore the possibility of measuring LET over extended volumes. This study has developed a method to measure the LET deposited by a proton beam over extended areas using a film dosimeter (radiochromic Gafchromic EBT2 film). Although the radiochromic film is equally sensitive to most kinds of radiation, this film sensitivity is diminished for radiation having large LET (Vanitsky 1997, Zhao et al. 2010, Arjomandy et al. 2012, Suchowerska et al. 2001).

BODY:

Background:

Radiochromic film EBT2 (ISP) (Figure 1) is composed of a single sensitive polymer layer (28 microns) sandwiched between protective sheets. The radiochromic film is essentially a two-dimensional detector. Ionizing radiation initiates polymerization within the sensitive layer and promotes film darkening. The film is scanned, digitized and the darkening correlated with dose. The sensitive layer is sufficiently thin to miss capturing all the desired particles. High LET radiation with limited range may result in under detection of dose. Specifically, if a proton reaches the end of its range within the supporting materials instead of depositing its dose (and ionizing the polymer), results in undetected dose.
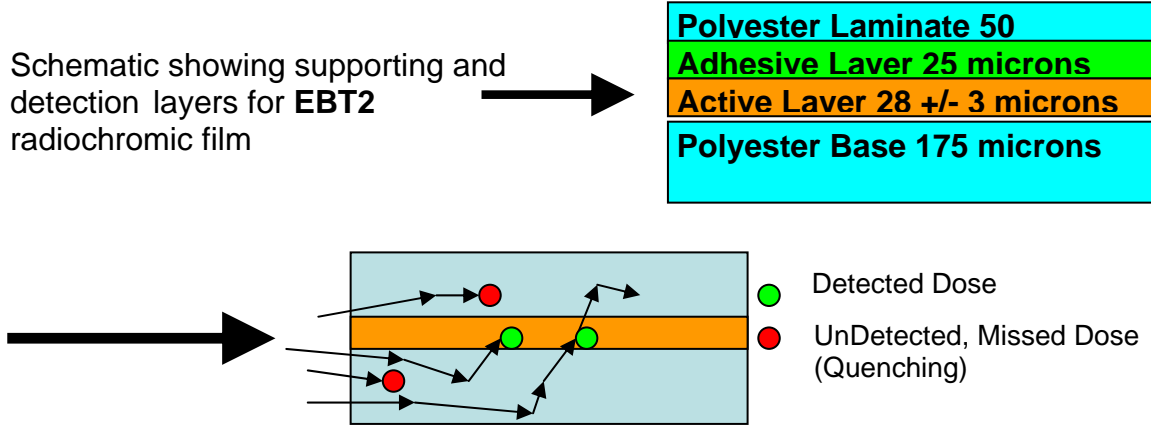
Schematic showing supporting and detection layers for **EBT2** radiochromic film

Polyester Laminate 50
Adhesive Layer 25 microns
Active Layer 28 +/- 3 microns
Polyester Base 175 microns

● Detected Dose

● UnDetected, Missed Dose (Quenching)

Figure 1 Schematic depicting high LET particles and reduced detected dose due to quenching effect.

Radiochromic film suffers from the "quenching" effect for high LET radiation. The quenching is observed especially when the radiation is directed parallel to the film. This phenomenon has been observed a number of times but has rarely been analyzed or discussed in detail. More importantly, it has only treated as a nuisance, rather than exploited for use as an areal detector for LET. Kirby (Kirby et al. 2010) examined the quenching problem by generating Monte Carlo simulations for radiochromic films containing two sensitive layers, not one as in this study. Kirby computed radiochromic film quality factors and found the relative proton stopping powers for protons exceeding 1 MeV was constant but varied substantially for lower energies, especially for protons nearing the end of their range. However, Kirby asserted that the quenching effect is due to differences in ionization. Kirby's relative effective (RE) factor may be consistent with depending on proton loss between the sensitive layers (see discussion).

To quantitatively account for the quenching effect, the sensitivity of radiochromic film is related to the number (or probability) of detected hits Specifically, the Poisson probability P(n,s) of a film with thickness s receives n hits (or ionizing events) from a proton with energy E, and LET is:

$$P(n,s) = \frac{\lambda^n}{n!} \exp(-\lambda)$$ (1)

Where

$$\lambda = \left\{ \frac{E}{LETs} \right\}$$ (2)

It is hypothesized that the relative sensitivity (RS) of the radiochromic film depends on suffering at least one (and possibly more) hits within the film of thickness s

$$RS = \sum_{n \neq 0}^{\infty} P(n,s) = \sum_{n=0}^{\infty} P(n,s) - P(n=0,s) = 1 - e^{-\lambda} \approx \lambda \ (\lambda << 1)$$ (3)

Photons have large energy (MeV) and low LET (0.5 KeV/micron) resulting in large distances between interactions (2000 microns >> 28 microns for film thickness). Therefore   is large (70) and implies a large sensitivity RS for x-rays using film (RS=1, Equation 3).

For protons near the end of its range or end of the Bragg peak, the story is different. At the end of the range, a typical proton energy is around 100 KeV, LET is higher (10 keV/micron) and the interaction length l is roughly 10 microns, smaller than the 28 microns and therefore   ~0.30, and RS is 0.74 (Equation 3), similar to the findings in this work and Kirby (Kirby et al. 2010). In contrast, extrapolating from Vynckier (Vynckier et al 1994), the radiochromic sensitivity RS falls precipitously with high LET (LET>>1) and q~40.

$$\lambda = \frac{E}{LET} \approx \frac{1}{LET}\{\frac{d}{LET-1}\}^q \approx \{\frac{1}{LET}\}^{1+q}$$ (4)

To highlight the effects of LET, the relative difference (r) of the calculated Treatment Planning Dose (D_{TPS}) to the dose measured from the radiochromic media (D_{RC})

$$r = \frac{D_{TPS}{}^p(D_{TPS}-D_{RC})}{(D_{TPS,0})^{p+1}} \propto \frac{1}{RS} \approx \frac{LET}{E/s} \quad (\lambda \ll 1)$$ (5)

and $D_{TPS,0}$, is a normalizer, (~200 cGy in this study). The experimental difference in the treatment planning dose and the measured dose (D_{TPS}-D_{RC}) is due to the high LET for protons. The residual proton energy E deposited within the thin film occurs at the end of the range and needs to be compensated and is very crudely accounted for i.e.

$$\frac{E}{s} \propto D_{TPS}^{-1}$$ (6)

The protons continuously slow at the end of their range (Vynkier et al. 1994) but are not directly accounted for in this analysis. It is hypothesized that the LET is related to a Scaled, Normalized Difference (SND) metric

$$LET \propto SND = \frac{D_{TPS}^{p+1}(D_{TPS}-D_{RC})}{D_{TPS,0}^{p+2}}$$ (7)

The SND is computed (p=0 and separately for p=1) using the registered treatment planning and measured doses at every pixel. This processed quantity SND (Equation 7) is studied to see if it is correlated with LET over a large dynamic range of SND values.

Methods (Overall):

Figure 2 summarizes the workflow. These ideas were tested using pencil beam dedicated nozzle located in the Roberts Proton Therapy Center. A mono-energetic proton pencil beam was directed parallel to radiochromic film sandwiched between solid water slabs. Varian ECLIPSE (EC) Treatment planning system calculated the proton dose deposition within solid water phantom. The darkening due to the proton radiation was converted to dose and the films were scanned with reflective scanner (CanoScan LIDE 700F) using calibration films (Mayer et al. 1994, Mayer et al. 1995). To autonomously handle media imperfections and scanner illumination inhomogeneity, Mayer (Mayer et al. 2012) and Micke (Micke et al. 2011) conceived and tested a multichannel optimization approach and found significant improvements relative to employing a single red channel. The multichannel approach uses all three channels (red, green,

blue) to extract a single dose for each pixel. The experimentally determined dose distribution image was spatially registered to the planned image using fiducial marks delineated using Teflon markers displayed in the CT image and "tattoos marked on the radiochromic film. The SND of the spatially registered images of the absolute planned dose and the detected dose correlated with the local LET. To validate this approach, Monte Carlo simulations were generated to emulate the experimental situation. The proton plan and radiochromic film using protons with a range of 20 cm and narrow and SOPB Bragg peak was used to generated polynomial fits corrections for all the other films with nominal proton ranges of 12.5, 15, and 20 cm. A central region was summed for the registered ECLIPSE treatment plan distribution and radiochromic film in the vertical direction to generate dose profiles. A polynomial fit (of varying degrees) was applied to the SND profiles and the Penn LET plan profile using the proton with 20 cm range. The parameters derived from the 20 cm range were then applied to the other files. Comparative LET profiles of the SND of the ECLIPSE plan with the experimental dose distribution with the Monte Carlo LET simulations. Gamma analysis (Low et al. 1998, Depuyt et al. 2002, Zeidan et al. 2006) was computed for the registered experimental and Monte Carlo simulations, albeit with a wider LET acceptance (25% of the MC LET, 3 mm. for two spatial dimensions)
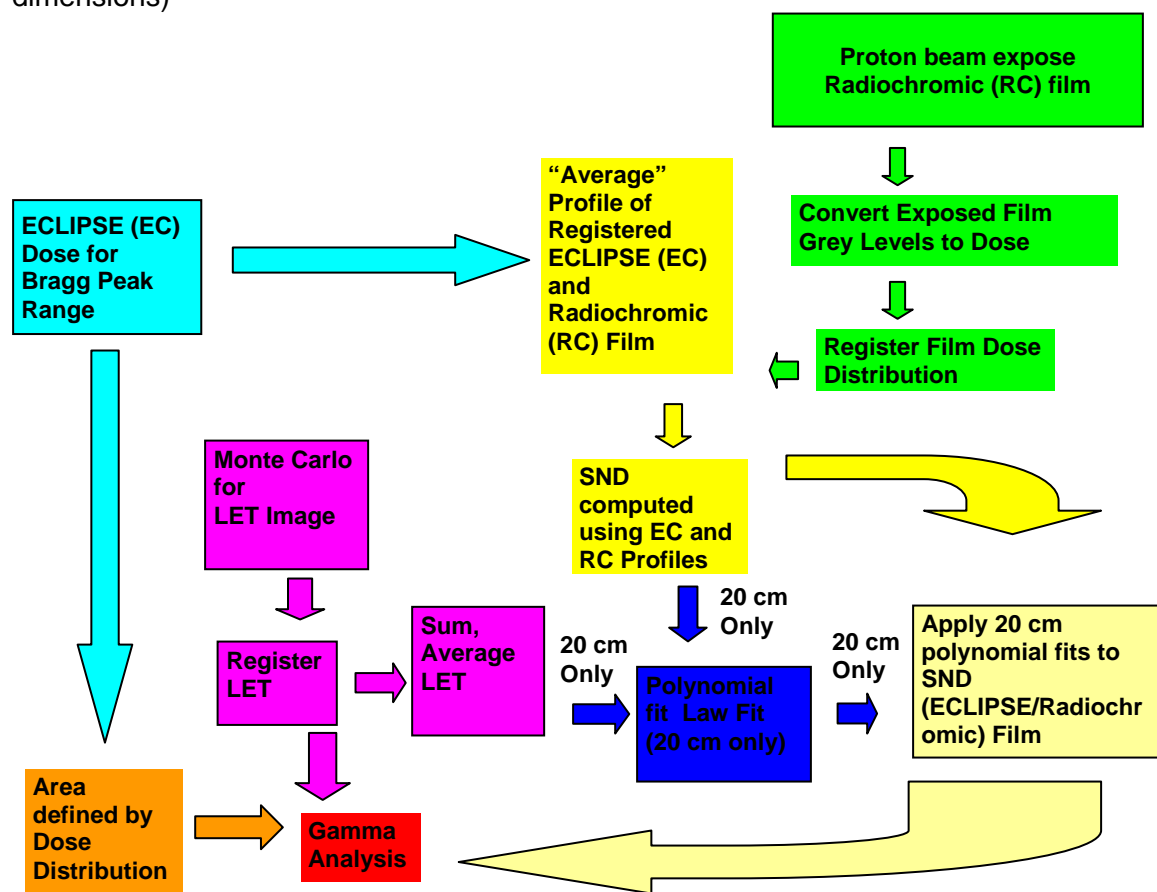

Figure 2. Schematic showing the processes used to generate SND from registered TPS dose, measured radiochromic film, corrections to film and comparison to MC LET.

The proton plan (Figure 3) was remotely generated using the ECLIPSE treatment planning system located at the University of Pennsylvania. and CTs of the phantom were scanned at Walter Reed National Military Medical Center. The distribution shows the familiar Bragg peak.

Protons collide with solid water from the top. Radiochromic film is sandwiched between slices of solid water protons mostly traverse parallel to film surface. Radiochromic grey levels are processed using multichannel optimization and registered
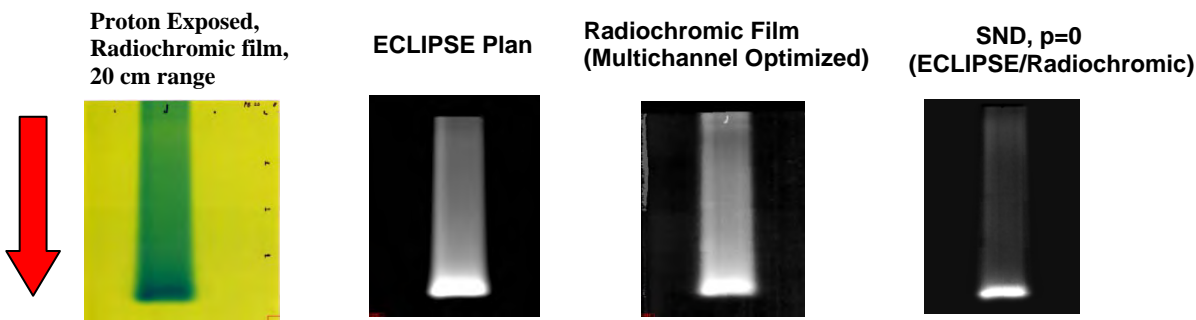
| **Proton Exposed, Radiochromic film, 20 cm range** | **ECLIPSE Plan** | **Radiochromic Film (Multichannel Optimized)** | **SND, p=0 (ECLIPSE/Radiochromic)** |

Figure 3: a) Unprocessed, exposed radiochromic film, b) TPS dose, c) multichannel optimized dose from film, and d) SND (p=0).

to the ECLIPSE calculation. The SNDs (Equation 7) of the doses from the ECLIPSE treatment plan and measured radiochromic film were computed and also shown (Figure 3d).

Proton distribution (Figures 3 a,b,c and 4) shows the familiar Bragg peak for protons bombarding a solid water phantom. The deeper the proton penetration, the larger the discrepancy between ECLIPSE calculation and the dose measured with film. The film is less sensitive to areas receiving high LET radiation relative to low LET. This disparity is highlighted in Figure 4 by comparing SND (p=0, multiplied 500 times) to ECLIPSE and Radiochromic film dose profiles and strongly resembles the MC LET profile (see below). Note the SND peak, similar to the peak LET, is shifted distally relative to the Bragg peak.
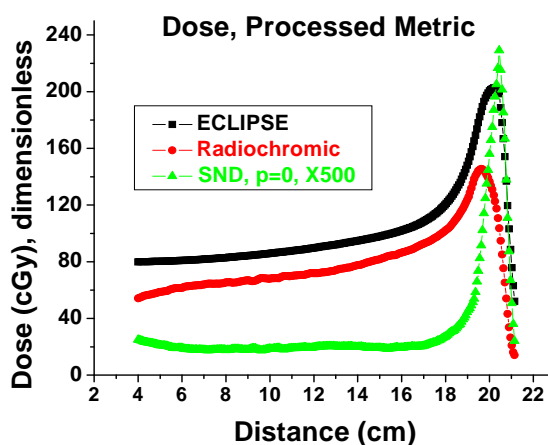

Figure 4. Dose profiles for proton range of 20 cm from TPS, Multichannel optimized dose from radiochromic film, SND for p=0

Monte Carlo Calculation

A Monte Carlo simulation (Figure 5a) was computed with OpenRT, an in-house simulation package based on Geant4. 570, 000 primary protons per spot were used at 92 different spots, which results in 52 million primaries. All particles were permitted down to zero velocity except for gammas and electrons, for which the transport threshold was set at 100 um. The
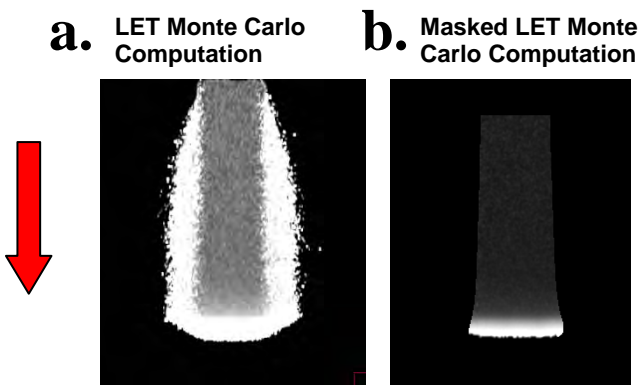

Figure 5. a) Image of LET distribution generated by Monte Carlo calculation for protons having 20 cm range b) Masked LET to only include areas that get > 70cGy

simulation took 350 processor hours split on 12 processors with 2.6 GHz with 4 Gb RAM each.

Figure 5a shows the LET distribution for protons bombarding solid water from the top. The central region is relatively flat corresponding to high energy protons. Near the end of the Bragg peak, the protons slow down considerably depositing energy over short distances resulting in high LET. Outside the field, the fluence is low, but the low energy protons deposit high LET radiation. This study does not examine these high LET protons due to low signal to noise for the radiochromic film. Figure 5b shows a masked region that delineates the actual area of study and only includes areas that exceed 70 cGy. Visually, the measured SND (Figure 5b) resembles the calculated LET (Figure 3d.).

This study assumed that the detection sensitivity only depended on LET variations and hence only on depth inside the material. A key issue is to find the relationship between the SND and the LET profile generated by the Monte Carlo distribution. Figure 6 directly shows that SND and MC LET are correlated and the curves from all proton ranges almost overlap with each other.

This correction is applied to all SND images and gamma analysis of the deviations of the corrected SND and the MC LET is computed.

Figure 6. The LET and SND (p=0) relationships are shown for protons ranges, 12.5, 15, and 20 cm

Results:

Profiles for protons with ranges of 20, 12.5, 15 cm for MC LET as well as polynomial fit using 3, 4, 5 degrees are shown in the Figure 7 a, b, c respectively. The polynomial fits (with varying degrees) were generated from the averaged (in the horizontal direction) SND and LET profiles for protons having 20 cm range. The coefficients from the fits are then applied to the processed (SND) radiochromic film image
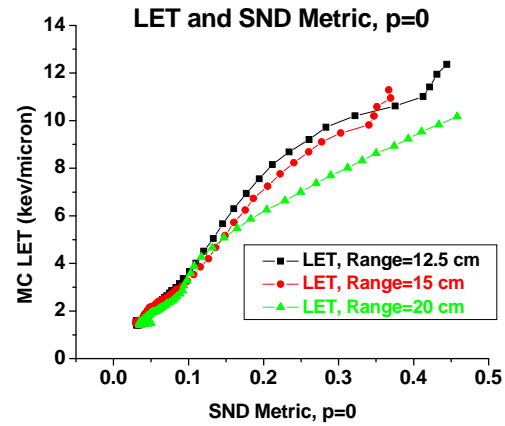

Figure 7. Summed profiles along beam direction (vertical, y direction in figures). Data shows profiles for Monte Carlo LET and corrections to SND (p=0) using 3, 4, 5 degrees in polynomial fits. a). Figure for proton range of 20 cm b) Profiles and corrections for proton range of 12.5 cm using parameters from proton range of 20 cm, Figure a. c) Profiles and corrections for proton range of 15 cm using parameters from proton range of 20 cm, Figure a

The gamma criterion is given by 3 mm in horizontal, vertical directions and 25 % of Monte Carlo LET. Analysis was computed for the area (purple) of doses between 70 cGy and 200 cGy from the ECLIPSE calculation. The discrepancies as measured by gamma analysis between the corrected radiochromic film and Monte Carlo LET were of 6.65 % for protons having a range of 20 cm with a narrow Bragg peak (Figure 8) for 5 degrees of freedom in the polynomial fit and used the SND having p=0. The most significant and largest differences in LET distribution generated by the Monte Carlo calculation relative to the corrected radiochromic film appear at the proximal edge and beam edges suggesting some possible unresolved registration issues.

a. **Area of Gamma (Dose >70 cGy)**
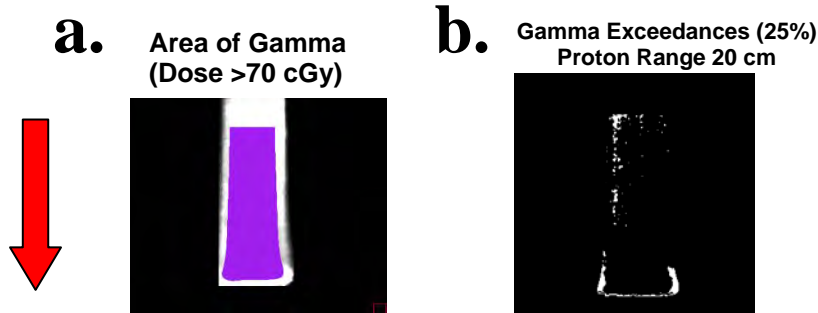
b. **Gamma Exceedances (25%) Proton Range 20 cm**

Figure 8 a) Dose distribution for protons of range of 20 cm. and area for gamma analysis (dose>70 cGy) b) Gamma exceedances for MC LET and correction to SND (p=0) using 5 degrees polynomial fit.

Similar displays of the gamma exceedances are shown in Figures 9 a, b for protons exposing film having ranges of 12.5 and 15 cm, respectively. As in Figure 8b, the displays used 5 degrees in the polynomial fit taken from the protons with a range of 20 cm and using the SND with p=0 for proton ranges 12.5 and 15 cm. In this case, the 9.67 % and 12.2% gamma exceedances were found for areas receiving dose between 70 cGy and 200 cGy.

a. **Gamma Exceedances (25%) Proton Range 12.5 cm**

b. **Gamma Exceedances (25%) Proton Range 15 cm**

Figure 9 a) Gamma exceedances for MC LET and correction to SND (p=0) using 5 degrees polynomial fit for proton range 12.5 cm.b) Gamma exceedances for MC LET and correction to SND (p=0) using 5 degrees polynomial fit for proton range 15 cm.

The exceedances shown in Figure 8b and 9a, 9b mostly occur at the edges of the distal edge of the Bragg peak. In addition, there are exceedances that occur in regions with sharp dose gradients where registration is difficult but also crucial. The LET distribution has greater spatial gradients than dose distributions and registration is a more critical feature.

The gamma exceedances as a function of number of degrees in the polynomial fit are shown in Figure 10 for protons having ranges of 12.5, 15, and 20 cm. Figure 10 also shows the gamma exceedances that result from using exponents of p=0 and p=1 (Equation 7). The gamma exceedances are relatively stable as a function of number of degrees in the polynomial fit, with a slight preference for higher number of degrees. The higher number of degrees however can be

more unstable especially for areas with high spatial gradients. The p=1 exponent yields slightly better and reduced number of gamma exceedances.
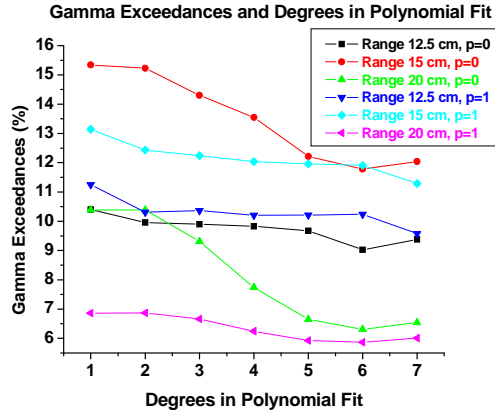

Figure 10. Gamma exceedances for proton ranges 12.5, 15, and 20 cm using polynomial corrections with degrees varying from 1 to 7 applied to SND (p=0,1).

A minimum detectable LET can be inferred from examining the polynomial fits of SND to LET. The average (over each of the seven fits) baseline value for LET (corresponding to SND=0) is 1.33 +/- 0.77 KeV/micron (p=0), 1.15 +/-0.11 KeV/micron (p=1) and 1.24 KeV/micron +/- 0.54 (p=0 and p=1). These minimum LET values exceed the LET for photons used for therapy.

The analysis that was applied to the narrow Bragg peaks was also conducted for the SOPB with modulation of 5 cm. Figures 11a, b, and c show the two dimensional images of the ECLIPSE calculated dose, the measured dose from the radiochromic film, and the LET Monte Carlo calculation for the SOPB for proton range of 20 cm. The broadened peak is evident in a, and b and the LET shows a more gradual increase in the broadened region.
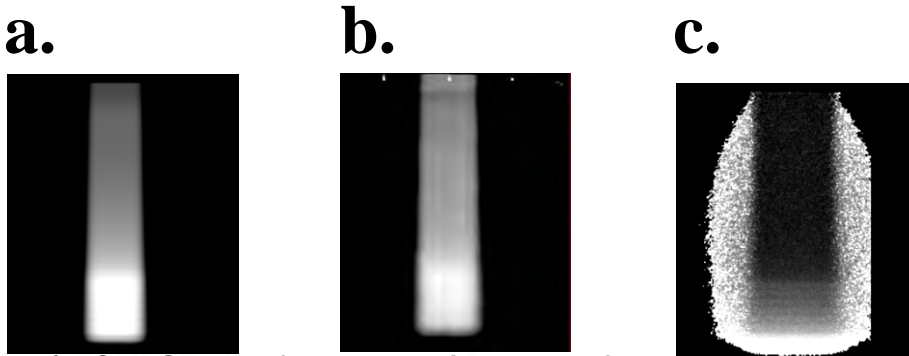

Figure 11, a) ECLIPSE plan for proton with range of 20 cm, Modulation 5 cm b) Measured dose from radiochromic film plan for proton with range of 20 cm, Modulation 5 cm c) Monte Carlo calculation of LET for proton with range of 20 cm, Modulation 5 cm

Profiles for the ECLIPSE and measured doses are shown in Figures 12a. The SND and the LET profile for the broadened Bragg peak are shown in Figure 12b. Figure 12c shows that SND profile is correlated with the LET profile for the SOPB, albeit not as strongly as for the narrow Bragg peak for proton ranges of 15, 17.5, and 20 cm. However, there is greater overlap in the curves relative to the narrower Bragg peak (Figure 6). The 3,4, and 5 degree polynomial fits applied to the SND are shown in Figure 12d.
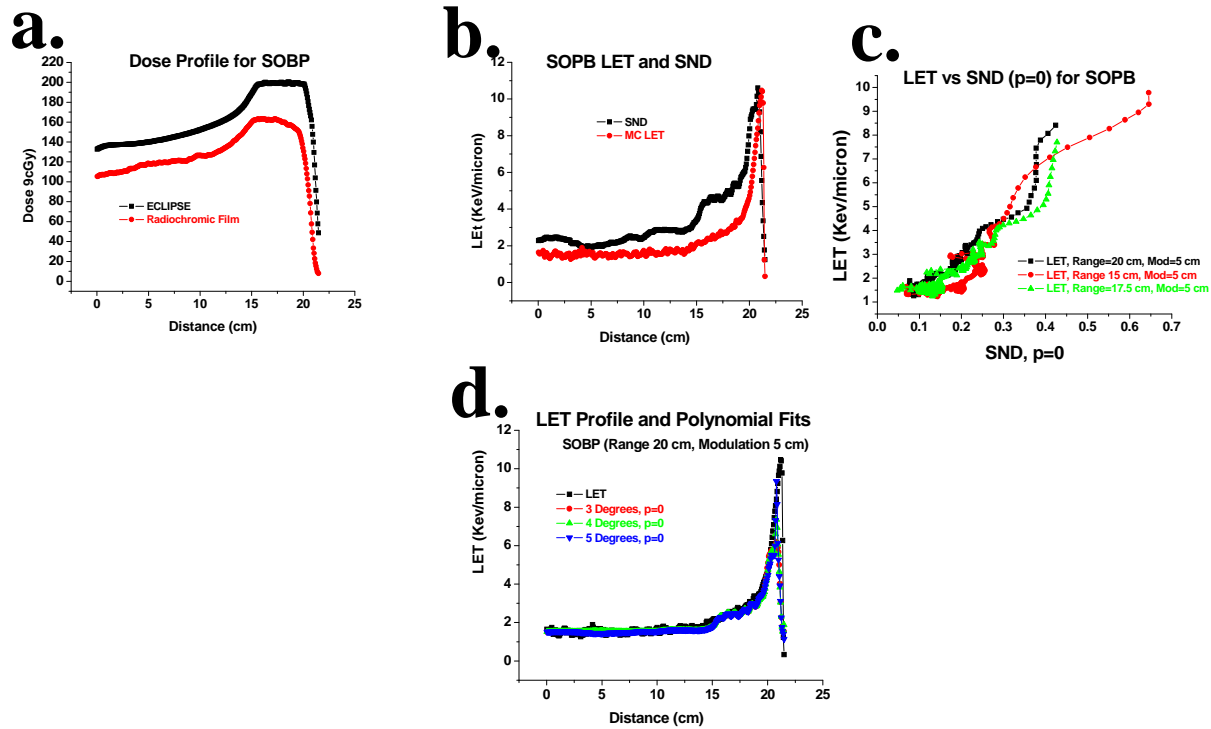
Figure 12. a) Dose profiles of SOPB from ECLIPSE and Radiochromic film b) SND and LET for SOPB, c) LET vs SND for SOPB for Ranges 15, 17.5, and 20 cm and modulation of 5 cm d) LET profile for SOPB, proton range 20 cm, modulation 5 cm. and polynomial fits using 3,4,5 degrees and applied to SND with p=0.

The gamma exceedances for the SOPB as a function of number of degrees in the polynomial fit are shown in Figure 13 for protons having ranges of 15, 17.5, and 20 cm. Figure 13 also shows the gamma exceedances that result from using exponents of p=0 and p=1 (Equation 7). For SOPB, the gamma exceedances are relatively stable as a function of number of degrees in the polynomial fit using degrees >2. The higher number of degrees however can be more unstable especially for areas with high spatial gradients. The p=0 and p=1 exponent SND yields comparable number of gamma exceedances. The SOPB gamma exceedances are slightly larger than those from the narrower Bragg peaks.
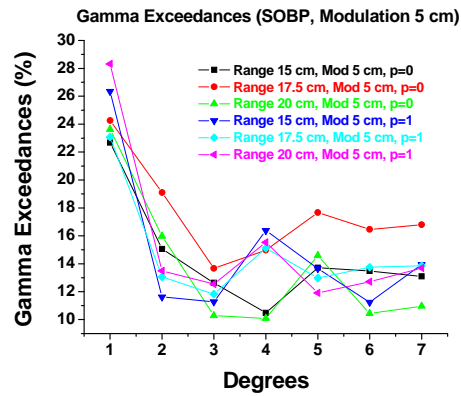
Figure 13. Gamma exceedances for SOPB (Modulation of 5 cm) proton ranges 15, 17.5, and 20 cm using polynomial corrections with degrees varying from 1 to 7 applied to SND (p=0,1).

Discussion:

This study examined a number of metrics to relate the disparity in the absolute measured and treatment dose to the LET before opting for the SND (Equation 7). Specifically, this study calculated and tested the ratio R1=(DTPS/DRC), R2=1-1/R1, and R3=R1*(DTPS-DRC) to assess the LET. R1, R2, and R3 qualitatively resemble the LET distribution Pixels with low R1, R2 were insensitive to LET (data not shown) and uncorrelated with LET. SND correlates better with the LET over all ranges of SND. Finding an appropriate mapping between SND and LET is simpler and more robust, especially when applying the corrections to the LET for protons with ranges of 12.5, 15 cm and SOPB with 15 cm and 17.5 cm. Although SND (Equation 7) is an admittedly crude measure for LET, it is empirically found to yield the best correlation with the MC LET over the largest dynamic range of SNDs.

The exact mechanism for quenching is uncertain. This study found a heuristic approach (Equation 3) and connects the disparity in proton detection to LET. Kirby (Kirby et al. 2010) found that the relative proton stopping powers remained constant (within 2%) for proton energies 1 to 300 MeV for the two sensitive layer detector but shows substantial changes below 500 KeV. Instead (Kirby et al. 2010) ascribed the quenching to energy dependence for ionizing the polymers within the sensitive layer. The sensitive layer separation (Kirby et al. 2010) of the EBT film was substantially less than the MD-55 film and also had a lower proton energy threshold for quenching. It should also be noted that the minimum RE (relative effectiveness, corresponding to 1/R1 from above paragraph) in Kirby's study was 60% to 70% or slightly higher than the 50% of detection (or one out of the two sensitive layers). The present study therefore instead posits the quenching to energy deposition outside the single sensitive layer (or between the two sensitive layers).

Alternative quenching mechanisms suggest saturation from the densely ionizing radiation. To test the saturation mechanism, the radiochromic film should be exposed and analyzed for varying dose rates and doses. Numerous studies found that radiochromic film is insensitive to dose rate deposition. However, the film's response to dose and/or dose rate was not tested in the far distal regions of the Bragg peak corresponding to especially large LET. This study exposed the film to a maximum of 200 cGy, far from the non linear response for this film and also from saturating dose. Dose rates in this study were low (~200 cGy/minute). The model also exhibits "saturation" behavior, albeit one that is relatively constant for large (not low) film sensitivity, RS (Equation 3) for sufficiently high   or E/LET.

Generating an LET spatial distribution map requires high degree of spatial registration between the treatment plan, the Monte Carlo LET calculation, and the measured dose distribution. The beam edges and distal edge of the Bragg peak showed enhanced number of gamma exceedances probably due to these registration issues.

This study confined its examination to the unscatterred, high energy primary protons. The current effort did not examine the scattered protons outside the main field. The scattered protons have very low energy but very high LET based on the Monte Carlo calculations (for example Figures 5a, 11c). To experimentally probe these low dose regions requires greater signal to noise from the radiochromic film and therefore greater proton exposure times These low dose regions may also require further examination of the SND and to possibly other exponents, beyond the p=0,1 and other metrics.

The techniques described in this study for measuring LET are unlikely to also be applied for photons. The minimum LET as determined using the polynomial fits exceed 1.1 KeV/micron corresponding to SND=0. The LET for therapeutic photons is < 1 KeV/micron, below the minimum measured LET in this study. However, dose distributions measured using photon beams directed parallel to the film therefore do not require corrections, as mentioned numerous times in the literature.

From examining the profiles, it appears additional work is needed to evaluate high LET. Nevertheless, this study seems to have successfully measured LET as high as 8 KeV/micron, which is larger than the 5 KeV/micron using BANG gels (Lopatiuk-Tirpak et al. 2012). The far, distal edge of the LET distribution merits further investigation and requires a better approximation than Equation 4.The approach discussed in this study is more appropriate for high LET, albeit for the proximal side of the Bragg peak.

This new tool can potentially measure and test LET in clinically significant configurations such as regions involving tissue heterogeneity. The radiochromic film, unlike the BANG gel may possibly be applied for measuring the LET in variable density regions by inserting the film between suitable phantom materials.

Summary:

Processing and analyzing radiochromic film in conjunction with treatment planning system is a viable method for the measuring LET. The modified film methodology provides a unique experimental areal LET measurement that can verify Monte Carlo measurements and support inferences from current point measurements of LET.

Multchannel Dosimetry

INTRODUCTION:

Quantitatively determine an optimum image analysis procedure to mitigate inhomogeneities within the EBT2 film and from scanning for accurate absolute dose measurement deposited by an external radiation therapy beam. Multichannel dosimetry procedures were conceived, described, and quantitatively tested against single and dual channel dosimetry.

BODY:

Background

Experimental verification of the external beam therapy calculations that account for tissue heterogeneities within the treatment volume requires accurate and robust detectors over the relevant areas. Radiochromic film darkens upon exposure to radiation without further film processing [1]. Radiochromic medium with its high spatial resolution and independent response to energy and particle type, and tissue equivalence can be a candidate as a two dimensional dosimeter for this application [1,2]. The high spatial resolution and sensitivity over extended spatial areas should provide an experimental platform for examining dose distribution perturbation due to tissue heterogeneity. The radiochromic films are tissue equivalent further promoting themselves as dosimetry materials. The EBT2 film [2] with the yellow marker dye was developed to reduce the spatial heterogeneity [2-10] due to manufacturing found in earlier versions of radiochromic film.

There are technical issues and challenges that must be addressed and resolved prior to their application for dosimetry over extended spatial areas. First, a number of researchers [4-11] have been concerned about the uniformity of dose responses of the radiochromic film due to variable thickness/composition generated by the manufacturing process, including the newer film such as EBT and EBT2. In addition, spatially varying illumination of the exposed EBT2 film during scanning to digitize the film contributes to the inhomogeneous dose calculation.

The recent advent of EBT2 radiochromic film has spawned a number of articles examining the new film's properties and procedures for achieving optimal dosimetry. Digitization of the radiochromic film through scanning with a flatbed scanner and exploiting its ability to extract individual color components for the imagery was examined some time ago [12-13] and has become a standard procedure [14,15]. Common mode rejection (taking the ratio of images from two different color channels) was employed to buck out the effect of thickness/composition variations, in particular, Ohuchia [3] used the red and green channels. The manufacturer recommends using red and the relatively insensitive blue channels and these ratios were studied by Pawlicki et al. [4] and Alami et al.[5]. Pawlicki et al. [4] found that taking the ratio of red to blue was essential but conflicted with Alami et al. [5] who found that using the red channel achieved better results than using the ratio of red to blue channels. Andres et al. [6] found that optimal dosimetry choice of red or green channels was dose dependent. McCaw et al [7] found some improvement but also some degradation using red to blue ratio to extract the dose from EBT2 film, depending on the analysis method. Devic et al.[8] extended the range of the dosimetry by stitching the dose from the red channel for low dose, green for intermediate dose, and blue for higher doses. Devic did not use ratios of channels to extend the dose range and also minimize dose heterogeneity issues.

Spatially inhomogeneous illumination for scanning the exposed film can also significantly degrade dosimetric accuracy, especially near the edges of the scan. This error is compounded by the level of dose exposure. Kairn et al.[9] corrected the spatial heterogeneity by using spatially registered, unexposed film and used the red channel but only employed comparison of dose profiles, not gamma analysis. Richley et al.[10] focused on mitigating scanner light scattering. Hartmann et al.[11] used the red channel to examine dose heterogeneity among cut up slices of EBT2 film. Devic et al. [16] characterized the scanner inhomogeneity and its effect on dose distribution. Fiandra et al.[17] and Sauer and Frengen [18] both provided a correction matrix for the scanner inhomogeneity using the red channel and they also incorporated dose levels into their corrections.

To simultaneously and autonomously handle film imperfections and scanner illumination inhomogeneity, Micke et al.[19] suggested a multichannel approach and found significant

improvements relative to employing a single red channel approach. The multichannel approach uses all three channels (red, green, blue) to extract a single dose for each pixel. Micke et al. [19] demonstrated significant alleviation of the spatial inhomogeneity issues. However, no equations were explicitly stated for the corrected dose at each pixel using the multichannel approach. It was not even clear whether an iterative search might have been employed to search for an optimal solution. Direct comparison with Micke et al.was therefore difficult and at best surmised.

This paper examined and resolved each of these technical issues by systematically exploring a number of different dosimetry procedures for reducing the thickness/composition variations within the EBT2 radiochromic film. Specifically this study examined the relative benefits of using the various color channels (red, green, and blue) or combinations of ratios of channels not previously studied. Gamma analysis provided the quantitative discriminator among the various single, dual, and triple channels methods for calculating dose distributions relative to the dose distribution calculated from the treatment plan.

Methods

The overall methodology is summarized by the block diagram shown in Figure 1. The goal was to analyze the absolute dose distribution deposited by a 6 MV photon beam (field size is 10 cm x 10 cm at the isocenter) from a Varian 2100 linear accelerator (linac) directed parallel to an EBT2 film sandwiched between slabs of solid water^{TM}. The phantom was positioned at 100 cm Source to Surface Distance (SSD) and 200 cGy was delivered to dmax. The three sets of images (CT, ECLIPSE Treatment Planner, Radiochromic Film) must be compatibly manipulated. The CT image set was treated as the "base" image because the treatment plan used and was fixed to the CT image. The Varian ECLIPSE plan and the measured dose distribution derived from the radiochromic film were translated and rotated to match reference points or fiducial points (Spee-D-Mark) within the CT image. The spatial resolution (40 dots per inch or dpi) was set by the ECLIPSE treatment plan and the CT was resampled and the radiochromic film was scanned at the same spatial resolution.

Gamma analysis compares the dose distribution from a standard such as a plan to the dose distribution form the test distribution. Gamma analysis (to be described in detail) requires input from registered dose distribution from the Eclipse treatment planning system and the dose extracted from the radiochromic films. In addition, this study, unlike many, applies the gamma analysis to selected regions such as regions of low scattered dose, plateau of high dose, and beam edges. Such an approach requires input of appropriate areas such as regions of interest (shown in Figure 1). In addition, the software development permits input of regions of interest form tissues in the CT, also shown in Figure 1.

All custom software development regarding registration and algorithms for converting exposed images to dose distributions was developed using the Interactive Development Language (IDL).
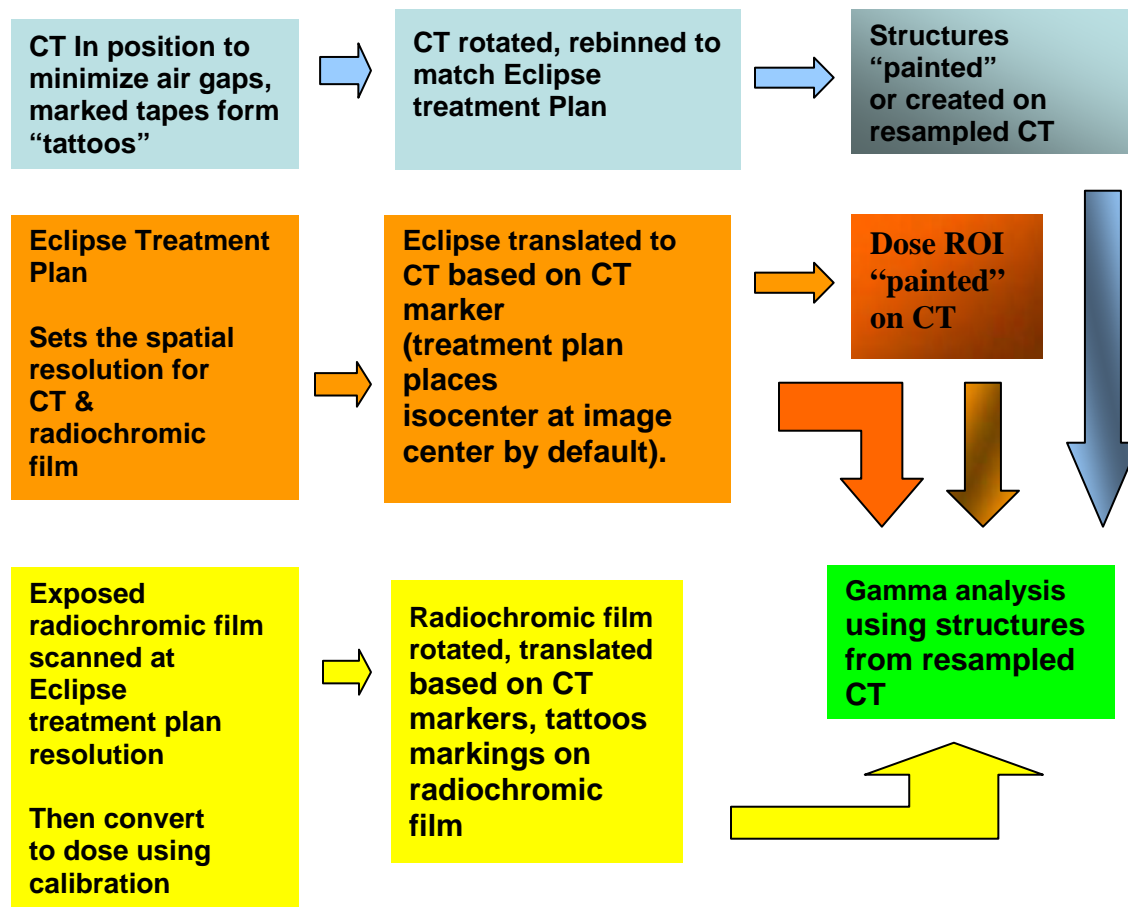
CT In position to minimize air gaps, marked tapes form "tattoos"	→	CT rotated, rebinned to match Eclipse treatment Plan	→	Structures "painted" or created on resampled CT

| Eclipse Treatment Plan

Sets the spatial resolution for CT & radiochromic film	→	Eclipse translated to CT based on CT marker (treatment plan places isocenter at image center by default).	→	Dose ROI "painted" on CT

| Exposed radiochromic film scanned at Eclipse treatment plan resolution

Then convert to dose using calibration	→	Radiochromic film rotated, translated based on CT markers, tattoos markings on radiochromic film		Gamma analysis using structures from resampled CT

Figure 1. A block diagram describing the procedures for comparing calculated and measured dose distributions

CT Rotation

The analysis from exposing film and/or radiochromic film is often problematic due to possible presence of small air gaps between the film and the solid phantom. The phantom was scanned in the CT in the transverse orientation (Figure 2a) so that the weight of the phantom was pressed onto the radiochromic film. In this configuration, additional weight was added if needed to further reduce air gaps. The treatment table supported and remained in contact with the flat part of the phantom, a configuration that is not available for humans. The entire phantom was scanned with spatial resolution of 27.1 dpi, not just the expected treatment area because all CT slices (2 mm spacing) were used to reconstruct the image of the phantom in an orthogonal direction. Nearest neighbor averaging was used to fill in the regions between the slices. The reconstructed and rotated CT (coronal orientation, see Figure 2b) was resampled, again using nearest neighbor averaging so that the CT had a spatial resolution of 40 dots per inch, matching the ECLIPSE treatment plan dose distribution and the scanned radiochromic film image. CT skin markers placed at known distances were used to test the fidelity of the resampling and rotation process and found to be accurate to within less than a pixel (<0.64 mm). The rotated CT was expanded (to 1000 x 1000 pixels) to accommodate the ECLIPSE plan which had a treatment isocenter placed in the center of the image. Marked tapes denoting the CT marker positions were also placed on the phantom and were used to align the phantom during radiation exposure.
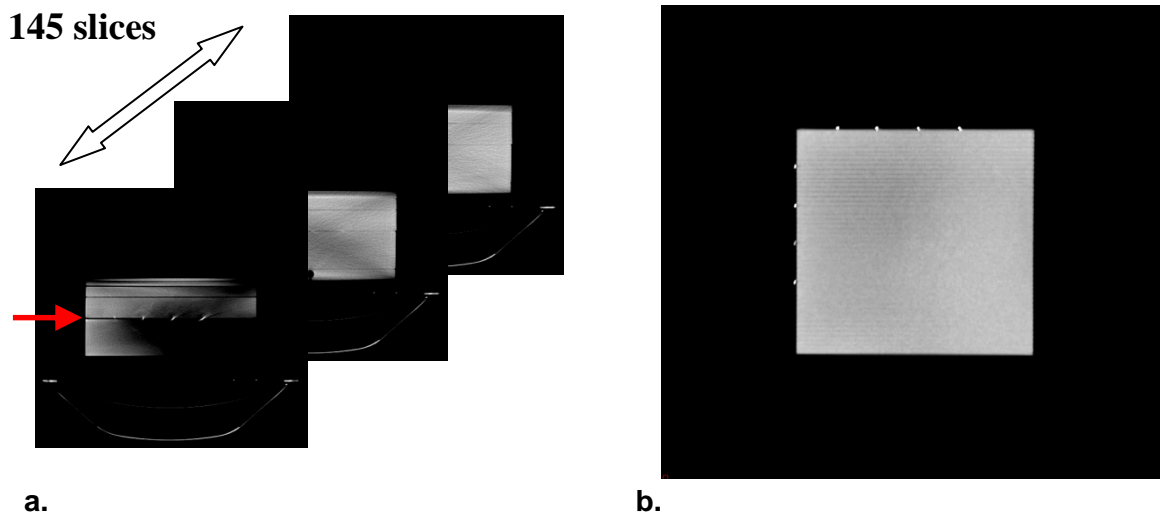
145 slices

a.   b.

Figure 2a. Selected three slices (out of 145) of solid phantom in transverse orientation. CT skin markers shown in first slice. Arrow denotes plane shown in Figure 2b. **Figure 2b.** Rotated image (coronal) of solid phantom. Only single slice of plane abutting placement of radiochromic film for this study is shown.

Scanning:

The exposed radiochromic film was scanned, similar to earlier studies [12-16], with a CanoScan LiDE 700F flatbed scanner in reflection mode using 48 bit digital resolution to digitize the three color channels (Red, Green, and Blue) at a spatial resolution of 40 dpi to conform to the ECLIPSE treatment planning system. All correction options were turned off. The orientation of the film was noted [2] with a small cut in the upper right hand corner. All radiochromic film were positioned identically on the flatbed scanner, after noting the orientation of the film. The lot number for the exposed EBT2 was A11051002A.Radiochromic film were scanned approximately 24 hours after exposure. The EBT2 film are particularly insensitive to visible light [2] but care is taken to minimize exposure to visible light. The radiochromic film grey-levels were converted to dose using calibration films. Smaller film (roughly 10 cm x 12.5 cm) were exposed to 0, 25, 50, 100, 150, 200, 250, 300 cGy placed perpendicular to the beam (10 cm x 10 cm field) sandwiched between solid water^{TM} slabs. In this configuration the monitor units equaled the dose in cGy and simplified the calibration procedure following procedures outlined in the report of Task Group 21. The 10 cm x 10 cm field exposed the solid water^{TM} phantom positioned at 100 cm source to axis distance and the film placed at dmax (1.5 cm), perpendicular to the 6 MV photon beam from the Varian 2100 machine.

The calibration films were scanned. An average grey-level was computed for each red, green, blue (R,G,B) channel using the central region (2 cm x 2 cm or roughly 1000 pixels) conforming to the most uniform dose. A Look Up Table (LUT) composed of the average grey-level (or ratio of grey levels) for each color channel was correlated with dose. The lines connecting the solid symbols in Figure 3 graphically shows the dose versus average detected intensity in the LUT for the red, green, blue channels. However, each pixel within the array may not conform to the average pixel due to differences in scanner illumination. So the dose extrapolated for the R,G,B channel (D_R, D_G, D_B) respectively may differ from each other due to varying response for a given perturbation. The multichannel approach autonomously projected a correction to an expected common dose D based on the individual slopes and response of each channel..
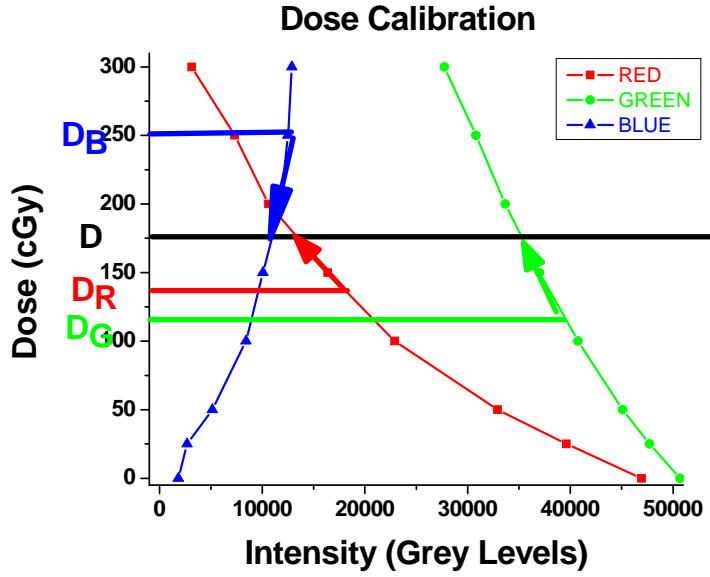
22

Figure 3. Calibration for converting grey levels to dose for red, green, blue channels. Optimized multichannel correction schematically shows the shifted extrapolated doses D_R, D_G, D_B relative to optimized D based on local derivatives $a_k(i,j)$ (Eq 3, used in Multichannel approach)

The test profile distribution was converted to dose through interpolating the LUT[1,7]. Globally the dose grey level functions are non-linear. Over small stretches of dose and grey levels, the calibration was essentially linear. In addition, using relatively low doses (<300 cGy) limits the degree of non-linearity of the LUT for EBT2. Higher doses beyond those used in this study will require a more refined calibration table to ensure linearity over the small dose and grey level intervals and possible higher order corrections beyond the first Taylor series approximation (Eq 2) for the multichannel algorithm..

This study tested various schemes for converting grey-levels to reduce the effects of the heterogeneity. These processes are applied to the calibration imagery (for a new LUT) and the test dose distribution. The manufacturer [2] recommends for individual pixels located at coordinate i,j (in the horizontal, vertical direction, respectively), taking the ratio of the red channel R(i,j) to the blue channel B(i,j) from scanning the film with a flatbed scanner. Using the Beer-Lambert Law, the grey-levels are normalized by the unattenuated, constant light source I_0 from the flatbed scanner and the ratio of the logarithms are computed or

$$\frac{R}{B}(i,j) = \frac{\log(\frac{R(i,j)}{I_0})}{\log(\frac{B(i,j)}{I_0})} \qquad (1)$$

A similar ratio Green to Blue ratio was computed using the green channel

Taking the ratio of the channel that is most sensitive to composition/exposure to one that is relatively independent of exposure but experienced the same dependence on thickness/composition to help suppress thickness/composition variations[2-11] of the film. In practice, the blue channel response weakly depends on radiation exposure. This study

generated dose distributions using the red channel R(i,j)) alone, green channel G(i,j) alone, ratios of the red to blue channel and green to blue channel and hybrid version that combined the green to blue ratio for higher doses (above 80 cGy or 0.20 optical density and was likely scanner specific) to the red to blue ratio for lower doses.

New Multichannel Approaches

Another approach employed all three color channels to autonomously correct for local inhomogeneous spatial distribution in film thickness and scanner. This version of the multichannel approach independently varied the dose D and disturbance   (or channel-independent perturbation, see Equations 2, 7) to search for the optimal dose at each pixel. This study proposed and found an equation for the corrected dose. Therefore the optimized dose was quickly computed at each pixel. The goal was to find a common and expected dose D derived from extracted red, green, blue channel doses. The algorithm applied a first order Taylor expansion to the dose due to a small perturbation (same for all channels) and minimized the cost function difference   i,j   (Equation 2) between the projected

$$\Phi(\Delta(i,j), D(i,j)) = \sum_{k=1}^{3} (D_k(i,j) + a_k(i,j)\Delta(i,j) - D(i,j))^2 \tag{2}$$

dose D_k i,j +a_k i,j   i,j   for each color channel k (red, green, blue) relative to the projected dose D. D_k i,j   was the dose directly derived from the LUT for each color (i.e. R(i,j), G(i,j), B(i,j) for the red, green, blue channels respectively), a_k i,j   was the derivative

$$a_k(i,j) = \frac{\partial D_k}{\partial I_k}(i,j) \tag{3}$$

of the LUT for the kth channel (see Figure 3), and   (i,j) is the local perturbation (illumination, thickness) that affected all channels, and I_k was the intensity for a given channel, i.e. (R(i,j),G(i,j),B(i,j)). Interpolation was required to accurately determine the slopes or $a_k(i,j)$. D(i,j) was the corrected dose generated from solving the simultaneous partial differential equations

$$\frac{\partial \Phi}{\partial \Delta}(i,j)(\Delta, D) = 0. \tag{4}$$

$$\frac{\partial \Phi}{\partial D}(i,j)(\Delta, D) = 0. \tag{5}$$

and resulted in the optimized dose D at pixel location i,j

$$D(i,j) = \frac{D_{ave}(i,j) - (wt(i,j))\dfrac{\sum_{k=1}^{3} D_k(i,j)a_k(i,j)}{\sum_{k=1}^{3} a_k(i,j)}}{1 - wt(i,j)} \tag{6}$$

The appropriate correction or "disturbance map" at each point was

$$\Delta(i,j) = \frac{\sum_{k=1}^{3}(D(i,j)-D_k(i,j))a_k(i,j)}{\sum_{k=1}^{3}a_k^2(i,j)} \tag{7}$$

Where the average dose $D_{ave}(i,j)$ was

$$D_{ave}(i,j) = \frac{1}{3}\sum_{k=1}^{3}D_k(i,j) = \frac{1}{3}(D_R(i,j)+D_G(i,j)+D_B(i,j)) \tag{8}$$

And the weight for the channels $wt(i,j)$

$$wt(i,j) = \frac{1}{3}\frac{(\sum_{k=1}^{3}a_k(i,j))^2}{\sum_{k=1}^{3}a_k^2(i,j)} \tag{9}$$

and $wt(i,j)$ ranged from $0 < wt_i < 1$. If $wt(i,j)$ was sufficiently small, then a valuable approximation for the corrected dose $D(i,j)$ was

$$D(i,j) \approx D_{ave}(i,j) \tag{10}$$

EBT2 film was sandwiched between slabs of solid water™ and exposed to 6 MV photon beam. Figure 4a. shows the rotated (by 90 degrees) uncorrected distribution from the single red channel. Figure 4b shows the optimized multichannel corrected dose distribution $D(i,j)$. (Equation 6) Figure 4c shows the disturbance distribution (i,j) (Equation 7) rotated by 90 degrees. Note the stripes from thickness variations in the film in Figure 4a and are also seen in Figure 4c. Figure 4d shows the residual error in dose (Equation 2)
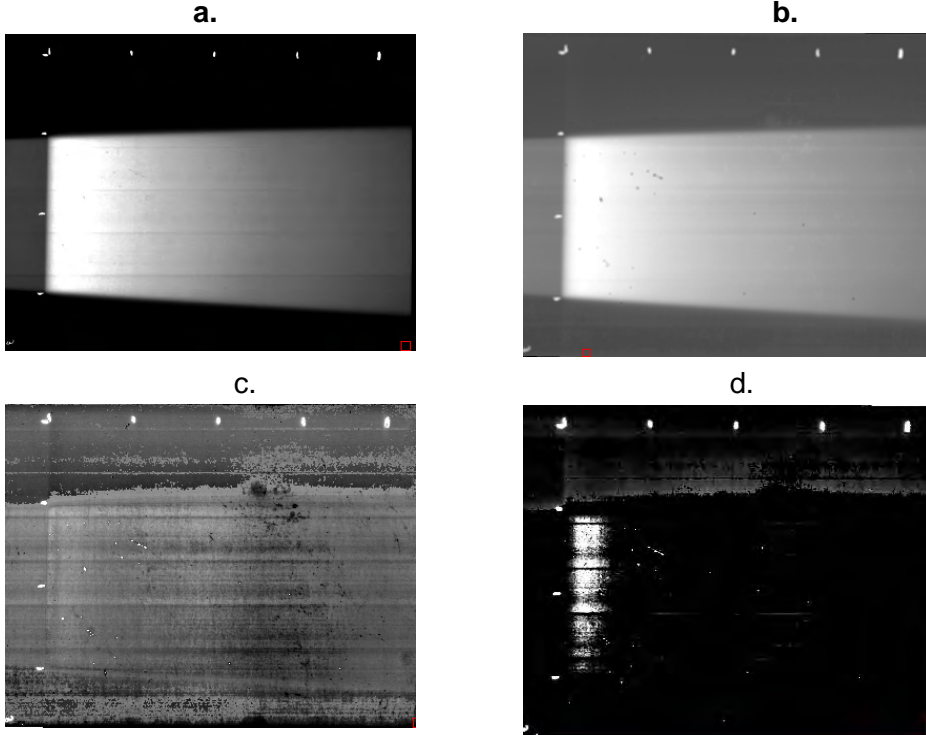

a.

b.

c.

d.

Figure 4a. Rotated (by 90 degrees) dose distribution using red channel. **4b** Corrected dose distribution.   D(i,j) (Equation 6) using the optimized approach. **4c** shows the disturbance distribution   (i,j) (Equation 7) rotated by 90 degrees. Note the stripes due to thickness variations **4d** Residual error in dose (Equation 2)

Previous Multichannel Efforts

Micke et al [19] recently suggested, tested, and broadly outlined a multichannel approach for correcting the inhomogeneities in the dosimetry process. The Micke et al. cost function differed from the multichannel process described in Equation 2. Following the approach of Micke et al., the cost function was

$$\Omega(i,j) = \sum_{k \neq m}^{3} (D_k(i,j) + a_k(i,j)\Delta(i,j) - (D_m(i,j) + a_m(i,j)\Delta(i,j)))^2 \tag{11}$$

Due to the different cost function, Micke et al generated and applied a different disturbance factor than used in equation 11. Micke et al. also applied his analysis to the fitted optical density calibration, not to the raw grey level calibration described in this study. For the Micke et al. approach, only single derivative with respect to   might have been applied to Equation 11 (but not two derivatives as in Equations 4, 5)

$$\frac{\partial \Omega}{\partial \Delta}(i,j) = 0 \tag{12}$$

The resulting shift   (i,j) might have been

$$\Delta(i,j) = -\frac{\sum_{k \neq m}^{3} (D_k(i,j) - D_m(i,j))(a_k(i,j) - a_m(i,j)}{\sum_{k \neq m}^{3} (a_k(i,j) - a_m(i,j))^2} \tag{13}$$

In this formulation, each channel might have been treated equally and corrected using the procedure outlined above, i.e.

$$D(i,j) = \frac{1}{3}\sum_{k=1}^{3} (D_k(i,j) + a_k(i,j)\Delta(i,j)) \tag{14}$$

The dose D might be generated by inserting the computed shift   (Equation 13) into the corrected average multichannel dose (Equation 14). This approach generated an identical dose distribution as that derived from Equation 6, although generated in a very different manner.

Summary of Dose Determination Algorithms

The list of conversion of grey-level processing algorithms is summarized in Table 1. The Table displays, names, a short description, and its associated equation.

Table 1: List of Grey-Level Processing Prescriptions

Name	Description	Formula
Red Channel	Red alone	$R(i,j)$
Green Channel	Green alone	$G(i,j)$
Red to Blue Ratio	Registered Red to Blue Ratio (Equation 1)	$R/B(i,j)=\dfrac{\log(\frac{R(i,j)}{I_0})}{\log(\frac{B(i,j)}{I_0})}$
Green to Blue Ratio	Registered Green to Blue Ratio (Equation 1)	$G/B(i,j)=\dfrac{\log(\frac{G(i,j)}{I_0})}{\log(\frac{B(i,j)}{I_0})}$
Hybrid	Apply Green to Blue Ratio for higher dose and Red to Blue Ratio for lower dose	$Hybrid(i,j)=R/B(i,j) + G/B(i,j)$
Average	Average over all channels (Equation 8)	$Ave(i,j)=(1/3)(D_{Red}+D_{Green}+D_{Blue})$
Optimize Multichannel	Optimize correction using all channels (Equation 6)	$Opt(i,j)=(Ave(i,j)-wt(i,j)\ a_k(i,j)D_k(i,j)/\ a_k(i,j))/(1-wt(i,j))$

Registration:

Comparing experimentally determined dose distributions with the corresponding calculated treatment plan required precise registration between the two sets of images. The solid water^{TM} was placed on the CT imaging and treatment table in a configuration convenient for placing CT markers. These markers were used for registering the CT to both the treatment plan and the detected radiation dose distribution from the radiochromic film. The CT images were digitally rotated for convenient volumetric contouring for dose area histograms and gamma analysis. The rotated CT image was resampled to match the spatial resolution of the scanned dosimetric distribution and treatment plan. The treatment plan was calculated using the CT image in the customary fashion. The treatment plan planes were translated through triangulation of the treatment isocenter to the CT markers in the CT image. The radiochromic film imagery was rotated and translated to the CT images using two coincident points from the CT skin markers in the CT image and "tattoos" marked on the radiochromic film.

This study used a "two-point" approach to translate and rotate the radiochromic film to the desired resampled CT slice. The common "pivot" point for the CT and radiochromic film was used to translate the radiochromic film and the radiochromic film image was then rotated about the pivot point. The average error in transforming the fiducial points (excluding the pivot) was 1.39 pixels or 0.883 mm. On average, a similar error was expected for transforming all points within the radiochromic film image.

Treatment Plan Procedures:

This study used Varian's ECLIPSE treatment planning system to compute the expected dose distribution. The plan computed the dose distribution intended to deliver 200 cGy to dmax and the phantom was positioned at 100 cm SSD. The treatment plan was generated from the CT scan of the phantom. The external beam depth profiles from Varian 2100 6 MV photon beam that characterize the dose deposition in water were stored and used to compute the dose deposition. The external beam was checked on a daily, weekly, yearly timetable to ensure agreement with the current condition of the beam and the stored data. The ECLIPSE plan generated DICOM image files for the predicted dose along desired planes. The spatial resolution for the image dose was chosen to be 40 dpi, conforming to the resampled CT image and scan of the exposed radiochromic film. The isocenter for the plan was placed at the image center, by default. The spatial transformation of the treatment plan simply meant translating the isocenter, or image center to the isocenter of the CT scan that was marked by a CT marker. No rotation was applied to the treatment plan image.

All registered images are shown in Figure 5. Figure 5a shows the rotated and resampled CT and the area of dose exceeding the 100 cGy within the treatment plan in magenta, the beam edge with doses ranging from 25 to 100 cGy in red, and scattered dose in yellow (5-15 cGy). The high dose gradients were extremely sensitive to misregistration between the plan and the experiments. Figure 5b shows the translated, rotated dose distribution derived from the radiochromic film. Figure 5c shows the translated ECLIPSE treatment plan.

Figure 5a shows the CT and the area of dose exceeding the 100 cGy (magenta), dose between 25-100 cGy (red), dose between 5 to 15 cGy) the beam edge (yellow). **Figure 5b** shows the translated, rotated dose distribution derived from the radiochromic film. **Figure 5c** shows the ECLIPSE treatment plan.

Quantitative Assessment of Agreement between Plan and Experiment (gamma analysis):

The various methods for scanning the exposed radiochromic film, grey-level conversion to dose, and dosimetry procedures, were tested by comparing them to the treatment plan through gamma analysis [20-22]. Gamma analysis examined the deviation of the treatment plan (considered to be the reference image) with the experimentally determined dose distribution at the pixel level. The gamma analysis procedure generated a difference image for the registered set of images and computed a "decision" surface with the geometry of a three dimensional ellipsoid. Calculated points that resided within the ellipsoid constitute good agreement between the treatment plan dose distribution and the experimentally derived dose. Conversely, points that appeared outside the ellipsoid are identified as areas of poor agreement or referred to as "exceedances" in this paper.

Figure 6a shows the gamma analysis display using the Red only processing. The white pixels show gamma values that exceed 1 and show regions of most serious disagreement between the plan and the experimentally derived dose distribution. Figure 6b shows exceedances using the optimized multichannel algorithm. Adding more channels such as the optimized multichannel algorithms for extracting dosimetry distributions reduced gamma exceedances from 8605 to 3110 (out of 74,312 pixels within the region of interest).(see Table 2).

a.   b.

Figure 6a shows the exceedances (depicted as white) for the gamma distribution from Red only processing. **Figure 6b** shows the exceedances for the gamma distribution from optimized correction.

Results:

The scanning, data processing, and phantom handling schemes were evaluated by computing the number of pixels within the treatment area having gamma values exceed 1 (see Table 2). The larger the number of these pixels, the poorer the agreement between the experimentally determined dose and the treatment plan. For this analysis, the ellipsoid axes were prescribed to the standard 3% of the maximum dose or 6 cGy (D_{gamma}) and 3 mm in horizontal, vertical directions (x_{gamma},y_{gamma}). If this minimum gamma exceeded 1, then the experiment was ruled to disagree with the treatment plan. Table 2 lists the results of applying the standard red channel, green channel, the manufacturer's recommendation for taking the ratio of red to blue channels (Equation 1), ratio of green to blue channels (Equation 1), the hybrid of green to blue ratio with the red to blue, Optimized multichannel (Equation 6) and averaged multichannel algorithms (Equation 8). The analysis examined the entire area, high dose regions, scattered dose, and the beam edge. The best agreement occurred in the relatively homogenous dose regions (high dose, scattered dose) and was weak in the high dose gradient and where a high degree of registration was required for accurate dose measurement.

Table 2. Gamma analysis fraction of exceedances (%) of total of pixels and scanning, image processing, region conditions

Name	Total 5 - 300 cGy (%) (74,312 pixels)	"High" Dose 100 - 300 cGy (%) (38,329 pixels)	Scatter 5 - 15 cGy (%) (26,307 pixels)	Beam Edge 25 – 100 cGy (%) (6679 pixels)
Red	11.6	14.7	5.3	28.3
Green	10.9	11.7	7.7	31.2
Red to Blue	6.3	6.0	5.2	21.6
Green to Blue	4.8	2.8	5.5	21.7
Hybrid Ratios	4.7	2.8	5.3	21.7
Optimized Multi	4.2	2.0	5.1	22.0
Average Dose	4.1	1.6	5.2	23.0

Although only an approximation, the average dose algorithm appeared to generate few exceedances (Table 2) relative to other algorithms. The computed weight (equation 9, Table 3) was low for all doses in this study. The small values for the weight factor wt (Table 3) implied that the average dose derived from the three color channels provided a valid approximation for the more exact analysis (Equation 6). The blue channel calibration curve was almost orthogonal to the red and green channels for most dose levels used in this study (see Figure 3).

Table 3 Weight factors (wt) (Equation 9) for the dose ranges in the optimized multichannel .algorithm

Dose Range (cGy)	Weight (Wt)
0.0-25.0	0.108
25.0-50.0	0.0153
50.0-100.0	0.0012
100.0-150.0	0.0235
150.0-200.0	0.00939
200.0-250.0	0.0822
250.0-300.0	0.206

Some general observations can be inferred from the gamma analysis. Processing with the green channel usually performed as well or better than the red channel. Using the blue channel required image averaging to sufficiently reduce the temporal noise.

Summary:

This study generated procedures and algorithms for accurately determining doses and compared the treatment planning dose distributions calculated from the planning system and measured from the EBT2 radiochromic film. Specifically, this study developed algorithms that handled issues of thickness/composition heterogeneity within the radiochromic film due to the manufacturing process on dose distribution and also reduced the effects of inhomogeneous illumination during the scanning of the EBT2 film. This methodology avoided using cumbersome, registered correction matrices.

This study conceived and tested the new hybrid combination of green to blue ratio to the red to blue ratios. Also this study proposed and tested a multichannel dose determination algorithm. Averaging the test image mitigated temporal noise in the blue channel and the reduced noise is essential for implementing blue channels in ratio and multichannel algorithms. This study explicitly described the algorithm and found a closed form (Equation 6 and 8). Micke et al. [19] did not explicitly state the corrected dose and disturbance and so it was difficult to directly compare this effort with the results from Micke et al. [19]. Micke et al. used a different disturbance map and also employed a fitted optical density, not the raw grey levels to extract doses from each channel. This study also compared the multichannel algorithms to those using two channels or channel ratios, not just to a single channel. The hybrid combination of the channel ratios performed at a similarly high accuracy level. The multichannel average (Equation 8) of the recorded doses taken from each channel performed well for this flatbed scanner operating in reflection mode. However, the high performance using the multichannel average may be due to the low weight factor and can be attributed to the blue channel calibration curve being almost orthogonal to the red and green channels for most dose levels used in this study

This study employed gamma analysis to compare processing schemes for measuring the absolute dose distributions from EBT2 radiochromic film. This study examined doses deposited parallel to the external beam, not perpendicular to it, as in most other efforts. In this study, the green channel generally performed as well or better than the red channel for this flatbed scanner. Pixel level corrections using channel ratios and multichannel approaches resulted in substantial improvement. This pixel level correction was efficient and the calculations were quick (less than 5 seconds) The speed of the calculation for each pixel was attributed to using the closed form (Equation 6) rather than iteratively searching for an optimal solution. The multichannel approach required three channels but also used the derivative of the look up table as input.

There were several additional features discussed in this study. To reduce the air gap between the film and solid water^{TM}, the phantom was scanned in a geometry that permitted compression without applying a bulky vice. The CT imagery was resampled and rotated for generating the desired regions of interest for gamma analysis. Due to the absence of bulky devices, the entire radiochromic film was simply inserted between slabs of phantom without requiring cutting the film to conform to the shape of anthropomorphic phantoms. In addition, the "two point" registration permitted registration among the CT imagery, treatment plan, and film dosimetry without assuming that the phantom and film were aligned during CT scanning.

Organ Motion

Jessica Sheehan / Arnaud Belard

INTRODUCTION:
In the United States, lung cancer is the leading cause of cancer deaths and the second most diagnosed cancer for both men and women. Lung cancer is typically classified as either small cell or non-small lung cancer. Radiation therapy is commonly delivered in combination with other modalities for a large number of patients with either small or non-small cell lung cancer. Radiation therapy utilizes ionizing radiation targeted locally to damage cancer cells in a manner that often leads to cell death; however, damage to normal tissues also occurs.

Accurate treatment of a patient's cancer while attempting to minimize damage to normal tissues is complicated by the presence of organ motion, with lung motion being the most formidable. Techniques to mitigate (ceasing the motion) or remove (gating of the treatment) the effects of

motion are employed in an attempt to minimize the damage and exposure of healthy tissue to radiation without compromising the treatment of the patient's cancer. Thus, for a radiation dose to be deposited effectively to the treatment site, tracking of the motion and adjusting delivered radiation is desired. The development of this technique requires a dynamic lung phantom that mimics human breathing, matches lung tissue density and heterogeneity, and can incorporate lung tumors for analysis.

This study designed, constructed, and is assessing a dynamic lung phantom for the use in radiation treatment verification. The dynamic lung phantom was designed to be progressively tested, permitting experimenters to examine healthy lungs and lungs with a tumor (varying locations possible).

BODY:

A custom inflatable was commissioned from Jet Creations. Several iterations of the inflatable have been produced and reviewed. Figure 1 shows a digital imagine of the latest version of the inflatable, however the next iteration is currently in production. Below outlines the various research phases that will followed to best utilize the custom inflatables once suitable lungs are produced. Testing of the implementation of these phases is being conducted on the imperfect inflatables to perfect the method.
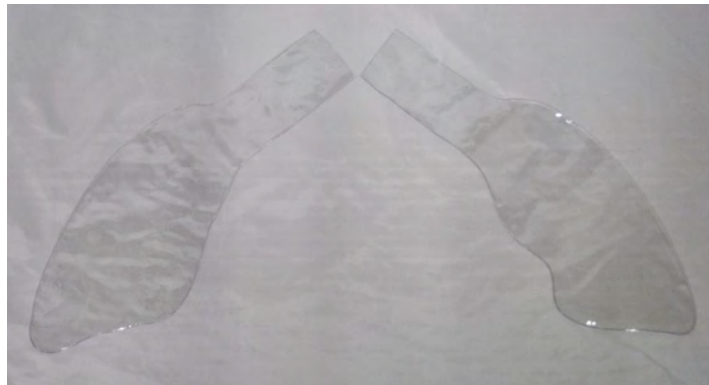

Figure 1: Digital Image of Custom Inflatable

Phase 1: Motion Exclusive Analysis

This phase would consist of limiting the analysis to lung motion of the dynamic phantom lung. The gafchromic medium would be placed externally on the phantom to determine accuracy of spot dosing, collect control data for future research, and foster understanding of the accuracy of predictive models with organ motion.
Figure 2 shows the dynamic lung phantom with externally placed gafchromic medium. Several locations are chosen to enhance understanding and robustness of the data sets generated. The locations should coincide with desired locations of tumor sites in later phases of this research.
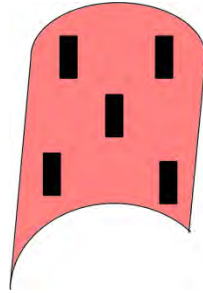
Figure 2: Dynamic Lung Phantom with Gafchromic Medium

Phase 2: Motion and Tumor Exclusive Analysis

Follow up research in phase 2 would incorporate the addition of one tumor site, centered to mimic the highest statistical location of a lung tumor. Two potential placement methods exist for the gafchromic medium for this phase, with the potential of utilizing both for robustness of data collection if desirable. Figure 3 a. and b. shows the two distinct methods of placing the gafchromic medium within the tumor.

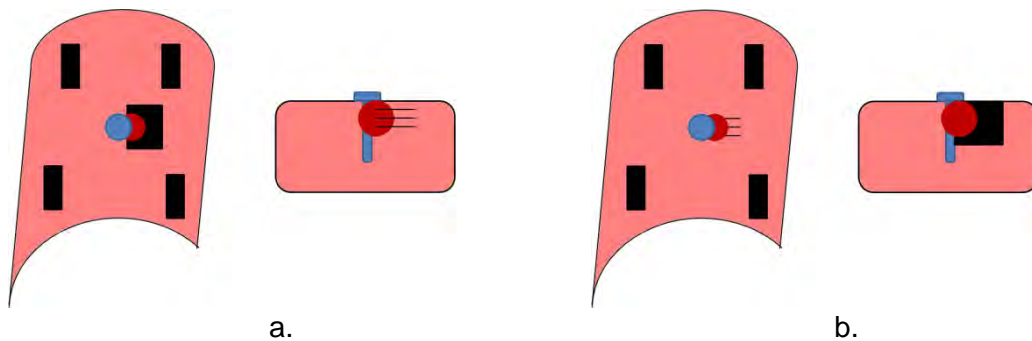a.   b.

Figure 3: Dynamic Lung Phantom with Centered Tumor Site: a.) Gafchromic Medium within Tumor Placed Horizontally and b.) Gafchromic Medium within Tumor Placed Vertically

Figure 3 a. demonstrating the horizontal to beam path placement, and Figure 3 b. showing the perpendicular to beam path orientation. The external gafchromic medium from the previous phase is shown to remain, and could be used to determine how the presents of a tumor affects these sites and predictive modeling accuracy.

Phase 3: Heterogeneous Tissues and Tumor Analysis

Phase 3 furthers the similitude of the dynamic phantom to human anatomy by including material to represent the heterogeneous lung tissue that would exist between the outer lung layer and the tumor. Figure 4 shows the centered tumor site with the addition of a piece of cork between the tumor and the outer lung layer. For robustness multiple materials can be used to generate comparison data, as well as the potential to layer the materials between the outer lung layer and tumor for increased accuracy.
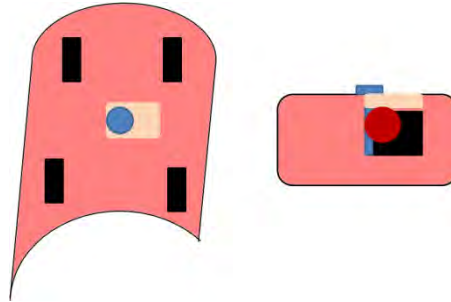
Figure 4: Dynamic Lung Phantom with Centered Tumor Site with Heterogeneous Tissue Material

Phase 4: Secondary Site Tumor Analysis

To further the understanding of how the tumor location affects lung motion and predictive modeling accuracy, a secondary tumor site can be chosen. Figure 5 shows the secondary tumor site in the upper left quadrant of the left lung. Once these sites are incorporated, they must remain, but the tumor and heterogeneous lung tissue material can be removed. Again, the external gafchromic medium has been left to continue to collect control data and determine the differences between motion and modeling when: no tumor is present, a centered tumor is present, a centered tumor is present with heterogeneous lung material, and a non-centered tumor site exists.
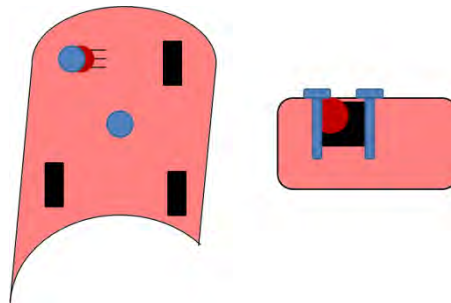

Figure 5: Dynamic Lung Phantom with Secondary Tumor Site

Phase 5: Secondary Site Heterogeneous Tissues and Tumor Analysis

Phase 5 would be a replication of phase 3 with the non-centered tumor site. Figure 6 shows the addition of the heterogeneous lung tissue material.
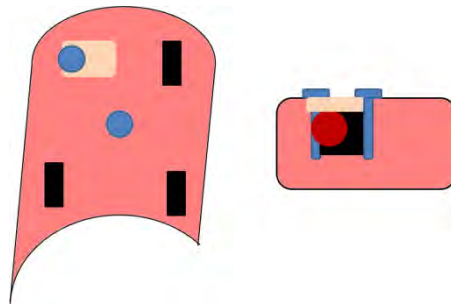

Figure 6: Dynamic Lung Phantom with Secondary Tumor Site with Heterogeneous Tissue Material

Phase 6: Dual Tumor Site Analysis

This phase would determine the effects of multiple tumor sites on lung motion and predictive modeling accuracy. Figure 7 shows the centered and secondary tumor sites with the external gafchromic medium for robustness. This phase would be a repetition of phase 2 or phase 4 with multiple tumor sites.
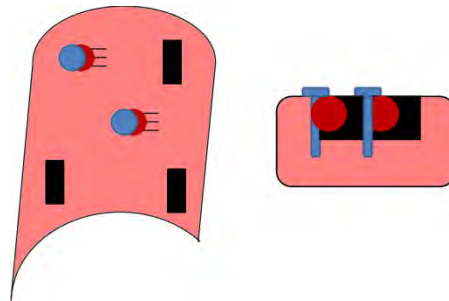

Figure 7: Dynamic Lung Phantom with Dual Tumor Sites

Phase 7: Dual Heterogeneous Tissues and Tumor Site Analysis

Phase 7 incorporates the heterogeneous lung tissue material with multiple tumor sites. Figure 8 shows the addition of the cork pieces representing the lung tissue. This phase will show how the dual tumor sites interact with the addition of dosing through the heterogeneous lung tissue material, with the external gafchromic medium as references.
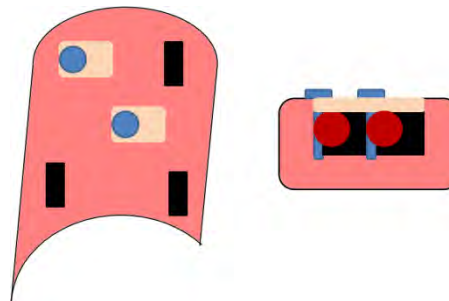

Figure 8: Dynamic Lung Phantom with Dual Tumor Sites with Heterogeneous Tissue Material
Potential Other Phases

In addition to the steps of research outlined previously, research could be conducted on the right lung implementing any or all the phases. This would be additional data that would foster greater understanding of lung motion and predictive modeling since it anatomically is unique from the left lung. In addition, some combination of tumors on both halves of the lungs could be examined.

Creation of Tumor Sites

The creation of the tumor sites needs to be impermeable to air and potentially water. Careful implementation of these sites is necessary to ensure repeatability and usability of the dynamic phantom lung. Figure 9 shows the assembly of the tumor site using a hex nut to create pressure between the cap screw and sealant creating an impermeable seal.
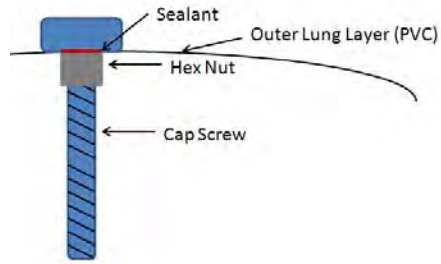
Figure 9: Schematic of Tumor Site

After several iterations of custom phantom lungs, a suitable lung set was created for the dynamic lung phantom. The final version of the inflatable lungs, as seen in Figure 9, has a centered seam that was not part of the initial design. Despite being an unforeseeable addition, the surface seam does not interfere with the motion of the dynamic lung phantom or the imaging that will occur during use. Since each subsequent set of lungs will require additional funds, testing is being conducted on the multiple sets of unsuitable inflatable lungs provided by the company. This will allow the techniques of creating the motion, attaching/detaching the tumor, and adding representative tissue material to be perfected before any additional modifications are made to the suitable lung set.

Figure 9: Custom inflatable lung set

Figure 10: Inflatable lung with addition of centered tumor site

Figure 10 shows the addition of a centered tumor site, using the methods previous outlined, revealing an impermeable seal can be created and a tumor site can be placed far from the opening. Figure 11 shows the addition of the representative tumor, black sphere, to the inflatable lung setup. Research continues to follow and improve upon the procedures outlined previously for modifying the inflatable lung setup and creating a fully function dynamic lung phantom with tumor sites.

Figure 11: Inflatable lung with centered tumor site and tumor

An additional pump was purchased that match the flow specifications, and will be used in the assembly. Construction of the dynamic continues using the samples provided the company to perfect assembly and installation. New projects have been developed to further investigate organ/tumor motion by creating coupled by independent motion of both the dynamic lung set and the embedded tumor using spare pumps.

Through an extensive literature a great interest in analyzing tumor motion separate from organ motion exists in the field. A twofold research effort has been devised to properly create the synced motion between the tumor and organ. This will be achieved through using the dynamic

phantoms coupled with an inflatable tumor that has independent tubing and pump supply to create the expansion and contractions that occur locally to the tumor due to the motion of breathing, Figure 12.
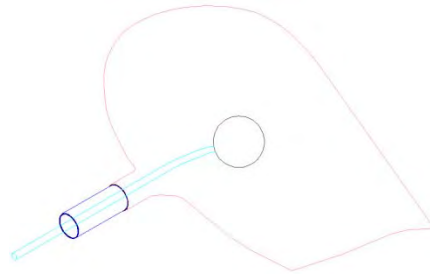

Figure 12: Tumor and Organ Motion Setup

This new project could easily lead to collaborations with Dr. Segars from Duke University, whom developed a digital phantom based on real patient data that can generate tumor and organ motion which could verify the mechanical phantom. Although the correct motion has not been developed in mechanical phantoms being currently researched by various other groups, another more interesting research avenue exist to properly monitor the tumor motion for real-time adjustment to radiation treatment. Many groups have developed tracking using algorithms and sensors; however, work to non-invasively monitor real-time motion in patients is the new target research path. Many groups are developing enhanced resolution imaging systems that reduce radiation doses that could be used to monitor tumor motion without markers or seeds. Research discussions are being conducted with several groups with various enhanced imaging techniques to determine collaborations and deepen understanding of this as a potential method of live tracking tumor motion during patient treatment.

In this context, a 3-D motion table was specified and purchased to generate comparison data. The data will be used to verify the dynamic lung phantom, and ultimately a comparison between the two methods will be conducted. The table was received but required addition components to be operational, as well as understanding of the proprietary program language used to command the motion of the table. The table is generally used for optical research, and standard optical tables come with tapped and drilled holes of a specific size. Since the use is non-traditional for this table, a platform was necessary to attach to the table for use.
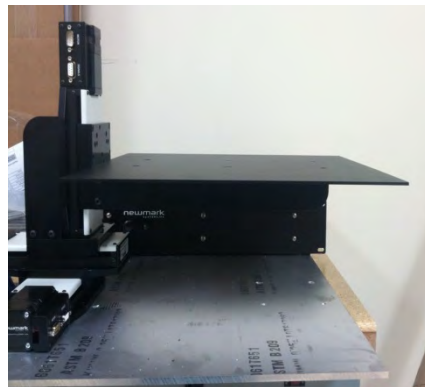

Figure 12: Three dimensional motion table setup

Figure 12 shows the three dimensional motion table setup with the addition of the base plate. The programming language is specific to the company the motion table was purchased from, and is not trivial to master. However, several sample programs have been written and tested. The code to create the synchronized motion between all three dimensions to mimic breathing is still being developed. Both the dynamic lung phantom and the 3-D motion table experimentation were found to be useful in collaboration with Dr Segars' (Duke University) digital phantom known as the XCAT.

Several research teleconferences were conducted to find possible synergies between the two groups' work. It was determined that a comparative study between digital and physical phantoms could be conducted. Currently, examination of the XCAT phantom's codes is being conducted to foster understanding and enhance collaboration. Due to the procedures already set at WRNMMC through the collaboration with the University of Pennsylvania, it was decided that testing of all phantoms would be conducted at the WRNMMC site.

Telemedicine

INTRODUCTION:
A major goal of phases IV and V was to develop a point-to-point and multi-point Remote Proton Radiation Therapy (RPRT) solution to 1) allow Walter Reed (WRAMC/WRNMMC) physicians to remotely plan treatments for patients and 2) conduct video-conferences with their counterparts at the Hospital of the University of Pennsylvania (HUP) to optimize/validate plans. Once tested and implemented, the solution was to be optimized and expanded to other satellite clinics within the Military Health System (MHS).

BODY:
1) Remote proton treatment planning

1.1)   Pre-BRAC (WRAMC)

Over the life of this grant, the search for a robust application-sharing tool to power our remote treatment planning solution has presented us with several challenges. Initially encouraged by the Directorate of Information Management (WRAMC-DOIM) to use Polycom PVX as a simple-to-use and cost-effective platform for the sharing of remote applications, we were then steered towards Defense Connect Online (DCO), a DoD-managed version of the popular Adobe Connect application.

Along the course of evaluating this package, we were told by DCO that due to sessions being recorded and stored (with data potentially accessed by non-HIPAA certified staff), the use of this platform as a virtual medical simulation tool would have to be suspended until the HIPAA issue could be addressed appropriately. Numerous exchanges took place between our group and DCO as we constantly engaged them on the possibility of using this particular platform for data-collaboration (other military treatment facilities have expressed interest in using this web-collaboration tool for clinical use so there seems to be MEDCOM-wide interest). The benefits of this existing solution were many (free, flexible, DOD-managed/sponsored, meets our 'application-sharing' requirements) and we felt confident we could make a case to either 1) have monitors receive HIPAA training or 2) receive an outright exemption from monitoring. Unfortunately, our efforts yielded little traction and we were thus forced to look to another alternative, one which would not only meet the security requirements of the DoD but also be HIPAA-certified.

Following a demonstration by Varian Medical Systems (provider of the Eclipse treatment planning package used for both conventional and proton radiation therapy), our program settled on the CITRIX solution to power the application-sharing portion of our telemedicine solution:

i) Ability to securely transfer CT sets from the local workstation (where the CITRIX client is activated, i.e. at WRAMC) to the remote workstation (where the patient plan will be generated and stored, i.e. at Penn);

ii) Ability to connect to the Penn workstation to engage in the remote treatment planning of DOD patients, as stated in the grant's research goals;

iii) Ability to application-share with the remote site (resolving, in an ad-hoc manner, planning and/or setup discrepancies).

The system was purchased in the first quarter of 2010 and subsequently delivered/installed at the UPHS Data Center in Newark in May. In parallel, the CITRIX client, a key component of the application-sharing solution, was installed on all providers' PCs and a 'shared drive' (onto which DICOM-RT sets were to be transferred from WRNMMC to UPenn) was configured.

The DoD proton calculation engine was transferred to HUP earlier this year. Following lengthy exchanges between the Army contract representative and the provider of the system (Varian Medical Systems), the transfer of licenses (needed for proton planning) and the maintenance of the workstation off-site was also arranged. This solution is presented in Figures 1 and 2 below.
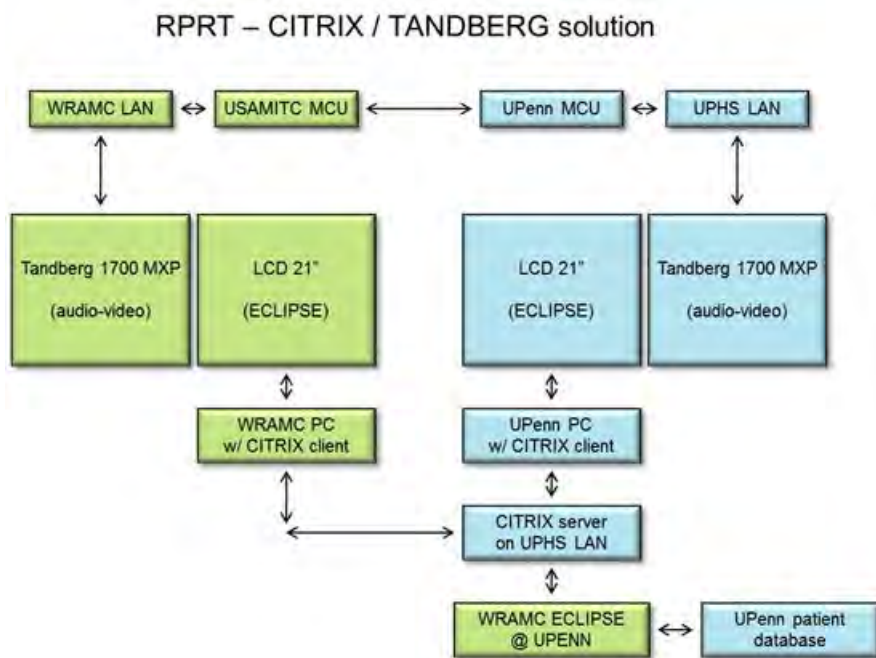

Figure 1 – Citrix powered solution (a)

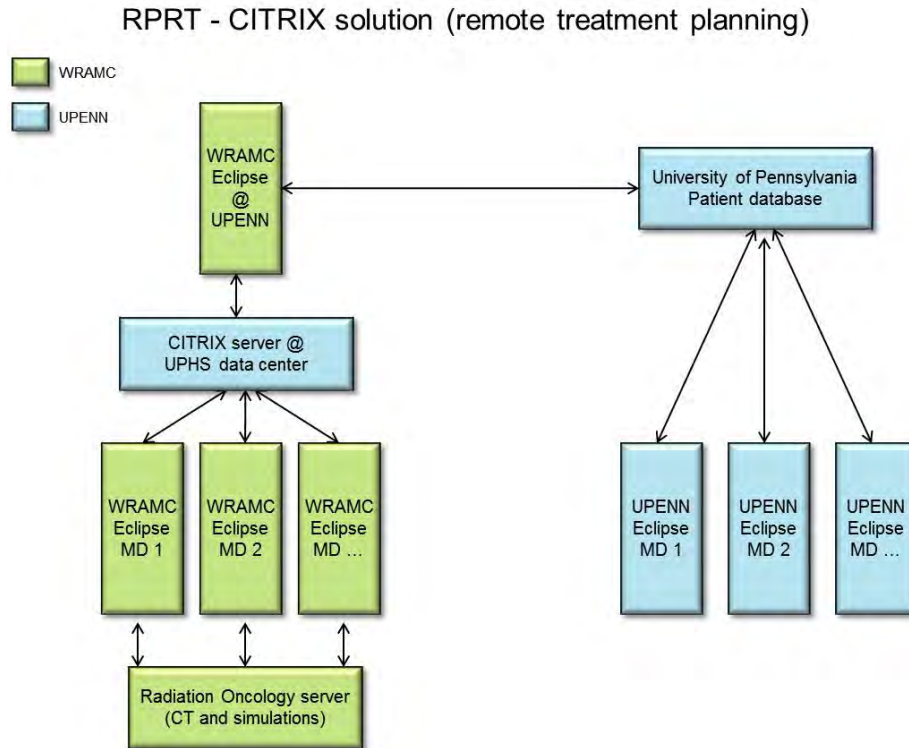## RPRT - CITRIX solution (remote treatment planning)

Figure 2 – Citrix powered solution (b)

As our Program readied the migration of its RPRT solution to WRNMMC (in the context of the BRAC), we were instructed by the National Naval Medical Center's Responsible Conduct of Research Service (RCRS) that the Data User Agreement guiding the use of the telemedicine solution between the two institutions would need to be folded into a comprehensive Navy Cooperative Research and Development Agreement (N-CRADA). Although the N-CRADA was not required for the work being conducted under this cooperative agreement, it was enforced by NNMC on the basis that DoD physicians and their proton patients would be involved in clinical trials run jointly with a civilian institution.

The development of this CRADA, with its associated Data Sharing Agreement and Security System Verification (SSV) questionnaire, took many months to finalize, thus delaying the operational launch of the RPRT system to treat DOD patients enrolled under joint proton clinical trials.

1.2) Post-BRAC (WRNMMC)

In December of 2012, a few months after the merger between WRAMC and NNMC, the Program was informed by the University of Pennsylvania Health System (UPHS) that the Junos client (Juniper) would replace the CITRIX Access Gateway (CAG) for VPN access. This decision to switch the 'client' was communicated to us abruptly (i.e. 24-hour shutoff window). With the help of the RadOnc IT staff, we made the case to UPHS that, Junos not being approved for deployment on a DoD network, a postponement was needed; an extension to MAR 01 2012 (three months) was granted.

We quickly identified that Junos was not approved for deployment on a DoD network ; however, the Juniper Net Connect client, a suitable alternative, was. Reaching to WRNMMC Information Technology Department (ITD), we quickly worked on getting this solution up-and-running, before the termination date of the CAG (FEB 29 2012).

Initial requests to have the client installed on all provider PCs, to include physicians, medical physicists and dosimetrists, were denied by WRNMMC ITD. Security concerns were raised. Our program floated the idea of having a single PC, to be placed on the DMZ, configured as a 'jump box', from which providers could launch the Juniper Net Connect Client and remotely access the proton treatment planning package at the University of Pennsylvania. This approach was approved and subsequently configured over the course of several weeks (Figure 3).
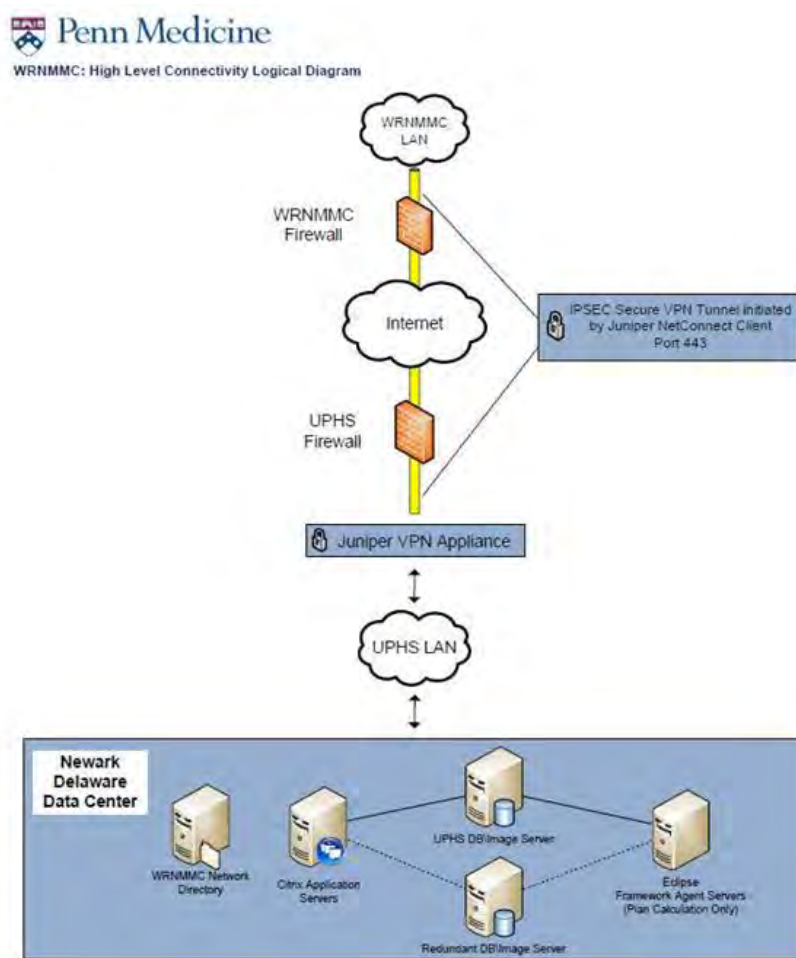
Figure 3 – RPRT connectivity logical diagram

While the solution does work today, it 1) forces users to work from a unique location when planning a proton plan remotely, and 2) does not integrate with our existing infrastructure since the 'jump box' does not touch the network (i.e. any treatment data has to be burned on a CD and manually transferred). This was, and continues to be, a major downgrade from the solution we had deployed at WRAMC (CITRIX-powered solution residing on all providers' PCs,

themselves paired with audio-videoconferencing units). System-performance under these new conditions was initially erratic (intermittent disconnection) but has since become much more stable.

2) Audio-video conferencing support

During the period of performance of this sub-award, eleven Tandberg units were acquired and deployed to locations likely to be involved in remote proton radiation therapy planning, now and in the future: National Naval Medical Center (NNMC), Walter Reed Army Medical Center (WRAMC), Madigan Army Medical Center (MAMC), Brooke Army Medical Center (BAMC), National Cancer Institute (NCI), and HUP. With the merger of WRAMC and NNMC in SEP 2011, some of the units were consolidated at the newly renamed Walter Reed National Military Medical Center (WRNMMC).

Full bilateral connectivity between WRAMC/WRNMMC and HUP remained a problem throughout the course of phases IV and V and was not fully addressed until Q1 of 2013. Initial problems were attributed to a configuration setting with the long-distance carrier HUP was using for outbound/inbound ISDN calls.

Multiple tests were conducted during the course of 2010, involving not only Walter Reed and HUP, but also Polycom, RoData (provider of the RMX2000 videoconferencing bridge), Criticom (provider of the Tanderbg 1700 MXP desktop VTC units), and USAMITC engineers. Per a request communicated by both RoData and Polycom, logs of calls placed by both institutions were captured and transmitted. We were subsequently asked to disable some of the features of the units to identify which of the protocols was/were causing the video transmission issue. H.239 (content-sharing) and H.264 / H.263 (transmission protocol for audio-video transmission) were disabled sequentially. We did achieve complete connectivity using the much older H.261 protocol, but the video-quality was sub-optimal.

To eliminate yet another potential cause, both Walter Reed and HUP upgraded their Tandberg 1700 MXPs and RMX2000 MCU to the latest software version (respectively 8.2 and 2.0). Subsequent tests showed that the upgrade had no meaningful impact on connectivity (i.e., the majority of calls still failed to produce incoming video for HUP). Further testing, this time involving engineers from the USAMITC bridge, offered a possible cause. According to the release notes for the CODIAN gateway 2.0, bug ID 2867 could explain our inability to have full connectivity. During this latest series of tests, logs were again captured and subsequently sent to the Tandberg development team (escalated to Tier 3 at Polycom as well). The 'bug ID 2867' entry is being inserted here for reference.

A subsequent update from Tandberg indicated the development team was able to replicate the issue in its own lab, and was now working with Polycom to address the problem.

With the merger of WRAMC and NNMC, the Tandberg 1700 MXP units transferred to the Walter Reed National Military Medical Center (WRNMMC) were initially not supported by the Information Technology Department (ITD), following guidance by the Joint Task Force (JTF) Chief Information Officer (CIO). At hand was the issue of the units not being owned by WRNMMC but by the Henry M. Jackson Foundation for the Advancement of Military Medicine (HJF). This lack of support prevented us from maintaining the units and assisting with troubleshooting.

The Program made the case that these units were purchased and deployed as part of a comprehensive remote proton radiotherapy treatment planning solution and that the design, testing and deployment of this system is one of the deliverables of our $43 million, seven-year on-going, research effort linking the Radiation Oncology departments of the University of Pennsylvania and the Walter Reed Army Medical Center (now the Walter Reed National Military Medical Center). The Program further articulated that this solution relied on our physicians' ability to conduct ad-hoc videoconference calls with their counterpart(s) at HUP, should problems occur during the planning of treatments and/or during the setup of patients (i.e. minutes before radiation treatment is to be delivered). While these units were indeed owned by the HJF, we argued they were purchased via a DoD research grant to fulfill a patient-care objective at this MTF. In addition, the units were certified by the Joint Interoperability Test Command (JITC), patched to the latest version, and under a maintenance contract until DEC 2013.

During the following months, the JTF CIO instructed his team to look into the matter. Following numerous exchanges, an agreement was reached to support these units. Realizing this telemedicine solution is integral to the care of cancer patients receiving proton radiotherapy, the ITD agreed to troubleshoot connectivity issues as they arose, to include gatekeeper/gateway registration with USAMITC.

During the course of the summer of 2012, our ability to connect was hindered Walter Reed Bethesda experienced a faulty network card, preventing ISDN calls from the outside (using the 210.250.xxxx prefix). This particular issue was eventually addressed and we now have the ability to once again conduct audio-video teleconferences with outside institutions.

Robust connectivity with the University of Pennsylvania's Radiation Oncology Department was finally resolved in the Q1 of 2013, following an upgrade of HUP's VTC system (to include a dedicated ISDN line).

Neutron and Microdosimetry of the Proton beam

Introduction
One goal of phase IV was to develop and implement radiation dose measurement devices to characterize the secondary radiation produced by proton interactions in the patient and in the beam modification devices that are used to deliver a therapeutically accurate and useful proton beam. The secondary radiation outside of the treatment volume of a proton field consists primarily of gamma and neutron radiation. Gamma ray and neutron radiation is known to have different biological effects relative to Cobalt-60 or x-ray radiation (RBE). The effects of proton induced gamma ray radiation on biological tissue are not strongly sensitive to the energy spectrum and have a RBE very nearly equal to 1 since the quality of this radiation is equivalent to the Cobalt-60 and x-ray baseline radiation. However, the RBE of neutron radiation depends strongly on the energy spectrum and patterns of microscopic energy deposition. Physical characterization of the neutron field is vital to understanding the role this radiation can have in adverse biological effects and this relies on measurements of absolute dose deposition and microdosimetric measurements of the spatial and temporal patterns of dose deposition in volumes approaching the micron (ie. 10^{-6} m) dimensions relevant to biological cells.

1 Microdosimetry

1.1 Microdosimetry Detector
We have constructed a tissue-equivalent proportional counter (P. Kliauga 1995) to be used for measurements of the lineal energy spectra of neutrons in the proton Bragg peak and surrounding volumes.   The detector is a miniature tissue-equivalent proportional counter (TEPC) and is based on a design (Burmeister 1999) with an active counting volume consisting of a 2.5 mm right cylinder with volume 12.27 mm^3.   A diagram depicting a cross sectional side view of the cylindrically symmetric detector is shown in Figs. 1 and 2. The detector consists of a thin-shelled aluminum capsule about 40 mm long and 9 mm in diameter attached to a long aluminum stem. A 10 μm diameter wire forms the anode of the proportional counter inside the thin aluminum shell. The cathode is constructed of A-150 tissue equivalent plastic. The anode wire runs through glass capillary tubing that is inserted into stainless steel field tubes that define a uniform electric field within the detector's 2.5 mm right circular cylindrical active area, Fig 3. A propane based tissue-equivalent (TE) gas (ICRU 1983) fills the active counting volume at a pressure determined by the desired simulation diameter X according to the equation, $X\rho_{tissue} = D\rho_{gas}$. Where D is the detector active volume diameter and ρ_{tissue}, ρ_{gas} are tissue and TE gas densities.
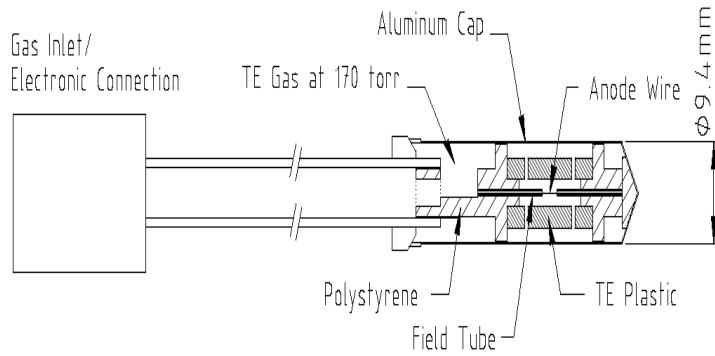

Figure 10. Cross sectional view of the cylindrically symmetric TEPC.
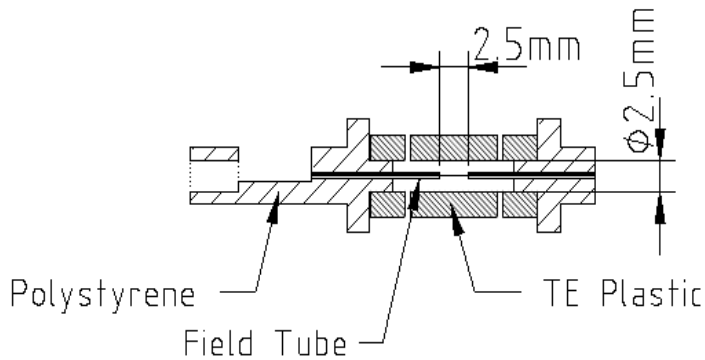

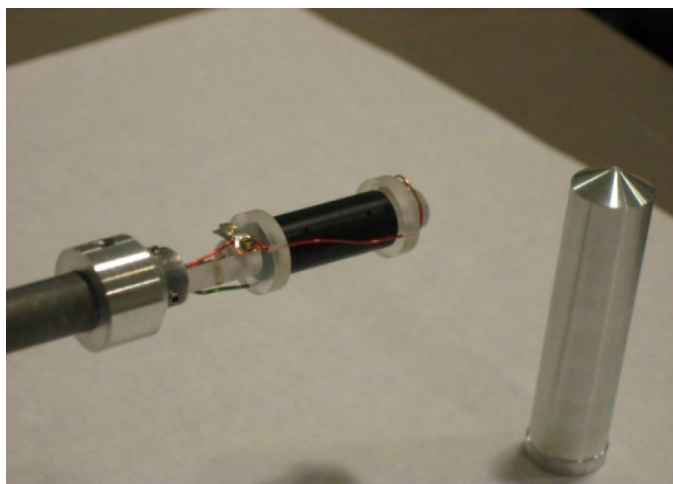Figure 11. Cross sectional diagram of the active area of the TEPC.

45

Figure 3. Completed TEPC shown with the aluminum shell removed.

1.2 Data Acquisition Electronics

The TEPC is a proportional counter that responds to a charged particle passing through its sensitive volume by producing an analog current pulse with charge integral which is proportional to the energy deposited in the sensitive volume. The pulse is amplified in a charge sensitive pre-amplifier and processed with an analog pulse shaping circuit. The resulting voltage pulse (Fig. 4) has amplitude proportional to the ionization in the detector and the pulse is shaped to minimize pile-up. The amplified and shaped pulses are digitized using a high-speed sampling ADC (National Instruments Model PXI-5105) residing in a PXI chassis which is connected to the PCI bus of a dual core notebook computer, Figs. 5 and 6. The digitizer card samples up to 8 channels simultaneously at a rate of 60MS/s. The graphical programming environment LabVIEW (National Instruments Corporation) is used to control the digitizer card and develop the data acquisition software. This software controls the digitization of analog pulses in the digitizer card, acquires the digitized pulses to disk, and extracts the amplitude from the digitized pulse. The amplitudes are calibrated in software and are displayed in a histogram to depict a lineal energy spectrum.
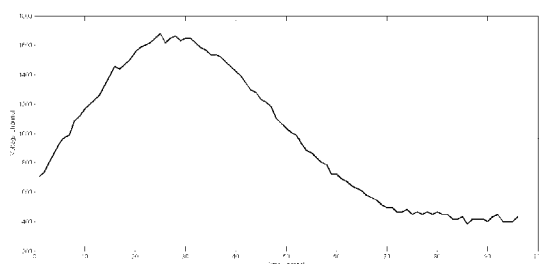

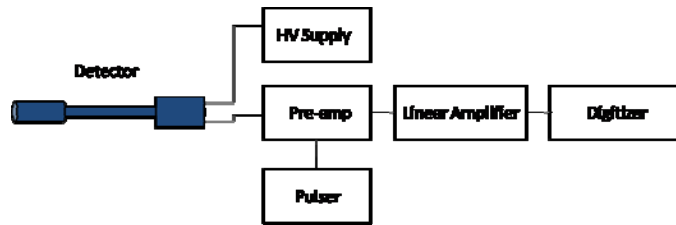**Figure 4.** Representative voltage pulse after digitization.

Figure 5. Diagram depicting the detector operation and pulse processing electronics.

Figure 6. Electronics rack housing the pulse processing and analysis electronics.

1.3 Data Acquisition and Analysis Software

The LabVIEW programming environment automatically parallelizes code and this feature was used to increase the throughput of the data acquisition system. A producer/ consumer architecture running in parallel is used to acquire and process analog pulse data. Data acquisition is performed in a producer loop running on one processor core, which places the digitized waveform in a buffer. The buffer is emptied by a consumer loop running in parallel on the second processor core writing the waveform to disk. This parallel software architecture has allowed us to attain maximum continuous pulse acquisition rates of up to 26 kHz. The limitations of the TEPC, digitizer board and PCI bus are considerably higher, around 100kHz, so an optimization of the acquisition routine has the potential to substantially improve the count rate capability of this system. The acquisition software records the digitized detector signal to a file written in binary format and simultaneously extracts pulse height and timing information. Pulse height histograms can be displayed in a separate LabVIEW program while data is being acquired. Alternatively, the recorded binary files can be read in and pulse height histograms and timing information are extracted and displayed using Matlab (The MathWorks, Inc.) scripts.
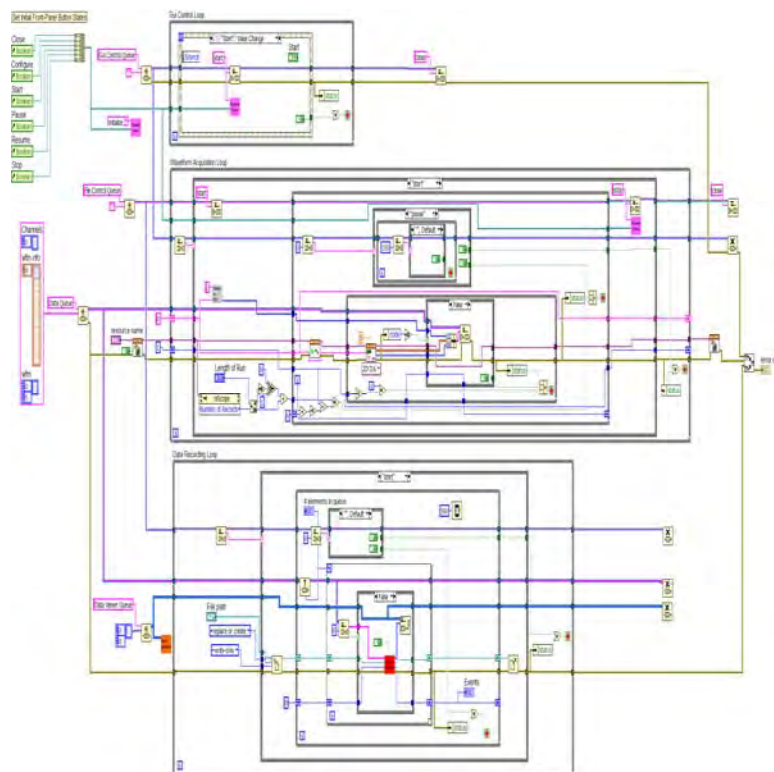
Figure 9. LabVIEW block diagram of the data acquisition software.

1.4 Charged Particle Veto

When a neutron interacts within the TEPC active volume the dominant physics process is primarily elastic scattering with protons in the tissue equivalent gas or plastic (Knoll 2000). These collisions can transfer up to the total kinetic energy of the neutron to a secondary proton. This secondary proton can then ionize the gas in the detector volume. Consequently, the response of the detector to proton radiation is indistinguishable from neutron radiation. This ambiguity can be resolved by using a proton veto detector in conjunction with the TEPC. The general concept is to surround the TEPC with another detector or array of detectors that are relatively insensitive to neutron radiation compared to its response to proton radiation. A proton detected in the veto detector in timing coincidence with a signal originating from the TEPC can then be discarded, Figs 9 and 10. The result is the ability to separate the portion of the lineal energy spectrum due to primary protons from the part due to protons secondary to neutrons. Two 300µm thick fully-depleted transmission-type silicon surface-barrier detectors will be used as veto detectors in conjunction with the TEPC.

Figure 9. Diagram depicting a primary proton event incident on the TEPC and silicon surface barrier veto detectors.
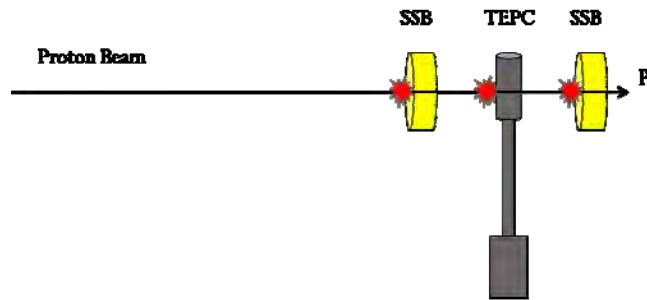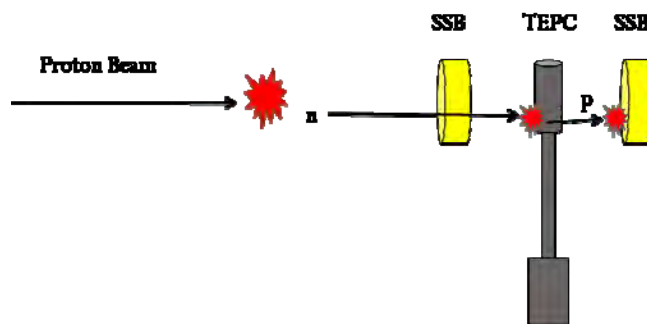

Figure 10. Diagram depicting a secondary proton due to a neutron interaction in the TEPC and silicon surface barrier veto detectors.

1.5 Microdosimetry measurements

The TEPC was filled with a low pressure propane based tissue equivalent gas mixture to simulate a 2 µm tissue volume. A proton beam with field size 10 cm x 10 cm, range of 25 cm, and modulation 10 cm was prepared and delivered into a stack of solid water plastic slabs totaling 30 cm in thickness. The TEPC was placed between the solid water plastic slabs at depths of 22 cm, 24 cm, and 25 cm. Spectra were acquired at these positions using the LabVIEW based data acquisition and analysis system that was developed in previous quarters. The pulse signal produced by the TEPC, operated with an electrical bias of 800V, was amplified in a Canberra model 2006PC pre-amplifier connected directly to the TEPC in the proton gantry room. This amplified signal was then run via coaxial cable to an electronic rack containing two NIM bins containing pulse processing modules, an oscilloscope for troubleshooting and system analysis, and a PXI crate containing the waveform digitizer and generator modules. The pre-amplified signal from the TEPC was split into 3 channels and each was amplified and shaped to suppress the exponential decay tail. The three channels were amplified with successively larger gains and the outputs were digitized in a LabVIEW controlled waveform digitizer. The LabVIEW data acquisition system uses a single trigger for all 3 inputs, so the waveform digitizer was triggered by the summed output of 3 Ortec timing single channel analyzers connected to the bipolar outputs of the shaping amplifiers. This triggering system ensures the system is still triggered by the lowest and highest amplitude pulses. The pulse waveforms were digitized at a sampling rate of 10 MS/s and waveforms of 500 samples for each of the three amplification channels and written to computer disk.

Each spectra was acquired in a file of approximately 500k such events and the data was analyzed using software developed in the LabVIEW language. The maximum amplitude of each waveform was measured and histogrammed. The three spectra obtained from the amplification channels were analyzed for overlap and combined to form a single matched spectrum covering 4 decades of dynamic range. The spectrum was rebinned using logarithmically sized bins and the bin contents were multpiplied by their value on the x-axis. This results in a spectrum of dose with lineal energy shown on the x-axis. The area of the spectrum between any two bins in lineal energy divided by the total area of the spectrum is equal to the fraction of absorbed dose from events with lineal energy between thos two bins.

This procedure was repeated for TEPC placements at solid water depths of 22 cm (Fig. 11), 24 cm (Fig. 12), and 25 cm (Fig. 13). The spectrum shown in Fig. 3 shows a distinct vertical edge at the high lineal energy end of the spectrum. This edge is presumed to be the proton edge which represents the maximum energy that can be deposited by a proton in a 2 μm tissue equivalent sphere, ie. 137 keV/μm. Identification of this edge allowed us to calibrate all 3 spectra in lineal energy. Edges seen at higher lineal energies are likely due to heavy ions such as alpha particles or carbon nuclei produced in nuclear reactions induced by the primary protons. The measurement of Fig. 3 was at the distall edge of the proton SOBP, so it follows that slower protons that have nearly stopped dominate the dose deposited in this area. As is well known, the LET of protons increases rapidly as they slow down producing a bragg peak at the end of their range in matter. Hence the prominance of the proton edge in Fig. 3, compared to the spectra of Fig. 1 and 2, where the measurements are taken closer to the middle of the SOBP with a larger fraction of low LET protons.
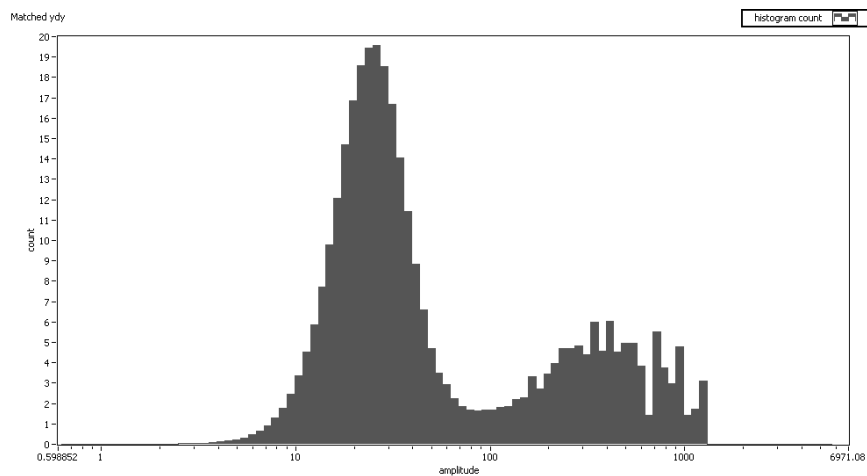

Figure 11. TEPC measurement at a depth of 22 cm in solid water plastic. Amplitude along the x-axis is calibrated to keV/μm. Counts on the y-axis are arbitrarily normalized.
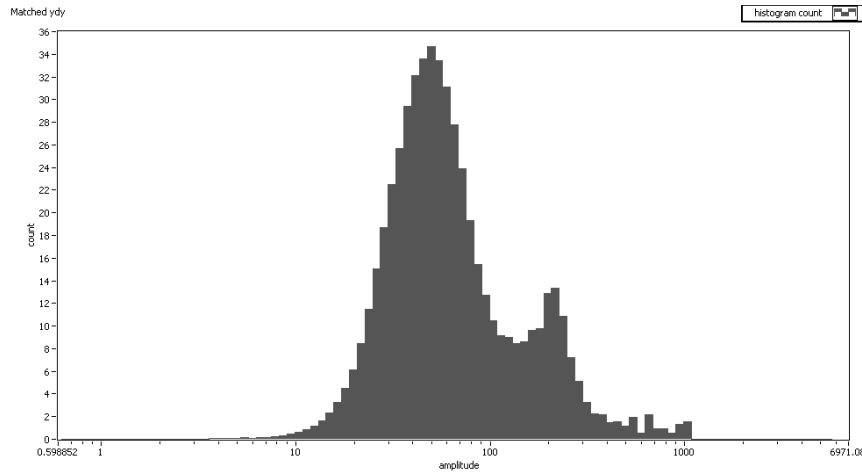
Figure 12. TEPC measurement at a depth of 24 cm in solid water plastic. Amplitude along the x-axis is calibrated to keV/μm. Counts on the y-axis are arbitrarily normalized.
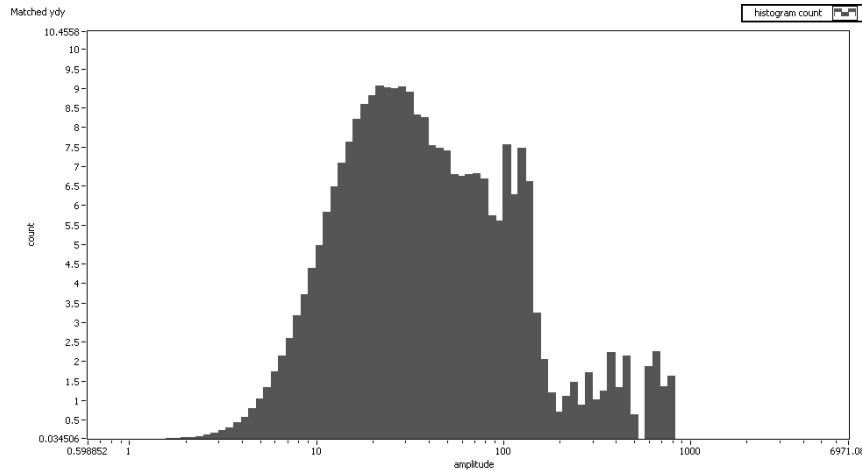
Figure 13. TEPC measurement at a depth of 25 cm in solid water plastic. Amplitude along the x-axis is calibrated to keV/μm. Counts on the y-axis are arbitrarily normalized. Calibration of this spectrum and those in Fig. 1 and 2, was obtained by identifying the vertical edge (calibrated to 137 keV/μm) as the proton edge.

2. Neutron Dosimetry

We have designed and built large volume ionization chambers for use with the dual-ionization chamber method (ICRU, 1977). This is a method used in gamma-neutron mixed field dosimetry where two dosimeters with different sensitivities to the two types of radiation are used to evaluate the separate absorbed doses. We have implemented this method to measure neutron dose contamination due to the proton beam incident on the patient and the beam modifying devices such as the Tungsten MLC. Previous measurements were done with commercially available chambers having a volume of 1cc. The small signal and relatively large leakage current present in these detectors made this measurement problematic. For this reason we decided to build a large volume Magnesium walled chamber and another chamber identical in every way aside from having a wall constructed of TE plastic. The chamber constructed with TE materials exhibits a stronger response to neutron dose compared to the chamber constructed of

Magnesium. We chose a volume of approximately 10cc for our chamber design, which increases the measured signal substantially and decreases the detector contribution to the leakage current by increasing the insulator thickness. The design follows a standard Farmer chamber design with a guard ring, Fig. 14 and Fig. 15.   The chambers were also equipped with gas flow inlets and outlets and a methane based TE gas was maintained with a constant flow through the TE chamber while Argon gas flowed through the Magnesium chamber.

As the secondary neutron field produced by the proton beam is predicted to be low (several mGy per Gy delivered), we have constructed our own chambers with considerably larger volumes than the commercially available chambers used in the literature. To accurately determine the neutron and gamma sensitivity of our custom chambers we developed Geant4 (Agostinelli et. al., 2003) Monte Carlo (MC) simulations which use MC generated neutron spectra data. The MC simulation accurately models the chamber geometry and uses the available neutron interaction cross section data to calculate energy deposition in the active volume of the chambers. By changing the material composition of the chambers in the simulation to match the composition of the chambers we have built, we can determine the relative sensitivity of the chambers in the field produced by the proton beam. Details of the implementation and measurements performed in the proton beam can be found in Diffenderfer et. al., 2011.
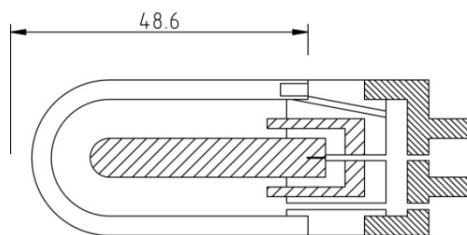
Figure 14. 10cc ionization chamber design. Dimension shown in millimeters.

Figure 15. A 10CC Magnesium walled ionization chamber (top) and tissue equivalent plastic walled ionization chamber (bottom).

Cone Beam Computed Tomography (CBCT)

INTRODUCTION:
The development of an on board cone beam computed tomography (CBCT) system for image guidance in proton therapy is a joint project between IBA proton therapy and the University of Pennsylvania. The availability to visualize soft tissue and 3D anatomy to set up patients in treatment position offers distinct advantages over conventional orthogonal kV X-ray imaging. While kV image guidance uses the bony anatomy or implanted fiducials as surrogates for

localization, CBCT enables more precise localization of the actual treatment volume and the surrounding organs at risk. Radiation dose delivered by protons is sensitive to changes in the proton beam path. One envisioned use of CBCT is to assess if patient anatomical changes may potentially impact the dose distribution.

A number of technical challenges need to be overcome in order to deploy a CBCT system mounted on a proton gantry. Due to the size and weight of the gantry, there is an angular dependent shift in the source and detector positions relative to the imaging isocenter. If left uncorrected, these shifts in the CBCT projection images will deteriorate the image quality and cause significant artifacts in the image. The design and implementation of a CBCT system includes the following:

(1) Development of analytical tools to quantify and correct X-ray source and detector tilt as a function gantry angle

(2) Evaluation of a new X-ray source with a higher heat capacity rating suitable for CT acquisition

(3) Evaluation of new larger area X-ray detector panel

(4) Development of CBCT image reconstruction software

(5) Development of a new imaging software suite (ImagX) for patient setup using kv/CBCT imaging

(6) Development of proton specific applications of CBCT.

BODY:

1. Geometrical Setup of On Board Proton CBCT System

CBCT systems have been used for external beam image guided radiation therapy since its development in 1999. It is now widely available as an on board imaging device that is mounted on the linac gantry [Jaffray 1999]. The geometry of the X-ray source and imager on a proton gantry differs from a linac in that the source to axis distance (SAD) is several times larger (Figure 1). As a consequence, the X-ray tube power requirement in the proton therapy system is about nine times greater than that in a compact linac system. This disadvantage is potentially outweighed by the reduction in off-axis image distortion that is present in all CBCT system owing to the smaller X-ray cone angle.

Figure 1. Comparison of the CBCT geometries between a proton gantry and a linac gantry. The proton gantry required a more powerful X-ray source than a linac gantry.
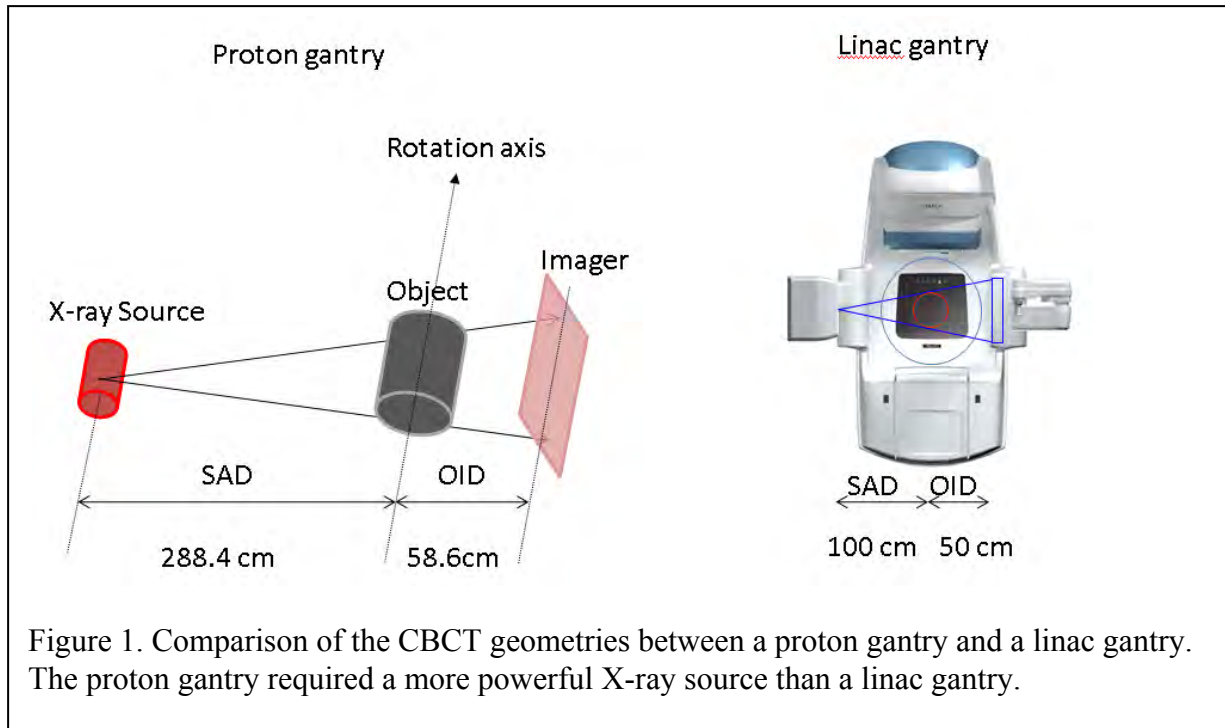
2. CBCT Geometrical Calibration

One of the biggest technical challenge in the development of a gantry based CBCT system is compensation for the angular dependence in the shift in source and detector positions relative to the imaging isocenter. If left uncorrected, these shifts in the CBCT projection images will deteriorate the image quality and reduce image resolution in the reconstructed image. The seven parameters that define the gantry flexmap are the two X-ray source transverse translations, two detector transverse translations and three detector rotations (Figure 2).

Figure 2. The seven geometrical parameters as a function of gantry angle that are needed to compensate for X-ray source and detector shifts.

54
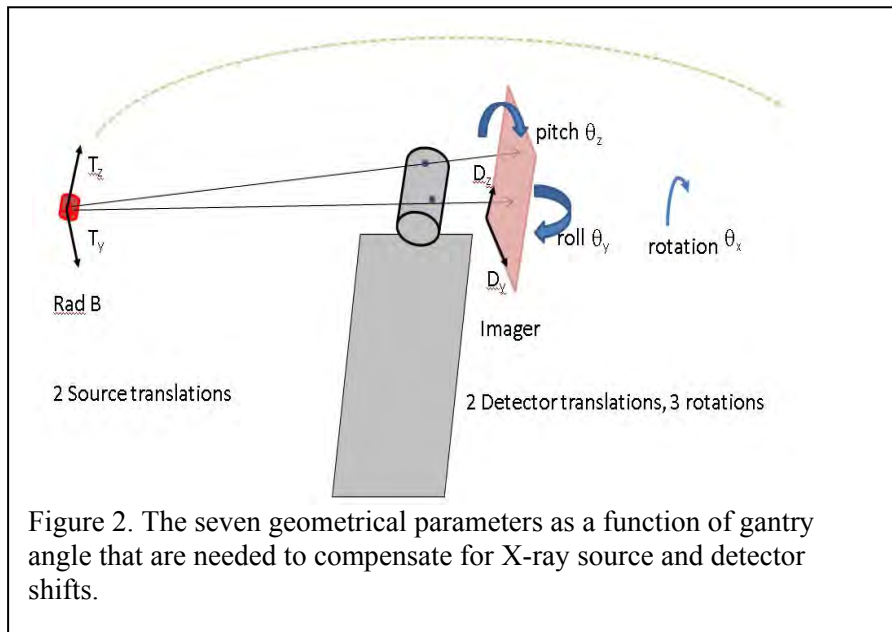
A calibration technique was developed and used to measure the geometrical parameters in treatment room 4 of the University of Pennsylvania Roberts Proton Center in 2012. The cylindrical calibration phantom consists of 37 precision mounted metal markers (Figure 3). By acquiring projections of the phantom at every 20 degrees, the seven geometrical parameters can be estimated by performing a least squares fit to minimize the difference in the relative positions between the measured and expected position of the 37 markers. The results presented in Figure 4 shows that the X-ray tube displacement exhibits a sinusoidal variation as a function of gantry angle. Further analysis reveals that the three most sensitive parameters that impact the image quality are the detector translations and rotation around the axis defined by the source to imager.

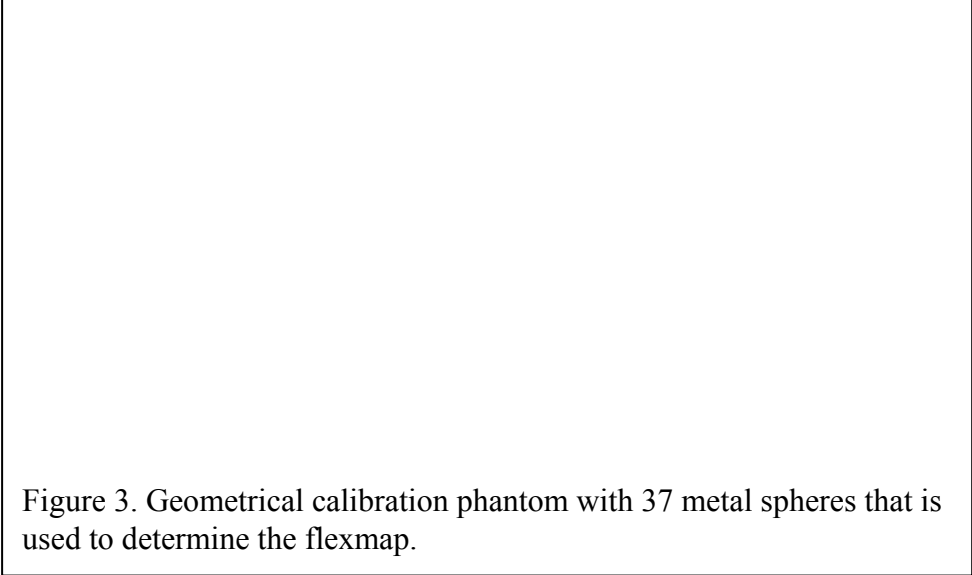Figure 3. Geometrical calibration phantom with 37 metal spheres that is used to determine the flexmap.

The results of this calibration measurement were presented as a poster at the PTOG 2012 annual meeting in Seoul, South Korea. Further calibration measurements will be made to quantify the reproducibility of these deformations.
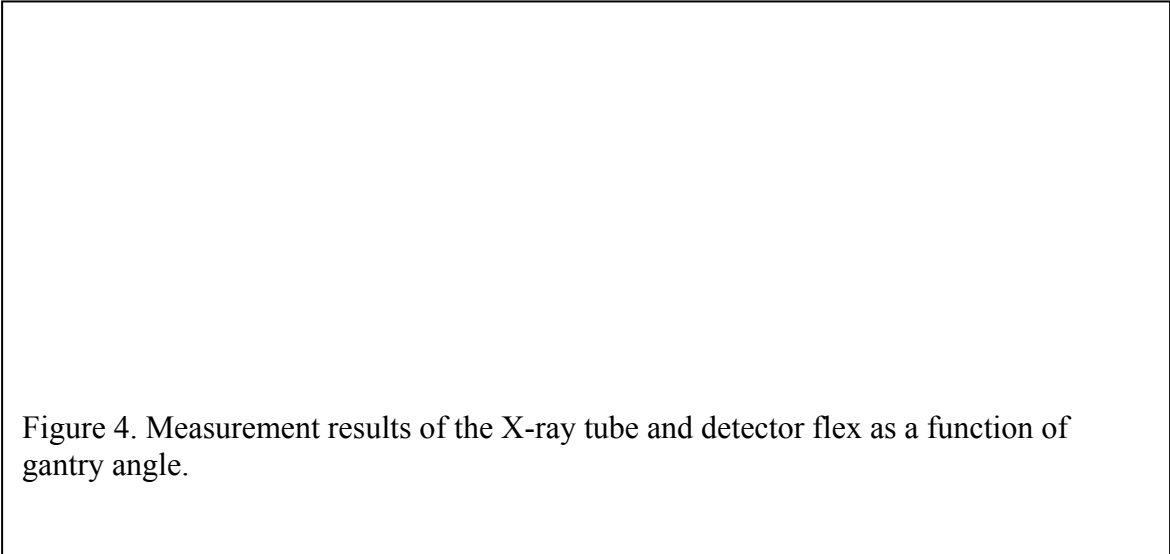
Figure 4. Measurement results of the X-ray tube and detector flex as a function of gantry angle.

3. Hardware Selection and Testing using a Bench Top CBCT System

Prior to CBCT installation on the proton gantry at the University of Pennsylvania Proton Therapy Center, the performance of the selected CBCT hardware were evaluated on a benchtop system at IBA. Using an identical geometrical setup as the proton gantry (Figure 5), CBCT projection images were acquired on a phantom placed on a rotating turnable. This benchtop system allowed IBA to evalute the X-ray source and imaging panel, tweak the image reconstruction software and optimize the image quality. The integration of the gantry control system with the new imaging software was successfully tested on the benchtop system. In addition, the benchtop CBCT system was able to achieve phantom CBCT images that were of comparable quality to linac based CBCT systems. Penn is working closely with IBA to use these benchtop CBCT images as benchmarks to define image quality metrics in the acceptance procedure of the first gantry CBCT system upon installation.
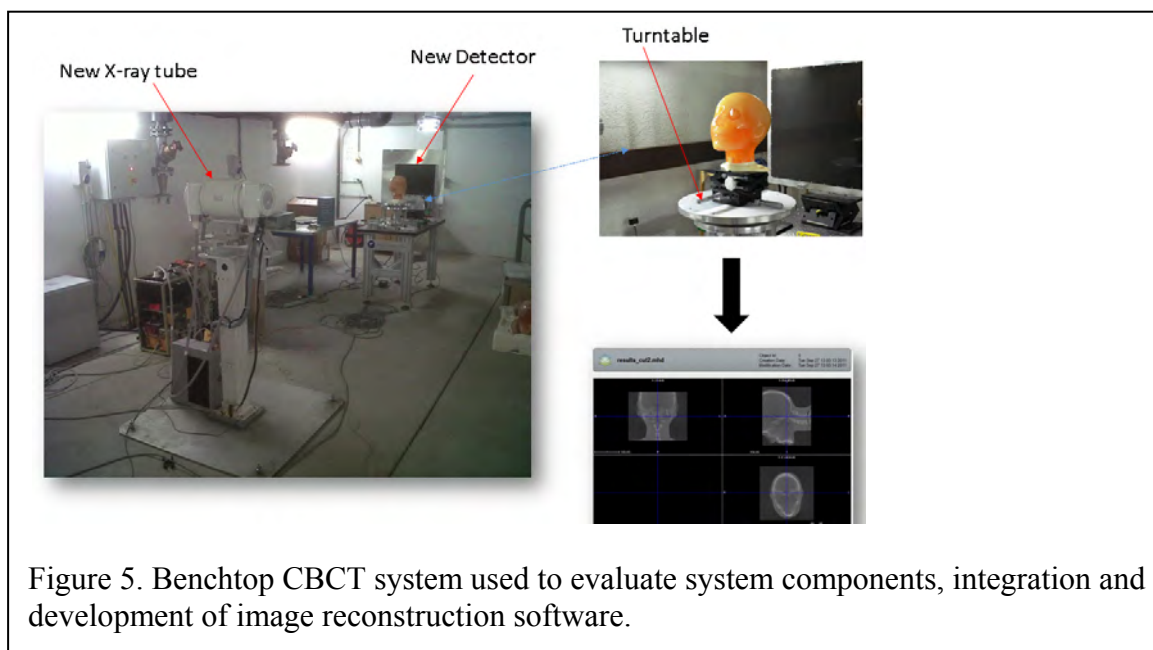
Figure 5. Benchtop CBCT system used to evaluate system components, integration and development of image reconstruction software.

As the CBCT system is a modification of existing components on the proton therapy imaging system, two major hardware changes were required. The first is the replacement of the X-ray tube and generator from one that could handle 445W to a more powerful tube that can handle 3200W. The other change is the replacment of the flat panel imager to a larger unit in order to increase the field of view (FOV). With these replacements a 34 cm (axial) and 35 cm (longitudinal) FOV CBCT system is expected. Additional increase in FOV will require the couch to be offset laterally and is planned for future development for this project.

4. Image Reconstruction, Scatter Correction and Software Development

The FDK method [Feldkamp 1984] for CBCT reconstruction was implemented and tested on the test workbench. This algorithm is commonly used in many CBCT systems as it is fast and can be implemented on high end graphical processor units using CUDA parallel computing platform. In addition a simple scatter correction technique [Boellaard 1997] based on a model to estimate the fraction of scatter within each projection image was implemented with satisfactory results. Figure 6 shows two axial slice of the Catphan image resolution phantom used to evaluate image resolution and CT number accuracy from he benchtop CBCT system. These images serve as a benchmark for image quality obtainable on the gantry mounted CBCT system. Other advanced image scatter correction techniques are currently being evaluated and tested on the image software platform.
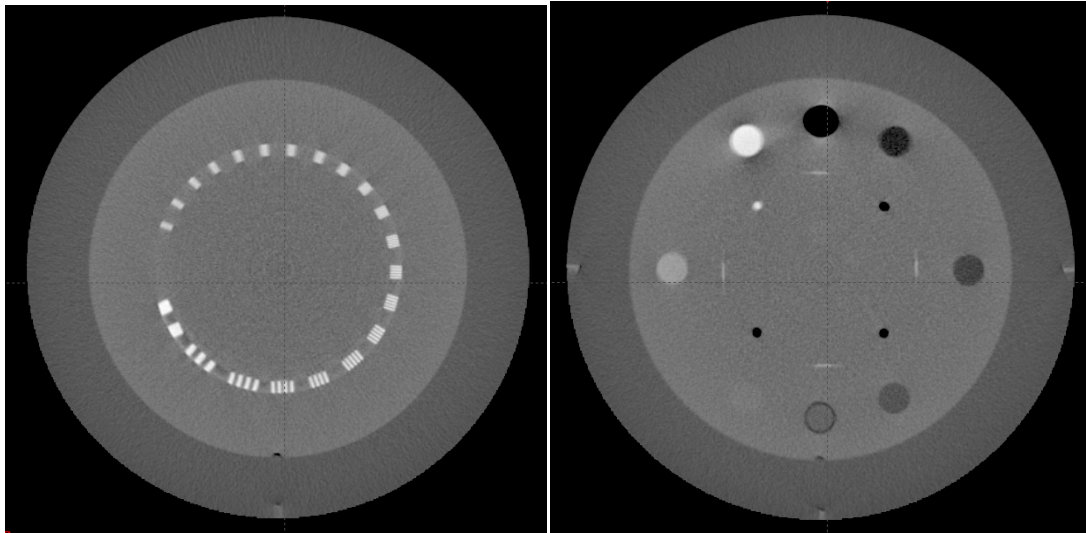
Figure 6. Benchtop CBCT images of a phantom used to evaluate the resolution (left) and Hounsfield number accuracy (right). These images are used to evaluate the image reconstruction software and serve as benchmarks for our gantry CBCT system.

5. Novel Clinical Applications of CBCT in Proton Therapy,

One important potential tool for the quality assurance of proton beam delivery is the ability to detect variations in proton beam path prior to treatment. Proton dose distributions are particularly sensitive to patient weight loss, tumor shrinkage and setup variations. CBCT from treatment setup may be used to estimate proton beam path through the conversion of CT Hounsfield Units (HUs) to proton stopping power. However, due to the large photon scatter in the CBCT geometry, the HU values from a CBCT varies slightly from diagnostic quality simulation CT, thereby introducing additional uncertainties in the conversion from HUs to proton stopping power. We tested and evaluated the Advanced Normalization Tools (ANTS) deformable image registration tool to map simulation CT HUs onto a treatment CBCT (Figure 7) for range verification or dose re-calculation during proton therapy treatment. The intensity corrected image may then be used to detect any local change in water equivalent thickness (WET) in the proton beam path.
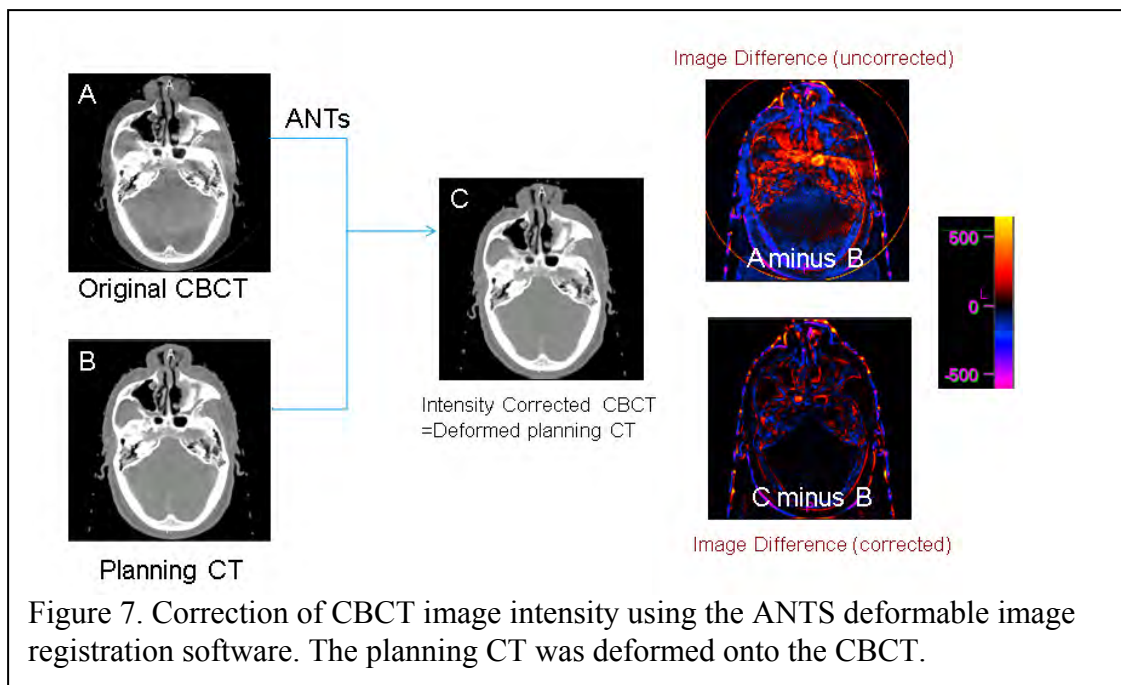
Figure 7. Correction of CBCT image intensity using the ANTS deformable image registration software. The planning CT was deformed onto the CBCT.
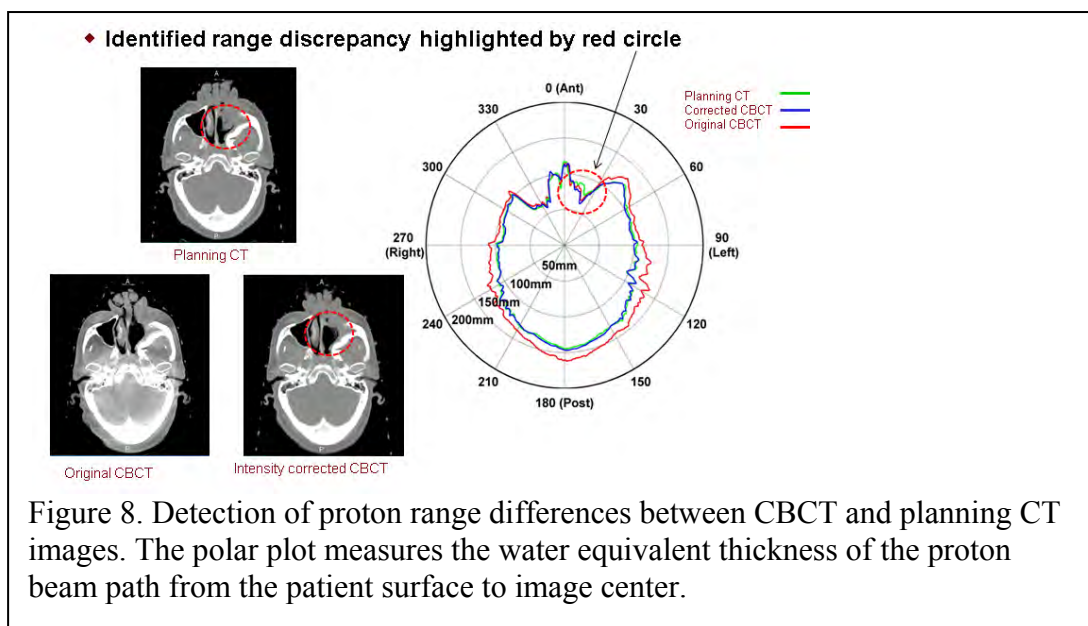
Figure 8. Detection of proton range differences between CBCT and planning CT images. The polar plot measures the water equivalent thickness of the proton beam path from the patient surface to image center.

In Figure 8, a patient with anatomical change (deformation in nasal cavity highlighted in circle) shows a deviation in the polar WET plot at 15 degrees between the planning CT (green) and the corrected CBCT (blue) at the time of treatment. Without the correction of the image intensity (red curve), the systematic error between the intensity levels of the CBCT and planning CT is larger than the WET change due to anatomical variation. Our results indicate that CBCT is a very promising tool for detecting potential dose delivery variations due to anatomical change or setup errors. This work was recently accepted as an oral presentation at the annual 2013 AAPM meeting.

Further development work is needed in this application of CBCT and we hope to be able to integrate this feature into the IBA CBCT system that the University of Pennsylvania is

58

developing jointly with IBA. During the last quarte of 2013r, the team at the University of Pennsylvania continued work on the development of proton therapy specific applications of on-line CBCT. CBCT has the potential to be used to validate and identify changes in patient anatomy that impacts proton dose distribution. Specifically, the algorithm used to correct the CBCT Hounsfield number is being validated so that CBCT image guidance can also be used to evaluate proton dose delivery in the treatment position. This validation process uses daily CBCT acquired for head and neck photon radiotherapy on the linac to simulate anatomical change during proton therapy. We envision clinical applications of CBCT to extend beyond conventional verification of treatment postion as is currently used in photon beam radiotherapy. We are presently developing tools to visualize changes in proton range based on comparision between the plannning CT and the acquired treatment CBCT so that therapists can alert physicians or physicists that treatment is not optimal and replanning may be required. We hope that this developmental tools will be integrated into the IBA CBCT system that the University of Pennsylvania is developing jointly with IBA.

Development of the Calypso System for use in proton therapy

Body

1.1 Installation of the Calypso System in Proton Room 4

The Calypso System is a system of implantable radio-transponders that can be used for patient localization and real-time tumor tracking. A Calypso System was obtained from Calypso Medical and installed in Proton Room 4 at Roberts. Calypso Medical has since been acquired and the System is now marketed by Varian Medical Systems.

The Calypso System was designed and approved by the FDA for clinical use during photon radiotherapy treatment. The installation at Roberts represents a first attempt to develop the system for use in proton therapy. During 2010-2011, tests were performed in the treatment room with proton beams to validate the performance of the system in the proton environment. See Figures 1 and 2. Some failures were observed and subsequent design modifications were performed by the Calypso Medical engineering team.
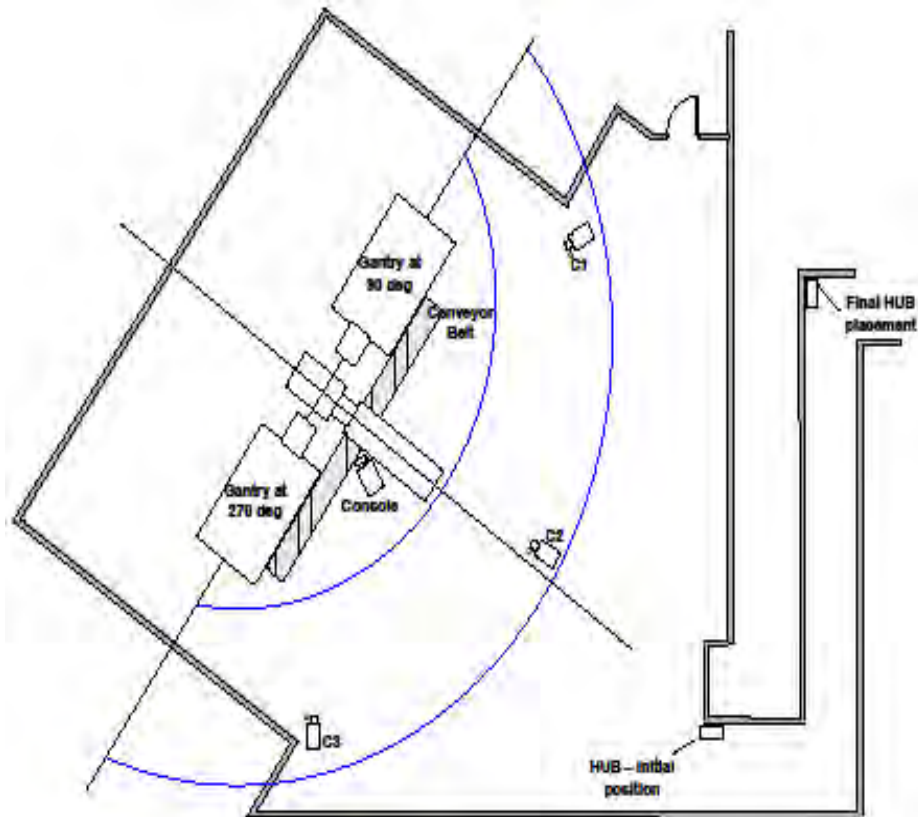
Figure 1. Schematic of the setup for Calypso System testing in Proton Room 4 in Roberts. The Camera Power Supply and Ethernet Switch electronics ("HUB") were moved from the initial position in the room back into the maze due to radiation susceptibility as part of the solution to reduce the system upset rate.

Figure 2. Test setup in Proton Room 4. The Calypso Beacons are located in the cylindrical test phantom, which can be registered into holes in the test platen. The platen is placed on top of a 16 cm wood box to move the Beacons away from the conductive table top. A larger wooden platform was constructed for the patient localization tests described in Section 1.3.

Here is a summary of the conclusions from tests performed by Calypso Medical:

- All localization accuracy tests passed their predefined acceptance criteria. The Calypso System accurately localizes LT and LO patients in the IBA proton therapy vault at the University of Pennsylvania.
- The carbon fiber table top will need to be replaced with a non-conductive version for clinical use of the Calypso System.
- System Design modifications were effective in reducing the upset rate from an estimated 15 upsets per month to <= 1 upset per month. The upset rate objective of <=1 upset per month was met. See Figure 3.
- The hard failure of the console's power supply has been effectively addressed by the power FET switch replacement.
- Camera Location and Mounting: No issues were identified with camera location or mounting in either the gantry or fixed-beam rooms.
- Console Placement in Fixed-Beam Room: No issues were identified with console placement in the fixed-beam room.
- MLC Susceptibility: No issues with MLC susceptibility to the Calypso excitation were identified (lateral beams)

- Interference from Proton Beam Scanning Magnets: No issues with scanning magnet operation interfering with Calypso operation were identified.
- Interference from MLC: MLC can be operated up to ~33 cm from isocenter with acceptable effect on Calypso operation (lateral treatments). Operation closer to isocenter may be possible with additional Calypso development.
- Activation of Transponders: No issues associated with activation of the Calypso transponders in a patient were identified.
- Carbon Fiber Table Extension: The carbon fiber table extension for the Schaer PPS is not compatible with the Calypso System.
- Calypso System Radiation Tolerance (Single Event Effects): The rate of single event upsets for the Calypso System operating with double scattering mode was unacceptably high. These upsets can result in both temporary disruption of Calypso operation during patient treatment (requiring reboot) and can result in hard failure of Calypso System.
- Calypso Console Placement in the Gantry Room: Lateral translation of the patient table during initial patient setup is not possible with the current production Calypso System, as the back wheels of the console would be on the conveyor belt, while the front wheels are off the conveyor belt.
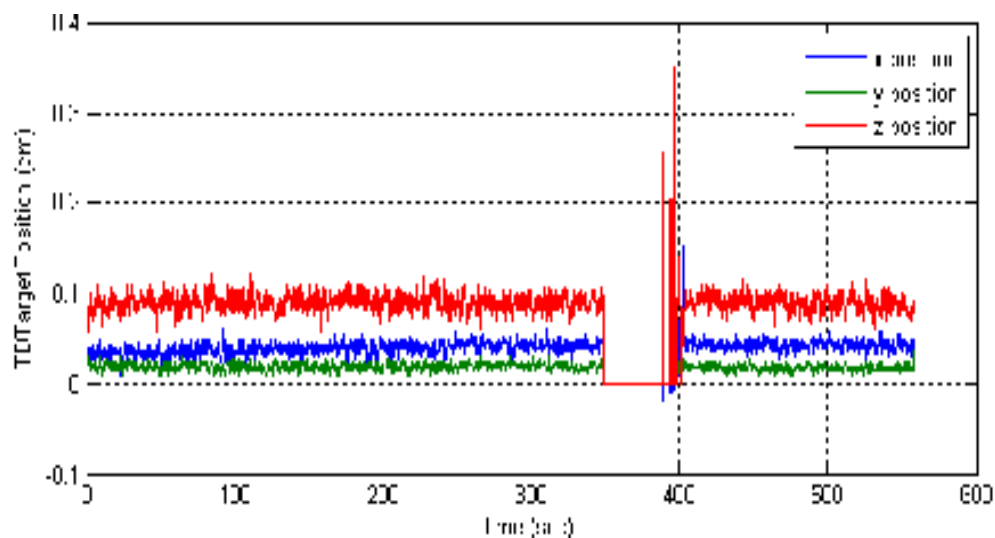
Figure 3. Example of a Radiation Susceptibility test. A front-end FPGA in the Calypso console was reconfigured to detect memory errors resulting from irradiation of the electronics by secondary scatter irradiation. In this test a memory error was detected after about 6 minutes of beam on. The FPGA identified the error, self-corrected, and recovered, although the recovery took 1 minute.

Here is a summary of the design modifications made by Calypso Medical for operation in the proton environment:
- The standard arm has been replaced with the extended arm. The reason for this is twofold:
  - Places electronics further away from the proton beam.
  - Allows the console to be placed inferior to the conveyor belt while maintaining the ability for the array to cover the tracking volume.

- The Advantech Console PC has been replaced with a passive touch panel display mounted on the mast and a separate single board computer equipped with ECC RAM. The single board computer has been placed in the console chassis, further from the radiation source. The cable assembly routed through the arm was modified to provide all signals required by the single board computer. Power for the passive touch panel display and the console PC was derived from the power supply assembly in the console chassis.
- The ST Microelectronics power MOS FET's in the power supply have been replaced with Fairchild parts
- The Ethernet switch located in the power supply assembly has been replaced with the 'Y' adaptor scheme.
- System software has been modified to allow continued tracking upon a loss of communication with the console PC.
- The OEM camera power supply and Ethernet switch has been installed in the vault maze, distant from the radiation source (see Figure 1).
- Field Programmable Gate Arrays (FPGAs) capable of configuration corruption detection and fast reconfiguration have been designed in to the console electronics.
- The treatment rooms at University of Pennsylvania are equipped with the 6 degree-of-freedom Schaer patient positioning system. This table incorporates a carbon-fiber insert (couch top) manufactured by Q-Fix. The Calypso System is not compatible with carbon-fiber inserts due to their electrical conductivity. Development of a Calypso-compatible couchtop for the Penn proton treatment rooms using Q-Fix technology is being discussed with Q-Fix.

1.2 Investigation of dose perturbations by the Calypso Beacon electromagnetic transponders

Though they are small, fiducial markers and transponders contain materials that are denser and have higher atomic number than patient tissues, and the result is a shadow region downstream of the transponder where the actual delivered dose is lower than what it would be were the implant not present. Dose shadows in excess of 20% have been demonstrated downstream of gold markers in megavoltage photon beams (Chow et al 2005,Chow et al 2006}. Perturbations of similar magnitude were observed in the vicinity of nickel-titanium urethra stents (Gez et al 1997). Carbon fiber markers are lower-Z and were found to perturb photon dose by only about a percent (Vassiliev_2012). In the case of proton therapy, studies have explored the dose perturbations from gold, titanium, and stainless steel fiducials, of various sizes and differing placement and orientation with respect to the proton beam (Newhauser et al 2007b, Matsuura et al 202)}. Another study examined the dose shadow produced by tantalum markers used in the treatment of uveal melanoma (Newhauser et al 2007c). Effects on dose were investigated for helical gold markers (Giebeler et al 2009), for novel fiducials composed of microscopic gold particles embedded in polymer (Lim et al 2009), and for a nickel-titanium stent (Herrmann et al 2010). Lower-Z alternatives such as carbon-coated ceramics, stainless steel, tungsten, platinum, and a polymer tube can have lower dose perturbations, but must be balanced against radiographic visibility (Cheung et al 2010, Huang et al 2011).

Electromagnetic transponders have dimensions similar to some of the implanted fiducials, and their constituent materials include soft ferrite, copper, and ceramics. The geometric arrangement of the materials is unique and may perturb dose differently than fiducials. The purpose of this study is to investigate the magnitude of the dose perturbations caused by the

presence of implanted electromagnetic transponders as part of an assessment of the feasibility of using electromagnetic transponders for proton therapy. The approach taken was to develop an accurate Monte Carlo model of the Calypso Beacon electromagnetic transponders, to validate the Monte Carlo simulations using measurements from some selected proton irradiation cases, and then to use the simulations to explore the effect of the transponders at different positions and orientations with respect to the proton beam.

Our investigations resulted in a publication in Physics in Medicine and Biology (Dolney et al 2013). That paper is included below in the appendix materials. The follow description of that work includes additional details not included in the paper in the interest of brevity.

A model of the Calypso transponder was implemented in Geant4 for Monte Carlo simulations. In Figure 4 is shown a photograph of a Calypso transponder. The transponder is an electromagnetic resonator: there is a wire coil wound around a soft ferrite core and connected to a capacitor. This resonator assembly is potted inside a glass vial with silicone adhesive and sealed with a laser. Calypso Medical provide detailed specifications regarding the dimensions and mass of each of the elements of the transponder. Unfortunately some of the materials were not completely specified because they are either not fully known or their compositions are IP. For example, the glass used for the vial is a patented formulation manufactured by the Schott Corporation known as Schott Glass 8625. It is a biocompatible soda-lime glass to which iron has been added. The iron makes the glass absorb infrared so that it can be sealed with a laser. The fraction of iron in this glass could not be found in the literature.

Figure 4. Photograph of a Calypso Transponder (left) and a wire-frame rendering of the Transponder as implemented in Geant4 simulation. The total length is 8.5 mm.

Because of the uncertainties involved, we validated our Monte Carlo simulations using data collected with sheets of Gafchromic EBT2 film placed at various depths downstream of transponders mounted in a stack of solid water slabs. Our machine shop fabricated a holder for three transponders from acrylic. The holder is shown in Figure 5. The three seeds are held in different orientations with respect to the beam: parallel, perpendicular, and 45 degree angle. The acrylic holder fits into a slab of solid water that had been previously milled out for a Capintec PS-033 chamber. We irradiated the solid water phantom with a uniform, double-scattered, R22M10, 13x13 square field. We scanned the films with an Epson 10000XL flat-bed scanner and applied our calibration curve for EBT2 OD-to-dose (see Figure 6). Using the OmniPro-ImRT software, we extracted the dose downstream of the Calypso seeds at the various depths and also in unperturbed regions of the film (see Figure 7). In this way we measure the dose perturbation downstream of Calypso transponders. We compared our measurements with simulation.

Figure 5. Holder constructed for Calypso seed. The holder is acrylic and fits inside the piece of solid water (yellow). Three seeds are fit into holder in different orientations.

Figure 6. Post-irradiation Gafchromic EBT2 films that were downstream of the Calypso transponders. The acrylic has a larger proton stopping power than the surrounding solid water, so that the shape of the acrylic holder can be seen in the deeper pieces of film (bottom row). Small dose shadows behind the transponders can also be identified, though in the picture they are difficult to see in most of the film pieces.
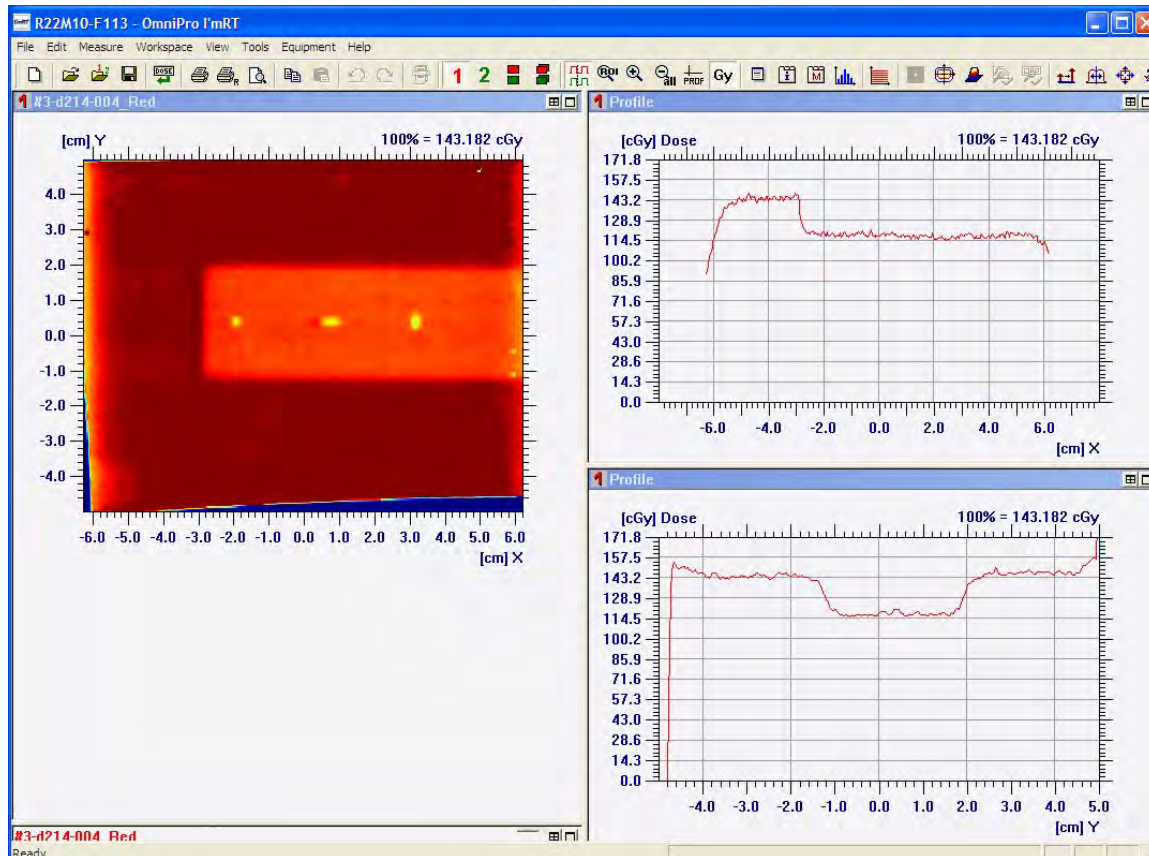
Figure 7. Film analysis using the OmniPro-ImRT software. The film was scanned with an Epson 10000XL flat-bed scanner. The image in the left pane is the film optical density converted to dose via our calibration curve for protons. The rectangle in the film is the shadow from the acrylic holder. Three dose shadows (yellow) from the Calypso seeds can be seen in the rectangle. We measure dose levels within these shadows relative to the surrounding medium.

The simulations use the IBA Universal Nozzle and MLC code implemented previously for Phase I studies by Chris Ainsley coupled with the voxelized phantom classed for scoring dose in 3D grids implemented by Derek Dolney for Phase II. For Phase II the voxelized phantoms were constructed from patient CT datasets. That code was modified slightly for this project to generate a phantom of uniform solid water, with the material specified by the vendor (Gammex). The voxelized phantom classes derive from G4PhantomParameterisation. It was previously not possible to place daughter geometries inside a G4PhantomParameterisation geometry. That is, Calypso seeds could not be placed inside a voxelized phantom. Given this limitation, the simulation geometry implemented for this work consisted of Calypso transponders inside a solid phantom of solid water material, with a voxelized cube of solid water placed downstream of the seeds only. This is acceptable for this phase of research, since we are comparing dose shadows from simulation with measurements taken in a solid water phantom. However, it would be useful to be able to calculate the effect on the dose distribution in real patients that have had Calypso transponders implanted. The simulation code at UPenn is well-developed at this point, and it would be a reasonable extension requiring a modest effort to implement this capability, assuming the new mechanism in Geant 4.9.5 performs as promised. That implementation could even be validated using the already collected solid-water phantom data just described. We can

consider validation measurements in a heterogeneous phantom beyond the scope of this Calypso phase, though that should be done to establish the validity of the patient simulation code, and we are discussing how best to approach that.

Most of the mass of a transponder comes from the coil. The coil is comprised of thin copper wire wound around a soft ferrite core. We initially attempted to implement a much-simplified version of the geometry as an iron cylinder placed within a larger copper cylinder, with the dimensions of each matching the vendor specifications. As shown in Figure 8, this implementation gave poor agreement (not better than 20%) with the film measurements and we were forced to refine the implementation.
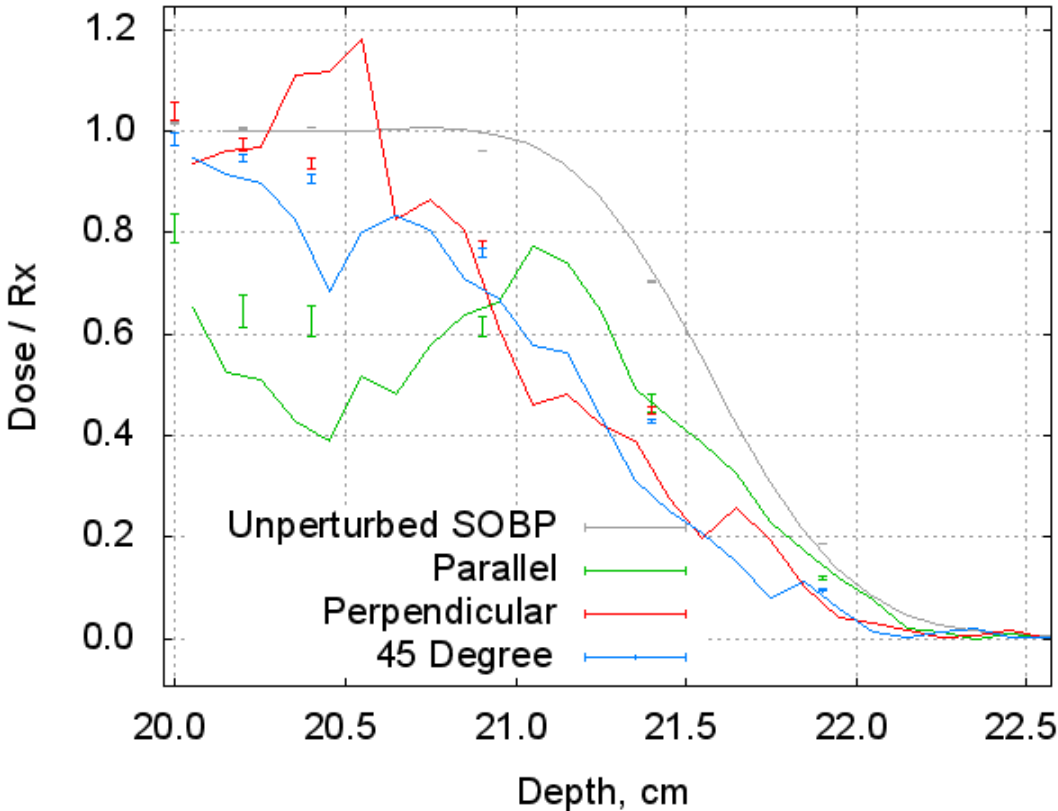
Figure 8. Proton dose shadow downstream of Calypso seeds: comparison between data measured with Gafchromic EBT2 film (points with errors) and Geant4 Monte Carlo simulations (lines) using a simplified implementation of the Calypso seed geometry comprised of an iron cylinder representing the ferrite core surrounded by a copper cylinder representing the coil. Agreement is not better than 20% using this geometry.

We completed a more thorough implementation of the Calypso transponder geometry in Geant4. We have included every detail of the Calypso transponders save for the silver-palladium connections on the capacitors and the thin (25 um) parylene coating that covers the resonator assembly. Some other assumptions and simplifications were necessary. We chose to use Pyrex with 5% Fe_2O_3. The density is specified to be 2.52 g/cm3. Given the dimensions of the glass vial, the shape of the vial endcaps were adjusted to achieve the total vial mass specified by Calypso. A coil of wire would be very difficult to implement in Geant4. The coil was implemented as a cylinder. The density of the coil itself is 6.15 g/cc, which is quite a bit less

68

than pure copper which is 8.96 g/cc. The wire used for the winding has a thin polyurethane insulation layer that is further covered by a polyvinylbutyral bond layer. Calypso says the copper is 39 um diameter and the total wire is 45 um, but this does not specify. There is a NEMA spec, MW 131, with these dimensions. One product meeting NEMA MW 131 is Butylbond AB15. These products appear to have equal thickness insulation and bond layers. Therefore we use 1.5 um thick insulation and 1.5 um bond layer. We have to use a generic molecular formula for polyurethane. There must also be some air between the wires in the winding, and so the copper core, insulation, and bond layer physical dimensions were used to fix the relative amounts of those elements, and derived that the coil must be about 12% air by volume, which is about equal to the volume of either the insulation or bond layer. This volume fraction is down-weighted by about 10^{-3} from the density of air, and can basically be ignored. The soft ferrite core is specified as Ferroxcube 3C91. Soft ferrites are iron oxides with some manganese and zinc added. The exact amount of these elements is probably secret. We assume a 1:1 Mn:Zn ratio. For the capacitors we assume the material is uniform titanium dioxide and do not include the silver-palladium terminals. There is some silicone adhesive in the glass vial to fix the resonator assembly. We fill the vial about halfway with polydimethylsiloxane, adjusting the amount to make the total mass of the transponder agree with measurement. We summarize these material choices in Table 1, and compare the mass of the components as implemented in our simulation with their actual physical masses in Table 2. In spite of our assumptions about the materials and some dimensions, the agreement with the measured data is much better, as shown in Figure 9. Agreement between the film and simulations is to within 3%. A large part of this error is probably systematic, as this is about the level of agreement between the measured and simulated SOBP, as can be seen from Figure 9. This could be improved by fitting per-room BCMs.

Table 1. Composition specification of the Calypso transponder and the materials used in the Geant4 implementation of the transponder geometry. Percentages are mass relative.

	Vendor Specified Material	Simulation Material
Core	Ferroxcube 3C91	$MnZnFe_4O_8$
Coil	Cu	96% Cu
	+ polyurethane	+ 2% $C_{17}O_4H_{16}N_2$
	+ polyvinylbutyral	+ 2% G4_POLYVINYL_BUTYRAL
Capacitors	Novacap NPO	TiO_2
Adhesive	Silicone	Polydimethylsiloxane
Vial	Schott Glass 8625	95% G4_Pyrex_Glass + 5% Fe_2O_3

Table 2. Account of the mass of a Calypso transponder. The actual mass of the transponder parts is compared with the mass of the geometry elements as implemented in Geant4.

|	Actual Mass (mg)	Simulation Mass (mg)
Core	2.9	2.9
Coil	36.0	36.0
Capacitors	1.3 x 2	1.1 x 2
Adhesive	not specified	0.8
Vial	20.0	20.0
TOTAL	61.8	61.8
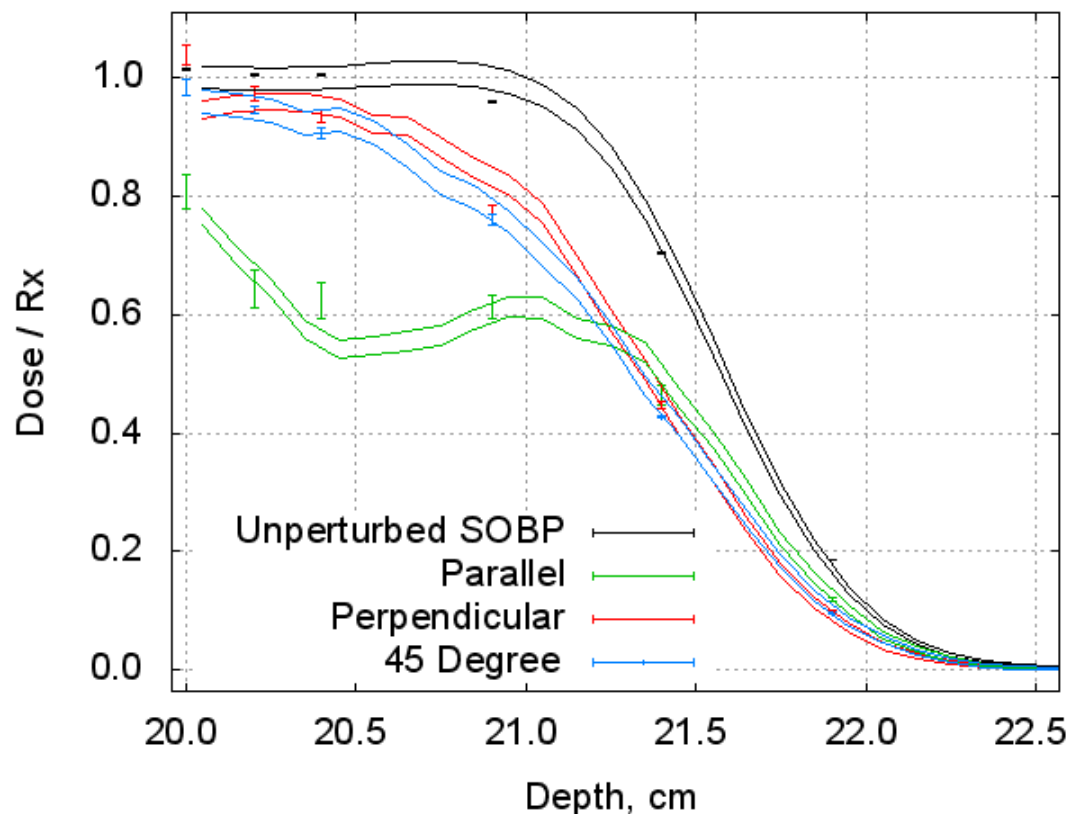
Figure 9. Proton dose shadow downstream of Calypso seeds: comparison between data measured with Gafchromic EBT2 film (points with errors) and Geant4 Monte Carlo simulations (lines) using a thorough implementation of the Calypso seed geometry including all elements in Table 4-1. The double lines for the simulation curves are meant to indicate the error bars, the upper line being the mean plus 1 and the lower the mean minus 1 . Agreement is within 3%.

We also measured data for Calypso seeds at 13 cm depth using the same R22M10 field. The simulations of that scenario also agree well with the measurements (see paper). A challenge for this phase of the project was the number of protons that must be simulated to get accurate doses in the small voxels downstream of the transponders. The transponders diameter is only 1.8 mm. We are using 1/3 mm voxels transverse to get good spatial resolution, comparable to the film digitization resolution (75 dpi). We generated 2×10^{10} primary protons to produce Figure 9. We used 64 cpus and the entire simulation still took 3 weeks.
 The long computation time for the Calypso transponder simulations was reduced by implementing the capability to store the proton beam phase-space to a file. To solve this problem, Derek made use of open-source code from two sources: the International Atomic Energy Agency (IAEA) phsp read/write routines available from http://www-nds.iaea.org/phsp/phsp.htmlx , and the Geant4 interface to use these routines G4IAEAphspInterface_v1.1 available from http://www-nds.iaea.org/phsp/Geant4/. A few bugs were found and fixed in both codes. Commands were added to our macro file interface for double-scattering simulations to allow the phase-space to be saved during a simulation, and to allow a simulation to use a previously stored phase-space file. In addition, the IAEA phsp routines support so-called phase-space "recycling", meaning the particles in the phase space file are generated and tracked more than once. This can reduce the statistical noise to an

extent, to the limit that is called the latent variance of the phase space file. It was found that a recycling value of 2, meaning each particle in the phase space file is generated three times, gives a good balance between statistical noise and simulation time. More particle recycling does not lower the noise much. More primaries would have to be generated during the first phase-space generation step to achieve higher statistics. Without using a phase-space file, the Calypso simulations took 3 weeks using 64 cpus for each depth to have reasonably low statistical noise, given the small voxels in which we are scoring dose behind the Calypso implants. Now, by storing the phase-space to a file, an initial run of about a week (using 64 cpus) is required to generate the phase space upstream of the water phantom containing the Calypso seeds, but then this phase space can be used for any Calypso depth, with each depth requiring only 4 days (on 64 cpus) simulation time.

The dose was measured with film downstream of Calypso seeds placed at depths 12 cm and 21 cm in solid water in an R22M10 spread-out Bragg peak (SOBP). The 21 cm data was compared with simulation results in the last report. The 12 cm simulations have finished and that comparison is presented in Figure 10. Like the 21 cm case, the agreement between measurement and simulation at 12 cm is also very good.
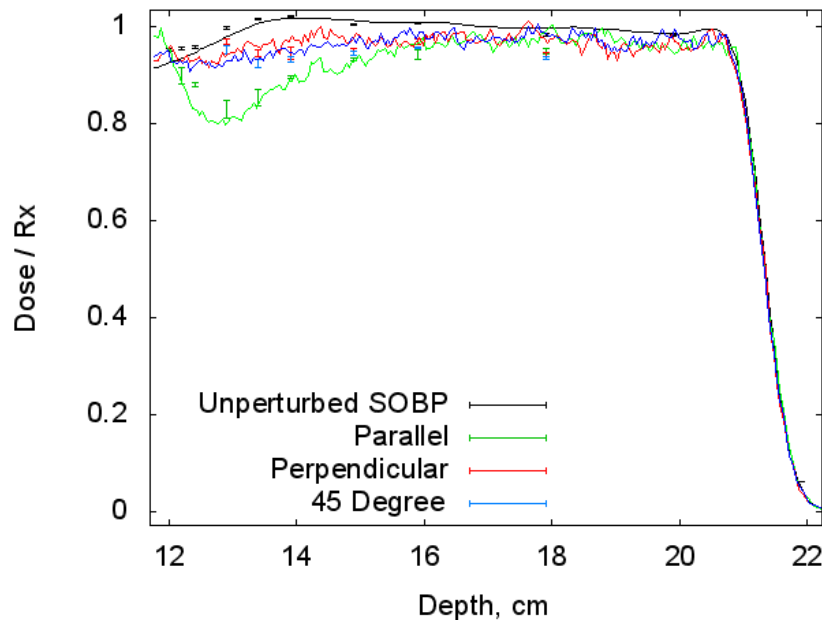
Figure 10. Comparison of dose shadow downstream of Calypso transponders in a proton SOBP measured with film (error bars) with Monte Carlo simulation (lines). The Calypso transponders were irradiated and simulated in three different orientations at 12 cm depth in solid water.

Monte Carlo simulations of Calypso transponders were completed for other depths in the R22M10 SOBP: 12, 13, 14, 15, 16, 17, 18, 19, 20, and 20.5 cm physical depths. These are presented here for completeness.
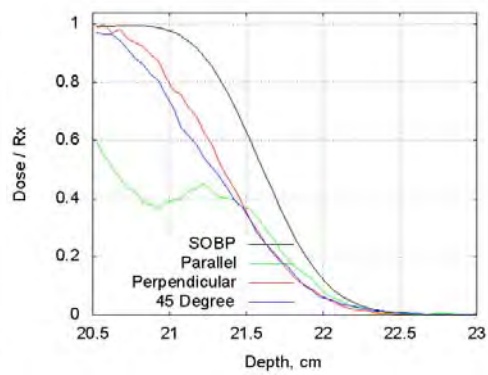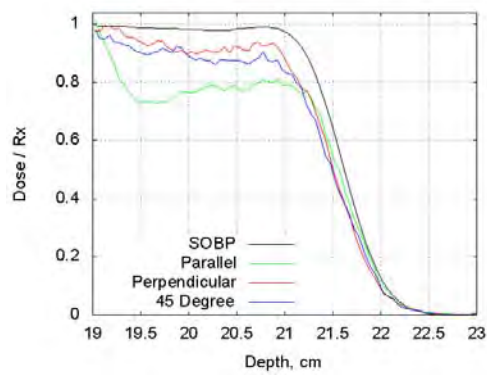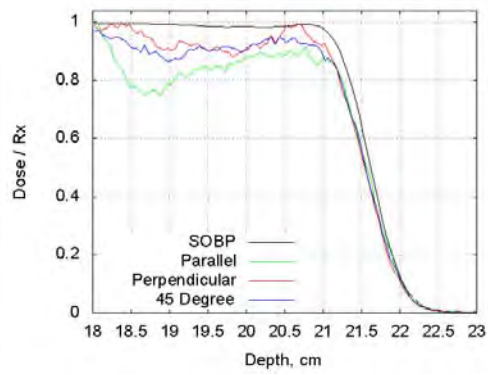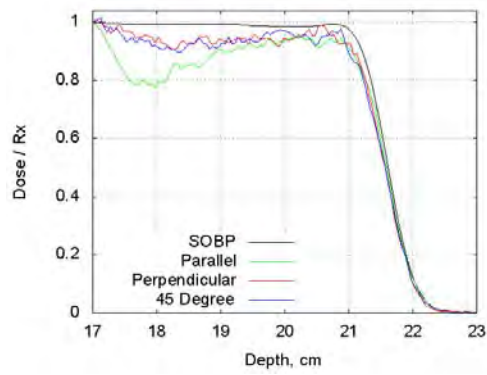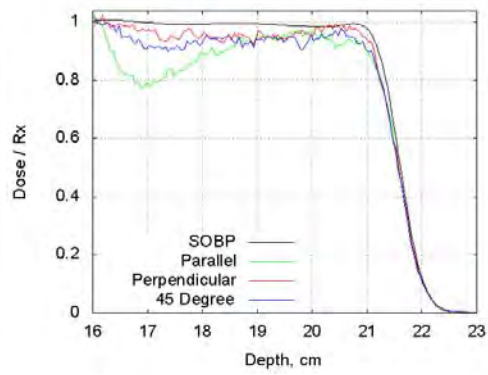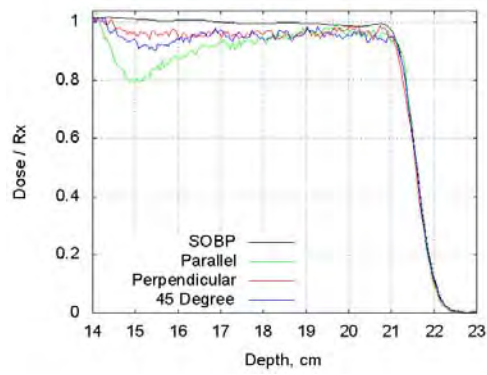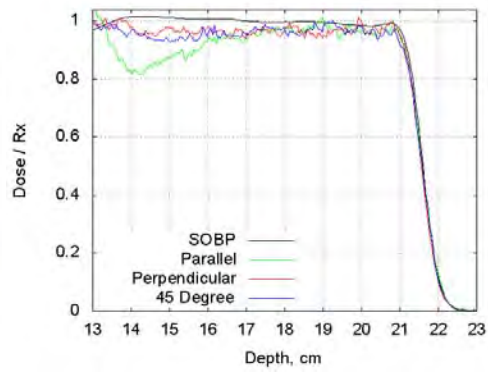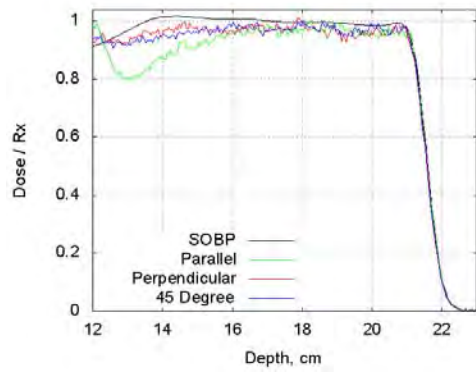
From these data, we extracted the maximum dose shadow for three different transponder orientations. That data is presented in Figure 11.
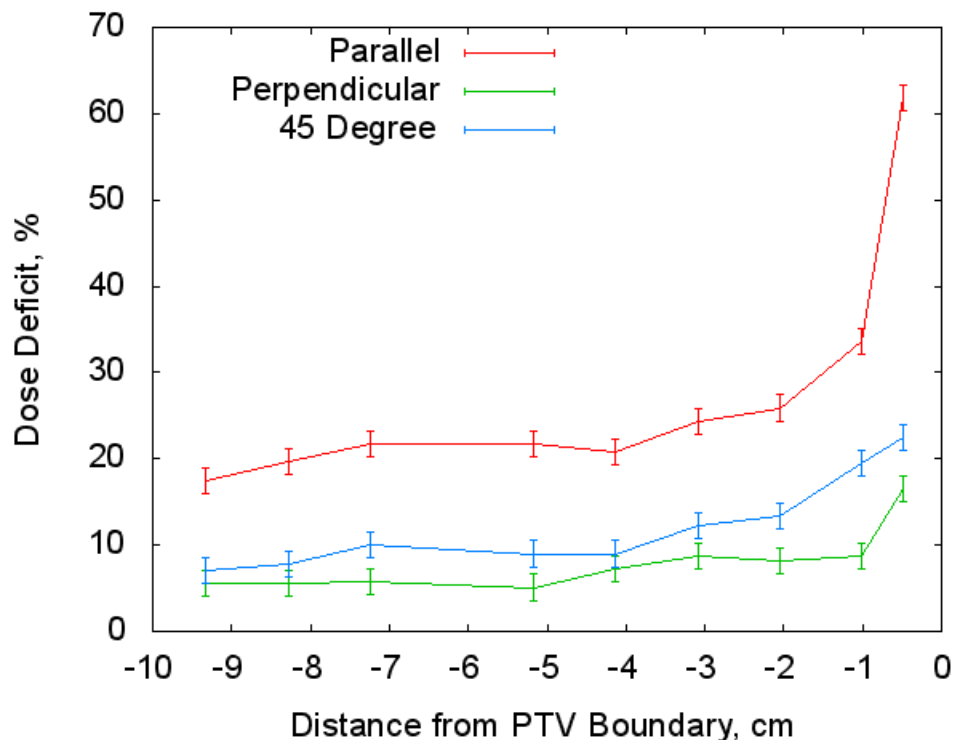
Figure 11. Maximum dose shadow downstream of Calypso transponders at different depths in a proton SOBP and in different orientations with respect to the beam. Typical dose shadow levels are less than 10%, arising because of increased lateral scatter in the high-Z metals inside the transponder. However, the dose deficit can be large when seeds are positioned near the distal falloff, in which case protons actually stop in the transponder.

Besides the published paper, a poster version was presented at the American Radium Society Annual Meeting (2012).

1.3 Testing the Calypso System for patient localization

We have begun testing of the Calypso system using patients previously implanted with Calypso Beacons and treated with photons at Penn. A platform was constructed of non-conductive material (wood) to permit testing using the existing couch tops before a non-conductive couchtop is purchased from a vendo. It was determined that 6" of wood is necessary to sufficiently separate the Calypso Beacons from the proton couchtop to allow the system to localize the Beacons.

There are 16 patients enrolled in a prostate research protocol making use of endorectal ballons and using Calypso for localization and real-time monitoring. Some of these patients have been solicited to participate in a localization study in Proton Room 4 to compare Calypso localization accuracy versus the orthogonal kV localization that is standard for prostate treatments at Roberts. So far one patient agreed to participate in the study. The patient was setup in P4 with rectal balloon and first localized using Calypso. It was found to be difficult to localize the patient with Calypso to better than 4 mm because of the way the IBA couch jogs. To improve this, we will use the couch "goto position" shifting for future patients. Next orthogonal kV imaging was performed as usual, with shift coordinates obtained from the imaging system and applied to the

couch. After the shift, the patient position was re-measured with Calypso to see the differences. The measurements are summarized in the following table.

Stage of localization	Vertical (cm)	Lateral (cm)	Longitudinal (cm)
First with Calypso We could not achieve 0,0,0	-0.20	0.05	-0.40
The imaging results (shift that was applied)	0.407	-0.222	0.414
Calypso after the patient was adjusted Based on imaging	0.25	-0.20	0.000

Calypso and imaging agree for the longitudinal coordinate system. For the vertical and lateral directions, Calypso and imaging agree to within 2 mm. One source of error can arise from transponder migration after CT simulation, however the therapist performing the orthogonal kV matching for this patient felt that the Beacon positions aligned well with the positions from the patient CT dataset. It is likely that the Calypso system needs to be recalibrated to bring its origin into agreement with the imaging system origin. The Calypso may have been commissioned to the room lasers, which are only rough guides. We will gain a better understanding as more patients are imaged. Any systematic error between the Calypso and imaging systems can be corrected by re-adjustment of the Calypso origin. Drift of the Calypso origin is monitored by daily Quality Assurance. Of interest for this study is the random error realized when localizing patients (of different sizes, implant locations, etc) with Calypso, since represents the System limitation to the localization accuracy.
This study is on-going and currently awaiting the agreement of patients to the additional imaging and localization study.

Radiobiology

INTRODUCTION
The goals of this project were the following:

1. Identify and develop appropriate model systems for preclinical testing proton RBE in the Penn proton beam facility.

2. Test and implement cell lines and methods as defined above with standard photon radiation.

3. Measure RBE for protons using the Penn proton beam facility and the dependence of this RBE on physical beam properties and biological cell properties.

BODY

Tasks 1 and 2:

These studies were designed to develop and test proton-compatible methods of determining cellular radiosensitivity using human cell based model systems that were defined in year 1. In the first quarter, the head and neck cancer cell lines SQ20b and FaDu and the immortalized human oral fibroblasts (MSK-LEUK1) have been cultured and the clonogenic (plating efficiency) was determined using standard initial plating (Table 1).

Table 1: Plating Efficiency (without irradiation)	
SQ20b	0.65
FaDu	0.55
MSK-LEUK1	0.33

Using these plating efficiencies and 60cm dishes in a horizontal 137Cs irradiation (Figure 1), the clonogenic survival of these cell lines was determined (Figure 2). Note that the initial plating efficiencies have been normalized to a surviving fraction of 1 to allow a comparison of the relative radiation sensitivities of each cell line. The range of radiosensitivity accounts for a dose modification at 10% survival of approximately 1.7 between the most and least radiosensitive cell lines.
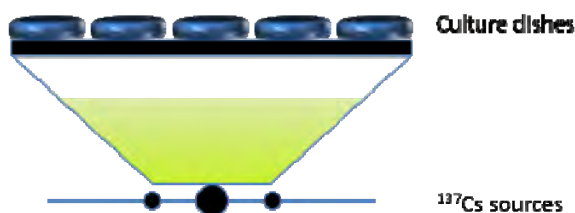
Figure 1: Irradiation set-up for initial experiments
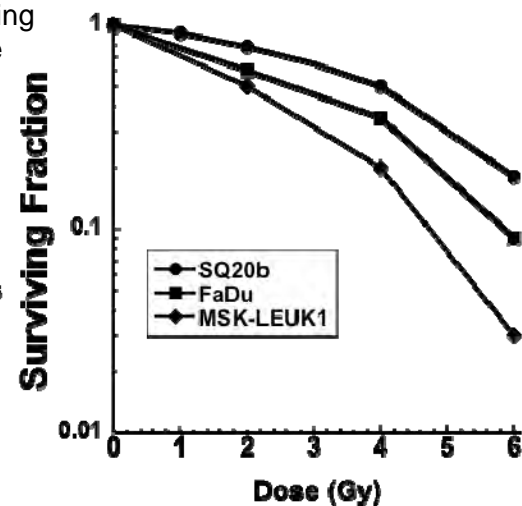
Figure 2: Clonogenic survival of head and neck cell lines

However, these techniques are not compatible with the fixed horizontal beam that will be used in proton irradiation. We have therefore begun to test whether using alternative techniques significantly alters the radiation response of these cell lines. We have employed 2 alternative methods for this analysis. The first is using tissue culture flasks with adherent cells filled with medium during radiation. As depicted in Fig 3, a turntable that rotates at approximately 4-5 rpm is used to provide a relatively homogenous dose for all flasks. . We also used a modification of this technique in which cells are trypsinized and irradiated as non-adherent cells in a sterile glass flask equipped with a magnetic stirring piece (Fig 4)

Culture flasks on turntable

137Cs sources
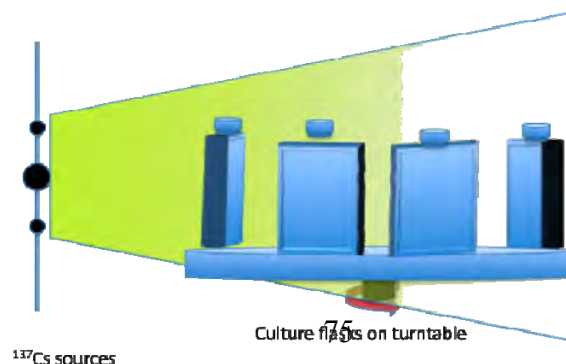
Figure 3: Horizontal irradiation set-up
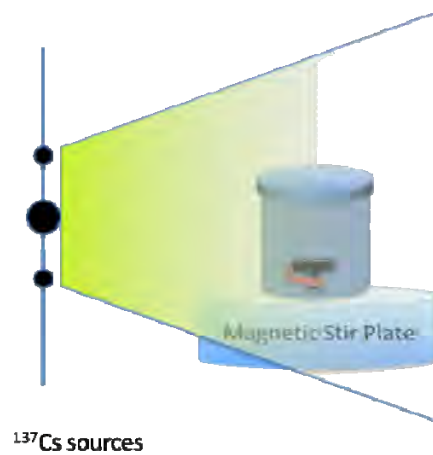
Figure 4: Cell suspension irradiation set-up

Using these set-ups, the radiosensitivity of wild-type fibroblast cells was analyzed. The results of these experiments suggest that the horizontal and vertical methods give similar results, but that there is a problem with the cell suspension method, especially at higher radiation doses (Fig 5).
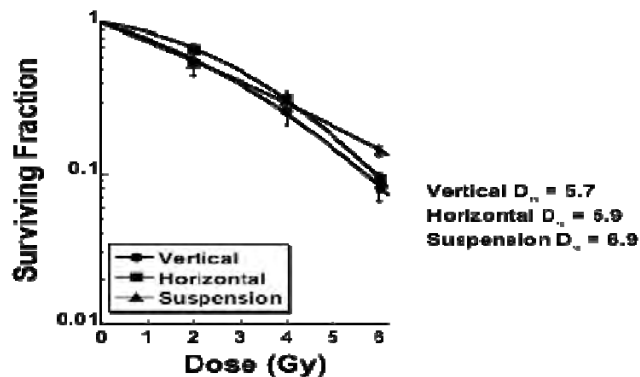
Figure 5: Irradiation of fibroblasts with different set-ups

Note that the difference in the radiation dose needed to achieve 10% survival (D_{10}) calculated from the linear-quadratic approximation of the survival curves is close to unity for the horizontal versus vertical methods. This suggests that these two methods are sufficiently robust to allow RBE comparisons for normal fibroblasts. However, when we compared the radiosensitivity of human A549 and SQ20b cancer cell lines using horizontal or vertical set-ups, we found conflicting results. For the A549 cell line, the methods showed good agreement, but the standard deviations on the flask (horizontal) method were significantly larger than the dish (vertical) method (Fig 6a). For the SQ20b cells, the vertical method showed a similar increase in standard deviation, but also demonstrated a markedly different radiosensitivity profile (Fig
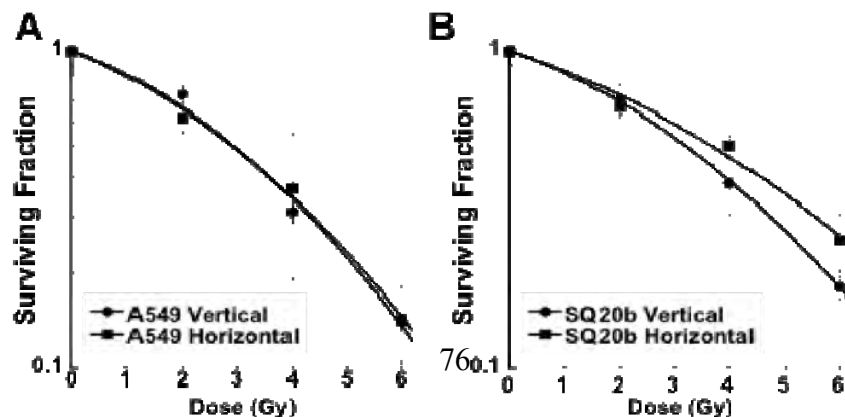
Figure 6: Horizontal vs Vertical Irradiation of A549(a) and SW20b(b) cells

6b).

To minimize need for beam time, we have designed and constructed a multi-dish irradiator box that will allow us to measure clonogenic survival at multiple points within the Bragg Peak (Fig 7). Note that this design allows simultaneous determination in triplicate samples for clonogenic survival at 4 points within a SOBP.
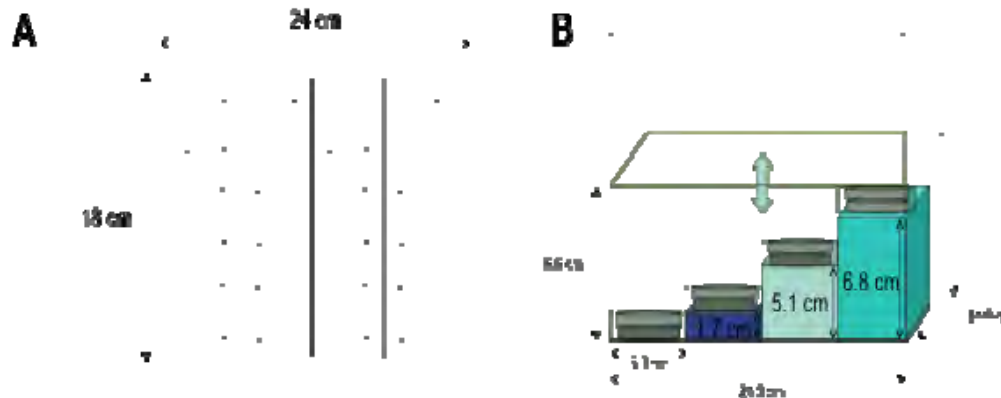
Figure 7: Top (a) and side (b) views of multi-plate, multi-level irradiation chamber

We have tested the variability of the vertical irradiation set-up using ^{137}Cs irradiator by performing separate, quadruplicate clonogenic survival experiments (with each data point representing the mean of triplicate measures of clonogenic survival within each experiment). These experiments reveal that the inter-experimental variability of radiosensitivity profile measured is less than the variability in intrinsic radiosensitivity for our 3 chosen head and neck cancer cell lines (Fig 8).
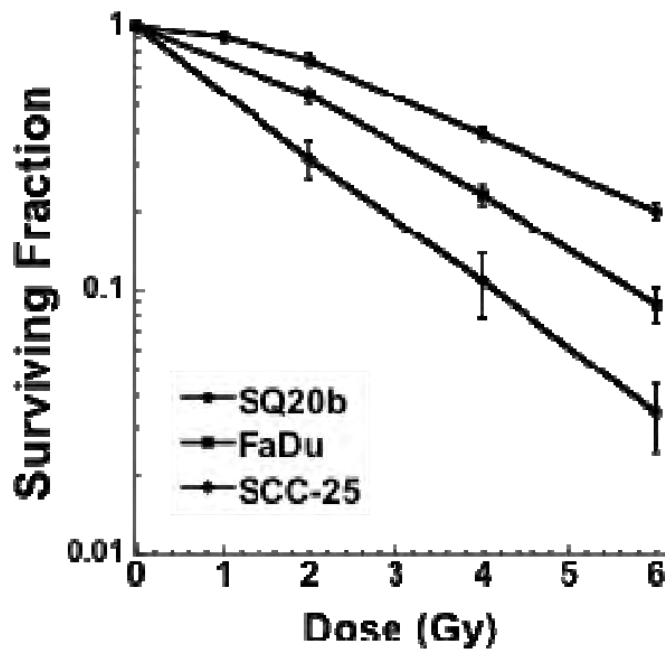
Figure 8: Replicate Vertical Irradiation using ^{137}Cs

Task 3:
Using the models and techniques developed in Tasks 1-2, we investigated the implications of the differential physical LET spectra along a SOBP and the radiosensitivity of cancer cells. (**Fig 9**).
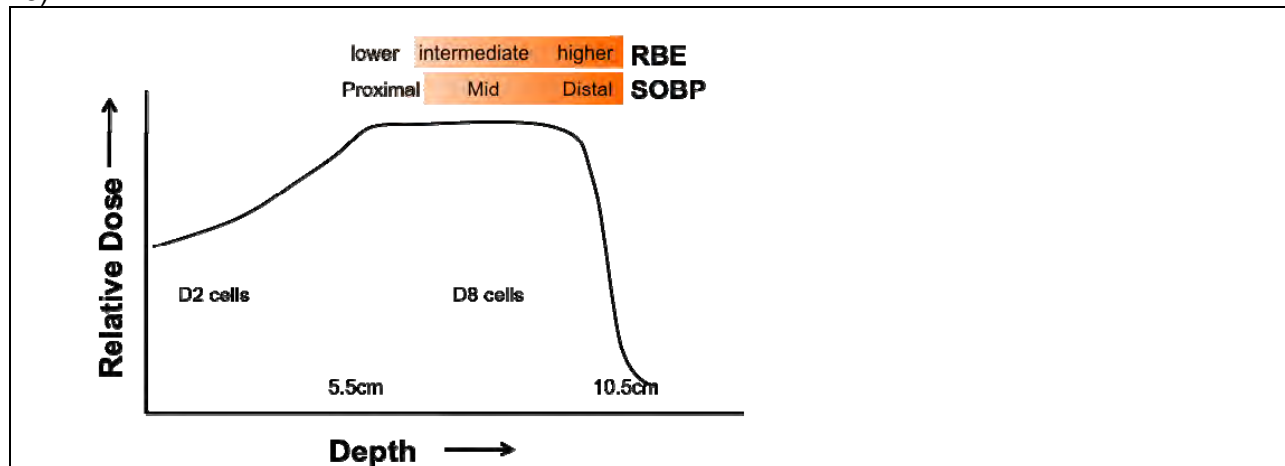
Figure 9: Cells were positioned at the 2 cm and 8 cm water equivalent thickness in a 10.5 cm range, 5 cm modulated SOBP.

We found that that, contrary to our previously stated hypothesis, these highly radioresistant cells do not display a dramatic difference in radiosensitivity for the plateau vs mid-SOBP portions of the proton depth dose distribution (**Fig 10**).
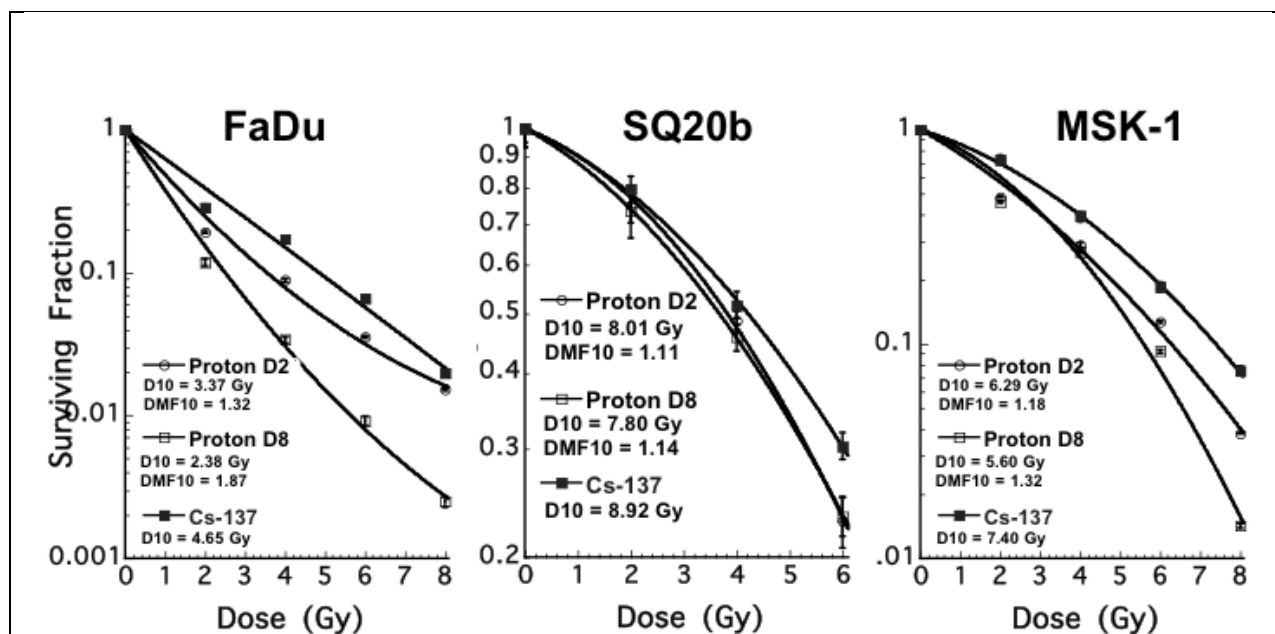
Figure 10: Radiosensitivity of FaDu and MSK-1 cells in high and intermediate LET proton regions. Clonogenic survival experiments were performed as described in methods and results are presented as mean +- sd for experiments performed with a minimum of 6 replicate plates per condition irradiated on the same day.

The radiosensitivity of SQ20b cells is primarily driven by over-activation of the EGFR-Ras-AKt signaling pathway. To determine whether inhibition of EGFR signaling would provide differential radiosensitization in different parts of the SOBP distribution, cells were pre-treated for 1h prior to irradiation with the EGFR inhibitor erlotinib or vehicle (control) and irradiated using a double scattered proton beam and a 10.5 cm range, 5 cm modulated SOBP (**Fig 9**). These positions were chosen to measure the RBE in the pleateu and mid-SOPB portions of the dose distribution and the particle fluence was adjusted for each to give final doses of 2, 4 or 8 Gy (note that this is measured in J/kg of protons or photons, not CGE) for each depth. The percentage of surviving cells was calculated by normalizing the percentage of cells forming colonies at a particular radiation dose relative to the percentage of cells forming colonies without irradiation. A linear-quadratic approximation of cell survival is presented for comparison of SQ20bcells with or without Erlotinib from previous experiments. We found a significant differential in the radiosensitization between low (D2) and high (D8) LET protons (**Fig 11**). These data suggest that there may the contributions of EGFR radioresistance pathway signaling to cellular radiosensitivity may be greater for higher LET radiation. Conversely, these experiments suggest caution should be advised when combining radiosensitizing chemotherapy/targeted therapy with proton radiation in patients.
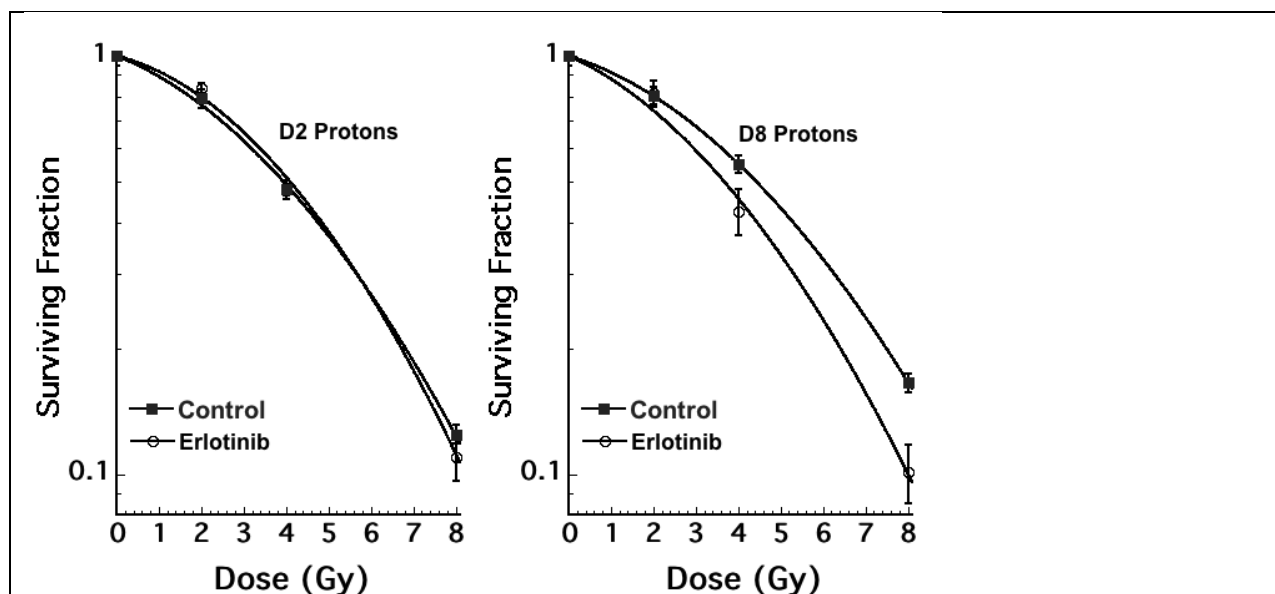
Figure 11: Radiosensitivity of SQ20b cells with or without the EGFR inhibitor Erlotinib in high and low LET proton or photons. Clonogenic survival experiments were performed as described in methods and results are presented as mean +- sd for experiments performed with a minimum of 6 replicate plates per condition irradiated on the same day.

Positron Emission Tomography (PET) of proton beams to verify dose deposition

INTRODUCTION
The goals of this project were the following:

1. PET Detector Development: Design a PET scanner optimized for the application of verifying the dose distribution deposited by proton therapy beams. This includes detector selection, electronic and mechanical engineering, data acquisition, and reconstruction software.

2. Cross-section measurements: Measure positron-emitting isotope production from the primary elements found in tissue and compare to the GEANT4 Monte Carlo simulation program.

3. Determination of elemental composition: The verification of the dose distribution cannot be done directly because the production of isotopes is not easily related to the dose deposited. Instead a Monte Carlo simulation program is used to calculate both dose deposited and isotopes produced and the latter is compared to the measured value. It is critical that the correct elemental composition be used in the simulation for this comparison to work. We are investigating how additional imaging methods, such as dual-energy CT, can help determine the composition.

BODY
We adapted the prototype RATX detector system so that it could be moved to the fixed proton beam room for testing, with completion of design and production of a series of modifications to the existing table. The mounting system and detector bed were designed and modified in order to allow the detector to be used in a clinically active area without risking damage to the system or interfering with clinical activities, and allow navigating in and out of the treatment room.

The prototype was moved to the PCAM facility and re-configured inside the fixed beam room. Detector calibrations were reproduced, demonstrating that the detector was moved safely and without damage. Data was taken using a phantom to confirm the uniformity of reconstruction and to measure the absolute sensitivity of the detector, as a pre-requisite to imaging the proton distribution following radiation., in order to ultimately determine the accuracy with which we can determine the range of the proton dose, and ultimately translate these results from phantoms to humans.

Calibration problems were corrected, resulting in substantially improved quality of image reconstruction. This correction was tested with a 20-cm diameter phantom, which then will enable further studies with large phantoms more representative of patients.

Due to higher than expected clinical downtime at the Roberts Proton Therapy Center since opening of the center for patient care, treatment operating hours for patient care have been routinely extended. As a result, we have had significantly less time that expected to continue work on this project.

Proton Beam Allocation Project

INTRODUCTION
The aim of this project was to develop a computer program to maximize the efficiency of the proton facility with respect to patient scheduling, beam allocation, and patient flow.

BODY

1. Designing the real-time beam allocation application.

Three sources of information are used for making real-time beam allocation decisions: 1) files containing the duration of preparation and field phases for each treatment protocol, 2) the file containing up-to-date patient scheduling information, and 3) the file containing the records of real-time events in each treatment room. Below we provide a description of each of these information sources and discuss how the beam allocation application can operate in real time.

1.1. Protocol durations files.

One of the issues that need to be addressed in designing the beam allocation application is how to model random durations of preparation and field phases for each treatment protocol. In particular, it is necessary to store data on those durations in a manner that can account for their random nature. An approach for storing these data that we adopt consists of defining, for each preparation or field duration for each treatment protocol, a number of "time buckets" covering time intervals from smallest to largest possible duration.

For example, consider an initial preparation phase for a treatment of "Prostate-2" patients (treatment protocol with 2 fields and prostate as an application site). Suppose that the minimum possible duration for this preparation phase is 1 minute and the maximum possible duration is 30 minutes. In order to store the data for actual durations of this preparation phase, we can define time buckets of size, for example, 0.1 minute, such that the entire interval between 1 minute and 30 minutes is covered by these buckets. In particular, in this case there will be 290 time buckets, with 1st one covering the time interval $[1, 1.1)$ minutes, the 2nd one – interval $[1.1, 1.2)$, etc., and the last one covering the time interval $[29.9, 30)$ minutes. Each time the actual duration falls within a particular bucket, the "count" of durations in this bucket is increased by 1. Thus, all realization of the actual duration of this preparation phase observed by a given moment in time can be expressed similar to the example in the following Table.

Time Bucket (in mins), i	Duration Count, c_i
$[1, 1.1)$	1
$[1.1, 1.2)$	5
...	...
$[29.9, 30)$	1

Table 1. An example of duration counts in each time bucket.

Such an approach to storing realizations of random durations is equivalent to recording an "empirical" probability distribution of a particular duration. For example, if we use N buckets to record a particular duration, and the current duration counts for each bucket are $(c_1, ..., c_N)$, we can define the probability that the random duration "falls" within bucket i as

$$p_i = \frac{c_i}{c_1 + \cdots + c_N}, i = 1, ..., N.$$

If the bucket size is small (e.g., 0.1 mins), we can approximate a given duration as being a random variable taking values equal to the midpoints m_i of each bucket[1] i with probabilities given by the above formula. Such probability model can be used to calculate various parameters used during real-time beam allocation. For example, the expected value of such duration can be estimated as

$$E = \sum_{i=1}^{N} p_i m_i = \frac{c_1 m_1 + \cdots + c_N m_N}{c_1 + \cdots + c_N}.$$

Duration observations for any field or preparation phase for any protocol can be stored in this way and then used during real-time beam allocation.

Protocol data files are created with the help of users who set the appropriate time-bucket size, and the maximum and minimum preparation and field duration parameters. As new treatment protocols are created, the corresponding protocol data files are added to the overall set of files. Realistic estimates for the initial duration counts should also be specified at the time a particular protocol data file is created.

All protocol data files are read at the beginning of each day, with the appropriate duration metrics (such as expected durations) calculated and stored for use during real-time beam allocation. Protocol data files are updated at the end of each day by adding duration counts for all observed preparation phases and fields to the appropriate files.

1.2. Patient Schedule file.

A Daily Schedule file (we assume it is presented in a CSV format) contains up-to-date information on the actual patients served up to the current moment and anticipated patients to be served form the current moment till the end of the day in each treatment room. The information includes scheduled patient arrival times and treatment protocols. The "up-to-date" feature implies that the initial schedule available in the beginning of the day and is automatically updated during the day in cases of patient no-shows, cancellations and new additions to the schedule. For each treatment room, a Daily Schedule file contains a list of patient scheduled arrival times and treatment protocols. An example of a Daily Schedule file is given in Table 2 below. In this example, the 1st patient to arrive at room 1 is scheduled for 8:00am and is to be served according to the treatment protocol 1, the next one is scheduled for 8:30am and is to be served according to the treatment protocol 7, etc.

---

[1] For example, the midpoint of the time bucket [1, 1.1) is $m_1 = 1.05$, and the midpoint of the time bucket [29.9, 30) is $m_{290} = 29.95$.

Room	Arrival	Protocol	Arrival	Protocol	Arrival	Protocol	Arrival	Protocol	Arrival	Protocol	Arrival	Protocol
1	480	1	510	7	540	1	570	4	600	2	630	2
2	480	2	510	5	540	1	570	3	600	1	630	3
3	480	2	510	3	540	3	570	13	600	12	630	1
4	480	3	510	4	540	2	570	10	600	1	630	5
5	480	1	510	1	540	1	570	1	600	1	630	9

Table 2. Example of a Patient Schedule file.

1.3. Real-Time Events file.

The Real-Time Events file stores (we assume, in the CSV format) information on patient-related and beam-related events since the beginning of the day up to the present moment. For each event, three pieces of information are recorded: "time stamp", "treatment room", and "event type". The "time stamp" records the time at which a particular event happened (expressed, for example, in minutes since midnight). The "treatment room" is the number of room in which event happened. The "event type"" describes one of (currently 5) possible events of importance to the beam allocation algorithm:

Event type 1 = "Patient has entered the treatment room"
Event type 2 = "Patient is ready for the beam"
Event type 3 = "Beam has been delivered to the room"
Event type 4 = "Beam has been returned from the room"
Event type 5 = "Patient has left the room"

An example of the Real-Time Events file is shown in Table 3 below.

Time Stamp	Room	Event Type
480	1	1
480	2	1
480	3	1
480	4	1
480	5	1
483.1	2	2
483.5	1	2
483.6	2	3
484.5	2	4
484.7	1	3
485.2	4	2
486.3	1	4
487.5	5	2

Table 3. An example of a Real-Time Events file.

In this example, the sequence of events is as follows: at 8:00am 5 patients enter rooms 1 through 5. Next, at 8:03:06am the patient in room 2 is ready for the beam, followed by a patient in room 1 that becomes ready for the beam at 8:03:30am. The beam is delivered to room 2 at 8:03:36am

and is returned at 8:04:30am. Beam is then delivered to room 1 at 8:04:42am. Next, the patient in room 4 gets ready for the beam at 8:05:12am. The beam is returned from room 1 at 8:06:18am. Finally, patient in room 5 gets ready for the beam at 8:07:30am.

1.4. How the beam-allocation application operates in real time.

It is assumed that when the beam allocation algorithm is invoked in real time, there is at least one room waiting for the beam. If there is only a single room waiting for the beam, the beam will be sent to that room. If there are two or more rooms waiting for the beam, the beam allocation algorithm will read the contents of the Daily Schedule and Real-Time Events files and will convert the information in these two files into the current "state" of the treatment system, representing a sequence of preparation and field times remaining to be delivered in each treatment room at a time when a beam allocation decision needs to be made, as well as the waiting time, if any, incurred so far by the next field ready to be served in each room. The idea behind a real-time single-field dynamic beam allocation algorithm (RTSFD) is based on analyzing the throughputs resulting from sending the beam to each of the currently waiting rooms, followed by first-ready first-serve beam allocation (FRFS) afterwards. In other words, the RTSFD algorithm operates on the assumption that all preparation and field durations are known with certainty. In the deterministic setting, comparison between the alternative beam trajectories takes very little time for any realistic number of fields/patients remaining to be served at the time the allocation is made. On the other hand, if the values of future preparation and field durations are random (and known only in distribution, as described in protocol data files), the goal of minimizing the throughput has to be adjusted, for example, to a goal of minimizing the expected throughput. In such settings, the task of calculating the expected throughput resulting from following a FRFS beam allocation approach is actually hard to accomplish, especially in real time, since the FRFS beam trajectory itself depends on the actual values of preparation and field durations. One adaptation of the deterministic version of the RTSFD algorithm to stochastic settings is, when making a beam allocation decision, to approximate the future (random) preparation and field durations by their expected values. Note that when a beam allocation decision is made in real time, the decision maker knows the actual values of the waiting times for those patients that are ready for the beam, and the elapsed preparation durations for those patients that have not yet completed their preparation phases. The idea of a "mixed" state of the system stems from the amount of information available to the decision maker at the time the beam allocation has to be made: the exact values of waiting and elapsed preparation durations as well as the distributional information on the remaining future preparation and field durations.

Once the mixed state of the treatment system is calculated, it is passed on to the beam allocation algorithm (such as RTSFD algorithm) that calculates which room should receive the beam next. Given that the Real-Time Events file records all beam and patient-service related events, at the end of each day it is possible to provide an analysis of the effect of alternative beam allocation approaches, such as FRFS.

2. **Simulating the performance of beam-allocation algorithms under different patient sequences and stochastic durations.**

At present, we have built a portfolio of alternative real-time beam allocation algorithms and in the past several months we have designed a simulation to test the performance of these algorithms under different patient sequences and deterministic and stochastic durations of the preparation and field phases for each treatment protocol. Below we report the results of several such test studies.

2.1. Data used in the numerical tests.

In our numerical tests we have used the data from the "Dataset 2" collected during the summer of 2010. This dataset represents the field and preparation durations for the treatment protocols shown in Table 4. The "% of Patients" field represents the fraction of patients treated according to a particular protocol.

Protocol	Site	Fields	% Patients
1	Prostate	2	49.73
2	Brain	2	5.41
3	Brain	3	20.54
4	Chest	2	3.78
5	Lung	2	3.24
6	Forearm	2	2.7
7	Sacrum	2	3.24
8	Spine	2	3.24
9	Sternum	2	2.16
10	Abdomen	2	1.62
11	Pelvis	2	1.08
12	Thymoma	2	1.63
13	Sacrum	3	1.63

Table 4. Treatment protocols used in the numerical study.

Using these treatment protocols, we have generated random daily patient sequences using the probabilities based on the % fractions from Table 4. For each daily patient sequence, we have assumed that the first patient arrives to each treatment room at 9:00am, and that each following patient enters a treatment room immediately after the departure of the previous patient. Table 5 shows an example of a randomly generated patient sequence with 15 patients in each treatment room.

Room	Patient 1	Patient 2	Patient 3	Patient 4	Patient 5	Patient 6	Patient 7	Patient 8	Patient 9	Patient 10	Patient 11	Patient 12	Patient 13	Patient 14	Patient 15
1	1	1	1	4	2	3	3	1	1	1	1	2	7	1	1
2	1	3	3	1	3	4	1	1	3	1	1	12	7	4	3
3	1	1	2	1	1	11	3	13	7	3	1	1	3	1	1
4	1	1	1	1	3	1	3	1	1	1	1	3	3	12	1
5	1	3	1	1	12	1	1	1	3	1	11	6	3	2	2

Table 5. An example of a daily patient sequence with 15 patients in each room.

In our numerical tests we have used both the deterministic and the stochastic durations of each preparation and field phase for each of the protocols in Table 4. In the "deterministic" experiments we have used the durations shown in Table 6.

Protocol	Name	Prep Phase 1	Field 1	Prep Phase 2	Field 2	Prep Phase 3	Field 3	Prep Phase 4
1	Prostate-2	7.8	1.4	3.7	1.4	2.8	N/A	N/A
2	Brain-2	11.7	0.7	3.3	1.0	3.4	N/A	N/A
3	Brain-3	10.9	0.6	3.4	0.4	3.5	0.4	3.2
4	Chest-2	13.2	1.2	2.9	0.6	2.2	N/A	N/A
5	Lung-2	12.4	0.6	3.0	0.7	3.5	N/A	N/A
6	Forearm-2	12.1	0.8	4.4	0.9	3.4	N/A	N/A
7	Sacrum-2	11.8	0.7	2.6	0.8	2.5	N/A	N/A
8	Spine-2	11.0	1.1	5.0	1.4	4.6	N/A	N/A
9	Sternum-2	10.0	1.0	4.1	0.7	2.2	N/A	N/A
10	Abdomen-2	18.3	0.5	3.7	0.5	3.9	N/A	N/A
11	Pelvis-2	11.5	0.5	3.6	0.5	2.1	N/A	N/A
12	Thymoma-2	6.0	0.3	3.8	1.3	2.6	N/A	N/A
13	Sacrum-3	12.4	0.5	2.7	0.4	1.1	0.4	3.5

Table 6. Expected durations (in minutes) of preparations and field phases for 13 treatment protocols.

In the "stochastic" experiments we have used the actual recorded durations, with expectations corresponding to the ones in Table 6. Below we report the results of both deterministic and stochastic numerical tests.

2.2. Deterministic durations.

In our numerical tests, in addition to testing the performance of the RTSFD algorithm, we have also focused on investigating the effectiveness of a simpler version of this beam allocation algorithm, namely, the one that applies the RTSFD approach only to the patients that are currently in the treatment rooms. We call this algorithm Real-Time Patients-In-Room, or RTPIR. The advantage of using RTPIR is in the fact that it utilizes a much shorter planning horizon, and, thus, relies on a much smaller information set.

2.2.1. RTSFD vs. RTPIR: fixed patient sequences.

As an initial check, we have applied both the RTSFD and RTPIR to 1000 randomly generated patient sequences consisting of $N=1$ patient in each room. By construction, both algorithms are producing identical results in this case. In our tests, we have kept track of 3 performance measures for each algorithm: throughput (time required to complete the last field of the last patient), the total patient waiting time (sum of all times spent by all patients waiting for the beam), and the maximum patient waiting time (the largest amount of time spent by any patient waiting for the beam). Note that since the total sum of all fields for all patients does not depend on the chosen beam allocation rule, the throughput minimization is

87

equivalent to minimizing the beam idle time, i.e., the total amount of time beam spends waiting for some patient to get ready. The results of these tests are presented in Table 7.

	Throughput RTSFD	Throughput RTPIR	Total Patient Wait RTSFD	Total Patient Wait RTPIR	Max Patient Wait RTSFD	Max Patient Wait RTPIR
Average Gap	0.029	0.029	0.009	0.009	-0.052	-0.052
St.Dev. Gap	0.041	0.041	0.025	0.025	0.104	0.104
Max Gap	0.129	0.129	0.227	0.227	0.264	0.264
Min Gap	0.000	0.000	-0.179	-0.179	-1.040	-1.040

	Gap T RTSFD	Gap T RTPIR	Gap W RTSFD	Gap W RTPIR	Gap Max W RTSFD	GAP Max W RTPIR
Gap T RTSFD	1.00					
Gap T RTPIR	1.00	1.00				
Gap W RTSFD	0.53	0.53	1.00			
Gap W RTPIR	0.53	0.53	1.00	1.00		
Gap Max W RTSFD	-0.64	-0.64	-0.33	-0.33	1.00	
GAP Max W RTPIR	-0.64	-0.64	-0.33	-0.33	1.00	1.00

Table 7. Performance of RTSFD and RTPIR for N=1 patient in each treatment room (1000 randomly generated patient schedules, deterministic durations).

As expected, both algorithms result in the same performance – on average (for a randomly selected patient schedule), they result in 2.9% improvement in generated throughput as compared to FRFS. In addition, both algorithms generated small (0.9%) reduction in total patient wait time, while increasing the maximum patient wait time, on average, by 5.2%. It is not surprising that the maximum patient wait time increases when beam allocation deviates from FRFS approach that allocates the beam to patient with the longest wait. A similar message is contained in the correlation matrix: throughput reduction is positively correlated with the reduction in total patient waiting time and negatively correlated with the reduction in maximum patient waiting time.

However, it is important to note that the actual patient sequences, of course, are not random and can be selected to maximize the impact of real-time beam allocation. As Table 7 indicates, the throughput improvement can vary from non-existent to 12.9%. Figure 8 shows the distribution of the throughput improvement for RTSFD and RTPIR in this case.
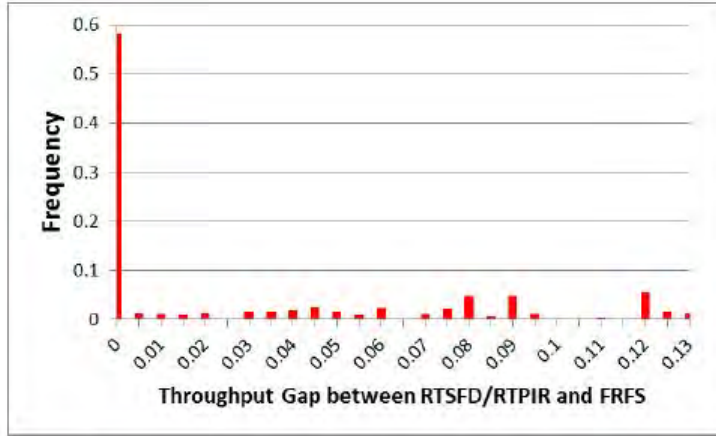
Figure 8. Distribution of the throughput performance gap for RTSFD and RTPIR algorithms (1000 randomly generated patient schedules with *N*=1 patient in each treatment room, deterministic durations).

Next, we conducted tests for patient sequences that include *N*=2 patients in each room. Table 9 reports the results on these tests.

	Throughput RTSFD	Throughput RTPIR	Total Patient Wait RTSFD	Total Patient Wait RTPIR	Max Patient Wait RTSFD	Max Patient Wait RTPIR
Average Gap	0.030	0.014	0.089	-0.008	-0.321	-0.063
St.Dev. Gap	0.024	0.023	0.090	0.076	0.331	0.131
Max Gap	0.120	0.093	0.341	0.340	0.356	0.318
Min Gap	0.000	-0.067	-0.196	-0.348	-1.844	-1.072

	Gap T RTSFD	Gap T RTPIR	Gap W RTSFD	Gap W RTPIR	Gap Max W RTSFD	GAP Max W RTPIR
Gap T RTSFD	1					
Gap T RTPIR	0.60347058	1				
Gap W RTSFD	0.42069701	0.091724481	1			
Gap W RTPIR	0.19121344	0.272998989	0.369948631	1		
Gap Max W RTSFD	-0.34371277	-0.039513219	-0.384679765	0.045792966	1	
GAP Max W RTPIR	-0.02326322	-0.139525213	0.110826305	0.21533004	0.15278711	1

Table 9. Performance of RTSFD and RTPIR for *N*=2 patient in each treatment room (1000 randomly generated patient schedules, deterministic durations).

As we observe, that performance of the RTSFD algorithm remains largely unchanged, with the average throughput performance improvement of 3.0%, and the maximum improvement of 12%. However, the performance of the RTPIR algorithm decreases to an average 1.4% improvement in throughput (with maximum improvement of 9.3%). Note that the worst-case performance of the RTPIR is an increase of 6.7% in the throughput as compared to FRFS. The correlation between the throughput gaps generated by RTSFD and RTPIR algorithms is 60%. Figure 10 shows the distribution of the throughput performance gap for the RTSFD

algorithm. As we observe, the proportion of cases in which RTSFD manages to generate an improvement over FRFS increases from 41.7% to 91.4%.
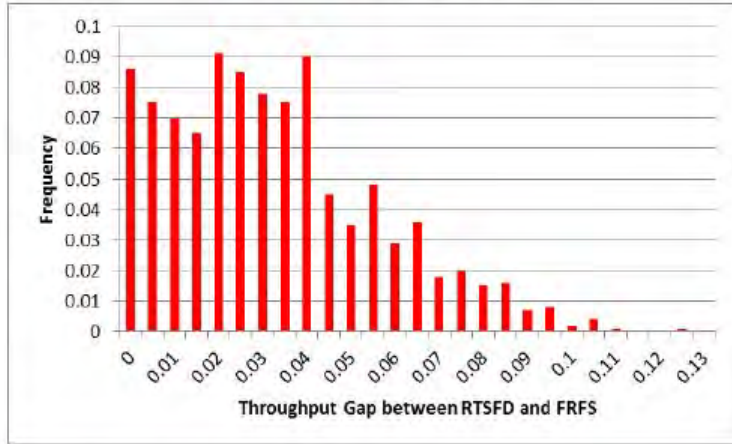
Figure 10. Distribution of the throughput performance gap for RTSFD and RTPIR algorithms (1000 randomly generated patient schedules with $N=1$ patient in each treatment room, deterministic durations).

As the next step, we have created patient sequences with up to $N=15$ patients in each treatment room. Figure 11 shows how the average (over 1000 random patient sequences generated for $N=1$, 2, and over 100 random patient sequences generated for $N=3,\ldots,15$) throughput gap (as compared to FRFS) changes with N for RTSFD and RTPIR algorithms.
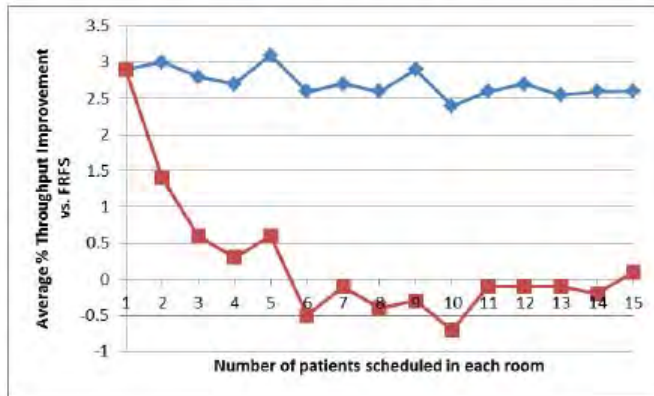
Figure 11. Average throughput gap for RTSFD and RTPIR vs. FRFS algorithms as a function of number of patients scheduled in each treatment room, N (deterministic durations).

As Figure 11 indicates, the average RTSFD performance is not substantially affected by the number of scheduled patients and remains between 2.5% and 3%. At the same time, average RTPIR performance drops as the number of scheduled patients increases. In particular, as N reaches 6, the average performance of the RTPIR drops to 0%. It is important, however, to also keep in mind that the choice of the patient sequence can significantly affect the performance of a particular algorithm. Figure 12 shows how the maximum throughput improvement values depend on the number of patients scheduled in each treatment room.
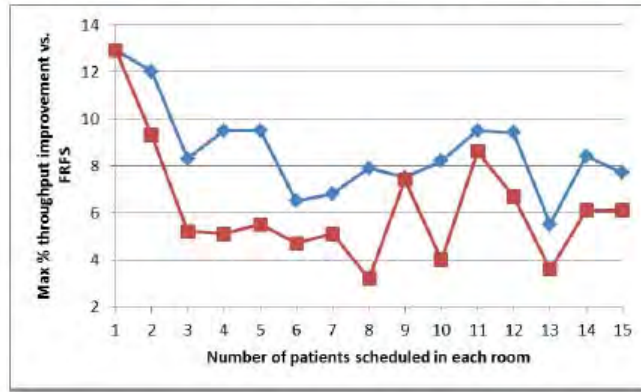
Figure 12. Maximum throughput gap for RTSFD and RTPIR vs. FRFS algorithms as a function of number of patients scheduled in each treatment room, N (deterministic durations).

As we observe from Figure 12, for $N>1$ patients per room, best RTSFD performance (over throughput generated by FRFS) is in the 5%-12% range, while best RTPIR performance is in the 3%-9% range.

It is interesting to look at how such throughput improvements can be translated into increases in the number of patients served each day. Figure 13 shows how the average (over 100 random patient sequences) throughput generated by a FRFS policy changes when the number of patients scheduled in each room increases from $N=1$ (5 total scheduled patients) to $N=15$ (75 total scheduled patients).
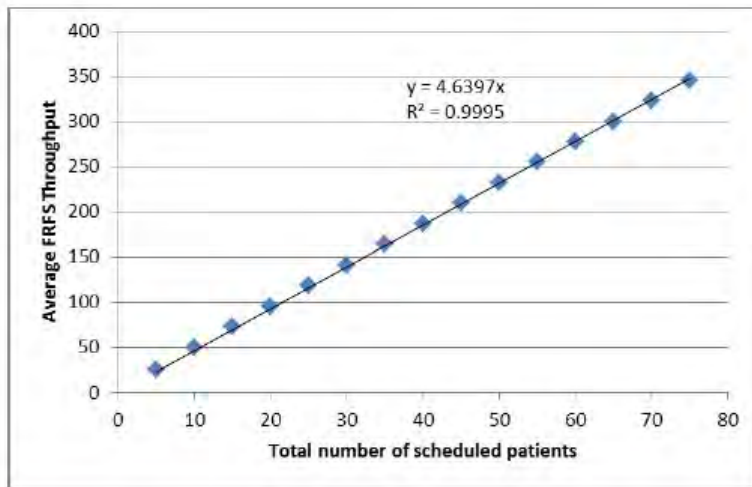
Figure 13. Average (over 100 random patient sequences) throughput generated by the FRFS algorithm as a function of total number of scheduled patients (deterministic durations).

A simple linear regression provides a very good fit to these values (with $R^2 = 0.995$) indicating that, when another 5 patients are added to the sequence, the throughput increases by about 4.64 minutes per patient, on average. Figure 14 "zooms in" on the region between 60 and 75 scheduled patients and adds the average throughput values for the RTSFD (in red) algorithm for comparison.
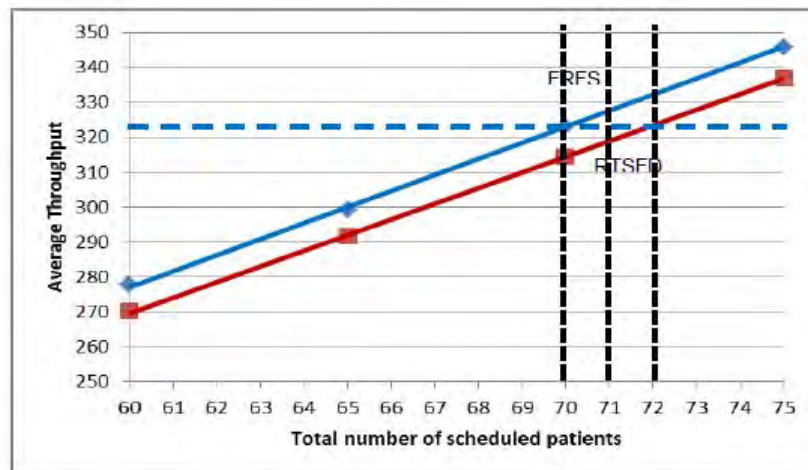
Figure 14. Average (over 100 random patient sequences) throughput generated by the FRFS (blue) and RTSFD (red) algorithms as a function of total number of scheduled patients (deterministic durations).

Figure 14 points out that, for example, for N=14 patients in each room (70 scheduled patients in total), moving from FRFS to RTSFD leaves time for 1-2 extra patients per day. Since the curves in Figures 13 and 14 are based on adding 5 patients (1 per room) at-a-time, it is important to analyze a more detailed setting in which patients are added to the sequence one-at-a-time.

Figure 15 shows the average (over 500 random patient sequences) throughput values for FRFS and RTSFD algorithms when the number of patients scheduled changes from 75 (15 patients in each room) to 76 (15 patients in 4 rooms and 16 in the 5th room), to 77 (15 patients in 3 rooms, and 16 patients in each of the remaining 2 rooms), to 78 (15 patients in 2 of the rooms, and 16 patients in the remaining 3 rooms), to 79 (15 patients in 1 room, and 16 in each of the remaining 4 rooms), to 80 (16 patients in each room). As Figure 15 indicates, depending on the patient configuration, the use of RTSFD instead of FRFS allows to "inject" between 1 and 3 extra patients within the throughput range generated by FRFS.
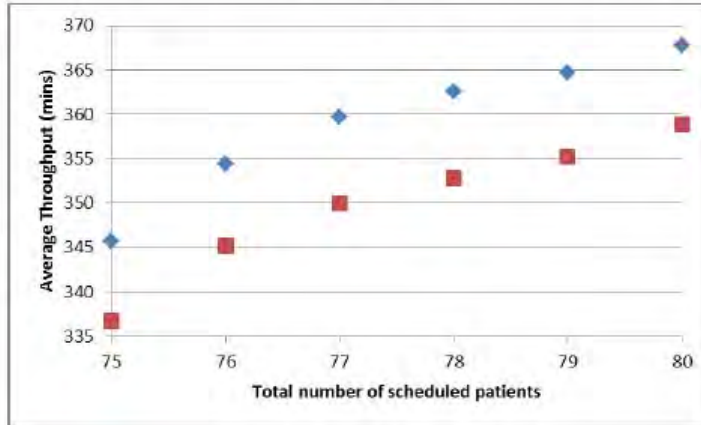
Figure 15. Average (over 500 random patient sequences) throughput generated by the FRFS (blue) and RTSFD (red) algorithms as a function of total number of scheduled patients (deterministic durations).

2.2.2. RTSFD performance: improving patient sequences.

One important factor in considering potential throughput improvement is optimizing patient sequencing. For the same patient arrival times in each room, simply switching the sequence in which patients are scheduled to arrive can have a measurable impact on the throughput,

and, consequently, on beam utilization. In this Section we report the results of numerical tests in which the improvements in real-time beam allocation are combined with those resulting from using better patient sequences. In our numerical tests, we first looked at the patient sequences with N=2 patients in each room. In particular, we have generated 500 random patient sequences. For each patient sequence, throughput values T^0_{RTSFD} and T^0_{FRFS} for RTSFD and FRFS algorithms are calculated. After that, a random permutation of patient sequence in each room is generated, and RTSFD and FRFS are applied again to this permuted patient sequence. Among the results for 50 random permutations, the one with lowest FRFS throughput value (T^b_{FRFS}) and the one with the lowest RTSFD throughput value (T^b_{RTSFD}) are selected, and the performance gaps $\varepsilon^0_{RTSFD} = (T^0_{FRFS} - T^0_{RTSFD})/T^0_{FRFS}$,

$\varepsilon^b_{FRFS} = (T^0_{FRFS} - T^b_{FRFS})/T^0_{FRFS}$, and $\varepsilon^b_{RTSFD} = (T^0_{FRFS} - T^b_{RTSFD})/T^0_{FRFS}$ are calculated. In other words, the first error term represents an improvement generated by applying RTSFD beam allocation to a random patient schedule, the second term represents an improvement generated by altering patient sequence, and the final one – an improvement generated by combining the two approaches. Table 16 shows the resulting values of these ε error terms.

	ε^0_{RTSFD}	ε^b_{FRFS}	ε^b_{RTSFD}
Average over 500 patient sequences	2.85%	4.92%	6.23%

Table 16. Combined performance of RTSFD and improved patient sequence (N=2 patients in each room, deterministic durations).

As we observe, the average RTSFD contribution of 2.85% can be enhanced to 6.23% by using better patient sequencing. On the other hand, using improved patient sequencing while retaining the FRFS beam allocation approach results in an average improvement of 4.92%. While the contribution of pure patient sequencing appears to be higher, it is in combination of these two approaches that the highest improvement is achieved.

Next, we have applied this approach to a "real-size" problem containing 15 patients in each room. For this larger problem, we have used 50 random patient sequences, and for each patient sequence, 25 different sequencing scenarios. The results are reported in Table 17.

	ε^0_{RTSFD}	ε^b_{FRFS}	ε^b_{RTSFD}
Average over 50 patient sequences	2.62%	3.26%	4.61%

Table 17. Combined performance of RTSFD and improved patient sequence (N=15 patients in each room, deterministic durations).

Table 17 illustrates the point that the effectiveness of joint application of effective real-time beam allocation approaches and improved patient sequencing enhances the overall impact on the resulting throughput: RTSFD alone generates an average 2.62% improvement in throughput, while combined with better patient sequencing brings the average improvement to 4.61%.

2.3. Stochastic durations.

We have extended our numerical experiments to the setting where the actual durations of the preparations phases and fields for all treatment protocols are random. In our numerical tests we have used the actual data from Dataset 2.

2.3.1. RTSFD vs. RTPIR: fixed patient sequences.

As was done for the setting with deterministic preparation and field times, we first have applied both the RTSFD and RTPIR to 100 randomly generated patient sequences consisting of $N=1$ patient in each room. As before, by construction of RTPIR algorithm, both algorithms are producing *statistically* identical results in this case. The results are presented in Table 18.

	Throughput RTSFD	Throughput Gap RTPIR	Total Patient Wait RTSFD	Total Patient Wait RTPIR	Max Patient Wait RTSFD	Max Patient Wait RTPIR
Average Gap	0.01512194	0.015565194	0.001212094	0.00188223	-0.046031444	-0.044940352
St.Dev. Gap	0.0088734	0.008853695	0.007162982	0.007187766	0.030105557	0.02992936
Max Gap	0.043998432	0.034632523	0.018419096	0.021117403	0.003177966	0.005498754
Min Gap	-0.000245909	-0.00057117	-0.023968103	-0.011273734	-0.124278677	-0.1328125

Table 18. Performance of RTSFD and RTPIR for $N=1$ patient in each treatment room (100 randomly generated patient schedules, random durations).

Note that, averaged over randomly-generated patient sequence, as compared to FRFS, RTSFD and RTPIR reduce throughput by about 1.5%, with minimum gap of about 0% and maximum gap of around 4.4%. On average, both algorithms reduced total patient wait time by about 0.1%, but increased maximum patient wait time by about 5%. As compared to Table 7, the average throughput gap in the presence of stochastic durations is reduced from 2.9% to 1.5%, and the maximum throughput gap is reduced from 12.9% to about 4.4%. The corresponding distribution of the throughput improvement gap is shown on Figure 19.
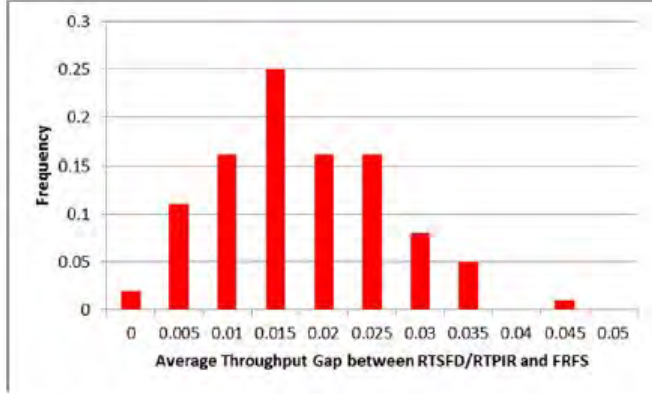
Figure 19. Distribution of the throughput performance gap for RTSFD and RTPIR algorithms (100 randomly generated patient schedules with N=1 patient in each treatment room, random durations).

2.3.2. Combining RTSFD with improved patient sequencing.

As in case of deterministic durations, the performance of the beam allocation algorithms strongly depends on the selected patient schedule. In order to verify the impact of patient sequencing on the overall throughput reduction, we have conducted the variant of the study described in Section 2.2.2 for N=2 patients in each treatment room. In particular, we have generated 50 random patient sequences, and for each patient sequence, we have applied the adapted version of RTSFD (as described in Section 1.4) and FRFS algorithms to 100 scenarios involving random durations for preparation phases and fields. After that, 10 random permutations of each patient sequence were generated, and the procedure repeated for each permutation. Among the results for 10 random permutations, the one with lowest *expected* FRFS throughput value (T_{FRFS}^{b}) and the one with the lowest *expected* RTSFD throughput value (T_{RTSFD}^{b}) are selected, with expectations calculated over 100 scenarios for each patient sequence. The resulting values of the performance gaps
$\varepsilon_{RTSFD}^{0} = (T_{FRFS}^{0} - T_{RTSFD}^{0})/T_{FRFS}^{0}$, $\varepsilon_{FRFS}^{b} = (T_{FRFS}^{0} - T_{FRFS}^{b})/T_{FRFS}^{0}$, and
$\varepsilon_{RTSFD}^{b} = (T_{FRFS}^{0} - T_{RTSFD}^{b})/T_{FRFS}^{0}$ are presented in Table 20.

	ε_{RTSFD}^{0}	ε_{FRFS}^{b}	ε_{RTSFD}^{b}
Average over 50 patient sequence	1.33%	1.97%	3.00%

Table 20. Combined performance of RTSFD and improved patient sequence (N=2 patients in each room, random durations).

96

Similar to the deterministic settings, the RTSFD algorithm and the improved patient sequencing enhance each other's effects on the throughput, resulting in overall 3% throughput improvement, on average.

Summary

We have developed a prototype beam allocation application, with simulation studies focused on investigating the performance of the beam allocation algorithms under stochastic durations of preparation and field times, and studying the infuence of different patient sequencing schemes on throughput performance. Clinical implementation will require software upgrades to be installed by the proton therapy vendor (IBA), scheduled for March 2014, which will increase the efficiency of beam delivery, beam switching and beam layering. Once the commercial software upgrade that is required for continued patient care is completed, the prototype beam allocation application will be tested in a clinical format.

KEY RESEARCH ACCOMPLISHMENTS

Tissue Heterogeneity:
- Built a heterogeneous phantom, exposed the radiochromic film to protons.

- Validated using WRNMMC CT-Simulator for imaging phantoms. WRNMMC CT numbers for a variety of materials close to CT numbers for University of Pennsylvania CT-Simulator. Look up table for proton stopping powers for WRNMMC are sufficiently close expected from those from University of Pennsylvania.

Linear Energy Transfer:
- First report for measuring LET over areas.

- First mathematical development for posited quenching mechanism

- Highest LET value measurement including preliminary volume measurement of LET.

- Tested LET measurement for protons for a variety of ranges.

- Tested LET measurement procedure for narrow Bragg peak and SOPB

Multichannel Dosimetry:
- Conceived, described, tested a multichannel (red, green, blue) film dosimetry for analyzing darkening of radiochromic films due to radiation such as x-rays and protons.

- Multichannel approach corrects small (but dosimetrically significant) scanner illumination variations and local imperfections in radiochromic film

- Demonstrated improvement of multichannel approach over single or dual channel film dosimetry.

- First detailed mathematical description of multichannel approach

- Conceived, tested new parameter (RS) or relative slope to ensure appropriate multichannel application and doses.

Organ Motion:

- Dynamic lung phantom for use in radiation treatment verification was designed and constructed
- Continued assessment and refinement of the phantom is still required prior to clinical implementation

Telemedicine:

- The RPRT telemedicine solution, developed, tested, and optimized over the course of phases IV and V, is currently being used to treat DOD beneficiaries. Preliminary results will be presented in an upcoming manuscript.
- The overarching intent of the telemedicine solution was to 1) keep WRAMC/WRNMMC providers involved in the care of their patients despite not having the capability to deliver proton radiation therapy on-site and 2) minimize patients' time away from home and/or work by taking-on some of the functions otherwise performed by the proton treatment center (staging, enrollment, and treatment planning). In this regard, the telemedicine solution should be considered a success since it has achieved, and will hopefully continue to realize, these two goals.
- Across cases, all patients have thus far been able to start their treatment on time (arriving at Philadelphia on Day 0 and beginning their course of proton radiation therapy on Day 1) and only one of the remotely generated treatment plans needed partial re-planning (the result of a software upgrade at HUP).
- The Standard Operation Procedure (SOP) for the RPRT process was refined from an early concept (Figure 4) to the one currently in use (Figure 5).
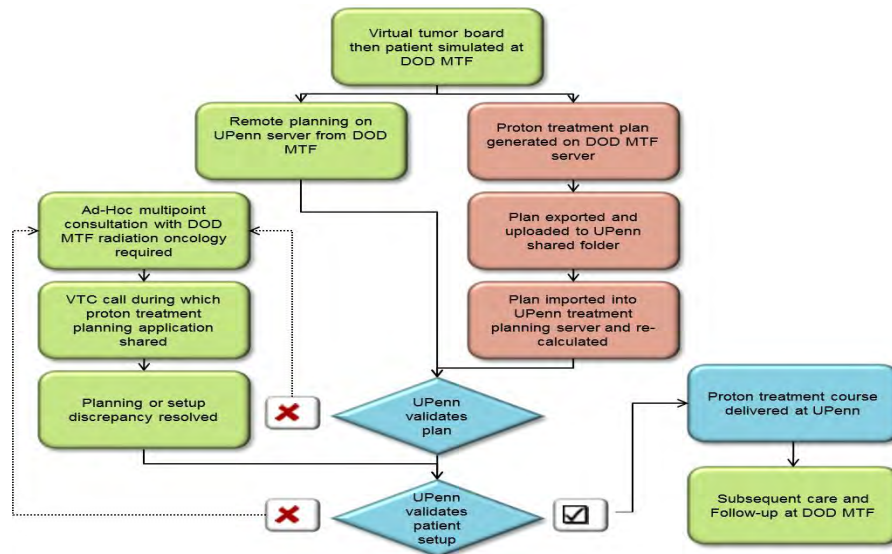
Figure 4 – SOP (early concept)
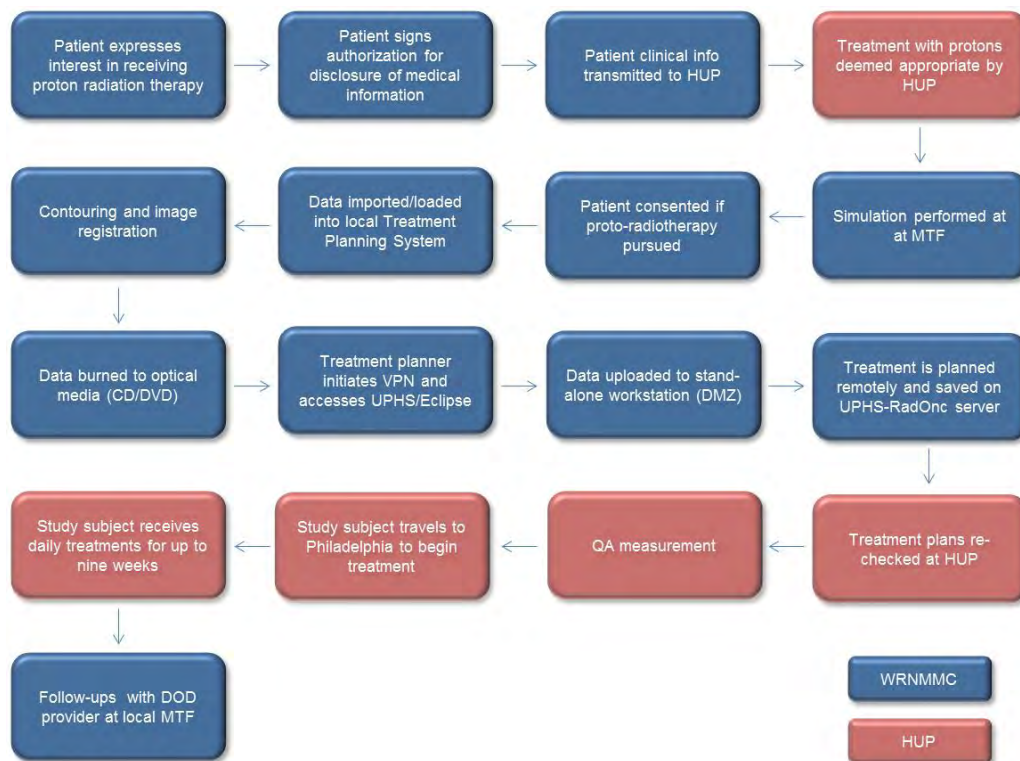
Figure 5 – SOP (in-use)

- The deployment of the telemedicine prompted the opening of proton-specific clinical trials (a parallel effort, not funded by this cooperative agreement).
  - Proton Radiation for Low-Grade Gliomas
  - A Trial of Proton Radiation Therapy Using Standard Fractionation for Low-Risk Adenocarcinoma of the Prostate
  - A Feasibility Trial of Proton Radiation Therapy or Intensity Modulated Radiation Therapy Using Mild Hypofractionation for Intermediate-Risk Adenocarcinoma of the Prostate

- Each trial takes the form of a Cooperative Research and Development Agreement (CRADA) between WRNMMC and HUP. Patients enrolled under the two prostate trials have benefitted from the use of the RPRT solution.

Neutron and Microdosimetry of the Proton Beam:
- A microdosimetry system was developed for characterizing microscopic patterns of dose deposition and relating these measurements to variations of the biological effect of proton induced secondary radiation. This development included fabrication of microdosimeters, construction and development of pulse processing electronics, software development for the data acquisition application, testing and troubleshooting in x-ray and proton fields.

99

- The system is currently being employed in experiments with the proton beam and many future experiments in collaboration with biological effect studies are in the planning stages.
- The first results from proton beam microdosimetry measurements will be detailed in an upcoming manuscript.
- A dual ionization chamber dosimetry system was developed for measurement of absolute dose in the mixed gamma-ray / neutron radiation field induced by protons interacting in the patient and the beam modification devices such as the Tungsten MLC. This development included fabrication of large volume ionization chambers from tissue equivalent plastic and Magnesium, and development of Monte Carlo simulations to determine the sensitivity of these chambers to gamma-rays and neutrons.
- The first results from measurements of the neutron dose produced by the Tungsten MLC compared to that produced by a brass collimator system has been published.
- The system is currently being employed to compare the neutron dose from the 3 proton beam delivery modalities (passive scattering, uniform scanning, and pencil beam scanning). The results of this study will be included in an upcoming manuscript.

Cone Beam Computed Tomography (CBCT):
- Designed and implemented a CBCT system on a test bench. Installation and deployment of the CBCT system at the University of Pennsylvania proton system is expected in early 2014.
- Developed software and image reconstruction platform for proton CBCT system
- Developed novel applications of CBCT specific to proton therapy to detect potential proton range deviations due to anatomical change.

Calypso:
- Procured, installed, tested, and upgraded the Calypso System for use in a proton treatment room at Roberts.
- Investigated the dose shadow effect downstream of the Calypso Beacon transponders and determined guidelines for the beacon implantation and treatment planning strategies.
- Further validated the Geant4-based Monte Carlo simulation code developed at the University of Pennsylvania under Phases I and II of this Award.
- Implemented a patient research protocol and began the collection of data using patients previously treated with photons to investigate the accuracy of Calypso localization *in vivo*. One patient has been setup with Calypso in the proton room and compared with imaging with positive results.

Radiobiology:

- Developed a model system for preclinical testing for proton RBE, via established cell lines and methods.
- Measure RBE for protons, detailing the dependence of RBE on physical beam and biological cell properties.

Positron Emission Tomography (PET) of proton beams to verify dose deposition:
- Developed prototype RATX detector system for testing, with completion of design and production of a series of modifications to the existing proton treatment table.

Proton Beam Allocation Project:

- Developed a prototype beam allocation application, with simulation studies focused on investigating the performance of the beam allocation algorithms under stochastic durations of preparation and field times, and studying the infuence of different patient sequencing schemes on throughput performance.

REPORTABLE OUTCOMES

Tissue Heterogeneity:
No reportable outcomes yet

Linear Energy Transfer:
Rulon Mayer, Marcus Fager, Alejandro Carabe, Liyong Lin, Jim McDonough, Donna Kessel, John O'Connell, "New Areal Proton LET Detector**",** Abstract/Poster presented at University of Pennsylvania Radiation Oncology Retreat. December 8, 2012.

Multchannel Dosimetry:
Mayer R Ma F, Chen Y, Miller R, Belard A, O'Connell J , McDonough J, 2012 Enhanced Dosimetry Procedures and Assessment for EBT2 Radiochromic Media, Medical Physics, **39** 2147-2155. (see Appendix for manuscript)

Organ Motion:
Jessica R. Sheehan, Rulon Mayer, Arnaud Belard, and John O'Connell, "Development of Dynamic Lung Phantom for Radiation Treatment Verification", Abstract presented at IMECE 2013-ASME 2013 International Mechanical Engineering Congress and Exposition, November 15-21, 2012 in San Diego, CA

Telemedicine:
Improving Proton Therapy Accessibility Through Seamless Electronic Integration of Remote Treatment Planning Sites. Belard A, Dolney D, Tochner, Z, McDonough J, O'Connell JJ – Telemed J., 2011, Vol. 17.

Development of a Remote Proton Radiation Therapy Solution over Internet2. Belard A, Tinnel B, Wilson S, Ferro R, O'Connell J. 10, s.l. : Telemed J., 2009, Vol. 15.

A Hybrid Integrated Services Digital Network-Internet Protocol Solution for Resident Education. Erickson D, Greer L, Belard A, Tinnel B, O'Connell J – Telemed J., 2010, Vol. 16.

Comparison of Intensity-modulated Radiotherapy, Adaptive Radiotherapy, Proton Radiotherapy, and Adaptive Proton Radiotherapy for Treatment of Locally Advanced Head and Neck Cancer. Simone C, Lyu D, Ondos J, Ning H, Miller R, Belard A, Simone N – Radiother Oncol. 2011 Jun 12. (see Appendix for manuscript)

Comparison of Predicted Excess Secondary Malignancies and Normal Tissue Toxicities Between Proton and Photon Radiation Therapy for Treatment of Stage I Seminoma. Simone C., Kramer K., O'Meara W., Belard A., McDonough J., O'Connell J. – Int J Radiat Oncol Biol Phys. 2011 Jan 13. (see Appendix for manuscript)

Neutron and Microdosimetry of the Proton Beam:

E. S. Diffenderfer, C. G. Ainsley, M. L. Kirk, J. E. Mcdonough, and R. L. Maughan, "Comparison of secondary neutron dose in proton therapy resulting from the use of a tungsten alloy MLC or a brass collimator system," Med. Phys., vol. 38, no. 11, pp. 6248–6256, 2011. (see Appendix for manuscript)

E. Diffenderfer , C. G. Ainsley, M. L. Kirk, J. E. Mcdonough, and R. L. Maughan, "Reply to " Comment on ' Comparison of secondary neutron dose in proton therapy resulting from the use of a tungsten alloy MLC or a brass collimator," Med. Phys., vol. 39, no. 4, pp. 2306–2309, 2012.

Cone Beam Computed Tomography (CBCT):
(1) J. Seabra, K. Teo, S. Brousmiche, R. Labarbe, D. Wikler, R. Maughan, J. Lee: Design and Deployment of a Proton Therapy Cone-Beam CT. Particle Therapy Co-Operative Group Annual Meeting 2012, Seoul South Korea(Poster).
(2) L. Yin, D. Dolney, A. Kassaee, J. Gee, P. Ahn, A. Lin, J. McDonough, R. Maughan, B. K. Teo: Image-Based Proton Range Verification Using Intensity-Corrected CBCT. AAPM Meeting 2013, Indiana, PA (Oral).

Calypso:
Publication: Derek Dolney, James McDonough, Neha Vapiwala and James M Metz, Dose perturbations by electromagnetic transponders in the proton environment, Phys. Med. Biol. 58 (2013) 1495150. (attached as Appendix)

Poster: Derek Dolney, James McDonough, Neha Vapiwala and James M Metz, Investigation of dose perturbations by electromagnetic transponders in the proton environment, American Radium Society Annual Meeting (2012).

Radiobiology:

Eblan, M, Cengel, KA: Biology of Proton Therapy, Old and New Considerations. Radiation Medicine Rounds: Proton Therapy. Metz, JMThomas, CR (eds.). 1(3): 441-454, 2011.

Positron Emission Tomography (PET) of proton beams to verify dose deposition:
Kirk ML, Teo B, Dolney D, McDonough JE, Tochner Z, Lin A, Lin L. Verification of Proton Treatment Dose Calculation and Delivery Using Monte Carlo Simulated Dose and Isotope Distribution and Measured Isotope Distribution. Presented in abstract form and oral presentation at the 2011 Annual Meeting of the American Society of Radiation Oncology, Miami, FL.

Proton Beam Allocation Project:
None to date.

CONCLUSIONS

Tissue Heterogeneity:
Building the heterogeneous phantom, developing techniques for achieving accurate radiochromic film dosimetry, testing and validating LET measurement tools provide the essential components for measuring the dose within heterogeneous materials. In addition, this research seeks to measure the LET within the heterogeneous materials and validate with Monte Carlo calculations.

Linear Energy Transfer:
Biological response to radiation depends on the dose, dose rate, and localized energy deposition patterns or linear energy transfer (LET). Most experiments that measure spatial distribution focus on dose and almost none on the LET patterns. This study describes and examines the first report of measured spatial distribution of the LET delivered by proton irradiation over an area using EBT2 radiochromic film The radiochromic film sensitivity diminishes with high energy deposition, or LET. A heuristic formulation connecting the film sensitivity and LET is presented. The discrepancy between the absolute measured and expected dose distribution is exploited to determine the LET. This study proposes a metric, the scaled, normalized difference (SND) between the treatment planning and measured dose. The SND is correlated with a Monte Carlo calculation of the LET spatial distribution for a large range of SNDs. A polynomial fit between the SND and Monte Carlo (MC) LET is generated for protons having range of 20 cm with narrow and Spread Out Bragg Peak (SOPB), modulated by 5 cm. Coefficients from these polynomial fits were applied to measured proton dose distributions with a variety of ranges. Gamma analysis is calculated for areas in the dose distribution between 70 cGy and 200 cGy using gamma analysis parameters of 25% of MC LET, and 3 mm in two dimensions. The processed dose distributions finds 5 to 10 % gamma exceedances for the narrow 12.5 and 15 cm proton ranges and 10 to 15 % for proton ranges of 15, 17.5 and 20 cm and modulated by 5 cm. The approach discussed in this study is not sensitive enough to measure a high energy photon LET.

Multchannel Dosimetry:
This study described, developed and tested new processing methods for reducing inaccuracies in absolute dose determination due to inhomogeneities within the film and from scanning. This study found better performance using optimized multichannel following averaging of all color channels. Combining the channel ratios in a hybrid approach also achieved high performance. Averaging the test films reduced temporal noise that severely degraded the blue channel. This methodology avoided using cumbersome, registered correction matrices. Novel registration and digital rotation of CT images enabled quantitative testing and helped improve contact between the radiochromic film and phantom.

Organ Motion:
Significant progress was made in designing and constructing a dynamic lung phantom for use in radiation treatment verification. Assessment and refinement of the prototype is on-going.

Telemedicine:
The overarching intent of the telemedicine solution was to 1) keep the MTF providers involved in the care of their proton patients despite not having the capability to deliver the treatment modality on-site and 2) minimize patients' time away from home and/or work by taking-on some of the functions otherwise performed by the proton treatment center (staging, enrollment, and treatment planning). Several DOD patients have benefitted from the system already and we expect more will with the opening of additional clinical trials.

The solution developed and deployed is a robust one and could be of great value to satellite clinics seeking to remain active participants in the delivery of care, despite the lack of a highly specialized treatment modality on-site. While it was not the intent of the cooperative agreement, we do hope this powerful telemedicine solution can also serve as a tool to support and improve graduate medical education and virtual tumor board, in the Military Health System (MHS) as well as on the outside.

Neutron and Microdosimetry of the Proton Beam:

The goal of this portion of phase IV was to develop and implement radiation dose measurement devices to characterize the secondary radiation produced by therapeutic proton beams with the overall goal of predicting and mitigating the adverse effects of secondary radiation produced by the proton beam. Two complete and complimentary dosimetry systems were developed from the ground up. These systems are being used to collect data that is vital to disentangling the role of secondary radiation on the biological effects of proton therapy.

Cone Beam Computed Tomography (CBCT):
CBCT is expected to be an important imaging modality for proton therapy. The sensitivity of the dose deposition in proton therapy compared to photon therapy provides unique applications of CBCT such as on line proton range verification. The work performed in the development of the CBCT system will guide the development of future imaging technologies and enable the precision of proton therapy to be harnessed. All the components and subsystems for the CBCT system have been completed and we expect the CBCT system at the University of Pennsylvania to be clinically available in 2014. Upon deployment, we expect an enhancement of the accuracy proton therapy system through the use of novel clinical applications of image guided proton therapy.

Calypso:
There are several very positive outcomes from Phase IV of the award. The Calypso System for target localization and real-time tracking has been developed for use in proton therapy. The system will permit more rapid localization and bring real-time tracking capabilities to proton therapy for the treatment of disease sites complicated by respiratory motion in particular. Varian Medical Systems is now pursuing FDA approval for the use of the Calypso System for proton therapy.
We have determined the level of dose shadow downstream of Calypso Beacon transponders in the proton beam by measurements and simulation. The dependence of the shadow on implant position relative to the proton Bragg peak has been determined and was published (Dolney et al 2013). In that publication, we describe some treatment planning strategies and approaches to minimize the level of dose shadow. Specific strategies will depend on disease sites and the local anatomy and approaches will be further developed in future studies.
A patient study is now underway to determine the accuracy of localization with the Calypso system *in vivo*. We expect the system to perform at least as well as orthogonal kV imaging and will represent an opportunity to spare patients the additional ionizing radiation of daily setup imaging and to increase throughput in the proton treatment rooms. Our first Calypso/imaging patient showed favorable results that justify this claim.

Radiobiology:
We have determined that the inter-experimental variability of radiosensitivity profile measure is less than the variability in intrinsic radiosensitivity for 3 head and neck cancer cell lines. Additionally, we have determined that contrary to our previously stated hypothesis, these highly radioresistant cells do not display a dramatic difference in radiosensitivity for the plateau vs mid-SOBP portions of the proton depth dose distribution.

Positron Emission Tomography (PET) of proton beams to verify dose deposition:

A prototype PET detector has been developed and tested for use to verify dose deposition from proton therapy. Further testing and validation is required prior to clinical implementation. In the meantime, a clinical pilot study of PET activation as a means of quality assurance for proton beam radiotherapy is ongoing and accruing patients, utilizing a standard PET/CT scanner

located in the Roberts Proton Therapy, with preliminary results verifying that proton dose deposition as measured reflects that calculated from the treatment planning system.

Proton Beam Allocation Project:
We have developed a prototype beam allocation application, with simulation studies focused on investigating the performance of the beam allocation algorithms under stochastic durations of preparation and field times, and studying the infuence of different patient sequencing schemes on throughput performance. Clinical implementation will require software upgrades to be installed by the proton therapy vendor (IBA), scheduled for March 2014, which will increase the efficiency of beam delivery, beam switching and beam layering. Once the commercial software upgrade that is required for continued patient care is completed, the prototype beam allocation application will be tested in a clinical format.

REFERENCES

Tissue Heterogeneity:
A V Chvetsov and S L Paige "The influence of CT image noise on proton range calculation in radiotherapy planning" Phys. Med. Biol. **55** N141–N149, 2010.

R Grant, G Ibbott, N Sahoo, S Tucker, X zhu, D Followill "Evaluation of an anthropomorphic pelvis phantom for proton therapy", Med Phys, **36** 2607-2607, 2009.

M F. Moyers,., M Sardesai, S Sun., and D W Miller. "Ion stopping powers and CT numbers" Medical Dosimetry, **35**, 179-194, 2010

D. Pflugfelder,_J. J. Wilkens, H. Szymanowski, and U. Oelfke,"Quantifying lateral tissue heterogeneities in hadron therapy"Med. Phys. **34** 1506-1513, 2007.

H Szymanowski and U Oelfke "Two-dimensional pencil beam scaling: an improved proton dose algorithm for heterogeneous media" Phys. Med. Biol. **47** 3313–3330, 2002.

G O Sawakuchi, U Titt, D Mirkovic and R Mohan "Density heterogeneities and the influence of multiple Coulomb and nuclear scatterings on the Bragg peak distal edge of proton therapy beams"
Phys. Med. Biol. **53**, 4605–4619, 2008.

B Schaffner and E Pedroni "The precision of proton range calculations in proton radiotherapy treatment planning: experimental verification of the relation between CT-HU and proton stopping power" Phys. Med. Biol. **43** 1579-1592, 1998.

U, Schneider, E. Pedroni and A, Lomax "The calibration of CT Hounsfield units for radiotherapy treatment planning" Phys. Med. Biol. **41** 111–124,. 1996.

Linear Energy Transfer:
Arjomandy L, Tailor B R, Zhao L, Devic S, 2012 EBT2 film as a depth-dose measurement tool for radiotherapy beams over a wide range of energies and modalities, Med Phys. **39**, 912-911

Borak, T B, Doke T, Fuse T, Guetersloh S, Heilbronn L., Hara K, Moyers M., Suzuki S., Taddei P, Terasawa K, Zeitlin C. J. 2004 Comparisons of LET distributions for protons with energies

between 50 and 200 MeV determined using a spherical tissue-equivalent proportional counter (TEPC) and a position-sensitive silicon spectrometer (RRMD-III). Radiat Res **162**, 687-692.

Bragg W H and Kleeman R 1904 On the ionization curves of radium, Philosophical Magazine **S6**, 726-738

Depuydt T, Van Esch A, Huyskens D P 2002 A quantitative evaluation of IMRT dose distributions: refinement and clinical assessment of the gamma evaluation Radiotherapy and Oncology **62** 309–319

Grassberger C, Trofimov A, Lomax A, and Paganetti H, 2011a Variations in linear energy transfer within clinical proton therapy fields and the potential for biological treatment planning, Int. J. Radiat. Oncol., Biol., Phys. **80**, 1559–1566.

Grassberger C and Paganetti H, 2011b Elevated LET components in clinical proton beams," Phys. Med. Biol. **56**, 6677–6691 .

Gustavsson H., Bjack S A J, Medin J, Grusell E, Olsson L E. 2004 Linear energy transfer dependence of a normoxic polymer gel dosimeter investigated using proton beam absorbed dose measurements. Phys Med Biol **49**, 3847-3855.

International Specialty Products, GAFchromic EBT2 Dosimetry Film Manual

Kirby D et al. 2010 LET dependence of GafChromic films and an ion chamber in low-energy proton dosimetry Phys Med Biol **55** 417-433.

Kohno T, Kiyota T, Matsufuji N, Futami Y, Kanai T 2000 Response of multiwire proportional counter for energy loss measurement. Nucl Instrum Meth A **450**, 456-466.

Lopatiuk-Tirpak O, Su Z, Li Z, Zeidan D O Meeks S L, Maryanski M J, 2012 Direct Response to Proton Beam Linear Energy Transfer (LET) in a Novel Polymer Gel Dosimeter Formulation Tech Can Res Treat, **11**, 441-445

Low D A et al. 1998 A technique for the quantitative evaluation of dose distributions. Med Phys **25** 656–661

Mayer R, et al., 1994 A New Method for Microdosimetry in Radioimmuno-Therapy Using Radiochromic Media, Int. J. Rad. Onc. Biol. Phys., **28** 505.

Mayer R, et al. 1995 Direct Measurement of Intratumor Dose-Rate Distributions in Experimental Xenograft Radio-immunotherapy with Anti-CEA Antibodies Labeled with ^{90}Y, Int. J. Rad. Onc. Biol. Phys. **32** 147-157.

Mayer R Ma F, Chen Y, Miller R, Belard A, O'Connell J , McDonough J, 2012 Enhanced Dosimetry Procedures and Assessment for EBT2 Radiochromic Media, Medical Physics, **39** 2147-2155.

Micke A Lewis D F, Yu X, 2011 Multichannel film dosimetry with nonuniformity correction Med Phys **38** 2523-2534

Paganetti H, 2003 Significance and implementation of RBE variations in proton beam therapy *Technol. Cancer Res. Treat.* **2** 413–26

Sawakuchi G O, Sahoo N, Gasparian P B R, Rodriguez M G, Archambault L, Titt U, Yukihara E G, 2010 Determination of average LET of therapeutic proton beams using Al2O3:C optically stimulated luminescence (OSL) detectors. Phys Med Biol **55**, 4963-4976.

Spurny F, Molokanov A G, Bamblevski V P, 2004 Passive spectrometry of linear energy transfer: development and use. Radiat Prot Dosimetry **110**, 675-679.

Suchowerska N et al. , 2001 Directional dependence in film dosimetry:radiographic and radiochromic film Phys. Med. Biol. **46** 1391–1397

Vatnitsky S M,1997 Radiochromic film dosimetry for clinical proton 13. beams. Appl Rad Isotopes **48**, 643-651.

Vynckier S, Bonnett D E, Jones D T L , 1994 Supplement to the code of practice for clinical proton dosimetry Radiother Oncol. **32** 174-179.

Zeidan O A et al., :2006 EBT radiochromic film for IMRT dose verification Med. Phys., **33**, 4064-4072

Zhao L and Das I J, 2010 Gafchromic EBT film dosimetry in proton beams" Phys. Med. Biol. **55** N291-N301

Multichannel Dosimetry:
1. W.L. MacLaughlin et al "Sensitometry of the response of a new radiochromic film dosimeter to gamma radiation and electron beams", Nucl Instrum Meth Phys. Rsrch A, **302**, 165-17 (1991).

2. International Specialty Products, GAFchromic EBT2 Dosimetry Film Manual

3. H. Ohuchia "High sensitivity radiochromic film dosimetry using an optical common-mode rejection and a reflective-mode flatbed color scanner" Med. Phys. **34** 4207-4212 (2007)

4. T. Pawlicki, G. Kim G, "SU-GG_T_275: On improving the accuracy of EBT2 film dosimetry using a flatbed scanner" Med Phys **37** 3248-3249 (2010).

 5. T. Alami, T Kairn, J Kenny "Evaluation of Gafchromic EBT2 dosimetry system for radiotherapy quality assurance" Australa Phys Eng Sci Med **34** 251-260 (2011)
6. C. Andres et al. "A comprehensive study of the Gafchromic EBT2 radiographic film. A comparison with EBT", Med Phys., **37** 6271-6278 (2010).

7. T. McCaw, J Micka, LA. DeWerd "Characterizing the marker-dye correction for Gafchromic EBT2 film: a comparison of three analysis methods", Med Phys. **38** 5771-5777 (2011)

8. S. Devic, N. Tomic, C. Soares, and E. Podgorsak, "Optimizing the dynamic range extension of a radiochromic film dosimetry system," Med. Phys. **36**(2), 429–437 (2009).

9. T. Kairn, T Aland, J Kenny, "Local heterogeneities in early batches of EBT2 film: a suggested solution" Phys. Med. Biol. **55** L37-L42 (2010)

10. L Richley. et al. "Evaluation and optimization of the new EBT2 radiochromic film dosimetry system" Phys Med Biol **55** 2601 (2010)

11. B. Hartmann et al. "Technical Note:Homogeneity of Gafchromic EBT2 film", Med Phys., **37** 1753-1756 (2010).

12. R. Mayer, et al.,' A New Method for Microdosimetry in Radioimmuno-Therapy Using Radiochromic Film', Int. J. Rad. Onc. Biol. Phys., **28** 505 (1994).

13. R. Mayer, et al. ' Direct Measurement of Intratumor Dose-Rate Distributions in Experimental Xenograft Radio-immunotherapy with Anti-CEA Antibodies Labeled with ^{90}Y', Int. J. Rad. Onc. Biol. Phys. **32** 147-157 (1995).

14. S Devic.et al. "Precise radiochromic film dosimetry using a flat-bed document scanner", Med Phys. **32** 2245-2253.(2005)

15. L. Menegotti et al. "Radiochromic film dosimetry with flatbed scanners: A fast and accurate method for dose calibration and uniformity correction with single film exposure" Med. Phys. **35** 3078-3085 (2008)

16. S. Devic et al. "Sensitivity of linear CCD array based film scanners used for film dosimetry", Med Phys. **33** 3993-3996 (2006).

17. C Fiandra et al. "Clinical use of EBT model Gafchromic film in radiotherapy", Med Phys **33** 4314-4319 (2006)

18. S Saur and J Frengen "Gafchromic EBT film dosimetry with flatbed CCD scanner: a novel background correction method and full dose uncertainty analysis", Med Phys. **35** 3094-3101 (2008).

19. A Micke D.F Lewis, X. Yu "Multichannel film dosimetry with nonuniformity correction" Med Phys **38** 2523-2534 (2011)

20. D.A. Low et al.. "A technique for the quantitative evaluation of dose distributions". Med Phys **25** 656–661 (1998)

21. T. Depuydt, A. Van Esch, D.P. Huyskens," A quantitative evaluation of IMRT dose distributions: refinement and clinical assessment of the gamma evaluation" Radiotherapy and Oncology **62** 309–319 (2002)

22. O.A. Zeidan et al.:" EBT radiochromic film for IMRT dose verification" Med. Phys., **33**, 4064-4072 (2006)

Telemedicine:
Comparison of intensity-modulated radiotherapy, adaptive radiotherapy, proton radiotherapy, and adaptive proton radiotherapy for treatment of locally advanced head and neck cancer.
Simone CB 2nd, Ly D, Dan TD, Ondos J, Ning H, Belard A, O'Connell J, Miller RW, Simone NL. 101(3):376-82, s.l. : European Society for Therapeutic Radiology and Oncology, 2011.

Predicted rates of secondary malignancies from proton versus photon radiation therapy for stage I seminoma. **Simone CB 2nd, Kramer K, O'Meara WP, Bekelman JE, Belard A, McDonough J, O'Connell J.** 1 82(1):242-9, s.l. : International Journal of Radiation Oncology, Biology, and Physics, 2012.

Telemedicine and tele-health services for cancer-care delivery in India. **Sudhamony S, Nandakumar K, Binu PJ, Niwas SI.** February 2008, Communications, IET, pp. 2;2:231-236. A pilot study of tele-oncology in Scotland. **Kunkler I, Rafferty P, Hill D, Henry M, Foreman D.** s.l. : J Telemed Telecare, 1998, Vols. 4:113-119.

A system of tele-oncology at the University of Wisconsin Hospital and Clinics and regional oncology affiliate institutions. **JA, Stitt.** s.l. : Wisc Med J, 1998, Wisc Med J, Vols. 97:38-42, pp. 97:38-42.

Telemedicine in radiotherapy: a study exploring remote treatment planning, supervision and economics. **Norym J, Bruland O, Spanne O, Trine B, Green T, Olsen D, Olsen J, Sjaeng E, Burkow T.** s.l. : J Telemed Telecare, 2005, Vols. 11:245-250.

A Pre-Post Evaluation of a Telehomecare Progam in Oncology and Palliative Care. **Paré G, Sicotte C, Chekli M, Jaana M, De Blois C, Bouchard M.** 2, s.l. : Telemed J, 2009, Vol. 15.

Development of a Remote Proton Radiation Therapy Solution over Internet2. **Belard A, Tinnel B, Wilson S, Ferro R, O'Connell J.** December 2009, Telemedicine and e-Health, pp. 15(10): 998-1004.

Improving Proton Therapy Accessibility Through Seamless Electronic Integration of Remote Treatment Planning Sites. **Belard A, Dolney D, Tochner Z, McDonough J, O'Connell J.** June 2011, Telemedicine and e-Health, pp. 17(5): 370-375.

Development of a Telemedical Cancer Center within the Veterans Affairs Health Care System. **Billingsley K, Schwartz D, Lentz S, Vallières E, Montgomery B, Schubach W, Penson D, Yueh B, Chansky H, Zink C, Parayno D, Stakerbaum G. , Telemed J, March 2002 and 8:123.** March 2002, Telemed J, p. 8:123.

Teleoncology in the Department of Defense: A Tale of Two Systems. **Hunter D, Brustrom J, Goldsmith B, Davis L, Carlos M, Ashley E, Gardner G, Gaal I.** 3, s.l. : Telemed J, 1999, Vol. 5.

Use of ISDN video-phones for clients receiving palliative and antenatal home care. **Miyazaki M, Stuart M, Liu L, Tell S, Stewart M.** s.l. : J Telemed Telecare, 2003, Vols. 9:72-77.

A tele-obstetric broadband service including ultrasound, videoconferencing and cardiotocogram. A high cost and a low volume of patients. **Norum J, Bergmo T, Holdo B, Johansen M, Vold I, Sjaaeng E, Jacobsen H.** s.l. : J Telemed Telecare, 2007, Vols. 13:180-184.

A remote collaboration system for telemedicine using the Internet. **Nagata H, Mizushima H.** s.l. : J Telemed Telecare, 1998, Vols. 4:89-94.

An experimental inter-expert telepathology network using static imaging. **Tucker JH, Busch C, Spatz A, Wells C, Brugal G.** 2001, J Clin Pathol, pp. 54:752-757.

Development and evaluation of a teleradiology and videoconferencing system. **Kaidu M, Toyabe S, Oda J, Okamoto K, Ozaki T, Shiina M, Sasai K, Akazawa K.** s.l. : J Telemed Telecare, 2004, Vols. 10:214-218.

Systematic Human Factors Evaluation of a Teledermatology System within the U.S. Military. **Stong A, Nichols T, Rogers W, Fisk A.** 1, s.l. : Telemed J, 2008, Vol. 14.

Usability of Robotic Platforms for Remote Surgical Teleproctoring. **Ereso A, Garcia P, Tseng E, Dua M, Victorino G, Guy T.** 5, s.l. : Telemed J, 2009, Vol. 15.

Clinical-Oriented Collaboration Over the Web During Interventional Radiology Procedures. **Gortzis L, Karnabatidis D, Siablis D, Nikiforidis G.** August 2006, Telemed J, pp. 12(4): 448-456.

Effect of time delay on surgical performance during telesurgical manipulation. **Fabrizio MD, Lee BR, Chan DY, Stoianovici D, Jarrett TW, Yang C, Kavoussi LR.** s.l. : J Endourol, 2000, Vols. 14:133-138.

A Hybrid Integrated Services Digital Network-Internet Protocol Solution for Resident Education. **Erickson D, Greer L, Belard A, Tinnel B, O'Connell J.** 4, s.l. : Telemed J, 2010, Vol. 16.

Hepatitis C Videoconferencing: The Impact on Continuing Medical Education for Rural Healthcare Providers. **Rossaro L, Tran T, Ransibrahmanakul K, Rainwater J, Csik G, Cole S, Prosser C, Nesbitt T.** June 2007, Telemed J, pp. 13(3): 269-278.

Tele-Education on Leprosy: Evaluation of an Educational Strategy. **Paixao M, Miot H, Wen C.** 6, s.l. : Telemed J, 2009, Vol. 15.

Interactive Internet-Based Clinical Education: An Efficient and Cost-Savings Approach to Point-of-Care Test Training. **Knapp H, Chan K, Anaya H, Goetz M.** s.l. : Telemedicine and e-Health, June 2011, Telemedicine and e-Health, pp. 17(5): 335-340.

Interactive teleeducation in Orthopedics and Orthopedic Trauma using Internet based videoconferencing. **Glinkowski W, Makoca K, Pawlica S, Marasek K, Górecki A.** Leipzig, Germany : s.n., October 2007. 12th Mednet World Conference.

Telehealth innovations in Health Education and Training. **Conde J, De S, Hall R, Johansen E, Meglan D, Peng G.** 1, s.l. : Telemed J, 2010, Vol. 16.

Evaluating the Experience of Training Through Videoconferences in Primary Care. **De Fátima dos Santos A, Haddad S, Alves H, Torres R, De Souza C, Do Carmo Barros de Melo M.** November 2011, Telemedicine and e-Health, pp. 17(9): 722-726.

Asynchronous Web-Based Learning, a Practical Method to Enhance Teaching in Emergency Medicine. **Pourmand A, Lucas R, and Nouraie M.** March 2013, Telemedicine and e-Health, pp. 19(3): 169-172.

Evaluation of videoconferenced grand rounds. **Allen M, Sargeant J, MacDougall E, O'Brien B.** s.l. : J Telemed Telecare, 2002, Vols. 8:210-216.

Ricur G, Batiz M, Romano A, Grandin JC, Arrieta J, Valdivia A. Clinical Grand Rounds and Corporate Training Trials Across Borders. American Telemedicine Association Meeting. Seattle, Washington : s.n., 6-8 April 2008.

Videoconferencing for gynaecological cancer care: an international tumour board. **Atlas I, Granai CO, Gajewski W, Steinhoff M, Steller M, Falkenberry S, Legare R, Szalb S, Prober A, Zafrir H, Farbstein J.** s.l. : J Telemed Telecare, 2000, Vols. 6:242-244.

A Review of Telemedicine Business Models. **Chen S, Cheng A, Mehta K.** 19(4): 287-297, s.l. : Telemedicine and e-Health, April 2013, Telemedicine and e-Health, Vol. April 2013, pp. 19(4): 287-297.

The Decreasing Cost of Telemedicine and Telehealth. **Doolittle G, O'Neal Spaulding A, Williams A.** November 2011, Telemedicine and e-Health, pp. 17(9): 671-675.

Economic impact of real-time teleradiology in thoracic CT examinations. **Takada A, Kasahara T, Kinosada Y, Hosoba M, Nishimura T.** s.l. : Euro Radiol, 2003, Vols. 13:1566-1570.

Cost issues surrounding the use of computerized telemedicine for obstetric ultrasonography. **Malone F, Athanassiou A, Craigo S, Simpson L, D'Alton M.** s.l. : Ultrasound Obstet Gynecol, 1998, Vols. 12:120-124.

Neutron and Microdosimetry of the Proton Beam:
Burmeister, Jay. "Specification of the physical and biologically effective absorbed dose in radiation therapies utilizing the boron neutron capture reaction." PhD Thesis, 1999.

ICRU. *Report 36: Microdosimetry.* Bethesda: International Commission on Radiation Units and Measurements, 75, 1983.

Knoll, Glenn F. *Radiation Detection and Measurement 3rd ed.* Hoboken: John Wiley & Sons, 2000.

P. Kliauga, A. J. Waker, J. Barthe. "Design of tissue-equivalent proportional counters." *Radiation Protection Dosimetry*, 309-322, 1995.

ICRU, Report 26, *Neutron Dosimetry for Biology and Medicine.* Bethesda, MD: International Commission on Radiation Units and Measurements, 1977.

S. Agostinelli, et. al., "Geant4—a simulation toolkit," Nucl. Instruments Methods Phys. Res. Sect. A Accel. Spectrometers, Detect. Assoc. Equip., vol. 506, no. 3, pp. 250–303, Jul. 2003.

E. S. Diffenderfer, C. G. Ainsley, M. L. Kirk, J. E. Mcdonough, and R. L. Maughan, "Comparison of secondary neutron dose in proton therapy resulting from the use of a tungsten alloy MLC or a brass collimator system," Med. Phys., 38,11, 6248–6256, 2011.

Cone Beam Computed Tomography (CBCT):
D. A. Jaffray, J. H. Siewerdsen, and D. G. Drake, "Performance of a volumetric CT scanner based upon a flat-panel imaging array," SPIE Phys. Med. Imaging 1999, 3659, 204–214.

Feldkamp A, Davis L C and Kress J W, "Practical cone-beam algorithm", Journal of the Optical Society of America A: Optics, Image Science, and Vision, 1984, Volume 1, Issue 6, 612-619.

R. Boellaard, M. van Herk, and B. J. Mijnheer, "A convolution model to convert transmission dose images to exit dose distributions", Med Phys 1997, 24(2) 189-199.

Calypso:
Balter J M, Wright J N, Newell L J, Friemel B, Dimmer S, Cheng Y, Wong J, Vertatschitsch E & Mate T P 2005 Int. J. Radiation Oncology Biol. Phys. 61(3), 933–937.

Cheung J, Kudchadker R J, Zhu X R, Lee A K & Newhauser W D 2010 Phys. Med. Biol. 55, 7135–7147.

Chow J C L & Grigorov G N 2005 Phys. Med. Biol. 50, N227–N234.

Chow J C L & Grigorov G N 2006 33(12), 4614–4621.

Derek Dolney, James McDonough, Neha Vapiwala and James M Metz, Dose perturbations by electromagnetic transponders in the proton environment, Phys. Med. Biol. 58 (2013) 14951505.

Gez E, Cederbaum M, Yachia D, Bar-Deroma R & Kuten A 1997 Med. Dosim. 22(22), 117–120.
Giebeler A, Fontenot J, an George Ciangaru P B, Zhu R & Newhauser W 2009 J. App. Clin. Med. Phys. 10(1), 63–70.

Herrmann R, Carl J, Jakel O, Bassler N & Petersen J B B 2010 Acta Oncol. 49, 1160–1164.
Huang J Y, Newhauser W D, Zhu X R, Lee A K & Kudchadker R J 2011 Phys. Med. Biol. 56, 5287–5302.

ICRU 2007 ICRU report 78: Prescribing, recording, and reporting proton-beam therapy Technical report International Commission on Radiation Units and Measurements.

Jarlskog C Z & Paganetti H 2008 IEEE Trans. Nucl. Sci. 55(3), 1018–1025.

Keall P J, Mageras G S, Balter J M, Emery R S, Forster K M, Jiang S B, Kapatoes J M, Murphy D A L M J, Murray B R, Ramsey C R, Herk M B V, Vedam S S, Wong J W & Yorke E 2006 Med. Phys. 33, 3874–3900.

Klassen N V, van der Zwan L & Cygler J 1997 Med. Phys. 24(12), 1924–1934.

Kupelian P, Willoughby T, Mahadevan A, Djemil T, Weinstein G, Jani S, Enke C, Solberg T, Flores N, Liu D, Beyer D & Levine L 2007 Int. J. Radiation Oncology Biol. Phys. 67(4), 1088–1098.

Langen K M, Willoughby T R, Meeks S L, Santhanam A, Cunningham A, Levine L & Kupelian P A 2008 Int. J. Radiation Oncology Biol. Phys. 71(4), 1084–1090.

Li H S, Chetty I J, Enke C A, Foster R D, Willoughby T R, Kupellian P A & Solberg T D 2008 Int. J. Radiation Oncology Biol. Phys. 71(3), 801–812.

Li H S, Chetty I J & Solberg T D 2008 Med. Phys. 35(5), 1703–1710.

Lim Y K, Kwak J, Kim D W, Shin D, Yoon M, Park S, Kim J S, Ahn S H, Shin J, Lee S B, Park S Y, Pyo H R, Kim D Y & Cho K H 2009 Int. J. Radiation Oncology Biol. Phys. 74(5), 1609–1616.

Lomax A J 2008a Phys. Med. Biol. 53, 1027–1042.

Lomax A J 2008b Phys. Med. Biol. 53, 1043–1056.

Matsuura T, Maeda K, Sutherland K, Takayanagi T, Shimizu S, Takao S, Miyamoto N, Nihongi H, Toramatsu C, Nagamine Y, Fujimoto R, Suzuki R, Ishikawa M, Umegaki K & Shirato H 2012 39(9), 5584–5591.

Newhauser W D, Koch N C, Fontenot J D, Rosenthal S J, Gombos D S, Fitzek M M & Mohan R 2007 Phys. Med. Biol. 52, 2979–3990.

Newhauser W, Fontenot J, Koch N, Dong L, Lee A, Zheng Y, Waters L & Mohan R 2007 Phys. Med. Biol. 52, 2937–2952.

Niroomand-Rad A, Blackwell C R, Coursey B M, Gall K P, Galvin J M, McLaughlin W L, Meigooni A S, Nath R, Rodgers J E & Soares C G 1998 Med. Phys. 25(11), 2093–2115.

Rajendran R R, Plastaras J P, Mick R, Kohler D M, Kassaee A & Vapiwala N 2010 Int. J. Radiation Oncology Biol. Phys. 76(4), 1092–1099.

Rau A W, Nill S, Eidens R S & Oelfke U 2008 Phys. Med. Biol. 53, 3789–3805.

Rossi B & Greisen K 1941 Rev. Mod Phys. 13, 240–309.

Santanama L, Noel C, Willoughby T R, Esthappan J, Mutic S, Klein E E, Low D A & Parikh P J 2009 Med. Phys. 36(8), 3477–3486.

Seiler P G, Blattmann H, Kirsch S, Muench R K & Schilling C 2000 Phys. Med. Biol. 45, N103–N110.

Shinohara E T, Kassaee A, Mitra N, Vapiwala N, Plastaras J P, Drebin J, Wan F & Metz J M 2012 Int. J. Radiation Oncology Biol. Phys. 83(2), 566–573.

Slater J D, Rossi C J, Yonemoto L T, Bush D A, Jabola R, Levy R P, Grove R I, Preston W &

Slater J M 2004 Int. J. Radiation Oncology Biol. Phys. 59(2), 348–352.

Smith A 2009 Med. Phys. 36, 556–568.

Su Z, Zhang L, Murphy M & Williamson J 2011 Int. J. Radiation Oncology Biol. Phys. 81(3), 880–887.

Tanyi J A, He T, Summers P A, Mburu R G, Kato C M, Rhodes S M, Hung A Y & Fuss M 2010 Int. J. Radiation Oncology Biol. Phys. 78(5), 1579–1585.

Vassiliev O N, Kudchadker R J, Kuban D A, Frank S J, Choi S, Nguyen Q & Lee A K 2012 Phys. Med. 28, 240–244.

Willoughby T R, Kupelian P A, Pouliot J, Shinohara K, Aubin M, Mack Roach I, Skrumeda L L, Balter J M, Litzenberg D W, Hadley S W, Wei J T & Sandler H M 2006 Int. J. Radiation Oncology Biol. Phys. 65(2), 528–534.

Zhang P, Mah D, Happersett L, Cox B, Hunt M & Mageras G 2011 Med. Phys. 38(7), 4001–4008.

APPENDICES

I. INTRODUCTION

Experimental verification of the external beam therapy calculations that account for tissue heterogeneities within the treatment volume requires accurate and robust detectors over the relevant areas. Radiochromic film darkens upon exposure to radiation without further film processing.[1] Radiochromic medium with its high spatial resolution and independent response to energy and particle type, and tissue equivalence can be a candidate as a two dimensional dosimeter for this application.[1,2] The high spatial resolution and sensitivity over extended spatial areas should provide an experimental platform for examining dose distribution perturbation due to tissue heterogeneity. The radiochromic films are tissue equivalent further promoting themselves as dosimetry materials. The EBT2 film[2] with the yellow marker dye was developed to reduce the spatial heterogeneity[2–10] due to manufacturing found in earlier versions of radiochromic film.

There are technical issues and challenges that must be addressed and resolved prior to their application for dosimetry over extended spatial areas. First, a number of researchers[4–11] have been concerned about the uniformity of dose responses of the radiochromic film due to variable thickness/composition generated by the manufacturing process, including the newer film such as EBT and EBT2. In addition, spatially varying illumination of the exposed EBT2 film during scanning to digitize the film contributes to the inhomogeneous dose calculation.

The recent advent of EBT2 radiochromic film has spawned a number of articles examining the new film's properties and procedures for achieving optimal dosimetry. Digitization of the radiochromic film through scanning with a flatbed scanner and exploiting its ability to extract individual color components for the imagery was examined some time ago[12,13] and has become a standard procedure.[14,15] Common mode rejection (taking the ratio of images from two different color channels) was employed to buck out the effect of thickness/composition variations, in particular, Ohuchia[3] used the red and green channels. The manufacturer recommends using red and the relatively insensitive blue channels and these ratios were studied by Pawlicki *et al.*[4] and Alami *et al.*[5] Pawlicki *et al.*[4] found that taking the ratio of red to blue was essential but conflicted with Alami *et al.*[5] who found that using the red channel achieved better results than using the ratio of red to blue channels. Andres *et al.*[6] found that optimal dosimetry choice of red or green channels was dose dependent. McCaw *et al.*[7] found some improvement but also some degradation using red to blue ratio to extract the dose from EBT2 film, depending on the analysis method. Devic *et al.*[8] extended the range of the dosimetry by stitching the dose from the red channel for low dose, green for intermediate dose, and blue for higher doses. Devic did not use ratios of channels to extend the dose range and also minimize dose heterogeneity issues.

Spatially inhomogeneous illumination for scanning the exposed film can also significantly degrade dosimetric accuracy, especially near the edges of the scan. This error is compounded by the level of dose exposure. Kairn *et al.*[9]

corrected the spatial heterogeneity by using spatially registered, unexposed film and used the red channel but only employed comparison of dose profiles, not gamma analysis. Richley *et al.*[10] focused on mitigating scanner light scattering. Hartmann *et al.*[11] used the red channel to examine dose heterogeneity among cut up slices of EBT2 film. Devic *et al.*[16] characterized the scanner inhomogeneity and its effect on dose distribution. Fiandra *et al.*[17] and Sauer and Frengen[18] both provided a correction matrix for the scanner inhomogeneity using the red channel and they also incorporated dose levels into their corrections.

To simultaneously and autonomously handle film imperfections and scanner illumination inhomogeneity, Micke *et al.*[19] suggested a multichannel approach and found significant improvements relative to employing a single red channel approach. The multichannel approach uses all three channels (red, green, and blue) to extract a single dose for each pixel. Micke *et al.*[19] demonstrated significant alleviation of the spatial inhomogeneity issues. However, no equations were explicitly stated for the corrected dose at each pixel using the multichannel approach. It was not even clear whether an iterative search might have been employed to search for an optimal solution. Direct comparison with Micke *et al.* was therefore difficult and at best surmised.

This paper examined and resolved each of these technical issues by systematically exploring a number of different dosimetry procedures for reducing the thickness/composition variations within the EBT2 radiochromic film. Specifically this study examined the relative benefits of using the various color channels (red, green, and blue) or combinations of ratios of channels not previously studied. Gamma analysis provided the quantitative discriminator among the various single, dual, and triple channels methods for calculating dose distributions relative to the dose distribution calculated from the treatment plan.

II. METHODS

The overall methodology is summarized by the block diagram shown in Fig. 1. The goal was to analyze the absolute dose distribution deposited by a 6 MV photon beam (field size is 10×10 cm at the isocenter) from a Varian 2100 linear accelerator (linac) directed parallel to an EBT2 film sandwiched between slabs of solid water™. The phantom was positioned at 100 cm source to surface distance (SSD) and 200 cGy was delivered to dmax. The three sets of images (CT, ECLIPSE treatment planner, radiochromic film) must be compatibly manipulated. The CT image set was treated as the "base" image because the treatment plan used and was fixed to the CT image. The Varian ECLIPSE plan and the measured dose distribution derived from the radiochromic film were translated and rotated to match reference points or fiducial points (Spee-D-Mark) within the CT image. The spatial resolution (40 dots per inch or dpi) was set by the ECLIPSE treatment plan and the CT was resampled and the radiochromic film was scanned at the same spatial resolution.

Gamma analysis compares the dose distribution from a standard such as a plan to the dose distribution form the test

I. INTRODUCTION

Experimental verification of the external beam therapy calculations that account for tissue heterogeneities within the treatment volume requires accurate and robust detectors over the relevant areas. Radiochromic film darkens upon exposure to radiation without further film processing.[1] Radiochromic medium with its high spatial resolution and independent response to energy and particle type, and tissue equivalence can be a candidate as a two dimensional dosimeter for this application.[1,2] The high spatial resolution and sensitivity over extended spatial areas should provide an experimental platform for examining dose distribution perturbation due to tissue heterogeneity. The radiochromic films are tissue equivalent further promoting themselves as dosimetry materials. The EBT2 film[2] with the yellow marker dye was developed to reduce the spatial heterogeneity[2–10] due to manufacturing found in earlier versions of radiochromic film.

There are technical issues and challenges that must be addressed and resolved prior to their application for dosimetry over extended spatial areas. First, a number of researchers[4–11] have been concerned about the uniformity of dose responses of the radiochromic film due to variable thickness/composition generated by the manufacturing process, including the newer film such as EBT and EBT2. In addition, spatially varying illumination of the exposed EBT2 film during scanning to digitize the film contributes to the inhomogeneous dose calculation.

The recent advent of EBT2 radiochromic film has spawned a number of articles examining the new film's properties and procedures for achieving optimal dosimetry. Digitization of the radiochromic film through scanning with a flatbed scanner and exploiting its ability to extract individual color components for the imagery was examined some time ago[12,13] and has become a standard procedure.[14,15] Common mode rejection (taking the ratio of images from two different color channels) was employed to buck out the effect of thickness/composition variations, in particular, Ohuchia[3] used the red and green channels. The manufacturer recommends using red and the relatively insensitive blue channels and these ratios were studied by Pawlicki *et al.*[4] and Alami *et al.*[5] Pawlicki *et al.*[4] found that taking the ratio of red to blue was essential but conflicted with Alami *et al.*[5] who found that using the red channel achieved better results than using the ratio of red to blue channels. Andres *et al.*[6] found that optimal dosimetry choice of red or green channels was dose dependent. McCaw *et al.*[7] found some improvement but also some degradation using red to blue ratio to extract the dose from EBT2 film, depending on the analysis method. Devic *et al.*[8] extended the range of the dosimetry by stitching the dose from the red channel for low dose, green for intermediate dose, and blue for higher doses. Devic did not use ratios of channels to extend the dose range and also minimize dose heterogeneity issues.

Spatially inhomogeneous illumination for scanning the exposed film can also significantly degrade dosimetric accuracy, especially near the edges of the scan. This error is compounded by the level of dose exposure. Kairn *et al.*[9]

corrected the spatial heterogeneity by using spatially registered, unexposed film and used the red channel but only employed comparison of dose profiles, not gamma analysis. Richley *et al.*[10] focused on mitigating scanner light scattering. Hartmann *et al.*[11] used the red channel to examine dose heterogeneity among cut up slices of EBT2 film. Devic *et al.*[16] characterized the scanner inhomogeneity and its effect on dose distribution. Fiandra *et al.*[17] and Sauer and Frengen[18] both provided a correction matrix for the scanner inhomogeneity using the red channel and they also incorporated dose levels into their corrections.

To simultaneously and autonomously handle film imperfections and scanner illumination inhomogeneity, Micke *et al.*[19] suggested a multichannel approach and found significant improvements relative to employing a single red channel approach. The multichannel approach uses all three channels (red, green, and blue) to extract a single dose for each pixel. Micke *et al.*[19] demonstrated significant alleviation of the spatial inhomogeneity issues. However, no equations were explicitly stated for the corrected dose at each pixel using the multichannel approach. It was not even clear whether an iterative search might have been employed to search for an optimal solution. Direct comparison with Micke *et al.* was therefore difficult and at best surmised.

This paper examined and resolved each of these technical issues by systematically exploring a number of different dosimetry procedures for reducing the thickness/composition variations within the EBT2 radiochromic film. Specifically this study examined the relative benefits of using the various color channels (red, green, and blue) or combinations of ratios of channels not previously studied. Gamma analysis provided the quantitative discriminator among the various single, dual, and triple channels methods for calculating dose distributions relative to the dose distribution calculated from the treatment plan.

II. METHODS

The overall methodology is summarized by the block diagram shown in Fig. 1. The goal was to analyze the absolute dose distribution deposited by a 6 MV photon beam (field size is 10×10 cm at the isocenter) from a Varian 2100 linear accelerator (linac) directed parallel to an EBT2 film sandwiched between slabs of solid water™. The phantom was positioned at 100 cm source to surface distance (SSD) and 200 cGy was delivered to dmax. The three sets of images (CT, ECLIPSE treatment planner, radiochromic film) must be compatibly manipulated. The CT image set was treated as the "base" image because the treatment plan used and was fixed to the CT image. The Varian ECLIPSE plan and the measured dose distribution derived from the radiochromic film were translated and rotated to match reference points or fiducial points (Spee-D-Mark) within the CT image. The spatial resolution (40 dots per inch or dpi) was set by the ECLIPSE treatment plan and the CT was resampled and the radiochromic film was scanned at the same spatial resolution.

Gamma analysis compares the dose distribution from a standard such as a plan to the dose distribution form the test
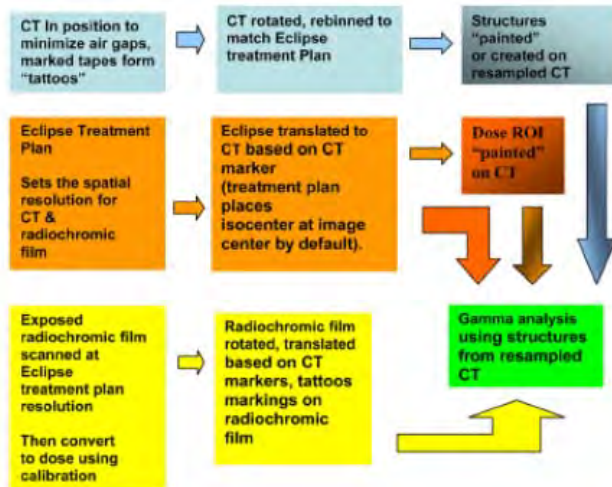
117

FIG. 1. A block diagram describing the procedures for comparing calculated and measured dose distributions.

distribution. Gamma analysis (Sec. II H) requires input from registered dose distribution from the ECLIPSE treatment planning system and the dose extracted from the radiochromic films. In addition, this study, unlike many, applies the gamma analysis to selected regions such as regions of low scattered dose, plateau of high dose, and beam edges. Such an approach requires input of appropriate areas such as regions of interest (shown in Fig. 1). In addition, the software development permits input of regions of interest form tissues in the CT, also shown in Fig. 1.

All custom software development regarding registration and algorithms for converting exposed images to dose distributions was developed using the Interactive Development Language (IDL).

II.A. CT rotation

The analysis from exposing film and/or radiochromic film is often problematic due to possible presence of small air gaps between the film and the solid phantom. The phantom was scanned in the CT in the transverse orientation [Fig. 2(a)] so that the weight of the phantom was pressed onto the radiochromic film. In this configuration, additional weight was added if needed to further reduce air gaps. The treatment table supported and remained in contact with the flat part of the phantom, a configuration that is not available for humans. The entire phantom was scanned with spatial resolution of 27.1 dpi, not just the expected treatment area because all CT slices (2 mm spacing) were used to reconstruct the image of the phantom in an orthogonal direction. Nearest neighbor averaging was used to fill in the regions between the slices. The reconstructed and rotated CT [coronal orientation, see Fig. 2(b)] was resampled, again using nearest neighbor averaging so that the CT had a spatial resolution of 40 dots per inch, matching the ECLIPSE treatment plan dose distribution and the scanned radiochromic film image. CT skin markers placed at known distances were used to test the fidelity of the resampling and rotation process and found to be accurate to within less than a pixel (<0.64 mm). The rotated CT was expanded (to 1000×1000 pixels) to accommodate the ECLIPSE plan which had a treatment isocenter placed in the center of the image. Marked tapes denoting the CT marker positions were also placed on the phantom and were used to align the phantom during radiation exposure.
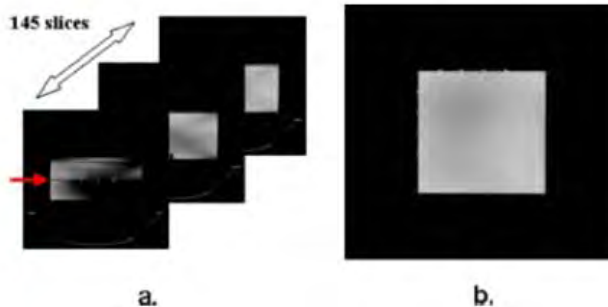

FIG. 2 (a) Selected three slices (out of 145) of solid phantom in transverse orientation. CT skin markers shown in first slice. Arrow denotes plane shown in Fig. 2(b). (b) Rotated image (coronal) of solid phantom. Only single slice of plane abutting placement of radiochromic film for this study is shown.

II.B. Scanning

The exposed radiochromic film was scanned, similar to earlier studies,[12–16] with a CanoScan LiDE 700F flatbed scanner in reflection mode using 48 bit digital resolution to digitize the three color channels (Red, Green, and Blue) at a spatial resolution of 40 dpi to conform to the ECLIPSE treatment planning system. All correction options were turned off. The orientation of the film was noted[2] with a small cut in the upper right hand corner. All radiochromic film were positioned identically on the flatbed scanner, after noting the orientation of the film. The lot number for the exposed EBT2 was A11051002A. Radiochromic film was scanned approximately 24 h after exposure. The EBT2 film are particularly insensitive to visible light[2] but care is taken to minimize exposure to visible light. The radiochromic film gray-levels were converted to dose using calibration films. Smaller film (roughly 10×12.5 cm) were exposed to 0, 25, 50, 100, 150, 200, 250, and 300 cGy placed perpendicular to the beam (10×10 cm field) sandwiched between solid water™ slabs. In this configuration, the monitor units equaled the dose in cGy and simplified the calibration procedure following procedures outlined in the report of Task Group 21. The 10×10 cm field exposed the solid water™ phantom positioned at 100 cm source to axis distance and the film placed at dmax (1.5 cm), perpendicular to the 6 MV photon beam from the Varian 2100 machine.

The calibration films were scanned. An average gray-level was computed for each red, green, and blue (R,G,B) channel using the central region (2×2 cm or roughly 1000 pixels) conforming to the most uniform dose. A look up table (LUT) composed of the average gray-level (or ratio of gray-levels) for each color channel was correlated with dose. The lines connecting the solid symbols in Fig. 3 graphically shows the dose versus average detected intensity in the LUT for the red, green, and blue channels. However, each pixel within the array may not conform to the average pixel due to
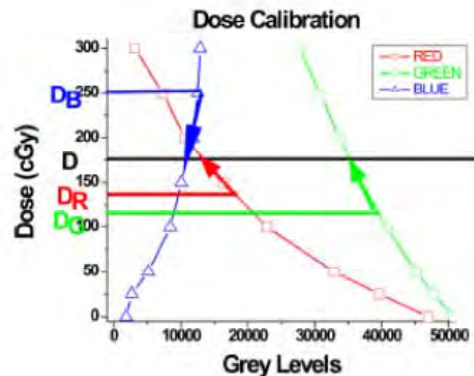

Fig. 3. Calibration for converting gray-levels to dose for red (square), green (circle), and blue (triangle) channels. Optimized multichannel correction schematically shows the shifted extrapolated doses D_R, D_G, D_B relative to optimized D based on local derivatives $a_k(i,j)$ [Eq. (3)], used in multichannel approach).

differences in scanner illumination. So the dose extrapolated for the R,G,B channel (D_R, D_G, D_B), respectively, may differ from each other due to varying response for a given perturbation. The multichannel approach autonomously projected a correction to an expected common dose D based on the individual slopes and response of each channel.

The test profile distribution was converted to dose through interpolating the LUT.[1,7] Globally the dose gray level functions are nonlinear. Over small stretches of dose and gray-levels, the calibration was essentially linear. In addition, using relatively low doses (<300 cGy) limits the degree of nonlinearity of the LUT for EBT2. Higher doses beyond those used in this study will require a more refined calibration table to ensure linearity over the small dose and gray level intervals and possible higher order corrections beyond the first Taylor series approximation [Eq. (2)] for the multichannel algorithm.

This study tested various schemes for converting gray-levels to reduce the effects of the heterogeneity. These processes are applied to the calibration imagery (for a new LUT) and the test dose distribution. The manufacturer[2] recommends for individual pixels located at coordinate i,j (in the horizontal, vertical direction, respectively), taking the ratio of the red channel $R(i,j)$ to the blue channel $B(i,j)$ from scanning the film with a flatbed scanner. Using the Beer-Lambert Law, the gray-levels are normalized by the unattenuated, constant light source I_0 from the flatbed scanner and the ratio of the logarithms are computed or

$$\frac{R}{B}(i,j) = \frac{\log\left(\frac{R(i,j)}{I_0}\right)}{\log\left(\frac{B(i,j)}{I_0}\right)}. \tag{1}$$

A similar ratio Green to Blue ratio was computed using the green channel.

Taking the ratio of the channel that is most sensitive to composition/exposure to one that is relatively independent of exposure but experienced the same dependence on thickness/composition to help suppress thickness/composition variations[2–11] of the film. In practice, the blue channel response weakly depends on radiation exposure. This study generated dose distributions using the red channel $R(i,j)$ alone, green channel $G(i,j)$ alone, ratios of the red to blue channel and green to blue channel and hybrid version that combined the green to blue ratio for higher doses (above 80cGy or 0.20 optical density and was likely scanner specific) to the red to blue ratio for lower doses.

II.C. New multichannel approaches

Another approach employed all three color channels to autonomously correct for local inhomogeneous spatial distribution in film thickness and scanner. This version of the multichannel approach independently varied the dose D and disturbance Δ (or channel-independent perturbation, see Eqs. (2) and (7) to search for the optimal dose at each pixel. This study proposed and found an equation for the corrected dose. Therefore, the optimized dose was quickly computed

119

at each pixel. The goal was to find a common and expected dose D derived from extracted red, green, and blue channel doses. The algorithm applied a first order Taylor expansion to the dose due to a small perturbation (same for all channels) and minimized the cost function difference $\Phi(i,j)$ [Eq. (2)] between the projected

$$\Phi(\Delta(i,j), D(i,j)) = \sum_{k=1}^{3} (D_k(i,j) + a_k(i,j)\Delta(i,j) - D(i,j))^2, \tag{2}$$

dose $D_k(i,j) + a_k(i,j) \Delta(i,j)$ for each color channel k (red, green, blue) relative to the projected dose D. $D_k(i,j)$ was the dose directly derived from the LUT for each color [i.e., $R(i,j)$, $G(i,j)$, and $B(i,j)$ for the red, green, and blue channels, respectively], $a_k(i,j)$ was the derivative

$$a_k(i,j) = \frac{\partial D_k}{\partial I_k}(i,j) \tag{3}$$

of the LUT for the kth channel (see Fig. 3), and $\Delta(i,j)$ is the local perturbation (illumination, thickness) that affected all channels, and I_k was the intensity for a given channel, i.e., $[R(i,j), G(i,j), B(i,j)]$. Interpolation was required to accurately determine the slopes or $a_k(i,j)$. $D(i,j)$ was the corrected dose generated from solving the simultaneous partial differential equations

$$\frac{\partial \Phi}{\partial \Delta}(i,j)(\Delta, D) = 0. \tag{4}$$

$$\frac{\partial \Phi}{\partial D}(i,j)(\Delta, D) = 0. \tag{5}$$

and resulted in the optimized dose D at pixel location i,j

$$D(i,j) = \frac{D_{ave}(i,j) - (wt(i,j)) \dfrac{\sum_{k=1}^{3} D_k(i,j) a_k(i,j)}{\sum_{k=1}^{3} a_k(i,j)}}{1 - wt(i,j)}. \tag{6}$$

The appropriate correction or "disturbance map" at each point was

$$\Delta(i,j) = \frac{\sum_{k=1}^{3} (D(i,j) - D_k(i,j)) a_k(i,j)}{\sum_{k=1}^{3} a_k^2(i,j)}. \tag{7}$$

where the average dose $D_{ave}(i,j)$ was

$$D_{ave}(i,j) = \frac{1}{3} \sum_{k=1}^{3} D_k(i,j)$$
$$= \frac{1}{3} (D_R(i,j) + D_G(i,j) + D_B(i,j)). \tag{8}$$

And the Relative Slope for the channels $RS(i,j)$

$$RS(i,j) = \frac{1}{3} \frac{\left(\sum_{k=1}^{3} a_k(i,j)\right)^2}{\sum_{k=1}^{3} a_k^2(i,j)}, \tag{9}$$

and $RS(i,j)$ ranged from $0 < RS < 1$. If $RS(i,j)$ was sufficiently small, then a valuable approximation for the corrected dose $D(i,j)$ was

$$D(i,j) \simeq D_{ave}(i,j). \tag{10}$$

EBT2 film was sandwiched between slabs of solid water™ and exposed to 6 MV photon beam. Figure 4(a) shows the rotated (by 90°) uncorrected distribution from the single red channel. Figure 4(b) shows the optimized multichannel corrected dose distribution $D(i,j)$ [Eq. (6)]. Figure 4(c) shows the disturbance distribution $\Delta(i,j)$ [Eq. (7)] rotated by 90°. Note the stripes from thickness variations in the film in Fig. 4(a) and are also seen in Fig. 4(c). Figure 4(d) shows the residual error in dose [Eq. (2)].

II.D. Previous multichannel efforts

Micke *et al.*[19] recently suggested, tested, and broadly outlined a multichannel approach for correcting the inhomogeneities in the dosimetry process. The Micke *et al.* cost function differed from the multichannel process described in Eq. (2). Following the approach of Micke *et al.*, the cost function was

$$\Omega(i,j) = \sum_{k \neq m}^{3} (D_k(i,j) + a_k(i,j)\Delta(i,j) - (D_m(i,j) + a_m(i,j)\Delta(i,j)))^2. \tag{11}$$

Due to the different cost function, Micke *et al.* generated and applied a different disturbance factor than used in Eq. (11). Micke *et al.* also applied his analysis to the fitted optical density calibration, not to the raw gray level calibration described in this study. For the Micke *et al.* approach, only single derivative with respect to Δ might have been applied to Eq. (11) (but not two derivatives as in Eqs. (4) and (5)

$$\frac{\partial \Omega}{\partial \Delta}(i,j) = 0. \tag{12}$$

The resulting shift $\Delta(i,j)$ might have been

$$\Delta(i,j) = -\frac{\sum_{k \neq m}^{3} (D_k(i,j) - D_m(i,j))(a_k(i,j) - a_m(i,j))}{\sum_{k \neq m}^{3} (a_k(i,j) - a_m(i,j))^2}. \tag{13}$$

In this formulation, each channel might have been treated equally and corrected using the procedure outlined above, i.e.

$$D(i,j) = \frac{1}{3} \sum_{k=1}^{3} (D_k(i,j) + a_k(i,j)\Delta(i,j)). \tag{14}$$

The dose D might be generated by inserting the computed shift Δ [Eq. (13)] into the corrected average multichannel dose [Eq. (14)]. This approach generated an identical dose distribution as that derived from Eq. (6), although generated in a very different manner.
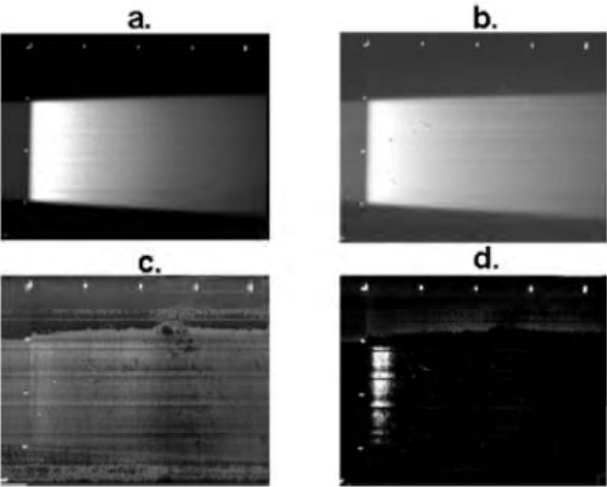
120

FIG. 4 (a) Rotated (by 90°) dose distribution using red channel. (b) Corrected dose distribution. $D(i,j)$ [Eq. (6)] using the optimized approach. (c) Shows the disturbance distribution $\Delta(i,j)$ [Eq. (7)] rotated by 90°. Note the stripes due to thickness variations. (d) Residual error in dose [Eq. (2)].

II.E. Summary of dose determination algorithms

The list of conversion of gray-level processing algorithms is summarized in Table I. The table displays, names, a short description, and its associated equation.

II.F. Registration

Comparing experimentally determined dose distributions with the corresponding calculated treatment plan required precise registration between the two sets of images. The solid water™ was placed on the CT imaging and treatment table in a configuration convenient for placing CT markers. These markers were used for registering the CT to both the treatment plan and the detected radiation dose distribution from the radiochromic film. The CT images were digitally rotated for convenient volumetric contouring for dose area histograms and gamma analysis. The rotated CT image was resampled to match the spatial resolution of the scanned dosimetric distribution and treatment plan. The treatment plan was calculated using the CT image in the customary fashion. The treatment plan planes were translated through triangulation of the treatment isocenter to the CT markers in the CT image. The radiochromic film imagery was rotated and translated to the CT images using two coincident points from the CT skin markers in the CT image and "tattoos" marked on the radiochromic film.

This study used a "two-point" approach to translate and rotate the radiochromic film to the desired resampled CT slice. The common "pivot" point for the CT and radiochromic film was used to translate the radiochromic film and the radiochromic film image was then rotated about the pivot point. The average error in transforming the fiducial points (excluding the pivot) was 1.39 pixels or 0.883 mm. On average, a similar error was expected for transforming all points within the radiochromic film image.

II.G. Treatment plan procedures

This study used Varian's ECLIPSE treatment planning system to compute the expected dose distribution. The plan computed the dose distribution intended to deliver 200 cGy

TABLE I. List of gray-level processing prescriptions.

| Name	Description	Formula
Red channel	Red alone	$R(i,j)$
Green channel	Green alone	$G(i,j)$
Red to blue ratio	Registered red to blue ratio [Eq. (1)]	$R/B(i,j) = \dfrac{\log\left(\frac{R(i,j)}{I_0}\right)}{\log\left(\frac{B(i,j)}{I_0}\right)}$
Green to blue ratio	Registered green to blue ratio [Eq. (1)]	$G/B(i,j) = \dfrac{\log\left(\frac{G(i,j)}{I_0}\right)}{\log\left(\frac{B(i,j)}{I_0}\right)}$
Hybrid	Apply green to blue ratio for higher dose and red to blue ratio for lower dose	$Hybrid(i,j) = R/B(i,j) + G/B(i,j)$
Average	Average over all channels [Eq. (8)]	$Ave(i,j) = (1/3)(D_{Red} + D_{Green} + D_{Blue})$
Optimize multichannel	Optimize correction using all channels [Eq. (6)]	$Opt(i,j) = \left(Ave(i,j) - RS(i,j)\sum a_k(i,j)D_k(i,j)/ \sum a_k(i,j)/(1 - RS(i,j))\right)$

121
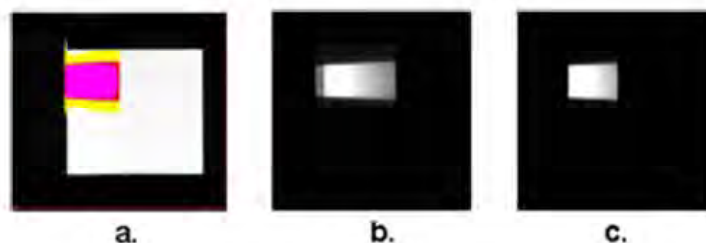
FIG. 5 (a) Shows the CT and the area of dose exceeding the 100 cGy (central), dose between 25–100 cGy (edge), dose between 5 and 15 cGy) (exterior), 5(b) shows the translated, rotated dose distribution derived from the radiochromic film, 5(c) shows the ECLIPSE treatment plan.

to dmax and the phantom was positioned at 100 cm SSD. The treatment plan was generated from the CT scan of the phantom. The external beam depth profiles from Varian 2100 6 MV photon beam that characterize the dose deposition in water were stored and used to compute the dose deposition. The external beam was checked on a daily, weekly, yearly timetable to ensure agreement with the current condition of the beam and the stored data. The ECLIPSE plan generated DICOM image files for the predicted dose along desired planes. The spatial resolution for the image dose was chosen to be 40 dpi, conforming to the resampled CT image and scan of the exposed radiochromic film. The isocenter for the plan was placed at the image center, by default. The spatial transformation of the treatment plan simply meant translating the isocenter, or image center to the isocenter of the CT scan that was marked by a CT marker. No rotation was applied to the treatment plan image.

All registered images are shown in Fig. 5. Figure 5(a) shows the rotated and resampled CT and the area of dose exceeding the 100 cGy within the treatment plan in the central area, the beam edge with doses ranging from 25 to 100 cGy and scattered dose in the exterior (5–15 cGy). The high dose gradients were extremely sensitive to misregistration between the plan and the experiments. Figure 5(b) shows the translated, rotated dose distribution derived from the radiochromic film. Figure 5(c) shows the translated ECLIPSE treatment plan.

II.H. Quantitative assessment of agreement between plan and experiment (gamma analysis)

The various methods for scanning the exposed radiochromic film, gray-level conversion to dose, and dosimetry procedures, were tested by comparing them to the treatment plan through gamma analysis.[20-22] Gamma analysis examined the deviation of the treatment plan (considered to be the reference image) with the experimentally determined dose distribution at the pixel level. The gamma analysis procedure generated a difference image for the registered set of images and computed a "decision" surface with the geometry of a three dimensional ellipsoid. Calculated points that resided within the ellipsoid constitute good agreement between the treatment plan dose distribution and the experimentally derived dose. Conversely, points that appeared outside the ellipsoid are identified as areas of poor agreement or referred to as "exceedances" in this paper.

Figure 6(a) shows the gamma analysis display using the Red only processing. The white pixels show gamma values that exceed 1 and show regions of most serious disagreement between the plan and the experimentally derived dose distribution. Figure 6(b) shows exceedances using the optimized multichannel algorithm. Adding more channels such as the optimized multichannel algorithms for extracting dosimetry distributions reduced gamma exceedances from 8605 to 3110 (out of 74 312 pixels within the region of interest) (see Table II).
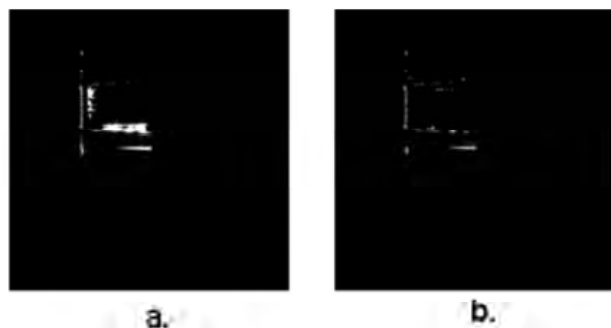

FIG. 6 (a) Shows the exceedances (depicted as white) for the gamma distribution from Red only processing.

122

TABLE II. Gamma analysis fraction of exceedances (%) of total of pixels and scanning, image processing, region conditions

Name	Total 5–300 cGy (%) (74 312 pixels)	"High" dose 100–300 cGy (%) (38 329 pixels)	Scatter 5–15 cGy (%) (26 307 pixels)	Beam edge 25–100 cGy (%) (6679 pixels)
Red	11.6	14.7	5.3	28.3
Green	10.9	11.7	7.7	31.2
Red to blue	6.3	6.0	5.2	21.6
Green to blue	4.8	2.8	5.5	21.7
Hybrid Ratios	4.7	2.8	5.3	21.7
Optimized multi	4.2	2.0	5.1	22.0
Average dose	4.1	1.6	5.2	23.0

III. RESULTS

The scanning, data processing, and phantom handling schemes were evaluated by computing the number of pixels within the treatment area having gamma values exceed 1 (see Table II). The larger the number of these pixels, the poorer the agreement between the experimentally determined dose and the treatment plan. For this analysis, the ellipsoid axes were prescribed to the standard 3% of the maximum dose or 6 cGy (D_{gamma}) and 3 mm in horizontal, vertical directions (x_{gamma}, y_{gamma}). If this minimum gamma exceeded 1, then the experiment was ruled to disagree with the treatment plan. Table II lists the results of applying the standard red channel, green channel, the manufacturer's recommendation for taking the ratio of red to blue channels [Eq. (1)], ratio of green to blue channels [Eq. (1)], the hybrid of green to blue ratio with the red to blue, optimized multi-channel [Eq. (6)] and averaged multichannel algorithms [Eq. (8)]. The analysis examined the entire area, high dose regions, scattered dose, and the beam edge. The best agreement occurred in the relatively homogenous dose regions (high dose, scattered dose) and was weak in the high dose gradient and where a high degree of registration was required for accurate dose measurement.

Although only an approximation, the average dose algorithm appeared to generate few exceedances (Table II) relative to other algorithms. The computed weight [Eq. (9), Table III] was low for all doses in this study. The small values for the weight factor wt (Table III) implied that the average dose derived from the three color channels provided a valid approximation for the more exact analysis [Eq. (6)]. The blue channel calibration curve was almost orthogonal to the red and green channels for most dose levels used in this study (see Fig. 3).

TABLE III. Relative Slope (RS) [Eq. (9)] for the dose ranges in the optimized multichannel algorithm.

Dose range (cGy)	Relative Slope (RS)
0.0–25.0	0.108
25.0–50.0	0.0153
50.0–100.0	0.0012
100.0–150.0	0.0235
150.0–200.0	0.00939
200.0–250.0	0.0822
250.0–300.0	0.206

Some general observations can be inferred from the gamma analysis. Processing with the green channel usually performed as well or better than the red channel. Using the blue channel required image averaging to sufficiently reduce the temporal noise.

IV. SUMMARY/CONCLUSIONS

This study generated procedures and algorithms for accurately determining doses and compared the treatment planning dose distributions calculated from the planning system and measured from the EBT2 radiochromic film. Specifically, this study developed algorithms that handled issues of thickness/composition heterogeneity within the radiochromic film due to the manufacturing process on dose distribution and also reduced the effects of inhomogeneous illumination during the scanning of the EBT2 film. This methodology avoided using cumbersome, registered correction matrices.

This study conceived and tested the new hybrid combination of green to blue ratio to the red to blue ratios. Also, this study proposed and tested a multichannel dose determination algorithm. Averaging the test image mitigated temporal noise in the blue channel and the reduced noise is essential for implementing blue channels in ratio and multichannel algorithms. This study explicitly described the algorithm and found a closed form [Eqs. (6) and (8)]. Micke *et al.*[19] did not explicitly state the corrected dose and disturbance and so it was difficult to directly compare this effort with the results from Micke *et al.*[19] Micke *et al.* used a different disturbance map and also employed a fitted optical density, not the raw gray-levels to extract doses from each channel. This study also compared the multichannel algorithms to those using two channels or channel ratios, not just to a single channel. The hybrid combination of the channel ratios performed at a similarly high accuracy level. The multichannel average [Eq. (8)] of the recorded doses taken from each channel performed well for this flatbed scanner operating in reflection mode. However, the high performance using the multichannel average may be due to the low Relative Slope and can be attributed to the blue channel calibration curve being almost orthogonal to the red and green channels for most dose levels used in this study.

This study employed gamma analysis to compare processing schemes for measuring the absolute dose distributions

from EBT2 radiochromic film. This study examined doses deposited parallel to the external beam, not perpendicular to it, as in most other efforts. In this study, the green channel generally performed as well or better than the red channel for this flatbed scanner. Pixel level corrections using channel ratios and multichannel approaches resulted in substantial improvement. This pixel level correction was efficient and the calculations were quick (less than 5 s) The speed of the calculation for each pixel was attributed to using the closed form [Eq. (6)] rather than iteratively searching for an optimal solution. The multichannel approach required three channels but also used the derivative of the look up table as input.

There were several additional features discussed in this study. To reduce the air gap between the film and solid water™, the phantom was scanned in a geometry that permitted compression without applying a bulky vice. The CT imagery was resampled and rotated for generating the desired regions of interest for gamma analysis. Due to the absence of bulky devices, the entire radiochromic film was simply inserted between slabs of phantom without requiring cutting the film to conform to the shape of anthropomorphic phantoms. In addition, the two-point registration permitted registration among the CT imagery, treatment plan, and film dosimetry without assuming that the phantom and film were aligned during CT scanning.

a)Author to whom correspondence should be addressed. Electronic mail: mayerru@yahoo.com

[1]W. L. MacLaughlin *et al.* "Sensitometry of the response of a new radiochromic film dosimeter to gamma radiation and electron beams," Nucl. Instrum. Methods Phys. Res. A **302**, 165–117 (1991).

[2]International Specialty Products, GAFchromic EBT2 Dosimetry Film Manual. Gafchromic EBT2 self-developing film for radiotherapy, ISP White Paper, October, 2010.

[3]H. Ohuchia "High sensitivity radiochromic film dosimetry using an optical common-mode rejection and a reflective-mode flatbed color scanner," Med. Phys. **34**, 4207–4212 (2007).

[4]T. Pawlicki and G. Kim G, "SU-GG_T_275: On improving the accuracy of EBT2 film dosimetry using a flatbed scanner," Med. Phys. **37**, 3248–3249 (2010).

[5]T. Alami, T. Kairn, and J. Kenny "Evaluation of Gafchromic EBT2 dosimetry system for radiotherapy quality assurance," Australas. Phys. Eng. Sci. Med. **34**, 251–260 (2011).

[6]C. Andres *et al.*, "A comprehensive study of the Gafchromic EBT2 radiographic film. A comparison with EBT," Med. Phys. **37**, 6271–6278 (2010).

[7]T. McCaw, J. Micka, and L. A. DeWerd "Characterizing the marker-dye correction for Gafchromic EBT2 film: A comparison of three analysis methods," Med. Phys. **38**, 5771–5777 (2011).

[8]S. Devic, N. Tomic, C. Soares, and E. Podgorsak, "Optimizing the dynamic range extension of a radiochromic film dosimetry system," Med. Phys. **36**(2), 429–437 (2009).

[9]T. Kairn, T. Aland, and J. Kenny, "Local heterogeneities in early batches of EBT2 film: A suggested solution," Phys. Med. Biol. **55**, L37–L42 (2010).

[10]L Richley *et al.*, "Evaluation and optimization of the new EBT2 radiochromic film dosimetry system" Phys. Med. Biol. **55**, 2601–2617 (2010).

[11]B. Hartmann *et al.*, "Technical note: Homogeneity of Gafchromic EBT2 film," Med. Phys. **37**, 1753–1756 (2010).

[12]R. Mayer *et al.*, "A new method for microdosimetry in radioimmunotherapy using radiochromic film," Int. J. Radiat. Oncol., Biol., Phys. **28**, 505–513 (1994).

[13]R. Mayer *et al.* "Direct measurement of intratumor dose-rate distributions in experimental xenograft radio-immunotherapy with anti-CEA antibodies labeled with ^{90}Y," Int. J. Radiat. Oncol., Biol., Phys. **32**, 147–157 (1995).

[14]S Devic *et al.*, "Precise radiochromic film dosimetry using a flat-bed document scanner," Med. Phys. **32**, 2245–2253 (2005).

[15]L. Menegotti *et al.*, "Radiochromic film dosimetry with flatbed scanners: A fast and accurate method for dose calibration and uniformity correction with single film exposure," Med. Phys. **35**, 3078–3085 (2008).

[16]S. Devic *et al.*, "Sensitivity of linear CCD array based film scanners used for film dosimetry," Med. Phys. **33**, 3993–3996 (2006).

[17]C Fiandra *et al.*, "Clinical use of EBT model Gafchromic film in radiotherapy," Med. Phys. **33**, 4314–4319 (2006).

[18]S Saur and J Frengen, "Gafchromic EBT film dosimetry with flatbed CCD scanner: A novel background correction method and full dose uncertainty analysis," Med. Phys. **35**, 3094–3101 (2008).

[19]A Micke, D. F Lewis, and X. Yu, "Multichannel film dosimetry with non-uniformity correction," Med. Phys. **38**, 2523–2534 (2011).

[20]D. A. Low *et al.*, "A technique for the quantitative evaluation of dose distributions," Med. Phys. **25**, 656–661 (1998).

[21]T. Depuydt, A. Van Esch, and D. P. Huyskens, "A quantitative evaluation of IMRT dose distributions: Refinement and clinical assessment of the gamma evaluation," Radiother. Oncol. **62**, 309–319 (2002).

[22]O. A. Zeidan *et al.*, "EBT radiochromic film for IMRT dose verification," Med. Phys. **33**, 4064–4072 (2006).

Particle beam radiotherapy

Comparison of intensity-modulated radiotherapy, adaptive radiotherapy, proton radiotherapy, and adaptive proton radiotherapy for treatment of locally advanced head and neck cancer

Charles B. Simone II [a], David Ly [a], Tu D. Dan [a], John Ondos [a], Holly Ning [a], Arnaud Belard [b], John O'Connell [c], Robert W. Miller [a], Nicole L. Simone [a,*]

[a] National Cancer Institute, Radiation Oncology Branch, Bethesda, USA; [b] Henry M. Jackson Foundation for the Advancement of Military Medicine; and [c] Walter Reed Army Medical Center, Radiation Oncology, Washington, DC, USA

ARTICLE INFO

ABSTRACT

Background and purpose: Various radiotherapy planning methods for locally advanced squamous cell carcinoma of the head and neck (SCCHN) have been proposed to decrease normal tissue toxicity. We compare IMRT, adaptive IMRT, proton therapy (IMPT), and adaptive IMPT for SCCHN.
Materials and methods: Initial and re-simulation CT images from 10 consecutive patients with SCCHN were used to quantify dosimetric differences between photon and proton therapy. Contouring was performed on both CTs, and plans (n = 40 plans) and dose–volume histograms were generated.
Results: The mean GTV volume decreased 53.4% with re-simulation. All plans provided comparable PTV coverage. Compared with IMRT, adaptive IMRT significantly reduced the maximum dose to the mandible ($p = 0.020$) and mean doses to the contralateral parotid gland ($p = 0.049$) and larynx ($p = 0.049$). Compared with IMRT and adaptive IMRT, IMPT significantly lowered the maximum doses to the spinal cord ($p < 0.002$ for both) and brainstem ($p < 0.002$ for both) and mean doses to the larynx ($p < 0.002$ for both) and ipsilateral ($p = 0.004$ IMRT, $p = 0.050$ adaptive) and contralateral ($p < 0.002$ IMRT, $p = 0.010$ adaptive) parotid glands. Adaptive IMPT significantly reduced doses to all critical structures compared with IMRT and adaptive IMRT and several critical structures compared with non-adaptive IMPT.
Conclusions: Although adaptive IMRT reduced dose to several normal structures compared with standard IMRT, non-adaptive proton therapy had a more favorable dosimetric profile than IMRT or adaptive IMRT and may obviate the need for adaptive planning. Protons allowed significant sparing of the spinal cord, parotid glands, larynx, and brainstem and should be considered for SCCHN to decrease normal tissue toxicity while still providing optimal tumor coverage.

Published by Elsevier Ireland Ltd. Radiotherapy and Oncology 101 (2011) 376–382

Radiation therapy with concurrent cisplatin-based chemotherapy is the standard treatment for patients with locally advanced SCCHN [1]. Chemoradiation can potentially allow for organ preservation and improve patient quality of life compared with surgery [2]. Concurrent chemoradiation in this region, however, is associated with significant morbidity. The close proximity to vital organs makes it difficult to deliver definitive radiation doses to diseased sites without compromising normal tissue function. Xerostomia from salivary gland dysfunction commonly results and is strongly associated with dysphagia, difficulty with social eating, increased oral bacteria colonization, dental caries, and decreased quality of life [3–5]. Radiation to the glottic larynx can result in poor voice

function, weight loss, swallowing dysfunction, and decreased quality of life [6]. Mucositis [7], osteoradionecrosis from dose to the mandible [8], and nausea from dose to the brainstem [7] can also occur. Conformal techniques such as intensity-modulated radiotherapy (IMRT) can decrease dose to defined critical normal tissues and achieve dose escalation to SCCHN target volumes [9].

Adaptive radiotherapy for SCCHN is increasingly being employed to account for anatomic changes that can lead to overtreatment of normal tissues or undertreatment of tumors. Since there is a steep dose gradient with conformal techniques between target and normal tissues, interfractional anatomical changes become significant. Interfractional patient weight loss or deformation of tumor or normal tissues are not accounted for with standard radiotherapy but can markedly alter head and neck anatomy and modify treatment parameters [10]. SCCHN often have rapid favorable responses to therapy with significant tumor shrinkage [11–15]. Such response can affect other nearby nontarget structures, particularly the parotid

glands. As primary tumors regress, parotid glands in the involved treatment fields often shrink and are displaced medially, potentially increasing radiation exposure [15–18].

Adaptive radiotherapy aims to modify treatment according to changes that occur during therapy. For SCCHN, this involves re-simulating patients during their radiotherapy and modifying target volumes and treatment plans to attempt to minimize effects of anatomic changes in tumors and surrounding structures. Preliminary studies assessing adaptive photon radiotherapy have reported improved sparing of organs at risk (OARs) [12–14].

Particle therapy may also provide a more favorable toxicity profile than IMRT. Proton therapy allows energy to be deposited at a specific depth known as the Bragg peak, with rapid energy falloff beyond this point [19]. Therefore, normal tissues on the distal side of the target volume can be spared. A single-institution report has documented excellent local control rates and reduced doses to OARs for the treatment of SCCHN with proton therapy [20].

To date, there is limited data directly comparing different radiotherapy modalities and treatment strategies for SCCHN, and to the authors knowledge, no data exists comparing adaptive photon radiotherapy to particle radiotherapy or assessing adaptive particle radiotherapy for SCCHN. This is the first study comparing dose-volume histograms (DVHs) of target volumes and normal tissue structures in photon-based versus proton-based plans using both fixed target volumes and adaptive planning for patients with locally advanced SCCHN.

Materials and methods

Ten consecutive patients with Stage IV locally advanced SCCHN treated at the National Institutes of Health Clinical Research Center (six patients) or Walter Reed Army Medical Center (four patients) from 1/2008 to 9/2009 who required repeat simulation during their course of radiotherapy due to changes in anatomy or difficulties that arose during treatment relating to patient set-up or thermoplastic immobilization devices were included in the present study. Most patients had oropharynx primary malignancies (seven patients), and all patients had N2 nodal disease, with three having bilateral nodal involvement and all but one having multiple positive lymph nodes [AJCC, 6th Ed.] (Table 1). All patients underwent a single repeat simulation planning session that occurred on average 2.9 weeks into treatment with concurrent chemoradiation and were treated to revised target volumes based on the second CT data set following repeat simulation. All patients were treated with IMRT in 2 Gy daily fractions to 70 Gy over 35 fractions with concurrent cisplatin.

The CT images from these patients were used to quantify dosimetric differences between photon and proton therapy. CT data

were acquired with a slice thickness of 3 mm. CT images were imported into a photon and proton commercial treatment planning system (Eclipse, Varian Medical Systems, Palo Alto, CA) for defining target and nontarget structures. OARs and planning target volumes (PTVs) were contoured on the initial and re-simulation CT images. Target and nontarget structure sets for a given patient CT image set were held constant for all plans. Assessed OARs included the bilateral parotid glands, glottic larynx, spinal cord, brainstem, and mandible. CT streak artifacts from metal were contoured and assigned a CT value equivalent to tissue prior to calculating all photon and proton plans. Artifacts from teeth were assigned a tissue equivalent value for all proton plans and as necessary for photon plans.

Gross Tumor Volume (GTV) was defined as the maximum extent of all known gross disease determined from clinical examination, endoscopy, or CT, MRI, or PET imaging. In all directions circumferentially, the margin between GTV and Clinical Target Volume 70 (CTV_{70}) was 1 cm to include all volumes of known tumor and suspected microscopic spread. This margin was reduced to $\geqslant 2$ mm for tumors in close proximity to bone or air not at risk for subclinical disease. High risk nodal regions, including small volume lymph nodes and all potential routes of spread for primary and nodal disease, were contoured and designated CTV_{64}. Nodal regions at lower risk of disease spread were designated CTV_{50}.

To account for set-up variation and organ and patient motion, a uniform margin of 5 mm was added around each corresponding CTV to define PTV_{70}, PTV_{64}, and PTV_{50}, respectively. To account for proton beam properties and range uncertainties, proton beam range compensators were designed to provide proximal and distal margins relative to each PTV, and blocking was designed to create a lateral margin relative to each PTV. These margins were individualized for each patient on the basis of the formulas by Moyers et al. [21]. PTV_{70} was planned to 70 Gy for photon plans or 70 cobalt Gray equivalents (CGE) for proton plans, with proton doses corrected with the accepted relative biologic effectiveness value of 1.1 [19]. PTV_{64} was planned to 64 Gy or 64 CGE, whereas PTV_{50} was planned to 50 Gy or 50 CGE. Plans were devised to initially target PTV_{50}, followed by a conedown to PTV_{64}, followed by a second conedown to PTV_{70}, with no integrated boost administration planned.

Four treatment plans were generated for each patient ($n = 40$ plans): (1) photon IMRT, with treatment planned to the target volumes and normal structures from the initial CT image set, (2) adaptive photon IMRT, with treatment planned to the target volumes and normal structures from the initial CT image set to 36 Gy and to the second CT simulation image set to 34 Gy, (3) spot scanning proton IMPT, with treatment planned to the target volumes and normal structures from the initial CT image set, and (4) adaptive proton IMPT, with treatment planned to the target volumes and normal structures from the initial CT image set to 36 Gy and to

Table 1
Patient characteristics.

Patient number	Primary disease	T Stage[*]	N Stage[*]	GTV initial volume (cm³)	GTV rescan volume (cm³)	PTV₇₀ initial volume (cm³)	PTV₇₀ rescan volume (cm³)
1	Supraglottic larynx	T2	N2c	41.2	30.6	164.4	124.6
2	Oropharynx: tonsil	T3	N2b	57.4	5.1	214.0	77.8
3	Oropharynx; base of tongue	T4	N2c	89.7	54.8	490.2	370.0
4	Supraglottic larynx	T2	N2b	40.4	6.6	193.8	120.3
5	Oropharynx: tonsil	T1	N2a	36.7	17.7	282.3	144.7
6	Oropharynx: tonsil	T2	N2b	173.0	62.2	514.0	268.1
7	Oropharynx: tonsil	T2	N2b	71.1	33.4	386.2	175.8
8	Oropharynx: tonsil	T4	N2b	23.0	11.7	194.9	131.0
9	Nasopharynx	T2	N2 (bilateral)	160.5	100.1	878.7	543.5
10	Oropharynx: tonsil	T1	N2b	67.6	32.4	403.5	288.0

[*] AJCC, 6th Ed.

the second CT simulation image set to 34 Gy. For all adaptive plans, following the first 36 Gy planned to the initial PTV$_{50}$ based on the initial CT data set, the remaining 14 Gy planned to a revised PTV$_{50}$ and both conedown doses to PTV$_{64}$ and PTV$_{70}$ were planned to new PTVs devised using the second CT data set. The initial and subsequent CT data sets were fused together to allow for plan sums and composite DVHs to be generated.

IMRT and adaptive IMRT plans were designed with seven equally spaced beams every 50° beginning at 30° (30°, 80°, 130°, 180°, 230°, 280°, 330°) centered on each corresponding PTV (Fig. 1A). These beam angles corresponded to the class solution employed by our clinic for treating locally advanced SCCHN. For proton and adaptive proton plans, patients were planned with five

beams centered on PTV$_{50}$ and PTV$_{64}$, with beam angles individualized for each patient. For the final three fractions of proton therapy, patients were planned with an individualized two-field technique, with beams centered on PTV$_{70}$ (Fig. 1B–C). For photon plans, 6 MV photons were used, whereas the maximum clinical beam energy was 235 MeV for proton plans.

For optimization purposes, dose objectives were created for PTVs and OARs. All plans were optimized via Helios Inverse Treatment Planning (Varian Medical Systems) to minimize dose to critical structure by increasing constraints on OARs and OARs with margin (spinal cord, brainstem), while maintaining optimal PTV coverage and dose homogeneity throughout target volumes. Planning was performed to achieve maximum doses to the spinal cord
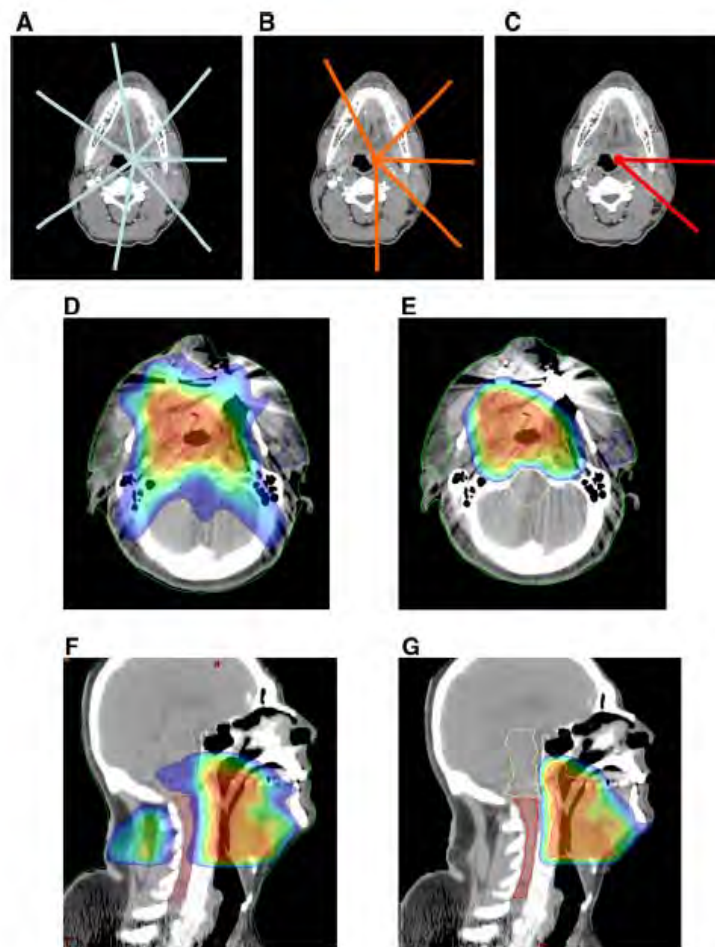
Fig. 1. Beam arrangements and treatment planning images. Representative beam arrangements used for (A) photon plans to treat PTV$_{70}$ with a seven-field technique, (B) proton plans to treat PTV$_{50}$ and PTV$_{60}$ with a five-field technique, and (C) proton plans to treat PTV$_{70}$ with a two-field technique. Beam angles for photon plans were equally spaced and centered on each corresponding PTV. Beam angles for proton plans were individualized for each patient to minimize dose to critical structures and maintain optimal PTV coverage and dose homogeneity throughout the target volumes. Representative treatment planning images for a patient with cT4N2cM0 stage IVA squamous cell carcinoma of the oropharynx (base of tongue) in axial planes for (D) IMRT and (E) proton therapy, and in sagittal planes for (F) IMRT and (G) proton therapy. Images depict treatment to PTV$_{70}$, the final treatment conedown targeting gross disease with margin. The same slices from the same initial CT data set were employed for Fig. 1D and E and Fig. 1F and G. Color coding: red = 100% to blue = 50% of 6 Gy in 2 Gy fractions.

less than 45 Gy, brainstem less than 54 Gy, and mandible no more than 1 cc to exceed 75 Gy, as well as mean doses to the parotid glands less than 26 Gy (or at least 50% of one gland less than 30 Gy) and glottic larynx less than 45 Gy. All plans were optimized to ensure 100% of the prescription dose covered $\geqslant 97\%$ of each PTV. DVHs of PTVs and OARs were generated for IMRT, adaptive IMRT, IMPT, and adaptive IMPT plans to compare doses to tumor volumes and normal structures.

Various methods were used to minimize bias in the present study. Ten consecutive patients who required re-planning were included in this study to minimize sampling bias. All contours were performed by a single radiation oncologist (CS) and approved by at least one additional radiation oncologist. A standard treatment planning optimization strategy was used for all photon and proton plans. Conformity indexes (see definition in Table 2) and DVHs were assessed to ensure comparable PTV coverage between plans to minimize any bias when comparing normal tissue dosimetry between plans. However, despite these measures, as with any retrospective study [22], it is possible that bias existed in the current study that may have favored a certain type of planning strategy. Furthermore, despite recontouring on and fusing the second CT data sets to the first CT data sets, as deformable registration was not employed and small changes were noted in normal tissue positioning on the second CT data sets following tumor response, a margin of error may exist in the dose accumulated between the initial and subsequent CTs.

Statistical analysis was performed using JMP 7.0 (SAS, Cary, NC). Because the population was not normally distributed, a non-parametric statistical hypothesis was utilized. The Wilcoxon Signed-rank test was used to evaluate the differences between pairwise comparisons. A two-tailed p-value was utilized and statistical significance was defined as $p \leqslant 0.050$.

Results

Patient statistics

The mean GTV volume from the initial CT image set obtained before concurrent chemoradiation was 76.1 cm^3 [range 23.0–173.0 cm^3] (Table 1). The mean GTV volume from the second CT image set decreased by 53.4% to 35.5 cm^3 [5.1–100.1 cm^3]. The corresponding mean PTV$_{70}$ volume decreased 39.7%, from 372.2 cm^3 [164.4–878.7 cm^3] to 224.4 cm^3 [77.8–543.5 cm^3]. No appreciable difference in tumor volume reduction was noted by tumor primary location.

Dose coverage

IMRT, adaptive IMRT, IMPT, and adaptive IMPT plans all provided acceptable target volume coverage, with no significant difference in coverage to PTV$_{70}$, PTV$_{64}$, or PTV$_{50}$ among the different plans (Table 2). In all cases, 100% of the prescription dose covered $\geqslant 97\%$ of each PTV, and no point dose within or outside PTVs was >114% of the prescribed dose (Fig. 1D–G). Overall, proton plans

and adaptive proton plans had superior conformity than either IMRT plans or adaptive IMRT plans, and they delivered less dose outside of target volumes, particularly among low to intermediate dose-volumes (Table 2).

IMRT versus adaptive IMRT

Compared with IMRT plans, adaptive IMRT significantly decreased the maximum point dose to the mandible ($p = 0.020$) and mean doses to the left parotid gland ($p < 0.002$) and glottic larynx ($p = 0.049$) (Table 3, Supplementary Table S1). The maximum dose to the brainstem was somewhat lower with adaptive plans, although this difference was not statistically significant ($p = 0.084$). There was no difference in the maximum dose to the spinal cord ($p = 0.770$) or mean dose to the right parotid gland ($p = 0.846$). When assessing the parotid glands relative to the site of primary disease for each patient, adaptive IMRT decreased the mean dose to the contralateral ($p = 0.049$) but not the ipsilateral parotid gland ($p = 0.160$) [Supplementary Fig. S1].

IMRT versus IMPT

Proton therapy significantly reduced the mean and maximum doses to most OARs examined. Compared with IMRT plans, IMPT reduced the maximum doses to the spinal cord ($p < 0.002$) and brainstem ($p < 0.002$), as well as the mean doses to the left ($p < 0.002$) and right ($p = 0.004$) parotid glands and larynx ($p < 0.002$). Both the ipsilateral ($p = 0.004$) and contralateral ($p < 0.002$) parotid glands showed significant sparing with proton therapy. Only the maximum dose to the mandible ($p = 0.275$) was not significantly reduced with proton therapy, although the mandible V60 ($p < 0.002$) and V70 ($p = 0.010$) were lower with IMPT (Fig. 1D–G).

Adaptive IMRT versus IMPT

When compared to adaptive IMRT, IMPT provided a significant dose reduction to all OARs other than the mandible ($p = 0.826$). Proton therapy reduced the maximum doses to the spinal cord ($p < 0.002$) and brainstem ($p < 0.002$), as well as the mean doses to the left ($p = 0.010$) and right ($p = 0.050$) parotid glands, ipsilateral ($p = 0.050$) and contralateral ($p = 0.010$) parotid glands, and larynx ($p < 0.002$).

IMRT versus adaptive IMPT

Adaptive IMPT significantly reduced the mean and maximum doses to all OARs examined. Compared with IMRT plans, adaptive IMPT reduced the maximum doses to the spinal cord ($p < 0.002$), brainstem ($p < 0.002$), and mandible (0.020), as well as the mean doses to the left ($p = 0.004$) and right ($p = 0.004$) parotid glands, ipsilateral ($p = 0.004$) and contralateral ($p = 0.004$) parotid glands, and larynx ($p < 0.002$).

Table 2
Comparison* of the mean dose to target volumes and conformity indexes* for IMRT, adaptive IMRT, IMPT, and adaptive IMPT.

	Volume of PTV receiving 100% of the prescribed dose			Conformity index		
	PTV$_{50}$	PTV$_{64}$	PTV$_{70}$	PTV$_{50}$	PTV$_{64}$	PTV$_{70}$
IMRT	99.9% (±0.2%)	99.1% (±0.3%)	98.6% (±0.7%)	1.97 (±0.48)	1.59 (±0.28)	1.49 (±0.26)
Adaptive IMRT	99.8% (±0.4%)	99.0% (±0.5%)	99.0% (±0.8%)	2.06 (±0.56)	1.53 (±0.39)	1.75 (±0.69)
IMPT	99.9% (±0.1%)	99.5% (±0.5%)	99.0% (±0.7%)	1.52 (±0.31)	1.30 (±0.18)	1.23 (±0.11)
Adaptive IMPT	99.9% (±0.1%)	99.5% (±0.5%)	99.4% (±0.7%)	1.64 (±0.38)	1.40 (±0.19)	1.54 (±0.46)

* Values listed for PTV volumes and conformity indexes are the mean values for the study population. The standard deviations for each comparison are listed in brackets.
* Conformity index was calculated as the ratio of the reference isodose–volume to the volume of each planning target volume being assessed, with the 95% isodose line of each PTV selected as the reference isodose–volume in accordance with ICRU 50 guidelines.

Table 3
Comparison of the average maximum or mean doses to normal tissues between IMRT, adaptive IMRT, IMPT, and adaptive IMPT.

	Spinal cord	Left parotid		Right parotid		Ipsilateral parotid		Contralateral parotid		Glottic larynx	Brainstem	Mandible		
	Max[†] (Gy)	Mean (Gy)	V20* (%)	Mean (Gy)	V20* (%)	Mean (Gy)	V20* (%)	Mean (Gy)	V20* (%)	Mean (Gy)	Max[†] (Gy)	Max[†] (Gy)	V60* (%)	V70* (%)
IMRT	42.1	37.8	60.4	32.0	55.5	43.1	68.4	26.8	47.5	45.4	44.8	75.1	34.2	15.0
Adaptive IMRT	41.7	32.8	54.0	31.6	54.8	39.0	63.6	25.3	45.2	41.8	42.2	73.0	25.3	6.7
IMPT	30.5	27.2	47.9	25.3	45.8	32.9	54.5	19.5	39.2	35.3	31.3	73.8	22.8	8.9
Adaptive IMPT	28.4	25.0	43.3	23.1	43.5	29.8	51.3	18.3	35.7	31.0	29.0	71.1	19.5	5.2

[†] Max = average maximum point dose.
* V20/60/70 = volume receiving 20/60/70 Gy.

Adaptive IMRT versus adaptive IMPT

When compared to adaptive IMRT, adaptive IMPT significantly reduced dose to all OARs examined. Adaptive IMPT reduced the maximum doses to the spinal cord ($p < 0.002$), brainstem ($p < 0.002$), and mandible ($p = 0.049$), as well as the mean doses to the left ($p = 0.020$) and right ($p = 0.010$) parotid glands, ipsilateral ($p = 0.010$) and contralateral ($p = 0.020$) parotid glands, and larynx ($p < 0.002$).

IMPT versus adaptive IMPT

When compared to IMPT, adaptive IMPT provided a further reduction in dose to several OARs. Adaptive IMPT reduced the maximum doses to the spinal cord ($p = 0.004$) and mandible ($p = 0.006$) and mean doses to the larynx ($p = 0.010$) and ipsilateral parotid gland ($p = 0.020$). Non-significantly lower mean doses to left ($p = 0.084$) and right ($p = 0.065$) parotid glands and maximum dose to the brainstem ($p = 0.106$) were also demonstrated with adaptive IMPT. There was no difference in mean dose to the contralateral parotid gland ($p = 0.160$).

Discussion

This study demonstrated that adaptive photon radiotherapy for locally advanced SCCHN can significantly decrease the maximum dose to the mandible and mean doses to the contralateral parotid gland and glottic larynx when compared with IMRT, while still maintaining optimal tumor coverage. Proton radiotherapy, however, allowed further benefits over standard IMRT and adaptive IMRT plans by decreasing the maximum doses to the spinal cord and brainstem and mean doses to the bilateral parotid glands and larynx, while still delivering optimal tumor coverage. Adaptive proton radiotherapy further reduced doses received by the spinal cord, ipsilateral parotid gland, glottic larynx, and mandible compared with non-adaptive proton plans, although this reduction was less clinically significant.

High dose homogeneity and target volume coverage were achieved despite a diverse patient population with varying primary tumor locations and extents of nodal involvement. Importantly, no significant difference in PTV coverage was demonstrated between all plans, thus minimizing bias when comparing normal tissue dosimetry. However, the sensitivity of proton plans to anatomic and target volume changes was generally greater than for photon plans. Plans with fewer beams and with beams in the direction of shrinkage of target volumes were most sensitive. For target volumes in this study that exhibited significant shrinkage following a partial course of chemoradiation prior to repeat CT simulation for adaptive radiotherapy, the actual doses delivered to critical structures just distal to shrinking target volumes varied from the doses expected based on the initial CT data sets more with protons than photons.

Adaptive radiotherapy

Supporting a potential benefit of adaptive radiotherapy in our study, when contours from the initial CT image sets were compared with those from the re-planning CT image sets, a significant reduction in mean GTV was demonstrated that was similar to tumor reductions reported in previous studies with an average reduction in GTV noted between 69% and 73% [11–15]. Several patients in this study underwent re-planning early in the course of their radiotherapy and, therefore, may have had more GTV reduction if re-planning was performed later in therapy.

Preliminary research on adaptive radiotherapy has demonstrated potential improvements in radiation treatment delivery which was also noted in our study. By evaluating serial CT images throughout radiotherapy, Barker et al. reported significant changes in size and positions of target volumes and OARs, suggesting dosimetric underdosing of PTVs or overdosing of parotid glands may occur if such changes are not accounted for with re-planning [13]. Another study demonstrated lack of re-planning decreased dose coverage of originally planned PTVs in 92% of patients and increased the maximum doses delivered to the spinal cord in 100% and brainstem in 85% [14]. Another study showed the dose delivered to parotid glands can be 5–7 Gy higher than what was planned at the time of initial simulation in 45% of patients [18]. Although small absolute differences in dose delivered to such organs as the mandible and spinal cord may be less clinically significant, such an increase in dose to parotid glands is not trivial. Parotid glands exhibit a steep dose–response relationship, with functioning impaired after a mean dose as low as 10 Gy and grade 4 xerostomia occurring in 70% of patients receiving mean doses greater than 26 Gy [4,5].

Although attempt was made to maintain the mean bilateral parotid gland dose under 26 Gy, PTVs and ipsilateral parotid glands overlapped in most patients. As the priority of sparing the parotid glands was lower than that for achieving the prescribed PTV coverage, few patients had mean ipsilateral parotid gland doses below 26 Gy, and the reduction in ipsilateral parotid gland mean dose from 43.1 Gy with IMRT to 39.0 Gy with adaptive IMRT in this study was not significant ($p = 0.160$). The contralateral parotid gland mean dose was lower with adaptive IMRT (25.3 Gy vs. 26.8 Gy, $p = 0.049$), which is in line with the magnitude of parotid gland dose reduction of up to 10% reported in prior studies assessing adaptive photon radiotherapy [12]. The mean doses to the ipsilateral and contralateral parotid glands with IMPT of 32.9 Gy and 19.5 Gy, respectively, and adaptive IMPT of 29.8 Gy and 18.3 Gy, suggest an even larger potential clinical benefit in preservation of parotid gland functioning with protons.

Several concerns exist with adaptive treatment planning. Since adaptive radiotherapy is labor intensive, deformable image registration, automated target delineation, and higher computational power likely will become more important. Additionally, the timing of when to re-plan during chemoradiation is not well-defined. While some practitioners utilize dose thresholds to perform re-simulation, others use anatomical thresholds such as GTV reduction. In this study, patients underwent a single repeat simulation. As has been demonstrated in prior studies [12], a greater benefit with adaptive radiotherapy might have been seen if re-planning occurred more frequently during radiotherapy.

Controversy also exists regarding local control when treating smaller target volumes based on re-planning CT data [23–24]. With tumor responses after both induction chemotherapy and a partial course of concurrent chemoradiation, concern exists that substantial numbers of tumor cells may remain in tissue volumes previously occupied by gross disease that are below the threshold of radiographic detection [23–25]. To evaluate these issues, there are currently three pilot trials lead by U.T.M.D. Anderson Cancer Center, Washington University School of Medicine, and University Hospital Ghent (Belgium) that aim to assess adaptive radiotherapy for the treatment of SCCHN [26]. A recent consensus conference assessing induction chemotherapy recommended treating patients based on prechemotherapy target volumes, regardless of tumor response, to avoid risking marginal recurrences. While no such consensus exists for adaptive radiotherapy, the multidisciplinary team concluded that "many of the same issues and recommendations will apply to adaptive RT..." [27].

Proton radiotherapy

Particle radiotherapy has also been shown in preliminary reports and modeling studies to improve tumor dose distribution and decrease normal tissue toxicity in the treatment of many cancers [28–30] SCCHN compared with photon therapy [31–36]. Cozzi et al. performed a treatment planning comparison of mixed photon-electron, 3D conformal photon, IMRT, and proton therapy (passively scattered and spot scanned) for patients with advanced SCCHN. Proton plans provided improved dose homogeneity and delivered the least dose to the spinal cord and parotid glands [31]. Investigators from Loma Linda University Medical Center treated 29 patients with stage II-IV oropharyngeal cancers using an accelerated fractionation schedule with a combination of photons and protons to 75.9CGE in 45 fractions. Their reported 84% locoregional control and 65% disease-free survival rates at five years compare very favorably to historical controls without increasing treatment toxicity [20]. Another dosimetric study of hypopharyngeal patients similarly demonstrated lower doses to non-target tissues with protons than photon IMRT [32].

The dosimetric advantages of proton radiotherapy demonstrated in this study might improve the therapeutic ratio for patients with locally advanced SCCHN. Based on historical dose–response relationships, with significantly lower radiation doses to several OARs demonstrated in this study, patients treated with protons may have improved quality of life and reduced rates of xerostomia, dental problems, voice changes, weight loss, swallowing dysfunction, mucositis, nausea, and other radiation-induced toxicities. Longitudinal studies examining normal tissue toxicities from photon and proton radiotherapy are needed to confirm the clinical significance of our findings.

In this study, although adaptive photon radiotherapy reduced dose to several OARs compared with standard IMRT, non-adaptive proton plans were dosimetrically superior to all photon plans despite planning to treat larger target volumes than were planned with adaptive photon radiotherapy. To date, no previous data exist assessing adaptive proton therapy for SCCHN, and adaptive proton therapy has only previously been evaluated in a single dosimetric analysis of patients with non-small cell lung cancer [37]. Although adaptive proton plans in this study, compared with IMPT, significantly lowered the radiation doses to the spinal cord, ipsilateral parotid gland, glottic larynx, and mandible, this dose reduction was less clinically significant and the magnitude of this reduction compared with IMPT plans was much less than the reduction in dose achieved by non-adaptive proton plans over IMRT and adaptive IMRT photon plans. With concerns regarding adaptive treatment strategies and the limited resources of the few proton therapy centers worldwide at this time, it is unlikely that adaptive proton therapy will become a clinically utilized modality for treating patients with SCCHN solely in an attempt to minimize the volumes of targets treated, particularly in light of the significant benefit demonstrated in this study with standard proton therapy over all photons plans. However, as proton plans are more sensitive than photon plans to interfractional changes in tumor volumes and patient anatomy, care must be taken to account for these changes or otherwise ensure accuracy of the beam range when using protons to treat SCCHN. The role of adaptive proton radiotherapy may best be answered in the context of a clinical trial with serially planning repeat CT simulations.

The possible advantages to proton therapy are being assessed in three phase II trials for SCCHN. Researchers at University of Florida and Massachusetts General Hospital are investigating proton therapy for the treatment of nasopharygeal carcinomas, and investigators at University of Florida are assessing proton therapy to treat oropharynx cancers. Each of these trials is enrolling patients with considerably less advanced disease than was included in the present study [26].

Standard vs. adaptive radiotherapy vs. proton radiotherapy

This study assessed a population of SCCHN patients with a high disease burden, all of whom had stage IV non-metastatic disease. The advanced nature of their diseases may have allowed for a greater advantage for adaptive plans over non-adaptive plans following an initial tumor response to chemoradiation. However, an even greater benefit to adaptive radiotherapy may have been demonstrated if the study population had been limited only to patients with clinically significant responses to initial partial courses of chemoradiation. Additionally, neither photon technique could maintain optimal PTV coverage while sparing OARs to the same extent as either proton technique. It is possible that the dosimetric advantage to OARs with protons demonstrated in this study would be even greater in patients with less advanced disease. As such, the study results may not be applicable to patients with early-stage SCCHN and may underestimate the potential benefit of proton therapy over photon therapy. However, it is also possible that the spot scanning proton techniques utilized in this study allowed for a greater benefit with proton therapy than would be seen in centers treating SCCHN patients with scattered beam delivery.

Conclusion

For patients with locally advanced SCCHN, adaptive photon radiotherapy offers some benefit over standard IMRT in reducing dose to several regional OARs. Proton therapy has a more favorable dosimetric profile than either standard IMRT or adaptive IMRT and significantly lower radiation doses to the spinal cord, bilateral parotid glands, glottic larynx, and brainstem. As such, the dosimetric advantage demonstrated with non-adaptive proton therapy in this study may obviate the need for adaptive treatment planning for patients with SCCHN. With decreased doses delivered to OARs, patients treated with proton therapy may benefit from fewer

radiation-induced side effects. Proton therapy should be considered for patients with locally advanced SCCHN to decrease normal tissue toxicity while still providing optimal tumor coverage.

Conflict of interest statement

None.

Appendix Supplementary. data

Supplementary data associated with this article can be found, in the online version, at doi:10.1016/j.radonc.2011.05.028.

References

[1] Calais G, Alfonsi M, Bardet E, et al. Randomized trial of radiation therapy versus concomitant chemotherapy and radiation therapy for advanced-stage oropharynx carcinoma. J Natl Cancer Inst 1999;91:2081-6.
[2] Fung K, Lyden TH, Lee J, et al. Voice and swallowing outcomes of an organ-preservation trial for advanced laryngeal cancer. Int J Radiat Oncol Biol Phys 2005;63:1395-9.
[3] Bussels B, Maes A, Flamen P, et al. Dose-response relationships within the parotid gland after radiotherapy for head and neck cancer. Radiother Oncol 2004;73:297-306.
[4] Li Y, Taylor JM, Ten Haken RK, Eisbruch A. The impact of dose on parotid salivary recovery in head and neck cancer patients treated with radiation therapy. Int J Radiat Oncol Biol Phys 2007;67:660-9.
[5] Blanco AI, Chao KS, El Naqa I, et al. Dose-volume modeling of salivary function in patients with head-and-neck cancer receiving radiotherapy. Int J Radiat Oncol Biol Phys 2005;62:1055-69.
[6] Dornfeld K, Simmons JR, Karnell L, et al. Radiation doses to structures within and adjacent to the larynx are correlated with long-term diet- and speech-related quality of life. Int J Radiat Oncol Biol Phys 2007;68:750-7.
[7] Rosenthal DI, Chambers MS, Fuller CD, et al. Beam path toxicities to non-target structures during intensity-modulated radiation therapy for head and neck cancer. Int J Radiat Oncol Biol Phys 2008;72:747-55.
[8] Melzner WJ, Lotter M, Sauer R, Strnad V. Quality of interstitial PDR-brachytherapy-implants of head-and-neck-cancers: predictive factors for local control and late toxicity? Radiother Oncol 2007;82:167-73.
[9] Corvò R. Evidence-based radiation oncology in head and neck squamous cell carcinoma. Radiother Oncol 2007;85:156-70.
[10] Chencharick JD, Mossman KL. Nutritional consequences of the radiotherapy of head and neck cancer. Cancer 1983;51:811-5.
[11] Fang FM, Tsai WL, Go SF, et al. Implications of quantitative tumor and nodal regression rates for nasopharyngeal carcinomas after 45 Gy of radiotherapy. Int J Radiat Oncol Biol Phys 2001;50:961-9.
[12] Wu Q, Chi Y, Chen PY, Krauss DJ, Yan D, Martinez A. Adaptive replanning strategies accounting for shrinkage in head and neck IMRT. Int J Radiat Oncol Biol Phys 2009;75:924-32.
[13] Barker Jr JL, Garden AS, Ang KK, et al. Quantification of volumetric and geometric changes occurring during fractionated radiotherapy for head-and-neck cancer using an integrated CT/linear accelerator system. Int J Radiat Oncol Biol Phys 2004;59:960-70.

[14] Hansen EK, Bucci MK, Quivey JM, Weinberg V, Xia P. Repeat CT imaging and replanning during the course of IMRT for head-and-neck cancer. Int J Radiat Oncol Biol Phys 2006;64:355-62.
[15] Castadot P, Geets X, Lee JA, Christian N, Grégoire V. Assessment by a deformable registration method of the volumetric and positional changes of target volumes and organs at risk in pharyngo-laryngeal tumors treated with concomitant chemo-radiation. Radiother Oncol 2010;95:209-17.
[16] Broggi S, Fiorino C, Dell'Oca I, et al. A two-variable linear model of parotid shrinkage during IMRT for head and neck cancer. Radiother Oncol 2010;94:206-12.
[17] Lee C, Langen KM, Lu W, et al. Evaluation of geometric changes of parotid glands during head and neck cancer radiotherapy using daily MVCT and automatic deformable registration. Radiother Oncol 2008;89:81-8.
[18] O'Daniel JC, Garden AS, Schwartz DL, et al. Parotid gland dose in intensity-modulated radiotherapy for head and neck cancer: is what you plan what you get? Int J Radiat Oncol Biol Phys 2007;69:1290-6.
[19] Gerweck LE, Kozin SV. Relative biological effectiveness of proton beams in clinical therapy. Radiother Oncol 1999;50:135-42.
[20] Slater JD, Yonemoto LT, Mantik DW, et al. Proton radiation for treatment of cancer of the oropharynx: early experience at Loma Linda University Medical Center using a concomitant boost technique. Int J Radiat Oncol Biol Phys 2005;62:494-500.
[21] Moyers MF, Miller DW, Bush DA, Slater JD. Methodologies and tools for proton beam design for lung tumors. Int J Radiat Oncol Biol Phys 2001;49:1429-38.
[22] Brown ML, Gersh BJ, Holmes DR, Bailey KR, Sundt 3rd TM. From randomized trials to registry studies: translating data into clinical information. Nat Clin Pract Cardiovasc Med 2008;5:613-20.
[23] Eisbruch A, Gregoire V. Balancing risk and reward in target delineation for highly conformal radiotherapy in head and neck cancer. Semin Radiat Oncol 2009;19:43-52.
[24] Orban de Xivry J, Castadot P, Janssens G, et al. Evaluation of the radiobiological impact of anatomic modifications during radiation therapy for head and neck cancer: can we simply summate the dose? Radiother Oncol 2010;96:131-8.
[25] Klug C, Keszthelyi D, Ploder O, et al. Neoadjuvant radiochemotherapy of oral cavity and oropharyngeal cancer: evaluation of tumor response by CT differs from histopathologic response assessment in a significant fraction of patients. Head Neck 2004;26:224-31.
[26] ClinicalTrials.gov, "Search for Clinical Trials," 11 May 2010, <http://clinicaltrials.gov/> [11.05.2010].
[27] Salama JK, Haddad RI, Kies MS, et al. Clinical practice guidance for radiotherapy planning after induction chemotherapy in locoregionally advanced head-and-neck cancer. Int J Radiat Oncol Biol Phys 2009;75:725-33.
[28] Schwarz M, Pierelli A, Fiorino C, et al. Helical tomotherapy and intensity modulated proton therapy in the treatment of early stage prostate cancer: a treatment planning comparison. Radiother Oncol 2011;98:74-80.
[29] Hoppe BS, Huh S, Flampouri S, et al. Double-scattered proton-based stereotactic body radiotherapy for stage I lung cancer: A dosimetric comparison with photon-based stereotactic body radiotherapy. Radiother Oncol 2010;97:425-30.
[30] Toscas JI, Linero D, Rubio I, et al. Boosting the tumor bed from deep-seated tumors in early-stage breast cancer: A planning study between electron, photon, and proton beams. Radiother Oncol 2010;96:192-8.
[31] Cozzi L, Fogliata A, Lomax A, Bolsi A. A treatment planning comparison of 3D conformal therapy, intensity modulated photon therapy and proton therapy for treatment of advanced head and neck tumours. Radiother Oncol 2001;61:287-97.
[32] Johansson J, Blomquist E, Montelius A, Isacsson U, Glimelius B. Potential outcomes of modalities and techniques in radiotherapy for patients with hypopharyngeal carcinoma. Radiother Oncol 2004;72:129-38.
[33] Brown AP, Urie MM, Chisin R, Suit HD. Proton therapy for carcinoma of the nasopharynx: a study in comparative treatment planning. Int J Radiat Oncol Biol Phys 1989;16:1607-14.
[34] Taheri-Kadkhoda Z, Björk-Eriksson T, Nill S, et al. Intensity-modulated radiotherapy of nasopharyngeal carcinoma: a comparative treatment planning study of photons, protons. Radiother Oncol 2008;3:4.
[35] Noël G, Boisserie G, Dessard-Diana B, et al. Comparison with dose-volume histograms of two conformal irradiation techniques used for the treatment of T2N0M0 nasopharyngeal cancer, one with association of photons and protons and another with photons alone. Cancer Radiother 2002;6:337-48.
[36] Steneker M, Lomax A, Schneider U. Intensity modulated photon and proton therapy for the treatment of head and neck tumors. Radiother Oncol 2006;80:263-7.
[37] Hui Z, Zhang X, Starkschall G, et al. Effects of interfractional motion and anatomic changes on proton therapy dose distribution in lung cancer. Int J Radiat Oncol Biol Phys 2008;72:1385-95.

131

ELSEVIER

CLINICAL INVESTIGATION   **Genitourinary Cancer**

PREDICTED RATES OF SECONDARY MALIGNANCIES FROM PROTON VERSUS PHOTON RADIATION THERAPY FOR STAGE I SEMINOMA

Charles B. Simone, II, M.D.,*† Kevin Kramer, Ph.D.,‡ William P. O'Meara, M.D.,¶
Justin E. Bekelman, M.D.,* Arnaud Belard, M.B.A.,‡ James McDonough, Ph.D.,*
and John O'Connell, M.D.§

*Department of Radiation Oncology, Hospital of the University of Pennsylvania, Philadelphia, Pennsylvania; †Radiation Oncology
Branch, National Cancer Institute, National Institutes of Health, Bethesda, Maryland; ‡Henry M. Jackson Foundation for the
Advancement of Military Medicine, Rockville, Maryland; ¶Division of Radiation Oncology, National Naval Medical Center, Bethesda,
Maryland; and §Radiation Oncology Service, Walter Reed Army Medical Center, Washington, DC

Purpose: Photon radiotherapy has been the standard adjuvant treatment for stage I seminoma. Single-dose carboplatin therapy and observation have emerged as alternative options due to concerns for acute toxicities and secondary malignancies from radiation. In this institutional review board-approved study, we compared photon and proton radiotherapy for stage I seminoma and the predicted rates of excess secondary malignancies for both treatment modalities.

Methods and Material: Computed tomography images from 10 consecutive patients with stage I seminoma were used to quantify dosimetric differences between photon and proton therapies. Structures reported to be at increased risk for secondary malignancies and in-field critical structures were contoured. Reported models of organ-specific radiation-induced cancer incidence rates based on organ equivalent dose were used to determine the excess absolute risk of secondary malignancies. Calculated values were compared with tumor registry reports of excess secondary malignancies among testicular cancer survivors.

Results: Photon and proton plans provided comparable target volume coverage. Proton plans delivered significantly lower mean doses to all examined normal tissues, except for the kidneys. The greatest absolute reduction in mean dose was observed for the stomach (119 cGy for proton plans vs. 768 cGy for photon plans; $p <$ 0.0001). Significantly more excess secondary cancers per 10,000 patients/year were predicted for photon radiation than for proton radiation to the stomach (4.11; 95% confidence interval [CI], 3.22–5.01), large bowel (0.81; 95% CI, 0.39–1.01), and bladder (0.03; 95% CI, 0.01–0.58), while no difference was demonstrated for radiation to the pancreas (0.02; 95% CI, −0.01–0.06).

Conclusions: For patients with stage I seminoma, proton radiation therapy reduced the predicted secondary cancer risk compared with photon therapy. We predict a reduction of one additional secondary cancer for every 50 patients with a life expectancy of 40 years from the time of radiation treatment with protons instead of photons. Proton radiation therapy also allowed significant sparing of most critical structures examined and warrants further study for patients with seminoma, to decrease radiation-induced toxicity.   © 2012 Elsevier Inc.

Seminoma, Secondary malignancies, Proton therapy, Dosimetry, Para-aortic.

INTRODUCTION

Testicular cancers are the most common solid malignancies among men 20 to 35 years old. In 2009, there were 8,400 new cases of testicular malignancies projected in the Unites States, with 380 deaths (1). Most of these malignancies represent primary germ cell tumors, with pure seminoma comprising 60% of these tumors. Approximately 80% of patients diagnosed with seminoma have stage I disease (2).

The standard initial treatment for stage I seminoma is radical inguinal orchiectomy. Since the mid-20th Century, photon external beam radiotherapy has been the standard adjuvant treatment. Patients receiving radiotherapy achieve cause-specific survival rates approaching 100% and long-term relapse-free survival rates exceeding 95%, with virtually no relapses within the radiation portal (3, 4).

However, significant treatment-related morbidities following radiotherapy have been reported. Although acute toxicities are generally mild and self-limiting, patients are at an increased risk for late gonadal toxicity (5) and cardiovascular disease (6, 7), particularly those patients receiving prophylactic mediastinal irradiation (6). Studies have also revealed increases in contralateral testicular germ cell tumors in the first decade following radiotherapy (8, 9) and increases in nongerm cell malignancies after 10 to 35 years (6, 7, 10–12). In the study assessing the largest population of seminoma patients for the development of secondary cancers, 40,576 patients with first primary cancers of the testis between 1943 and 2001, who survived at least 1 year, were evaluated (10). Patients treated with adjuvant radiotherapy alone had a significantly increased risk of solid cancers (relative risk [RR] = 2.0; 95% confidence interval [CI], 1.9–2.2), with the highest risk in patients treated at younger ages. Among organs in the standard para-aortic field radiation portal, secondary cancer rates were elevated for the stomach (RR = 4.1, 95% CI, 3.2–5.2), large bowel (RR = 1.9; 95% CI, 1.5–2.5), pancreas (RR = 3.8; 95% CI, 2.7–5.0), and bladder (RR = 2.7; 95% CI, 2.1–3.3). These risks were slightly higher for patients with seminoma than for patients with nonseminoma malignancies. As seminoma largely affects younger patients and cure rates are excellent, second primary cancers are a leading cause of death among testicular cancer survivors (6, 7, 12).

Attempting to decrease radiation-associated treatment morbidities and secondary malignancies, studies have investigated reducing the adjuvant radiotherapy dose and treatment volume. The United Kingdom Medical Research Council (MRC) randomized 625 patients with stage I seminoma to receive a 20-Gy or 30-Gy dose in 200-cGy fractions following orchiectomy. Rates of acute toxicities were lower among patients receiving 20 Gy, with no difference in relapse-free survival or overall survival (3). With the recognition that prophylactic mediastinal irradiation increases cardiac mortality (6), treatment to the mediastinum was largely abandoned by the mid-1980s. Following the Royal Marsden Hospital report in which no differences in relapse patterns were found for patients with scrotal violations and following the International Consensus Conference in Leeds in 1989, radiotherapy to the ipsilateral groin and scrotum is typically avoided (13). Following an MRC randomized trial of 478 patients with stage I seminoma that demonstrated no improvement in overall survival or relapse-free survival in those patients who received treatment to the ipsilateral pelvis, radiotherapy to the para-aortic region alone has become an acceptable target volume for patients with undisturbed lymphatic drainage (4).

Despite reductions in radiation doses and fields, concerns for late toxicities and secondary malignancies persist. Proton therapy may provide equivalent rates of disease control while improving the toxicity profile of photon therapy. Protons allow energy deposition at a specific depth, known as the Bragg peak, with rapid energy falloff beyond that point

(14). Therefore, protons can allow normal tissues distal to the target volume to be spared.

To date, there are no published data directly comparing different types of ionizing radiotherapy for treatment of stage I seminoma, and no data exist that predict the risk of secondary malignancies from proton therapy in this patient population. In this study, we compared dose-volume histograms (DVHs) of target volumes and normal tissue structures in photon-based versus proton-based plans in patients with stage I seminoma, and we determined the excess absolute risk (EAR) of secondary malignancies for photon versus proton plans.

METHODS AND MATERIALS

Ten consecutive patients with stage I seminoma treated with radiotherapy at Walter Reed Army Medical Center (WRAMC), who had computed tomography (CT) simulation images that included the entire bladder, were assessed in the present study. This study was approved by the WRAMC institutional review board. All patients underwent radical orchiectomy and received adjuvant fractionated two-dimensional (2D) radiotherapy with megavoltage photons to the para-aortic lymph node region from June 2006 to September 2008. Their CT images were used to quantify and compare dosimetric differences between photon and proton radiotherapy. CT acquisition data included slice thicknesses of 3 mm. CT images were imported into a commercial treatment planning system (Eclipse; Varian Medical Systems, Palo Alto, CA) to define target and nontarget structures.

Planning target volumes (PTVs) and adjacent organs at risk (OARs) were delineated on simulation CT images. Organs in the treatment field previously reported to be at increased risk for developing secondary malignancies (10), including bladder, stomach, pancreas, and large bowel, were contoured. In-field critical structures, including liver and kidneys, were also contoured. All contouring was performed by a single radiation oncologist (C.S.) and reviewed by two additional radiation oncologists (J.O'C. and W.O.). Target and nontarget structure sets for a given patient CT image set were held constant for all treatment plans.

Two plans were generated for each patient (n = 20 plans). For photon plans, patients were treated with an anteroposterior–posteroanterior (AP–PA) direction technique, whereas only a PA field was used for proton plans. For photon plans, patients were treated with a standard 2D rectangular treatment field, with field borders defined by the T10–T11 intervertebral space cranially, the L5–S1 intervertebral space caudally, and 2.0 cm laterally beyond the lateral edge of the vertebral bodies, bilaterally.

Because all patients had node-negative disease, no gross tumor volume was used. For the proton therapy para-aortic nodal clinical target volume (CTV_{proton}), defined as regions of potential microscopic disease, the aorta and common iliac vessels from the mid-T11 vertebral body cranially to the caudal third of the L5 vertebral body caudally were contoured together as a single structure. These vessels served as surrogates for para-aortic lymph node positioning and represented the region at risk for para-aortic lymph node metastasis. In patients with bifurcation of the aorta above the caudal third of L5, contours from both the right and the left iliac branches were included. The cranial and caudal extents of vessel contours were derived to allow the cranial and caudal extents of irradiation volumes to be equal for photon and proton plans. A radial expansion of 1.3

133

cm was added to this structure to include the CTV$_{proton}$. Bone was excluded from CTV$_{proton}$.

To account for set-up variation and organ and patient motions, a radial expansion of 0.7 cm was added to the CTV$_{proton}$ to define the PTV$_{proton}$. To account for proton beam properties and range uncertainties, based on the application of Moyer's formula to the average range of values of the study population, proton beam range compensators were designed to provide 0.6-cm proximal and 0.9-cm distal margins relative to the PTV$_{proton}$, and blocking was designed to create a 1.3-cm lateral margin relative to the PTV$_{proton}$.

Plans were calculated to deliver 25.5 Gy with photons or 25.5 cobalt Gray equivalents with protons over 17 fractions, with proton doses corrected with the accepted relative biologic effectiveness value of 1.1 (15). All plans were optimized to provide optimal target volume coverage and dose homogeneity throughout the target volumes. DVHs of target volumes and OARs were generated to compare doses to tumor volumes and normal structures.

Previously reported models of organ-specific radiation-induced cancer incidence rates based on organ equivalent dose (OED) were used to determine the EAR of secondary malignancies for photon and proton plans. OED is a tool used to describe radiation-induced malignancies for nonuniform dose distributions. The organ-specific cancer incidence rate was calculated according to the equation, $I^{org} = I_o^{org} D e^{-\alpha org^D}$, where I_o^{org} is the organ-specific cancer incidence rate for a low dose (EAR per 10,000 patients/year/Gy), D is the total dose administered, e is the base of the natural logarithm, and α_{org} is an organ-specific cell sterilization parameter. The OED for radiation-induced cancer was calculated according to

$$OED_{org} = \frac{1}{N} \sum_{i=1}^{N} D_i e^{-\alpha org^D i}$$

where the sum is taken over N dose calculation points. This approach has been previously described in detail by Schneider et al. (16–18). Calculated predicted values for secondary malignancies were compared with tumor registry population-based reports of the EAR of secondary solid cancers among testicular cancer survivors (10).

Statistical analysis was performed using Microsoft Excel for Windows (Microsoft Office Excel 2003 version). A paired t test was used to evaluate differences between pairwise comparisons. A two-tailed p value was used, with statistical significance defined as a p value of ≤ 0.05.

RESULTS

Among the study population, the mean age was 31 years old (range, 22–48 years) (Table 1). Patients had stage pT1 (8 patients) or pT2 (2 patients) disease (American Joint Committee on Cancer. Testis. In AJCC Cancer Staging Manuel, Seventh Edition. Chicago, Il: Springer; 2010, pp. 469-78.). Seven patients had right-sided primary testicular seminomas, whereas 3 patients had left-sided tumors.

All photon and proton plans provided acceptable and comparable target volume coverage. Although dose distributions for proton plans were typically more homogenous throughout the target volumes than photon plans, this difference did not appear to be clinically significant. Furthermore, no target or nontarget volume received >114% of the prescribed dose in any photon or proton plan.

Table 1. Patient characteristics

Patient number	Patient age (years)	T stage*	Side of primary tumor
1	31	pT1	Right
2	35	pT2	Left
3	34	pT1	Right
4	31	pT1	Right
5	25	pT1	Left
6	28	pT1	Left
7	22	pT1	Right
8	48	pT1	Right
9	23	pT2	Right
10	28	pT1	Right

* American Joint Committee on Cancer.

Overall, proton plans had superior dose conformality, with significant sparing of most normal tissues examined (Fig. 1). Among OARs examined, the largest absolute difference in mean dose between proton and photon plans was observed for the stomach (Table 2). Compared with photon radiation, proton radiation significantly reduced the mean dose to the stomach (119 cGy vs. 768 cGy, respectively; $p < 0.0001$) (Fig. 2). Protons also achieved respective significant reductions in mean doses to the pancreas (1,697 cGy vs. 1,991 cGy; $p = 0.0002$), large bowel (352 cGy vs. 651 cGy; $p = 0.0015$), and liver (33 cGy vs. 313 cGy; $p = 0.0006$). The average maximum point dose to the large bowel was also lower with protons (2,618 cGy vs. 2,732 cGy; $p = 0.0096$). The maximum doses to the liver (2,141 cGy vs. 2,591 cGy; $p = 0.0689$) and stomach (2,147 cGy vs. 2,678 cGy; $p = 0.0791$) trended lower with protons, while no difference was observed for the pancreas (2,634 cGy vs. 2,657 cGy; $p = 0.4072$). Both the mean (0 cGy vs. 1 cGy; $p = 0.0304$) and the maximum (11 cGy vs. 51 cGy; $p = 0.0071$) doses to the bladder were lower with proton therapy, although the differences between these doses were not clinically significant. There were no differences in mean or maximum doses received by the kidneys between the two treatment modalities.

Previously reported tumor registry population-based studies of EAR of second solid cancers revealed that for patients diagnosed with seminoma at age 35, the cumulative risk of solid cancer 40 years later was 36%, compared with 23% for the general population (10). From among the 9,551 testicular cancer 10-year survivors reported by cancer registries from Denmark, Finland, and Norway and the National Cancer Institute's Surveillance, Epidemiology, and End Results Program (10), we estimated 8,986 patients received radiotherapy alone based on ratios of relative risks and reported numbers of second solid tumors for patients treated with radiotherapy alone, chemotherapy alone, and radiotherapy and chemotherapy. Using models of organ-specific radiation-induced cancer incidence rates to determine the EAR of secondary malignancies, we predict 6.94 excess bladder, large bowel, pancreas, and stomach secondary malignancies per 10,000 patients/year from photon radiotherapy to the para-aortic region (Table 3). Based on this calculation, for a population of 10,000 patients followed for 40 years after photon
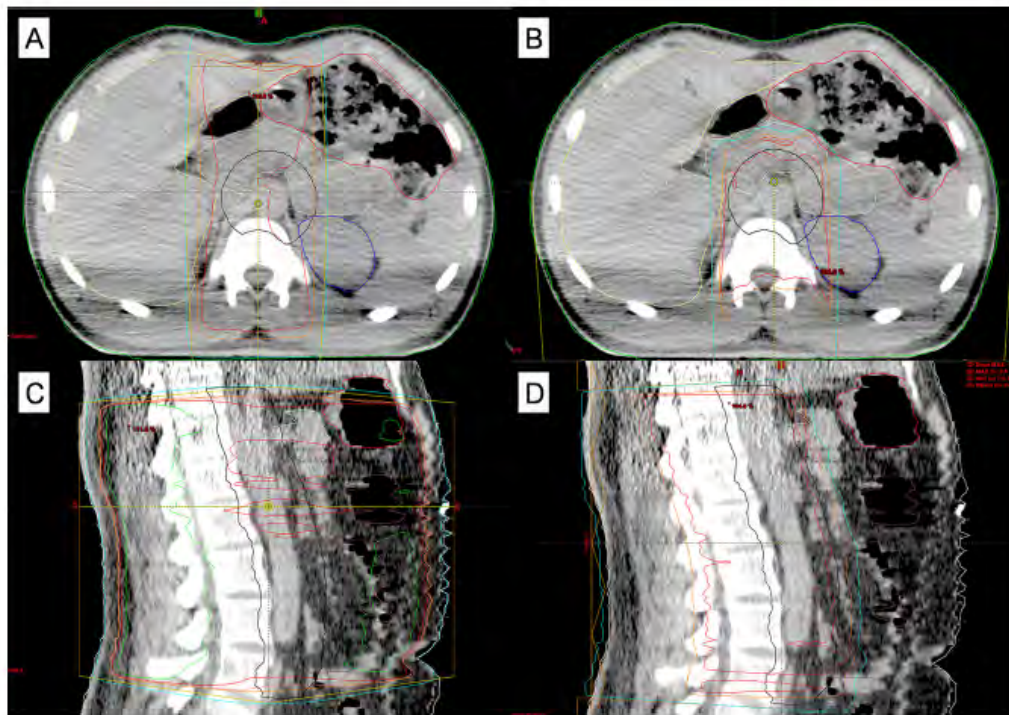
Fig. 1. Representative treatment planning images in axial planes for (A) photon therapy and (B) proton therapy, as well as sagittal planes for (C) photon therapy and (D) proton therapy.

therapy, we predict 278 radiation-induced in-field excess solid secondary malignancies. For a population of 8,986 patients, therefore, we predict 249 such secondary malignancies. This prediction compares very favorably with the 246 in-field excess solid secondary malignancies reported among the actual 8,986-patient cohort receiving photon radiotherapy described by Travis et al. (10).

Significantly more excess secondary malignancies per 10,000 patients/year were predicted with photon than proton therapy. When assessing OARs in the treatment field previously reported to be at increased risk for developing secondary malignancies, respectively higher rates of secondary cancers were predicted with photons than with protons for the stomach (5.21 vs. 1.10; 95% CI, 3.22–5.01), large bowel (1.12 vs. 0.31; 95% CI, 0.39–1.01), and bladder (0.03 vs. 0.00; 95% CI, 0.01–0.58), whereas no respective differences

were predicted for the pancreas (0.58 vs. 0.56; 95% CI, −0.01 to 0.06). In total, we predicted 4.97 (95% CI, 3.99–5.97) excess secondary malignancies per 10,000 patients/year from photon therapy compared with proton therapy. For patients with a life expectancy of 40 years from the time of radiotherapy treated with photons instead of protons, 198.80 excess secondary malignancies per 10,000 patients are predicted. Therefore, approximately one excess secondary malignancy per 50 patients would be avoided by treating with protons instead of photons.

DISCUSSION

This study demonstrated that adjuvant proton radiotherapy, compared with photon radiotherapy, significantly reduced the predicted secondary cancer risk for patients with

Table 2. Comparison of photon and proton doses to normal tissues

Dose	Bladder		Large bowel		Liver		Pancreas		Stomach	
	Mean	Max*	Mean	Max	Mean	Max	Mean	Max	Mean	Max
Photon	1	51	651	2732	313	2591	1991	2657	768	2678
Proton	0	11	352	2618	33	2141	1697	2634	119	2147
p value	0.0304	0.0071	0.0015	0.0096	0.0006	0.0689	0.0002	0.4072	<0.0001	0.0791

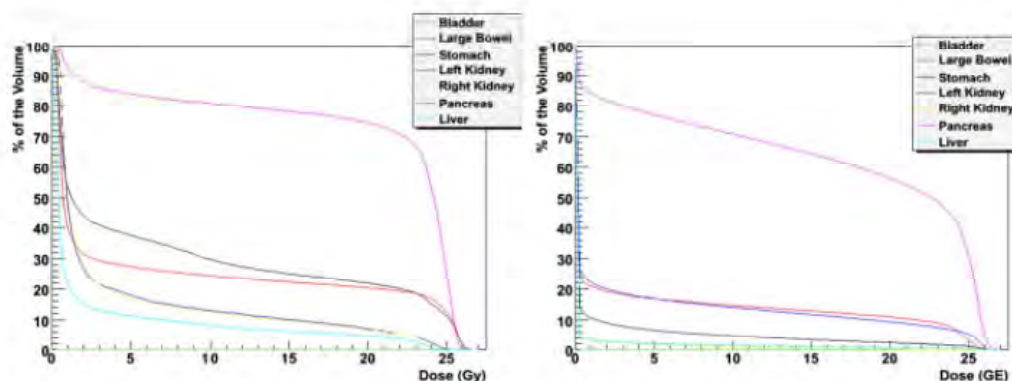* Max = average maximum point dose (cGy).

135

Fig. 2. Comparison of mean dose-volume histograms of photon (left panel) and proton (right panel) radiation treatment plans.

stage I seminoma. This reduction was greatest for radiation-induced gastric and large bowel malignancies. A reduction of one additional secondary cancer for every 50 patients with life expectancies of 40 years from the time of therapy treated with protons instead of photons was predicted. A high degree of dose homogeneity was achieved for all plans, and there was no significant difference in target volume coverage between photon and proton plans. Proton therapy in this study achieved superior normal tissue sparing and significantly reduced the mean doses delivered to the stomach, pancreas, large bowel, liver, and bladder. Additionally, the maximum doses delivered with protons were significantly lower to the large bowel and bladder and trended lower to the liver and stomach.

Over the past 2 decades, despite reductions in radiation doses and treatment fields, due to concerns for late complications, many practitioners have increasingly offered surveillance or single-dose carboplatin therapy as alternative adjuvant courses for stage I seminoma. Approximately 15% to 20% of unselected patients with stage I seminoma who undergo surveillance following orchiectomy develop disease recurrence (19). Because greater than 80% of relapses occur in para-aortic lymph nodes, deferring immediate adjuvant therapy and administering chemotherapy or radiotherapy upon relapse allows for successful salvage in most patients (19). However, treatment for patients who relapse is usually more intensive and associated with increased morbidity (20). More recent risk-adapted strategies recom-

mended surveillance only for low-risk patients committed to long-term follow-up with stage pT1–T2 histologies, lack of rete testis invasion, and tumors less than 4 cm (19–21).

Over the past decade, there has been increasing interest in adjuvant short-course carboplatin therapy. Reports from phase II trials and single-institution retrospective experiences indicate 5-year recurrence rates of less than 5% with adjuvant carboplatin treatment (20, 22). An MRC and European Organization for Research and Treatment of Cancer trial randomized 1,447 patients with stage I seminoma to one course of carboplatin or adjuvant radiotherapy to 20 to 30 Gy in 200-cGy daily fractions primarily to the para-aortic region (8, 9). At a median follow-up of 6.5 years, there was no difference in 5-year relapse-free survival rates between patients who received carboplatin and those who underwent radiotherapy (95% vs. 96%, respectively; 90% CI, 0.83–1.89). While patients receiving carboplatin had higher rates of hematologic toxicities, patients receiving radiation had more dyspepsia and an increased tendency for acute lethargy and time off work. Additionally, fewer new cases of contralateral testicular germ cell cancers were observed in patients who received carboplatin therapy (0.4% vs. 1.7%, respectively; p = 0.03). Despite these promising findings, with more limited long-term data than adjuvant radiotherapy, carboplatin is associated with an uncertain frequency of late relapses and the need for more rigorous CT surveillance with abdominal

Table 3. Predicted secondary malignancies per 10,000 patients/year

Source	Bladder	Large bowel	Pancreas	Stomach	In-field totals
Photon therapy	0.03	1.12	0.58	5.21	6.94
Proton therapy	0.00	0.31	0.56	1.10	1.97
Excess malignancies from photons	0.03	0.81	0.02	4.11	4.97
95% CI*	0.01–0.58	0.39–1.01	−0.01–0.06	3.22–5.01	3.99–5.97

* Confidence Interval is expressed as the range of predicted excess secondary malignancies per 10,000 patients/year from photon radiotherapy compared with proton radiotherapy. The null value is defined as 0, with statistical significance achieved for all ranges not overlapping 0.

and pelvic CT imaging at every visit for up to 10 years (20, 21). The radiation exposure from this more frequent CT surveillance may result in an increase in secondary malignancies (23).

Carboplatin also poses potential risks of acute nephrotoxicity, ototoxicity, neurotoxicity, and gonadal damage, as well as long-term cardiac disease and secondary malignancies (10). Population-based cancer registry studies of patients primarily treated with combination chemotherapy reveal an increased risk of secondary solid malignancies is highest among patients receiving both chemotherapy and radiotherapy (RR = 2.9; 95% CI, 1.9–4.2), with similar risks for patients treated with radiotherapy alone (RR = 2.0; 95% CI, 1.9–2.2) and with adjuvant chemotherapy alone (RR = 1.8; 95% CI, 1.3–2.5) (10). Several studies also report increased risks of secondary leukemias and myelodysplastic syndrome following chemotherapy for testicular cancer (24, 25). Longer follow-up after prospective trials is needed to determine the risk of secondary cancers from single-agent carboplatin therapy.

Although no clinical trials or published data exist assessing proton therapy to treat patients with testicular malignancies, proton therapy may represent a viable alternative to photon therapy, surveillance, and carboplatin therapies for stage I seminoma. The dosimetric advantages of protons demonstrated in this study might improve the therapeutic ratio for stage I patients. Based on historical dose-response relationships, with the significantly lower radiation doses to several OARs demonstrated in this study, patients treated with proton therapy may have improved quality of life and reduced rates of acute toxicities previously reported in seminoma patients receiving adjuvant radiotherapy, including nausea, lethargy, and delay in return to work. Longitudinal studies comparing normal tissue toxicities from photon versus proton radiotherapy are needed to confirm the clinical significance of our findings.

While this study evaluated radiotherapy as the primary inducer of secondary cancers, patients with testicular malignancies, particularly seminomas, are at increased risk for developing subsequent cancers, regardless of their testicular cancer treatment course. Patients with testicular malignancies undergoing orchiectomy alone still have an increased risk of developing a second cancer compared with the general public (26), likely from increased genetic susceptibility for extragonadal secondary tumors in this patient population (27). By comparing one type of radiation therapy to another and reporting findings as an absolute excess risk of secondary malignancies for one radiation treatment type over another, we have attempted to control for this increased genetic susceptibility.

The predicted rates of secondary malignancies calculated in this study were based on previously reported models of organ-specific radiation-induced cancer incidence rates based on OED. The effect of radiotherapy on secondary cancer risk for stage I seminoma patients has previously been assessed using OED models (27). In that dosimetric study, AP–PA treatment plans with 6-MV photons were predicted

to result in a 20.8% to 23.3% risk of secondary cancers for a 75-year-old patient treated with radiotherapy to the para-aortic region at age 35, compared with a 19.8% risk for the general population.

As CT simulation images used in this study were from patients previously treated with radiotherapy to the para-aortic region alone, the lack of images encompassing the entire scrotum and total lung volume limits our ability to predict secondary cancer rates for these organs. Of the lung volume imaged, however, the mean lung volume irradiation was significantly lower with protons than photons ($p < 0.01$).

The model used for predicting secondary cancer risk does not allow for predictions of radiation-induced leukemia risk. While a significant risk of treatment-induced leukemia has been reported following adjuvant chemotherapy (RR, 5.0), seminoma patients have a nonsignificant increased risk of developing leukemia following radiotherapy (RR, 3.1), and this risk is lowest among patients treated after 1974 and whose radiotherapy was limited to abdominal and pelvic fields. This risk of leukemia is significantly lower than the risk of radiation-induced solid tumor induction (10, 24).

The significant risk reduction in secondary malignancies predicted with proton radiotherapy must be measured relative to the potential risks for neutron contamination that may decrease the magnitude of benefit of proton radiotherapy in preventing secondary malignancies. However, this study demonstrated a 2% reduction in risk of gastric malignancies for patients with life expectancies of 40 years from the time of proton radiotherapy compared with photon radiotherapy. Previous studies have demonstrated the lifetime attributable risk of second cancers from neutron dose from proton radiotherapy to be approximately 0.2% (28), 1 order of magnitude lower than the benefit predicted in this study from proton radiotherapy. To further minimize the risk of neutron contamination, this study used scanned proton therapy, which is associated with an out-of-field neutron equivalent dose 1 order of magnitude lower than that for passive scattered proton therapy (29).

Although OED may better take into account inhomogeneities of clinical dose distributions in organs of interest, this model, which uses a linear-exponential function, may be subject to inherent errors due to lack of accuracy in dose reconstruction for patients treated in the more distant past that contributed to the development of the model (17). Furthermore, although prevailing dose-response paradigms for secondary cancer induction include linear, linear-exponential, and plateau models, the true risk of radiation-induced cancers may not perfectly fit any such model and may lie between linear and linear-exponential models (27). Therefore, the accuracy of any estimate of radiation-induced oncogenesis may be limited. However, the linear-exponential model was used in this study to provide a conservative estimate of secondary cancer risk, as the predicted risk with this model is lower at 25.5 Gy than with the other models (30). Furthermore, predicted secondary malignancies calculated in this study were very similar to the actual EAR of second solid cancers among testicular cancer

survivors, based on population-based reports (10). Longitudinal studies are needed to validate the predictions from these models.

Various methods were used to minimize bias in the present study. Ten consecutive patients with stage I seminoma were included to minimize sampling bias. All contours were performed by a single radiation oncologist and reviewed by two additional radiation oncologists. Standardized target volume expansions were used for all plans. Beam range compensators and blocking relative to PTV$_{proton}$ to account for beam properties and range uncertainties for proton plans were used for all plans and not optimized on a patient-by-patient basis. There was a high correlation between PTV$_{proton}$ volumes irradiated and the superior, inferior, and lateral extents of photon 2D volumes irradiated. As the aorta and common iliac vessels were used as surrogates for para-aortic lymph node positioning, there was less correlation in a few patients with more lateralized vasculature. In these patients, the widths of irradiation volumes with proton plans was similar to that for photon plans, but the centers of the fields were shifted laterally in proportion to the displacement of the vessels from the midline, particularly in the cranial-most portions of proton target volumes. In none of the patients was this shift greater than 2.7 cm from the midline. As the level of bifurcation of the aorta and location of the aorta and common iliac vessels relative to the midline are patient-dependent factors, consideration should be given to design treatment to accommodate anatomic features of individual patients when using vasculature as lymph node surrogates.

Furthermore, the volumes treated with proton therapy in this study corresponded well with the distribution of nodal spread from testicular malignancies, based on historical reports of lymphangiographies and lymph node dissections (31, 32). Additionally, no significant differences in target volume coverage were demonstrated between photon and proton plans, thus minimizing bias when comparing dosimetry between plans. Despite these measures, as with any retrospective study (33), it is possible that bias existed in the current study that may have favored a certain treatment strategy.

CONCLUSIONS

Compared with photon radiotherapy, proton radiotherapy reduced the mean doses delivered to most normal organs adjacent to the radiation treatment field for patients with stage I seminoma. Proton therapy also reduced the predicted incidence of radiation-induced secondary malignancies. These findings served as the basis for pursuing the feasibility and Phase II study anticipated to open at the University of Pennsylvania Roberts Proton Facility in early 2011 that will assess adjuvant proton radiotherapy for the treatment of patients with stage I seminoma.

REFERENCES

1. Jemal A, Siegel R, Ward E, et al. Cancer statistics, 2009. CA Cancer J Clin 2009;59(4):225–249.
2. Sokoloff MH, Joyce GF, Wise M. Testis cancer. J Urol 2007; 177(6):2030–2041.
3. Jones WG, Fossa SD, Mead GM, et al. Randomized trial of 30 versus 20 Gy in the adjuvant treatment of stage I testicular seminoma: a report on Medical Research Council Trial TE18, European Organisation for the Research and Treatment of Cancer Trial 30942 (ISRCTN18525328). J Clin Oncol 2005;23(6):1200–1208.
4. Fossá SD, Horwich A, Russell JM, et al. for the Medical Research Council Testicular Tumor Working Group. Optimal planning target volume for stage I testicular seminoma: a Medical Research Council randomized trial. J Clin Oncol 1999; 17(4):1146.
5. Bieri S, Rouzaud M, Miralbell R. Seminoma of the testis: is scrotal shielding necessary when radiotherapy is limited to the para-aortic nodes? Radiother Oncol 1999;50(3):349–353.
6. Zagars GK, Ballo MT, Lee AK, et al. Mortality after cure of testicular seminoma. J Clin Oncol 2004;22(4):640–647.
7. Hanks GE, Peters T, Owen J. Seminoma of the testis: long-term beneficial and deleterious results of radiation. Int J Radiat Oncol Biol Phys 1992;24(5):913–919.
8. Oliver RT, Mead GM, Fogarty PJ, et al. Radiotherapy versus carboplatin for stage I seminoma: updated analysis of the MRC/EORTC randomized trial (ISRCTN27163214). J Clin Oncol 2008;26(Suppl 15). A–1.
9. Oliver RT, Mason MD, Mead GM, et al. Radiotherapy versus single-dose carboplatin in adjuvant treatment of stage I seminoma: a randomised trial. Lancet 2005;366(9482):293–300.
10. Travis LB, Fossá SD, Schonfeld SJ, et al. Second cancers among 40,576 testicular cancer patients: focus on long-term survivors. J Natl Cancer Inst 2005;97(18):1354–1365.
11. Robinson D, Moller H, Horwich A. Mortality and incidence of second cancers following treatment for testicular cancer. Br J Cancer 2007;96(3):529–533.
12. Schairer C, Hisada M, Chen BE, et al. Comparative mortality for 621 second cancers in 29356 testicular cancer survivors and 12420 matched first cancers. J Natl Cancer Inst 2007; 99(16):1248–1256.
13. Kennedy CL, Hendry WF, Peckham MJ. The significance of scrotal interference in stage I testicular cancer managed by orchiectomy and surveillance. Br J Urol 1986;58(6):705–708.
14. Suit H, Goldberg S, Niemierko A, et al. Proton beams to replace photon beams in radical dose treatments. Acta Oncol 2003;42(8):800–808.
15. Paganetti H, Niemierko A, Ancukiewicz M, et al. Relative biological effectiveness (RBE) values for proton beam therapy. Int J Radiat Oncol Biol Phys 2002;53(2):407–421.
16. Schneider U, Kaser-Hotz B. A simple dose-response relationship for modeling secondary cancer incidence after radiotherapy. Z Med Phys 2005;15(1):31–37.
17. Schneider U, Zwahlen D, Ross D, et al. Estimation of radiation-induced cancer from three-dimensional dose distributions: Concept of organ equivalent dose. Int J Radiat Oncol Biol Phys 2005;61(5):1510–1515.
18. Schneider U, Lomax A, Besserer J, et al. The impact of dose escalation on secondary cancer risk after radiotherapy of prostate cancer. Int J Radiat Oncol Biol Phys 2007;68(3):892–897.
19. Warde P, Specht L, Horwich A, et al. Prognostic factors for relapse in stage I seminoma managed by surveillance: a pooled analysis. J Clin Oncol 2002;20(22):4448–4452.

20. Krege S, Beyer J, Souchon R, et al. European consensus conference on diagnosis and treatment of germ cell cancer: a report of the second meeting of the European Germ Cell Cancer Consensus group (EGCCCG): part I. Eur Urol 2008;53(3):478–496.

21. National Comprehensive Cancer Network. The NCCN clinical practice guidelines in oncology: testicular cancer, version 1.2010. August 28, 2009. National Comprehensive Cancer Network, Inc. Available at: NCCN.org. Accessed February 22, 2010.

22. Aparicio J, García del Muro X, Maroto P, et al. Multicenter study evaluating a dual policy of postorchiectomy surveillance and selective adjuvant single-agent carboplatin for patients with clinical stage I seminoma. Ann Oncol 2003;14(6):867–872.

23. Tarin TV, Sonn G, Shinghal R. Estimating the risk of cancer associated with imaging related radiation during surveillance for stage I testicular cancer using computerized tomography. J Urol 2009;181(2):627–632.

24. Travis LB, Andersson M, Gospodarowicz M, et al. Treatment-associated leukemia following testicular cancer. J Natl Cancer Inst 2000;92(14):1165–1171.

25. Howard R, Gilbert E, Lynch CF, et al. Risk of leukemia among survivors of testicular cancer: a population-based study of 42,722 patients. Ann Epidemiol 2008;18(5):416–421.

26. Travis LB, Curtis RE, Hankey BF. Second malignancies after testicular cancer. J Clin Oncol 1995;13(2):533–534.

27. Zwahlen DR, Martin JM, Millar JL, et al. Effect of radiotherapy volume and dose on secondary cancer risk in stage I testicular seminoma. Int J Radiat Oncol Biol Phys 2008;70(3):853–858.

28. Zacharatou Jarlskog C, Paganetti H. Risk of developing second cancer from neutron dose in proton therapy as function of field characteristics, organ, and patient age. Int J Radiat Oncol Biol Phys 2008;72(1):228–235.

29. Athar BS, Bednarz B, Seco J, et al. Comparison of out-of-field photon doses in 6 MV IMRT and neutron doses in proton therapy for adult and pediatric patients. Phys Med Biol 2010;55(10):2879–2891.

30. Schneider U, Lomax A, Pemler P, et al. The impact of IMRT and proton radiotherapy on secondary cancer incidence. Strahlenther Onkol 2006;182(11):647–652.

31. Donohue JP, Zachary JM, Maynard BR. Distribution of nodal metastases in nonseminomatous testis cancer. J Urol 1982;128(2):315–320.

32. Gagnon JH, Mount BM, Khonsari H, et al. Lymphography in germinal tumours of the testis. Br J Urol 1972;44(2):136–142.

33. Brown ML, Gersh BJ, Holmes DR, et al. From randomized trials to registry studies: translating data into clinical information. Nat Clin Pract Cardiovasc Med 2008;5(10):613–620.

Comparison of secondary neutron dose in proton therapy resulting from the use of a tungsten alloy MLC or a brass collimator system

Eric S. Diffenderfer, Christopher G. Ainsley, Maura L. Kirk, James E. McDonough, and Richard L. Maughan
Department of Radiation Oncology, University of Pennsylvania, Philadelphia, Pennsylvania 19104

Purpose: To apply the dual ionization chamber method for mixed radiation fields to an accurate comparison of the secondary neutron dose arising from the use of a tungsten alloy multileaf collimator (MLC) as opposed to a brass collimator system for defining the shape of a therapeutic proton field.

Methods: Hydrogenous and nonhydrogenous ionization chambers were constructed with large volumes to enable measurements of absorbed doses below 10^{-4} Gy in mixed radiation fields using the dual ionization chamber method for mixed-field dosimetry. Neutron dose measurements were made with a nominal 230 MeV proton beam incident on a closed tungsten alloy MLC and a solid brass block. The chambers were cross-calibrated against a ^{60}Co-calibrated Farmer chamber in water using a 6 MV x-ray beam and Monte Carlo simulations were performed to account for variations in ionization chamber response due to differences in secondary neutron energy spectra.

Results: The neutron and combined proton plus γ-ray absorbed doses are shown to be nearly equivalent downstream from either a closed tungsten alloy MLC or a solid brass block. At 10 cm downstream from the distal edge of the collimating material the neutron dose from the closed MLC was $(5.3 \pm 0.4) \times 10^{-5}$ Gy/Gy. The neutron dose with brass was $(6.4 \pm 0.7) \times 10^{-5}$ Gy/Gy. Further from the secondary neutron source, at 50 cm, the neutron doses remain close for both the MLC and brass block at $(6.9 \pm 0.6) \times 10^{-6}$ Gy/Gy and $(6.3 \pm 0.7) \times 10^{-6}$ Gy/Gy, respectively.

Conclusions: The dual ionization chamber method is suitable for measuring secondary neutron doses resulting from proton irradiation. The results of measurements downstream from a closed tungsten alloy MLC and a brass block indicate that, even in an overly pessimistic worst-case scenario, secondary neutron production in a tungsten alloy MLC leads to absorbed doses that are nearly equivalent to those seen from brass collimators. Therefore, the choice of tungsten alloy in constructing the leaves of a proton MLC is appropriate, and does not lead to a substantial increase in the secondary neutron dose to the patient compared to that generated in a brass collimator. © 2011 American Association of Physicists in Medicine. [DOI: 10.1118/1.3656025]

I. INTRODUCTION

In recent years, most effort in measuring secondary neutron doses in proton therapy has focused on estimating the dose to the patient outside of the treatment field either laterally or beyond the spread out Bragg peak. Secondary neutrons produced by interactions of the proton field with beam modifying devices (e.g., double scattering system, beam shaping collimators, and range compensators) and the patient have been studied by many authors.[1-23] These secondary neutrons are responsible for whole body irradiation of high LET particles at low dose levels where the long term effects are not fully understood.[24-27] Consequently, there is some concern of radiation-induced secondary cancers in patients treated therapeutically with protons.[28]

These concerns are also important when using a multileaf collimator (MLC) in place of brass or Lipowitz's metal collimators because of the effect that the MLC may have on secondary neutron dose. Moyers et al.[10] found that most secondary neutrons are produced in the final collimator of a passive scattering proton system. Tayama et al.[8] measured secondary neutron dose from a passively scattered proton beam and determined that adjustment of the aperture diameter of a brass MLC precollimator can reduce the neutron dose equivalent outside of the treatment field. Taddei et al.[11] found a reduction in neutron equivalent dose through Monte Carlo simulations replacing the brass final collimator with a tungsten collimator of the same thickness. Brenner et al.[13] used Monte Carlo simulation to study changes in neutron dose as a function of collimator material and thickness. Daartz et al.[14] used a Bonner sphere to measure an increase of up to two-fold in neutron equivalent dose when using a tungsten MLC in place of a brass final collimator.

In the present paper, we are interested in comparing the secondary neutron dose arising from the use of a tungsten alloy MLC, which is in use on the double scattering and uniform scanning beam lines at the University of Pennsylvania Roberts Proton Therapy Center, to a brass collimator system for defining the lateral field shape. We have measured neutron absorbed dose due to a proton beam of the highest energy available from our cyclotron. Measurements were performed downstream from a closed tungsten alloy MLC or solid brass block. This is an extreme case which does not represent a realistic clinical situation, but offers the best

geometry for making a quantitative comparison of secondary neutron production for a tungsten alloy MLC and brass collimator system.

Based on nuclear cross-sections for proton–neutron interactions in tungsten or brass, one would expect tungsten to produce the greater neutron flux. However, when constructing the MLC it is necessary to use a thickness of tungsten alloy equivalent to slightly greater than twice the range of the highest energy protons, because the leaf design must incorporate side- and end-steps to prevent interleaf leakage. In a solid brass collimator, a thickness equivalent to just over one proton range is used and the thickness can be adjusted according to the energy of the incident protons. Although more neutrons are produced in a tungsten alloy MLC, due to increased thickness there is substantial self attenuation[13] of the neutron flux which is not present in the thinner brass collimator, the difference being particularly pronounced at the highest proton energies.

Previous efforts aimed at measuring the out-of-field neutron doses produced by a therapeutic proton beam have employed instruments that are traditionally used in a radiation protection setting such as Bonner spheres,[29] long counters,[30] scintillation counters,[30] superheated neutron bubble detectors,[31] or foil activation techniques.[32] Measurements with these instruments are reported in terms of dose equivalent (Sv), which is a product of the absorbed dose (Gy) and a neutron energy-dependent radiation weighting factor. Often commercial devices are used for these measurements with vendor-supplied calibrations that give no specifics of the radiation weighting factors used. Bonner spheres employ a boron trifluoride (BF_3) or ^{3}He filled counter to detect neutrons which have been thermalized by a thick polyethylene moderator. The size of the moderator, which must be increased to accommodate higher energy neutrons, therefore limits their spatial resolution. Although neutron bubble detectors can have good spatial resolution, their accuracy is statistically constrained by the maximum number of bubbles that can be reliably counted, a number that is on the order of 100 bubbles per exposure.[31,33] The energy response of these detectors is often limited and they are, therefore, expected to under-respond to the secondary neutron dose produced by high energy therapeutic proton beams ($\sim$230 MeV), since these beams contain large numbers of high energy neutrons. Typically Bonner spheres, long counters, and bubble detectors respond to neutrons with energies up to 10–20 MeV. Recently, survey instruments have been developed with extended energy response. Such instruments include a Bonner sphere[34] and a long counter[35] with modified moderator, and an instrument based on scintillation counters.[36] These devices have large volumes and therefore poor spatial resolution and the uncertainties in their calibration factors can be considerable.

The measurements of Binns *et al.*[1] used a tissue-equivalent proportional counter (TEPC) to study the microdosimetric spectra resulting from proton interactions with the dose delivery system. Such measurements have the advantage of providing absorbed dose measurements as a function of lineal energy. This can then be used to assign appropriate radiation weighting factors or relative biological effectiveness (RBE) for calculating dose equivalent in Sv or Gy(RBE).[37] While a commercial instrument is available which incorporates a TEPC and multichannel analyzer in a single portable device (REM 500, Far West Technology, Inc., Goleta, CA), this instrument lacks the spectral dynamic range that is required for precision microdosimetric measurements. Precise measurements require careful control of gas pressure in the TEPC and the use of 2–4 amplification channels to acquire the entire signal dynamic range. It is likely due to the increased challenge these difficulties present that this method has not been widely pursued for measuring secondary dose in proton therapy fields.

Ionization chambers such as those that are routinely used in radiation therapy dosimetry and quality assurance would tend to alleviate these issues were it not for the large background of leakage protons passing through the interleaf gaps of the MLC and γ-rays induced through (p,γ) and (n,γ) reactions. These chambers are typically constructed of tissue-equivalent (TE) materials and respond to neutrons, protons, and γ-rays with equivalent sensitivities. However, the neutrons display different LET and radiation weighting factors from the protons and γ-rays, so their respective dose contributions must be separated in some way.

We determine the absorbed neutron and combined leakage proton plus γ-ray (p + γ) absorbed doses directly by means of a dual ionization chamber method originally developed as a mixed-field dosimetry technique used to separate the neutron dose from the background neutron-induced γ-ray dose in fast neutron therapy beams.[38] An advantage of this technique is that it determines absorbed dose and allows the user to input appropriate radiation weighting factors or RBE to calculate dose equivalent or RBE-weighted dose, respectively. In this technique, two ionization chambers with different sensitivities to the two types of radiation are used to evaluate the separate absorbed doses of neutrons and γ-rays. The contribution from interleaf leakage protons to the absorbed dose cannot be separated from that due to γ-rays, but this has little impact because the RBE of protons and γ-rays are relatively close and generally small compared to that of neutrons.[39] The chambers are constructed to have approximately the same sensitivity to protons and γ-rays, while one of the two is designed to be relatively insensitive to neutrons compared to the other. This was accomplished by constructing one chamber using materials that closely mimic the dose response of tissue exposed to proton, γ-ray, and neutron radiation; for neutrons, this ideally requires the chamber wall and gas to simulate the atomic composition of tissue exactly. In practice, this is not possible in a solid material and matching hydrogen content (i.e., using hydrogenous materials) is a good compromise since most of the neutron kerma originates from (n,p) elastic scattering interactions.[38] In contrast, the other chamber is constructed using materials with relatively low neutron interaction cross-sections (i.e., using nonhydrogenous and higher atomic number (Z) materials).

The absorbed dose of secondary neutron or p + γ radiation downstream of a closed collimator or outside of a

therapeutic proton beam is expected to be in the range 0.01%–0.5% of the primary open field proton dose,[1,2,7,32] depending on the delivery mode (e.g., scattering or scanning). Collection volumes of commercially available ionization chambers suitable for use in the dual ionization chamber method are on the order of 1 cm^3. The charge collected in a volume of this size for doses on the order of 0.2 mGy may therefore be as low as 5 pC. With a measured leakage charge of 2–4 pC over the elapsed time of dose delivery, the secondary radiation signal is easily lost in the noise due to current leakage. Therefore, we have designed and built a set of larger volume ionization chambers that increase the charge collection efficiency to an extent that exceeds the signal to noise ratio limits imposed by the leakage current. For instance, with a ten-fold increase in chamber volume over commercially available chambers and with reproducible charge leakage in the range of 2–4 pC, we estimate that doses as low as 0.2 mGy can be measured with an accuracy of approximately 6%.

II. METHODS AND MATERIALS

In the dual chamber method,[38] the two chambers are first calibrated in a reference photon field. When placed at the same point in a mixed field each exhibits an independent response according to its relative sensitivity to neutrons and p + γ radiation. The dose responses of the chambers can be described as a simple sum of the products of their sensitivity to the separate types of radiation with the dose due to the respective radiation. In the following we will assign the subscript T to the chamber designed to have equal sensitivity to both neutrons, protons, and γ-rays and we will assign U to the chamber designed to have lower relative neutron sensitivity. In the mixed field, the ratio of the dosimeter responses with their sensitivities to the photon field used for calibration, R_T' and R_U', are given by

$$R_T' = k_T D_n + h_T D_{p+\gamma}, \tag{1}$$

and

$$R_U' = k_U D_n + h_U D_{p+\gamma}, \tag{2}$$

in units of absorbed dose. The parameters k and h are the respective sensitivities of the dosimeters to neutrons and p + γ radiation relative to their sensitivities to the photon field used for calibration. Then, the absorbed dose to water from neutrons and p + γ radiation, D_n and $D_{p+\gamma}$ is obtained by solving Eqs. (1) and (2) simultaneously

$$D_n = \frac{(h_U R_T' - h_T R_U')}{(h_U k_T - h_T k_U)}, \tag{3}$$

$$D_{p+\gamma} = \frac{(k_T R_U' - k_U R_T')}{(h_U k_T - h_T k_U)}. \tag{4}$$

The two components of dose as they are presented in Eqs. (3) and (4) depend on the relative sensitivities of the chambers to p + γ and neutron radiation.

To implement the dual chamber method we have built a chamber using TE materials with nearly equal proton, γ-ray, and neutron sensitivities and a second chamber constructed using higher Z material to obtain a lower sensitivity to neutron radiation. Both were based on a thimble-type ionization chamber design, providing an active volume of 9.14 cm^3. The walls of the ionization chambers are 0.318 cm thick with an inner diameter of 1.91 cm, Fig. 1. A Rexolite 1422 (C-Lec Plastics, Philadelphia, PA) polystyrene base supports the outer shell, the electrode, and the guard ring which reduces leakage current between the outer shell and inner electrode. The polystyrene base also provides an inlet and outlet port to the ionization chamber for gas flow through the active volume. The gas flow is metered using an adjustable-rate flow-meter at a rate low enough to ensure that air is completely flushed from the system without increasing the chamber above atmospheric pressure. A thin-walled 1/4″ diameter aluminum stem attached to an aluminum base provides a means of supporting the chamber in the radiation field as well as routing the tri-axial cable and the 1/16″ PVC tubing that is used to provide gas flow. The TE chamber was constructed with the outer shell, the inner electrode, and the guard ring composed of A-150 TE plastic.[40] Methane-based TE gas[38] flows through the chamber's active volume. For the nonhydrogenous chamber, magnesium, and argon were the wall material and gas of choice, respectively, due to their
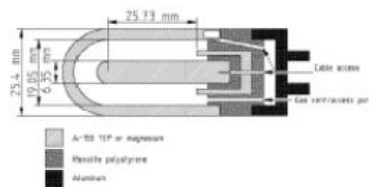
a   b

Fig. 1. (a) Drawing of the large volume ionization chambers designed and built for use at the University of Pennsylvania's Roberts Proton Therapy Center. (b) Image of the assembled Mg-Ar (top) and TE-TE (bottom) ionization chambers.

142

relatively low neutron interaction cross-sections. The construction of this chamber is identical to the TE chamber except that the magnesium components have been substituted for the A-150 TE plastic components.

The chambers were cross-calibrated against a ^{60}Co-calibrated Exradin A12 (Standard Imaging, Middleton, WI) Farmer-type ionization chamber (0.65 cm^3 active volume) using the 6 MV x-ray beam of a Varian Clinac iX (Varian Medical Systems, Palo Alto, CA) linear accelerator. The large volume chambers were placed in 3.3 mm thick waterproof PMMA sleeves within a $30 \times 30 \times 30$ cm water phantom with 0.5 cm thick PMMA walls at an SSD of 100 cm, with the x-ray beam delivered horizontally. Readings were taken at a depth of 10 cm with stabilized gas flow through the large volume chambers. The Exradin A12 readings were corrected with the x-ray beam quality factor, $k_Q = 0.994$, which was determined using the beam quality specification procedure of Almond *et al.*[41] Additional corrections for leakage current, temperature and pressure variations, polarity effects, ion collection efficiency, and the electrometer calibration factor were applied to all chamber readings. Table I shows active volumes and calibration factors for the dosimeters.

Dual chamber measurements were made in air to compare the secondary neutron dose for tungsten alloy and brass collimators. All measurements of secondary radiation dose from tungsten alloy were done with the MLC fully closed, Fig. 2(a). Measurements with brass were completed by placing a 12 cm diameter and 6.5 cm thick cylindrical brass block directly downstream from the MLC with 20 open leaf pairs of the MLC (each of physical width 4.35 mm and roughly 9 cm thick) forming an 8.7 cm diameter circle, Fig. 2(b). An unmodulated proton beam with kinetic energy of 230 MeV was delivered in uniform scanning mode with no lateral deflection and with all beam-line scatterers removed so that the neutron production would be confined to the MLC or brass collimator material. Readings were taken with the chambers placed at isocenter 10 cm from the distal edge of the closed MLC or brass block. To obtain a comparable neutron source to detector distance and accounting for the difference in collimator thickness, readings were also taken 50 cm downstream from the proximal edge of the closed MLC or brass block. Gas flow through the chambers was allowed to stabilize at the same flow rate used for calibration and chamber readings were corrected for all previously mentioned effects.

The proton beam used in this study was characterized with film and ionization chamber measurements. Lateral beam dose profiles with the MLC fully open were measured with film (Gafchromic EBT2, International Specialty Prod-
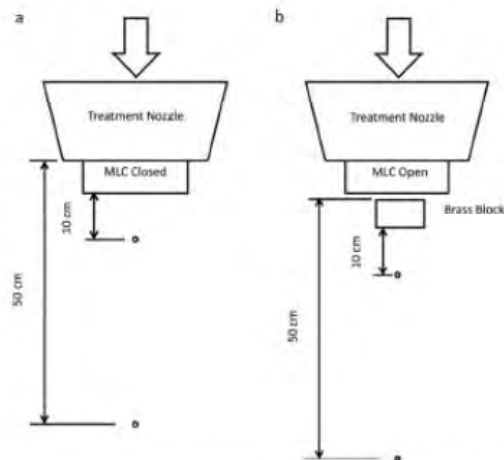

Fig. 2. Experimental setup (not to scale) showing the measurement points 10 cm downstream from the distal side and 50 cm downstream of the proximal side of either the closed MLC (a) or a 6.5 cm thick brass block placed downstream of the MLC with leaves open to form an 8.7 cm diameter circle (b).

ucts, Wayne, NJ) placed at 0 and 32 cm depths in solid water plastic, where 32 cm depth is at isocenter. An 8.4 cm diameter plane parallel ionization chamber (Model 34070, PTW, Freiburg, Germany) was scanned in a water tank along the beam axis to measure the fractional depth dose profile.

Implementation of the dual chamber method requires knowledge of the neutron energy spectrum for an accurate assessment of the dose response of the chambers. To this end, we have performed simulations of secondary radiation production from the proton beam at the University of Pennsylvania using the Geant4 simulation toolkit.[42] The simulations incorporate beam shaping components of the universal nozzle and tungsten alloy MLC and have been experimentally verified in separate measurements to be published later. Secondary neutron fluence spectra is recorded in a 1 cm diameter sphere at the measurement positions distal to the closed tungsten alloy (92.5% W, 5.2% Ni, and 2.3% Cu by weight) MLC or 6.5 cm brass block (62% Cu, 35% Zn, and 3% Pb by weight).

The relative neutron sensitivities, k_U and k_T, as a function of incident neutron energy up to 50 MeV have been computed iteratively by Waterman *et al.*[43] using tabulated tissue kerma factors and experimentally determined chamber responses in a number of neutron fields with known neutron energy spectra. However, since neutron sensitivities are also a function of chamber gas composition, wall material, and chamber size,[44–46] and in our case the secondary neutron energies are expected to approach the primary proton energy, we have developed Monte Carlo simulations to calculate the sensitivities of our large volume chambers. We modeled the magnesium-walled and argon gas-filled (Mg-Ar) chamber as well as the A150 TE plastic-walled and methane-based TE gas-filled (TE-TE) chamber using dimensions and material

TABLE I. The dose to water calibration factors, N_{DW}, for the chambers used in the measurements.

Chamber	Active volume (cm^3)	N_{DW} (Gy/C)
Exradin A12	0.65	5.040×10^7
TE-TE	9.14	3.44×10^6
Mg-Ar	9.14	2.33×10^6

143

compositions based on the design drawings and measurements of the finished chambers. Each chamber was uniformly irradiated with a simulated neutron beam having a circular diameter sufficient to fully encompass the entire chamber with the beam oriented perpendicular to the chamber's cylindrical axis. The dose deposited within the gas volume of the chamber was scored as a function of incident neutron energy which ranged 0–250 MeV. We are interested in the absorbed dose to water, so the sensitivities were calculated as the ratio of the dose deposited in the chamber gas volume to the dose deposited in the gas volume of an identical chamber composed of water. The water density of the wall and gas is adjusted such that the total areal density of each is equivalent to the areal densities of the Mg-Ar or TE-TE chambers. Relative sensitivities were calculated by taking the quotient of the neutron sensitivity with the sensitivity obtained through simulating exposure of the chamber to a photon field with an energy spectrum that approximates the 6 MV photon field used for calibration.

To test the reliability of the above method for calculating k_U and k_T, we have also calculated relative sensitivity functions for the chambers described in the Waterman study. In this case, dimensions of the Mg-Ar chamber were modeled after an Exradin model 2 Spokas thimble chamber with 0.54 cm^3 active volume and dimensions of the TE-TE chamber were modeled on the FWT IC-17 (Far West Technology, Inc.) chamber with 1.0 cm^3 active volume. Since the neutron sensitivities given by Waterman *et al.*[43] are relative to tissue, the Mg-Ar and TE-TE chamber sensitivities are calculated relative to a chamber composed of ICRU muscle[47] with the density of the wall and gas adjusted appropriately. The results fall within the errors (1–2 s.d.) and deviations from the measured values can be attributed to a lack of neutron cross-section data above 20 MeV (Ref. [47]) and ambiguities in Waterman *et al.*[43] regarding the dimensions of the chambers, the material composition of the TE-TE chamber, and the elemental composition of tissue.

Since measurements are performed in a spectrum of neutron energies, the effective relative neutron sensitivity of an ionization chamber in any given neutron energy spectrum replaces the energy dependent neutron sensitivity in Eqs. (3) and (4). Effective sensitivity can be expressed as the dose-weighted average of relative neutron sensitivity[43]

$$k_i = \frac{\int k_i(E) D_W(E) dE}{\int D_W(E) dE}, \tag{5}$$

where i represents the chambers T or U, $D_W(E)$ is the dose to water as a function of neutron energy, and $k_i(E)$ is neutron sensitivity relative to the sensitivity to the photon field used for calibration.

The systematic errors in Monte Carlo calculated chamber sensitivities are difficult to estimate and a detailed analysis of dose measurement errors arising from these calculations is beyond the scope of this work. However, the overall measurement uncertainties (ΔD_n and $\Delta D_{p+\gamma}$) can be derived through error propagation of Eqs. (3) and (4) (Ref. [48]) assuming the uncertainties are uncorrelated

$$\Delta D_n^2 = \left[\frac{R'_U - k_U D_n}{h_U k_T - h_T k_U}\right]^2 \Delta h_T^2 + \left[\frac{R'_T - k_T D_n}{h_U k_T - h_T k_U}\right]^2 \Delta h_U^2$$
$$+ \left[\frac{h_U D_n}{h_U k_T - h_T k_U}\right]^2 \Delta k_T^2$$
$$+ \left[\frac{h_T D_n}{h_U k_T - h_T k_U}\right]^2 \Delta k_U^2, \tag{6}$$

$$\Delta D_{p+\gamma}^2 = \left[\frac{k_U D_{p+\gamma}}{h_U k_T - h_T k_U}\right]^2 \Delta h_T^2 + \left[\frac{k_T D_{p+\gamma}}{h_U k_T - h_T k_U}\right]^2 \Delta h_U^2$$
$$+ \left[\frac{R'_U - h_U D_{p+\gamma}}{h_U k_T - h_T k_U}\right]^2 \Delta k_T^2$$
$$+ \left[\frac{R'_T - h_T D_{p+\gamma}}{h_U k_T - h_T k_U}\right]^2 \Delta k_U^2. \tag{7}$$

In the following, the component of the uncertainty in p+γ sensitivity (Δh_T and Δh_U) arising from sensitivity to γ-rays is ignored because the chambers are calibrated in a photon field. The sources of error inherent in calculating neutron sensitivity as a ratio of doses can be estimated by approximating neutron dose as the product of the neutron kerma factor (K) with the neutron fluence (Φ). Then, the neutron sensitivity error is a function of the errors in the neutron kerma factor, neutron fluence, and the sensitivity to the photon field used for calibration. Systematic error in the fluence calculations is primarily dependent on neutron emission cross-section uncertainties which are estimated to be 20–40% for protons and neutrons.[47] As an approximation, we ignore this error because the neutron sensitivity is calculated as a ratio of doses which are each affected by fluence error in largely the same manner. Sensitivity to the calibration field is also calculated as a dose ratio, so the effects of systematic error in the estimation of photon fluence for the calibration field are also ignored. Then, with the uncertainty in the mass attenuation coefficient being 1%–2% in the energy range of the photons used for calibration,[49] an estimate of 2.5% uncertainty in the sensitivity of the dosimeters to the calibration field agrees with that of ICRU Report 78.[37] The remaining systematic errors in neutron sensitivity can be attributed to uncertainty in the neutron kerma factors which are directly related to uncertainty in neutron interaction cross-sections. Kerma factor uncertainty is estimated to be up to 2% for water and 5% for A-150 TE plastic or TE gas when uncertainty in elemental composition and the neutron spectra used to measure the kerma factors is considered.[50] Kerma factors for magnesium and argon are not well known and their uncertainties are estimated to be up to 20%.[47] Analogous to our approach with neutrons, the uncertainty in relative proton sensitivity can be estimated by taking a fluence based approach to calculate the doses that are used in the ratio for relative proton sensitivity. Then, the error depends on proton stopping power uncertainty, which has been estimated at less than 2% for elements and 4% for compounds.[51]

III. RESULTS AND DISCUSSION

Shown in Figs. 3(a) and 3(b) are Gafchromic EBT2 film absorbed dose profiles along the lateral x- and y-axis for 0
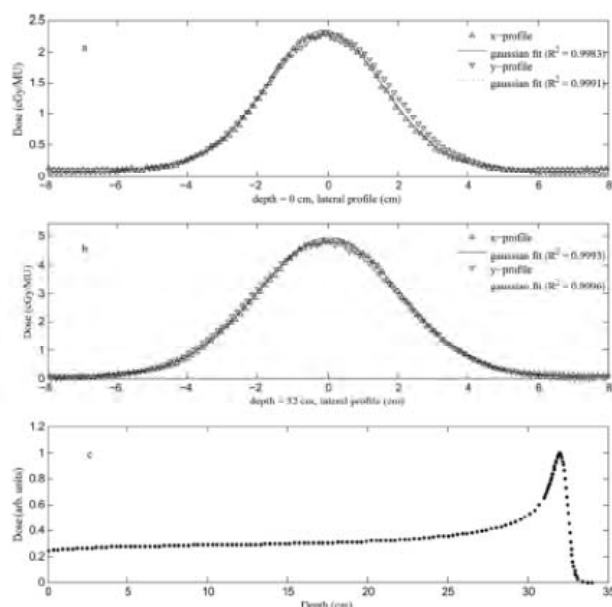
144

FIG. 3. Lateral beam profiles, taken with radiochromic film, along the x- and y-axis for 0 cm (a) and 32 cm (b) depth in solid water plastic, where the 32 cm measurement is at isocenter. The fractional depth dose profile (c) in water measured with the PTW 8.4 cm diameter plane parallel chamber.

and 32 cm depth in solid water plastic, displayed in units of cGy per machine monitor unit (MU). Gaussian functions with a constant background were fit to the profiles to determine the beam width. At 0 cm depth (32 cm upstream from isocenter), $\sigma_x = 1.66$ cm and $\sigma_y = 1.84$ cm. The 32 cm depth measurement is at isocenter and the widths are $\sigma_x = 2.04$ cm and $\sigma_y = 2.17$ cm. During the neutron measurements the proximal face of the MLC is approximately 19 cm upstream from isocenter. When measurements are made with the brass block and the MLC open to form an 8.7 cm diameter circle, less than 4% of the proton dose is deposited in the MLC. Therefore, the effect on measurements with the brass block is negligible because the neutron and p + γ doses are less than 0.01% of the dose delivered to isocenter with an open collimator, as shown below.

A fractional depth dose profile in water measured with the PTW plane parallel chamber is shown in Fig. 3(c). The peak absorbed dose at isocenter was determined to be 6.95 cGy/MU using the product of the surface dose (2.33 cGy/MU), the peak to surface ratio obtained from Fig. 3(c), and the ratio of fractional profile areas measured by the 8.4 cm plane parallel chamber at the surface to the peak at 32 cm.

Simulated neutron fluence spectra 10 cm from the distal edge of the closed tungsten alloy MLC or 6.5 cm brass block are shown in Fig. 4(a). The fluence spectra 50 cm from the proximal edge of the closed MLC and the brass block are shown in Fig. 4(b). In all cases, the spectra are heavily dominated by low energies with a long tail approaching the incident proton energy. The mean neutron energies from the MLC, which has a thickness equivalent to twice the proton range, are notably lower than the mean energies from the

brass block, whose thickness is <10% greater than the proton range. The simulations also indicate that dose due to interleaf leakage protons greatly outweighs γ-ray dose distal to the closed MLC while almost no protons pass completely through the brass block.

The sensitivity functions, k_T and k_U, calculated from Monte Carlo simulations of the large volume chambers are plotted as a function of neutron energy in Fig. 5. The Mg-Ar relative sensitivity, k_U, falls rapidly to zero with decreasing neutron energy so integration, in Eq. (5), of the sensitivity function with a dose distribution that is heavily weighted toward low energy neutrons will result in a small effective neutron sensitivity. Conversely, the TE-TE relative sensitivity, k_T, varies little with neutron energy and is found to be nearly unity after integration with the neutron dose distribution.

Given the chambers are calibrated in an x-ray field, then each chamber's γ-ray sensitivity relative to the radiation used for calibration can be assumed to be unity because the Compton effect predominates in both the x-ray calibration and in the γ-rays of the mixed field. Where interleaf leakage protons outnumber secondary γ-rays, as is the case downstream of the closed MLC, the proton sensitivity was calculated using the same Monte Carlo model used to find the neutron sensitivities. The proton sensitivity was found to be approximately invariant with proton energy for both chambers. Furthermore, the TE-TE chamber is constructed of hydrogenous materials with proton stopping powers close to that of water and therefore exhibits a relative sensitivity to protons that is equivalent to its relative sensitivity to γ-rays. The calculated sensitivities of the Mg-Ar and TE-TE chambers to p + γ radiation are approximately 0.9 and 1.0,
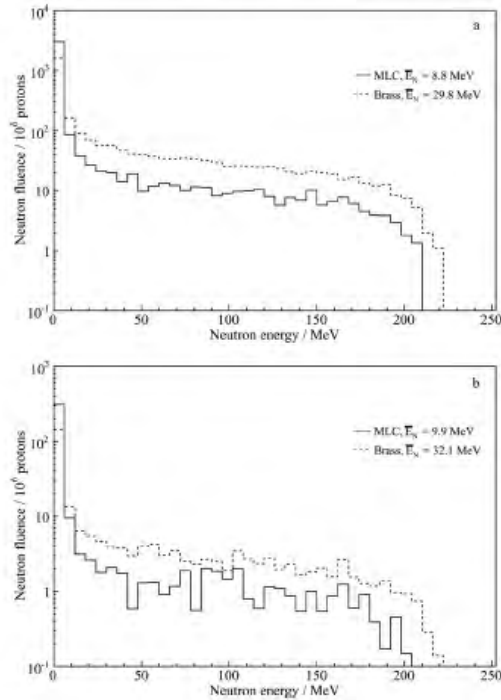
145

FIG. 4. Simulated neutron fluence spectra through a 1 cm diameter sphere placed 10 cm from the distal edge of the closed MLC or the brass block (a), and 50 cm from the proximal edge of the MLC or the brass block (b).
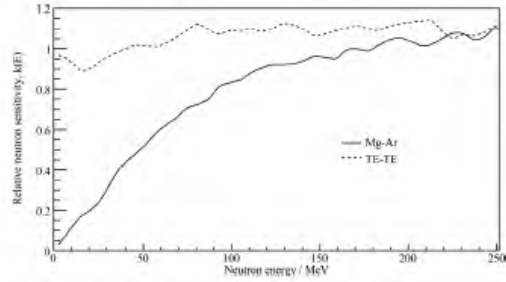

FIG. 5. Relative chamber sensitivity as a function of incident neutron energy for the large volume Mg-Ar and TE-TE chamber. The sensitivities are calculated with the Geant4 (Ref. 42) Monte Carlo toolkit using detailed geometrical models of the chambers.

respectively, for the MLC measurements where the interleaf leakage protons dominate over γ-rays. When measurements are performed downstream of the brass block, the γ-rays dominate over protons and the sensitivities of both chambers are approximately 1.0.

Shown in Table II are effective sensitivities for each of the measurements described above along with the absorbed dose responses of the dosimeters and calculated neutron and p $+ \gamma$ doses in units of 10^{-5} Gy absorbed dose to water per Gy of absorbed dose to water delivered to isocenter at 32 cm

depth by a pristine 230 MeV proton beam. Relative uncertainties were approximated at 5% for p $+ \gamma$ sensitivities, 20% for k_U, 6% for k_T, and inserted into Eqs. (6) and (7) to estimate the relative uncertainty of the dose calculations. Approximate uncertainties in the MLC doses are 8% for neutrons and 9% for p $+ \gamma$ radiation. A higher mean neutron energy of 29 MeV in the brass spectra compared to the tungsten MLC, Figs. 4(a) and 3(b), leads to a higher effective neutron sensitivity, k_U, which in turn leads to higher uncertainties. Consequently, the brass measurements exhibit uncertainties of approximately 11% in neutron dose and 20% in p $+ \gamma$ dose.

The respective neutron and p $+ \gamma$ doses due to protons are nearly equivalent for a closed tungsten alloy MLC or a brass block. This disagrees with the results of Daartz *et al.*[14] who used a 25.4 cm Bonner sphere to measure neutron doses at isocenter for a 185 MeV proton beam fully blocked by either a brass collimator or tungsten MLC. Neutron dose equivalents of 3×10^{-4} and 5×10^{-4} Sv/Gy for a 10 cm air-gap and 1.3×10^{-4} and 2.3×10^{-4} Sv/Gy with a 30 cm air-gap were reported for the brass collimator and tungsten MLC, respectively. These correspond to a nearly two-fold increase in neutron dose equivalent at isocenter when switching from a closed brass collimator to a tungsten MLC. In contrast, using their stated radiation weighting factor of 5.9, we measure 3.2×10^{-4} Sv/Gy and 3.8×10^{-4} Sv/Gy for an 8.7 cm air-gap to the brass block and MLC, respectively. For 42.2 cm

TABLE II. Relative p $+ \gamma$ and neutron sensitivities of the Mg-Ar chamber (h_U and k_U) and the TE-TE chamber (h_T and k_T), dosimeter response (R'_U and R'_T), neutron (D_n) and p $+ \gamma$ ($D_{p+\gamma}$) absorbed doses to water per Gy of absorbed dose to water delivered at isocenter by a pristine 230 MeV proton beam. Relative uncertainties of approximately 5% for p $+ \gamma$ sensitivities (h_U and h_T), 20% for k_U, and 6% for k_T are inserted into Eqs. (6) and (7) to determine the relative uncertainty of the absorbed dose calculations. The materials used in this experiment are an MLC with tungsten alloy leaves and a 6.5 cm thick brass block used for custom-milled proton collimators. Measurements are at isocenter 10 cm from the distal edge and 50 cm from the proximal edge of the collimating material.

Material	Position	h_U	h_T	k_U	k_T	$R'_U{}^a$	$R'_T{}^a$	$D_n{}^a$	$D_{p+\gamma}{}^a$
Tungsten	10 cm distal	0.9	1.0	0.10	0.97	1.95	6.77	5.3 ± 0.4	1.6 ± 0.2
Brass	10 cm distal	1.0	1.0	0.25	0.98	3.89	8.57	6.4 ± 0.7	2.3 ± 0.5
Tungsten	50 cm proximal	0.9	1.0	0.11	0.97	0.369	1.00	0.69 ± 0.06	0.33 ± 0.03
Brass	50 cm proximal	1.0	1.0	0.26	0.98	0.393	0.846	0.63 ± 0.07	0.23 ± 0.05

^{a}Dosimeter response and absorbed dose are in units of 10^{-5} Gy/Gy.

146

(brass) or 39.7 cm (MLC) air-gaps, we measure 0.41×10^{-4} and 0.37×10^{-4} Sv/Gy for the brass block and MLC, respectively. The discrepancy must also be considered in light of the differences in beam characteristics, materials, collimator design, and measurement techniques. The collimator leaf design is particularly important for reducing interleaf proton leakage. Unlike the proton MLC used here, the MLC used in the Daartz *et al.* experiment was intended for use in a clinical linear accelerator and may not incorporate the same design considerations, such as multiple steps on abutting leaves that went into the development of the MLC made specifically for proton therapy. In addition, our simulations indicate that the mean neutron energy increases with a brass collimator compared to the tungsten MLC, Figs. 4(a) and 4(b). We further expect the mean neutron energy to increase with primary proton energy, and this may lead to differences in the neutron spectra produced in this experiment with a 230 MeV beam versus the 185 MeV proton beam used in the study of Daartz *et al.* The Bonner sphere used in those measurements underresponds to neutrons greater than ~15 MeV compared to the response of the dual ionization chambers which show better than 20% separation between hydrogenous and nonhydrogenous chambers up to 100 MeV, Fig. 5. Moreover, the large diameter of the Bonner sphere leads to much greater positional uncertainty over the ionization chambers described here, which makes comparison difficult.

The neutron absorbed dose is typically 3 times the $p + \gamma$ absorbed dose in the measurements observed here. Therefore, the impact of uncertainty in $p + \gamma$ absorbed dose on the total absorbed dose is minor. If the neutron dose is expressed in Gy(RBE)[37] or dose equivalent (Sv) then the impact of uncertainties in the $p + \gamma$ absorbed dose becomes negligible when considering the summed dose in Gy(RBE) or the total dose equivalent (Sv). While this is not important for the relative dose measurements required to make a comparison between tungsten alloy and brass as collimator materials, it will be an issue when the dual ionization chamber method is used to make quantitative measurements outside the treatment volume for realistic geometries (i.e., open fields) where RBE or dose weighting factors should be taken into consideration.

Even though the production of secondary neutrons in tungsten alloy is higher than that of brass, in practice this effect is mitigated because a proton MLC must be designed to incorporate side- and end-steps into the leaves to prevent interleaf leakage of protons, resulting in a leaf thickness equivalent to at least twice the proton range in the collimating material. A custom-milled brass collimator is typically designed with a thickness of just over one proton range to reduce weight since the device must be manually exchanged for each new treatment field. The additional material in the tungsten alloy collimator compared to brass has a self-attenuating effect on the neutrons produced within the collimating material.

IV. CONCLUSION

Using the dual ionization chambers and Monte Carlo simulations described above, dose measurements were performed in the mixed neutron and $p + \gamma$ field produced by the proton beam at The University of Pennsylvania Roberts Proton Therapy Center. Of particular interest is the production of secondary neutron radiation by the collimation of a proton beam with the newly developed tungsten alloy MLC in comparison to the conventional brass collimation system, and the potential for an increase in secondary neutron dose to the patient during treatment. Our results indicate that secondary neutron production in a tungsten alloy MLC leads to doses that even in an overly pessimistic clinical worst-case scenario are no greater than those seen from brass collimators. The doses measured here have been obtained in a nonclinical geometry, which was chosen to illustrate that the tungsten alloy MLC produces a secondary neutron dose comparable to that of a brass collimator system.

This study also serves to demonstrate the value of the dual ionization chamber method of mixed-field dosimetry, which was developed for fast neutron beam dosimetry, in measuring the secondary neutron dose associated with therapeutic proton beams. The absolute values of the secondary neutron and $p + \gamma$ absorbed doses measured here should not be considered representative of the absorbed doses that will be seen outside a collimated therapeutic proton field, since these measurements have been made with a closed tungsten alloy MLC or a solid brass collimator to maximize neutron production. Furthermore, this study was limited to only two measurement positions along the proton beam axis in order to provide a timely comparison of the secondary neutron dose due to the newly implemented proton MLC at the University of Pennsylvania Roberts Proton Therapy Center. Additional measurements using the dual ionization chamber technique to map the neutron dose outside of an open proton field shaped with the tungsten alloy MLC are planned for the future.

[1]P. J. Binns and J. H. Hough, "Secondary dose exposures during 200 MeV proton therapy," Radiat. Prot. Dosim. **70**, 441–444 (1997).

[2]H. Paganetti, "Nuclear interactions in proton therapy: dose and relative biological effect distributions originating from primary and secondary particles," Phys. Med. Biol. **47**, 747–64 (2002).

[3]U. Schneider, S. Agosteo, E. Pedroni, and J. Besserer, "Secondary neutron dose during proton therapy using spot scanning," Int. J. Radiat. Oncol., Biol., Phys. **53**, 244–51 (2002).

[4]X. Yan, U. Titt, A. Koehler, and W. Newhauser, "Measurement of neutron dose equivalent to proton therapy patients outside of the proton radiation field," Nucl. Instrum. Methods Phys. Res. A **476**, 429–434 (2002).

[5]H. Jiang, B. Wang, X. G. Xu, H. D. Suit, and H. Paganetti, "Simulation of organ-specific patient effective dose due to secondary neutrons in proton radiation treatment," Phys. Med. Biol. **50**, 4337–4353 (2005).

[6]J. C. Polf and W. D. Newhauser, "Calculations of neutron dose equivalent exposures from range-modulated proton therapy beams," Phys. Med. Biol. **50**, 3859–3873 (2005).

[7]G. Mesoloras, G. A. Sandison, R. D. Stewart, J. B. Farr, and W. C. Hsi, "Neutron scattered dose equivalent to a fetus from proton radiotherapy of the mother," Med. Phys. **33**, 2479–2490 (2006).

[8]R. Tayama, Y. Fujita, M. Tadokoro, H. Fujimaki, T. Sakae, and T. Terunuma, "Measurement of neutron dose distribution for a passive scattering nozzle at the Proton Medical Research Center (PMRC)," Nucl. Instrum. Methods Phys. Res. A **564**, 532–536 (2006).

[9]Y. Zheng, W. Newhauser, J. Fontenot, P. Taddei, and R. Mohan, "Monte Carlo study of neutron dose equivalent during passive scattering proton therapy," Phys. Med. Biol. **52**, 4481–4496 (2007).

[10]M. F. Moyers, E. R. Benton, A. Ghebremedhin, and G. Coutrakon, "Leakage and scatter radiation from a double scattering based proton beamline," Med. Phys. **35**, 128–144 (2008).

[11]P. J. Taddei, J. D. Fontenot, Y. Zheng, D. Mirkovic, A. K. Lee, U. Titt, and W. D. Newhauser, "Reducing stray radiation dose to patients receiving passively scattered proton radiotherapy for prostate cancer," Phys. Med. Biol. **53**, 2131–2147 (2008).

[12]S. Yonai, N. Matsufuji, T. Kanai, Y. Matsui, K. Matsushita, H. Yamashita, M. Numano, T. Sakae, T. Terunuma, T. Nishio, R. Kohno, and T. Akagi, "Measurement of neutron ambient dose equivalent in passive carbon-ion and proton radiotherapies," Med. Phys. **35**, 4782–4792 (2008).

[13]D. Brenner, C. Elliston, E. Hall, and H. Paganetti, "Reduction of the secondary neutron dose in passively scattered proton radiotherapy, using an optimized pre-collimator/collimator," Phys. Med. Biol. **54**, 6065–6078 (2009).

[14]J. Daartz, M. Bangert, M. R. Bussière, M. Engelsman, and H. M. Kooy, "Characterization of a mini-multileaf collimator in a proton beamline," Med. Phys. **36**, 1886–1894 (2009).

[15]J. D. Fontenot, A. K. Lee, and W. D. Newhauser, "Risk of secondary malignant neoplasms from proton therapy and intensity-modulated x-ray therapy for early-stage prostate cancer," Int. J. Radiat. Oncol. Biol. Phys. **74**, 616–622 (2009).

[16]A. Pérez-Andújar, W. D. Newhauser, and P. M. Deluca, "Neutron production from beam-modifying devices in a modern double scattering proton therapy beam delivery system," Phys. Med. Biol. **54**, 993–1008 (2009).

[17]D. Shin, M. Yoon, J. Kwak, J. Shin, S. B. Lee, S. Y. Park, S. Park, D. Y. Kim, and K. H. Cho, "Secondary neutron doses for several beam configurations for proton therapy," Int. J. Radiat. Oncol. Biol. Phys. **74**, 260–265 (2009).

[18]A. Wroe, B. Clasie, H. Kooy, J. Flanz, R. Schulte, and A. Rosenfeld, "Out-of-field dose equivalents delivered by passively scattered therapeutic proton beams for clinically relevant field configurations," Int. J. Radiat. Oncol. Biol. Phys. **73**, 306–313 (2009).

[19]B. Clasie, A. Wroe, H. Kooy, N. Depauw, J. Flanz, H. Paganetti, and A. Rosenfeld, "Assessment of out-of-field absorbed dose and equivalent dose in proton fields," Med. Phys. **37**, 311–321 (2010).

[20]D. Hecksel, V. Anferov, M. Fitzek, and K. Shahnazi, "Influence of beam efficiency through the patient-specific collimator on secondary neutron dose equivalent in double scattering and uniform scanning modes of proton therapy," Med. Phys. **37**, 2910–2917 (2010).

[21]X. Wang, N. Sahoo, R. X. Zhu, J. R. Zallo, and M. T. Gillin, "Measurement of neutron dose equivalent and its dependence on beam configuration for a passive scattering proton delivery system," Int. J. Radiat. Oncol. Biol. Phys. **76**, 1563–1570 (2010).

[22]M. Yoon, S. H. Ahn, J. Kim, D. H. Shin, S. Y. Park, S. B. Lee, K. H. Shin, and K. H. Cho, "Radiation-Induced Cancers From Modern Radiotherapy Techniques: Intensity-Modulated Radiotherapy Versus Proton Therapy," Int. J. Radiat. Oncol. Biol. Phys. **77**, 1477–1485 (2010).

[23]R. Zhang, A. Pérez-Andújar, J. D. Fontenot, P. J. Taddei, and W. D. Newhauser, "An analytic model of neutron ambient dose equivalent and equivalent dose for proton radiotherapy," Phys. Med. Biol. **55**, 6975–6985 (2010).

[24]E. J. Hall, "Intensity-modulated radiation therapy, protons, and the risk of second cancers," Int. J. Radiat. Oncol. Biol. Phys. **65**, 1–7 (2006).

[25]D. J. Brenner and E. J. Hall, "Secondary neutrons in clinical proton radiotherapy: a charged issue," Radiother. Oncol. **86**, 165–170 (2008).

[26]F. A. Cucinotta, R. Katz, J. W. Wilson, L. W. Townsend, J. Shinn, and F. Hajnal, "Biological effectiveness of high-energy protons: Target fragmentation," Radiat. Res. **127**, 130–137 (1991).

[27]A. M. Kellerer, "Risk estimates for radiation-induced cancer—The epidemiological evidence," Radiat. Environ. Biophys. **39**, 17–24 (2000).

[28]X. G. Xu, B. Bednarz, and H. Paganetti, "A review of dosimetry studies on external-beam radiation treatment with respect to second cancer induction.." Phys. Med. Biol. **53**, R193–R241 (2008).

[29]R. L. Bramblett, R. I. Ewing, and T. W. Bonner, "A new type of neutron spectrometer," Nucl. Instrum. Methods **9**, 1–12 (1960).

[30]G. F. Knoll, *Radiation detection and measurement*, 3rd ed. (John Wiley & Sons, Inc., New York, 2000).

[31]L. Bourgois, D. Delacroix, and A. Ostrowsky, "Use of bubble detectors to measure neutron contamination of a medical accelerator photon beam," Radiat. Prot. Dosim. **74**, 239–246 (1997).

[32]S. Agosteo, C. Birattari, M. Caravaggio, M. Silari, and G. Tosi, "Secondary neutron and photon dose in proton therapy," Radiother. Oncol. **48**, 293–305 (1998).

[33]F. Vanhavere and F. d'Errico, "Standardisation of superheated drop and bubble detectors," Radiat. Prot. Dosim. **101**, 283–287 (2002).

[34]R. M. Howell, E. A. Burgett, B. Wiegel, and N. E. Hertel, "Calibration of a Bonner sphere extension (BSE) for high-energy neutron spectrometry," Radiat. Meas. **45**, 1233–1237 (2010).

[35]R. H. Olsher, H. Hsu, A. Beverding, J. H. Kleck, W. H. Casson, D. G. Vasilik, and R. T. Devine, "WENDI: an improved neutron rem meter," Health Phys. **79**, 170–181 (2000).

[36]R. H. Olsher, D. T. Seagraves, S. L. Eisele, C. W. Bjork, W. A. Martinez, L. L. Romero, M. W. Mallett, M. A. Duran, and C. R. Hurlbut, "PRESCILA: A new, lightweight neutron rem meter," Health Phys. **86**, 603–612 (2004).

[37]ICRU, "Prescribing, Recording, and Reporting Proton-Beam Therapy," Report No. 78, International Commision on Radiation Units and Measurements (Bethesda, MD, 2007).

[38]ICRU, Neutron Dosimetry for Biology and Medicine, Report No. 26, (International Commission on Radiation Units and Measurements, Bethesda, MD, 1977).

[39]E. J. Hall and A. J. Giaccia, *Radiobiology for the Radiologist*, (Lippincott Williams & Wilkins, Philadelphia, 2006).

[40]J. B. Smathers, V. A. Otte, A. R. Smith, P. R. Almond, F. H. Attix, J. J. Spokas, W. M. Quam, and L. J. Goodman, "Composition of A-150 tissue-equivalent plastic," Med. Phys. **4**, 74–77 (1977).

[41]P. R. Almond, P. J. Biggs, B. M. Coursey, W. F. Hanson, M. S. Huq, R. Nath, and D. W. O. Rogers, "AAPM's TG-51 protocol for clinical reference dosimetry of high-energy photon and electron beams," Med. Phys. **26**, 1847–1870 (1999).

[42]S. Agostinelli *et al.*, "Geant4—a simulation toolkit," Nucl. Instrum. Methods Phys. Res. A **506**, 250–303 (2003).

[43]F. M. Waterman, F. T. Kuchnir, L. S. Skaggs, R. T. Kouzes, and W. H. Moore, "Energy dependence of the neutron sensitivity of C-CO_2, Mg-Ar and TE-TE ionisation chambers," Phys. Med. Biol. **24**, 721–733 (1979).

[44]A. Rubach and H. Bichsel, "Neutron dosimetry with spherical ionisation chambers I. Theory of the dose conversion factors r and W_n," Phys. Med. Biol. **27**, 893–904 (1982).

[45]A. Rubach and H. Bichsel, "Neutron dosimetry with spherical ionisation chambers IV. Neutron sensitivities for C/CO_2 and tissue-equivalent chambers," Phys. Med. Biol. **27**, 1455–1463 (1982).

[46]A. Rubach, H. Bichsel, and A. Ito, "Neutron dosimetry with spherical ionisation chambers V. Experimental measurements and comparison with calculations of the cavity size dependence of the specific ionization," Phys. Med. Biol. **28**, 913–924 (1983).

[47]ICRU, Nuclear Data for Neutron and Proton Radiotherapy and for Radiation Protection, Report No. 63 (International Commission on Radiation Units and Measurements, Bethesda, MD, 2000).

[48]A. Nohtomi, N. Sugiura, T. Itoh, T. Sakae, T. Terunuma, and T. Fujibuchi, "An alternative method of neutron–gamma mixed-field dosimetry by using paired ionization chambers," Nucl. Instrum. Methods Phys. Res. A **614**, 159–161 (2010).

[49]J. H. Hubbell, "Review of photon interaction cross-section data in the medical and biological context," Phys. Med. Biol. **44**, R1–R22 (1999).

[50]M. Awschalom, I. Rosenberg, and A. Mravca, "Kermas for various substances averaged over the energy spectra of fast neutron therapy beams: A study in uncertainties," Med. Phys. **10**, 395–409 (1983).

[51]ICRU, Stopping Powers and Ranges for Protons and Alpha Particles, Report No. 49 (International Commission on Radiation Units and Measurements, Bethesda, MD, 1993).

148

Dose perturbations by electromagnetic transponders in the proton environment

Derek Dolney, James McDonough, Neha Vapiwala and James M Metz

Department of Radiation Oncology, University of Pennsylvania, Philadelphia, PA 19104, USA

E-mail: Derek.Dolney@uphs.upenn.edu

Abstract

Surgically implanted electromagnetic transponders have been used in external beam radiotherapy for target localization and position monitoring in real time. The effect of transponders on proton therapy dose distributions has not been reported. A Monte Carlo implementation of the transponder geometry is validated against film measurements in a proton SOBP and subsequently used to generate dose distributions for transponders at different positions and orientations in the proton SOBP. The maximum dose deficit is extracted in each case. Dose shadows of up to 60% occur for transponders positioned very near the end of range of the Bragg peak. However, if transponders are positioned further than 5 mm from the end of range, and are not oriented parallel to the beam direction, then the dose deficit can be kept below 10%.

(Some figures may appear in colour only in the online journal)

1. Introduction

Proton therapy is an attractive option for external beam radiotherapy due primarily to the fact that the proton Bragg peak has practically no exit dose (Smith 2009, ICRU 2007). This potentially allows delivery of radiation to the target, with much less dose to surrounding normal tissues. Proton therapy is more sensitive to heterogeneity and motion issues than conventional radiation therapy (Lomax 2008a, 2008b); the larger dose gradients that allow the proton dose distribution to be tailored to the target volume create the potential for delivering large doses to the wrong location. The consequence is that uncertainties in proton treatment delivery need to be precisely understood and controlled.

Various strategies for target localization have been developed. Modern linear accelerators are built with specialized imaging hardware to make use of skeletal anatomy for patient localization. However, tumors can migrate with respect to the skin and skeleton. Radiopaque fiducial markers, surgically implanted within or near the tumor, more directly define the target location, at the cost of some additional ionizing radiation to the patient. As an alternative, a system of wireless electromagnetic transponders was developed, providing submillimeter

localization accuracy (Balter *et al* 2005). The transponders have been used in prostate x-ray external beam radiotherapy treatments (Willoughby *et al* 2006, Kupelian *et al* 2007). Three transponders were implanted transrectally, one in the apex, one in the left base and one in the right base of each prostate. A dosimetric study found improved target coverage and lower rectal dose by use of transponder localization, as compared with localization by reference points on the skin (Rajendran *et al* 2010).

Another significant source of uncertainty for external beam radiotherapy concerns motion of the target, and both intra-fraction and inter-field motion need to be considered (Lomax 2008b). Approaches to the management of target motion were reviewed by Keall *et al* (2006) and include motion-encompassing methods, respiratory gated techniques, breath-hold techniques, forced shallow-breathing methods, and respiration-synchronized techniques. Wired electromagnetic transponders were first used in phantoms for continuous position monitoring by Seiler *et al* (2000), with gating of the proton beam during delivery. The use of wireless, implanted electromagnetic transponders for real-time, continuous tracking was first reported by Balter *et al* (2005) using results from phantom measurements. Other studies have compared transponder electromagnetic localization with that obtained by gantry-mounted fluoroscopic imaging in phantoms and animal (Rau *et al* 2008, Santanama *et al* 2009). Intrafraction motion of the prostate gland has been examined using transponders implanted in patients (Willoughby *et al* 2006, Kupelian *et al* 2007, Langen *et al* 2008), and the dosimetric consequences of prostate motion have been quantified (Li *et al* 2008a, 2008b). It has been demonstrated that use of transponders for localization and motion monitoring allows for a reduction of treatment margins while maintaining target dose coverage (Tanyi *et al* 2010, Su *et al* 2011). Another study considered volumetric modulated arc therapy for the prostate and derives action thresholds for treatment interruption and patient repositioning based on dosimetric requirements (Zhang *et al* 2011). Transponders have also been used to monitor pancreatic motion during irradiation (Shinohara *et al* 2012).

Though they are small, fiducial markers and transponders contain materials that are denser and have a higher atomic number, Z, than patient tissues, and the result is a shadow region downstream of the transponder where the actual delivered dose is lower than what it would be were the implant not present. In the case of fiducials, there is a compromise for the marker design that must balance good visibility with respect to radiographic imaging, low artifacts in CT, and a low dose shadow effect with respect to the treatment beam. Dose shadows in excess of 20% have been demonstrated downstream of gold markers in megavoltage photon beams (Chow and Grigorov 2005, 2006). Perturbations of similar magnitude were observed in the vicinity of nickel-titanium urethra stents (Gez *et al* 1997). Carbon fiber markers are lower-Z and were found to perturb photon dose by only about a percent (Vassiliev *et al* 2012). In the case of proton therapy, studies have explored the dose perturbations from gold, titanium, and stainless steel fiducials, of various sizes and differing placement and orientation with respect to the proton beam (Newhauser *et al* 2007b, Matsuura *et al* 2012). Another study examined the dose shadow produced by tantalum markers used in the treatment of uveal melanoma (Newhauser *et al* 2007a). Effects on dose were investigated for helical gold markers (Giebeler *et al* 2009), for novel fiducials composed of microscopic gold particles embedded in polymer (Lim *et al* 2009), and for a nickel–titanium stent (Herrmann *et al* 2010). Lower-Z alternatives such as carbon-coated ceramics, stainless steel, tungsten, platinum, and a polymer tube can have lower dose perturbations, but must be balanced against radiographic visibility (Cheung *et al* 2010, Huang *et al* 2011).

Electromagnetic transponders have dimensions similar to some of the implanted fiducials, and their constituent materials include soft ferrite, copper, and ceramics. The geometric arrangement of the materials is unique and may perturb dose differently than fiducials. The
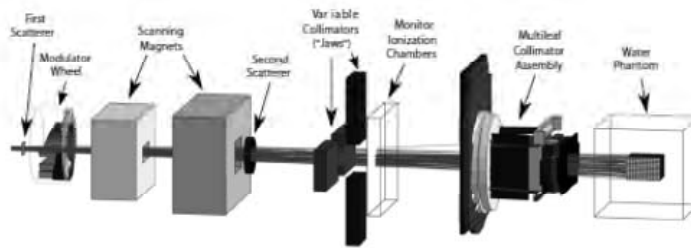
150

Figure 1. Implementation of the IBA Universal Nozzle for Monte Carlo simulation using the Geant4 toolkit. The water phantom at right contains a voxelized sub-volume just downstream of the electromagnetic transponders where dose is scored on a grid.

purpose of this study is to investigate the magnitude of the dose perturbations caused by the presence of implanted electromagnetic transponders as part of an assessment of the feasibility of using electromagnetic transponders for proton therapy. The approach taken was to develop an accurate Monte Carlo model of the Calypso Beacon® electromagnetic transponders, to validate the Monte Carlo simulations using measurements from some selected proton irradiation cases, and then to use the simulations to explore the effect of the transponders at different positions and orientations with respect to the proton beam.

2. Methods and materials

A research Calypso® System (Willoughby et al 2006) from Varian Medical Systems was installed in a proton therapy gantry room at the University of Pennsylvania. Analysis of equipment tolerance to the proton environment was performed along with hardening of the equipment for stabilized operation.

We have implemented, using the Geant4 simulation toolkit v9.4 Patch-01 (Agostinelli et al 2003), a detailed model of the proton delivery equipment at the Roberts Proton Therapy Center, as shown in figure 1. The simulation geometry includes the treatment nozzles provided by Ion Beam Applications (IBA) and the multileaf collimator (MLC) provided by Varian Medical Systems. Our physics list is based on one reported to give good agreement with depth-dose measurements in water and multilayer Faraday cup measurements (Jarlskog and Paganetti 2008). The Geant4 standard electromagnetic physics models, the UHElastic nuclear elastic scattering model and the binary cascade nuclear inelastic model are used as recommended in that reference. Since that physics list was published, newer versions of Geant4 require and provide different multiple scattering models for electrons and positrons and for hadrons/ions. We use G4eMultipleScattering for electrons and positrons and G4hMultipleScattering for hadrons. We have implemented the modulator wheels and scattering elements in the nozzle based on IBA specifications and optimized the beam current modulation using least-squares fitting in order to reproduce commissioning measurements. Our simulation software reproduces the beam range to within 2 mm and 2% dose accuracy for both the double-scattering and the uniform-scanning modalities.

The implementation of the Beacon transponder geometry in simulation is rendered in figure 2 beneath a photograph of a transponder. The masses and materials of the components that comprise a transponder are summarized in table 1. We scored dose downstream of
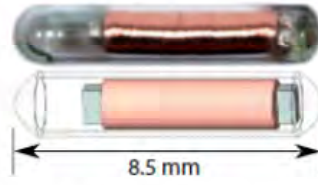
Figure 2. Photograph of a Beacon electromagnetic transponder (top) and the implementation in Geant4 simulation (bottom).

Table 1. Components of the electromagnetic transponders and their corresponding masses. Also shown is the mass and material of each element as implemented for simulation using Geant4.

	Actual Mass (mg)	Simulation Mass (mg)	Simulation Material
Core	2.9	2.9	$MnZnFe_4O_8$
Coil	36.0	36.0	96% Cu + 2% $C_{17}O_4H_{16}N_2$ + 2% G4_POLYVINYL_BUTYRAL
Capacitors	1.3 ($\times$ 2)	1.1 ($\times$ 2)	TiO_2
Adhesive	not specified	0.8	Polydimethylsiloxane
Vial	20.0	20.0	95% G4_Pyrex_Glass + 5% Fe_2O_3
Total	61.8	61.8	

transponders using a G4PhantomParameterisation, which is a voxelized rectangular solid, that is filled with solid water material and divided into voxels of dimensions 113 μm $\times$ 113 μm transverse $\times$ 0.5 mm in depth. The transponders do not have a symmetry that makes it obvious where the point of maximum dose deficit will be located in the transverse directions, and so we window-averaged the fine dose grid over 3 $\times$ 3 groups of voxels to locate the dose minimum in the transverse planes.

Measured data to validate the Monte Carlo simulations was collected using the experimental setup shown schematically in figure 3. The electromagnetic transponders were placed in a block of acrylic with cavities drilled to hold the seeds at three orientations with respect to the proton beam. The acrylic holder was 13 cm $\times$ 3 cm transverse $\times$ 1.2 cm thick in the beam direction. We placed this acrylic holder in a stack of solid water with the film located at several depths downstream of the transponders. The position of the holder in the solid water and film stack was varied to obtain data with the transponders at two different depths, 12 and 20 cm in the phantom. We irradiated the solid water and film stack using a double-scattered proton spread-out Bragg peak (SOBP) of range 22 cm in water (measured to the point distal to the peak where the dose falls to 98% of the peak level, i.e. R_{98}), modulation 10 cm, field size 10 cm $\times$ 10 cm. Our terminology follows that of the ICRU (2007). The film was irradiated to a dose of 2 Gy at field center in mid-SOBP. In simulation, the transponders were placed in the three orientations in an acrylic slab contained in a uniform solid water cube to match the validation setup. For each transponder depth, 19 billion primary protons were generated upstream of the modulator wheel and tracked through the nozzle.
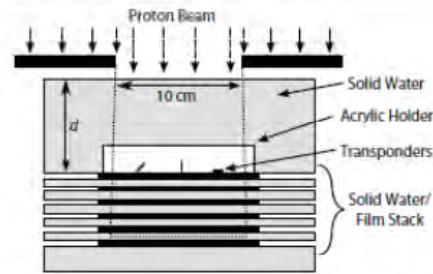
Figure 3. Schematic diagram, not to scale, of the geometry used to measure dose shadows downstream of electromagnetic transponders. A proton beam was collimated with a multi-leaf collimator and irradiated a plastic phantom. A milled acrylic block holding transponders in three orientations was embedded in solid water. Pieces of film were positioned downstream of the transponders. Irradiations were performed with transponders positioned with the depth in phantom, d, equal to 12 and 20 cm.

Dose was measured using Gafchromic EBT2 film (Ashland Specialty Ingredients, Wayne, NJ). The film was digitized using an Epson Expression 10000XL scanner operated in transmission mode, 48-bit color, at 75 dots per inch, with all filters and image enhancement options disabled. A calibration curve to relate the red-channel optical density to dose was obtained by irradiating film from the same batch to seven dose values ranging from 0.2 to 4 Gy. An additional unirradiated piece of film was used for background subtraction. For the calibration irradiations, solid water was used to position the film in the middle of an SOBP of range 15 cm, modulation 10 cm, and field size 10 cm × 10 cm. Irradiated film was allowed to develop for 48 h before scanning. The suitability of radiochromic film for proton dosimetry is well documented in Niroomand-Rad *et al* (1998) and references therein. With care, measurement uncertainty below 1% can be achieved using radiochromic film (Klassen *et al* 1997). However, those measurements rely on absorbance measurements taken over an area of film of a few tens of mm^2. The uncertainty is expected to be greater for dose values that are extracted from small shadow regions. We obtained the per-pixel dose uncertainty from the distribution of dose values inside a 1 cm × 1 cm square in an unperturbed region of irradiated film.

Having validated the Monte Carlo simulations, we then used the simulations to generate dose distributions with transponders at eight additional depths within the proton SOBP and extracted the maximum dose perturbation for each depth.

3. Results

An example dose distribution calculated with Monte Carlo is shown in figure 4. Dose deficit can be seen downstream of the transponders. It is worst for the transponder oriented parallel with the beam. Figure 5 compares the simulation with the film measurements for the transponders at 12 cm depth and 20 cm depth. The Monte Carlo statistical uncertainty is 1–2% depending on the local dose. The uncertainty for film measurements was found to be 3–5%, depending on the dose, by inspecting the distribution of pixel values in an unperturbed region of film. Note that the range appears shorter than the requested 22 cm in water because we are plotting
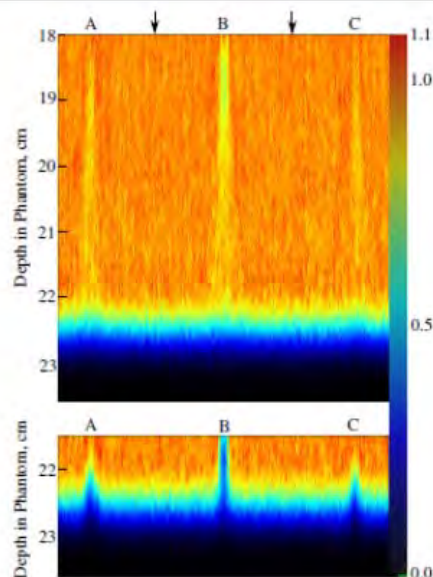
153

Figure 4. Profile of the dose deposited by protons downstream of electromagnetic transponders at depth 18 cm in solid water (upper profile) and 21.5 cm in solid water (lower profile). The proton beam comes from above as indicated by the arrows. The position of the transponders is indicated by the letters, and their orientation is 45 degrees (A), parallel (B), and perpendicular (C) with respect to the beam direction. Redder colors indicate higher doses according to the color band on the right, where the numbers indicate the fraction of D_{SOBP}.

physical depth. The range in solid water is about 4% less due to the slightly higher stopping power of the solid water material, and the stopping power of the acrylic holder is about 16% higher than water. Accounting for these differences, the range is within 0.5 mm of what was expected.

Monte Carlo results indicating the magnitude of the dose shadow for transponders at ten different positions in the SOBP are presented in figure 6. The magnitude of the dose shadow depends on the orientation of the transponder with respect to the treatment beam and the distance of the transponder from the end of range of the SOBP.

Clinicians will typically be most interested in the level of dose shadow that occurs inside the irradiation target. In practice, the treatment delivery is designed so that the target is covered by the part of the SOBP where the dose is 98% or higher than the dose measured in the middle of the SOBP, which we will denote D_{SOBP}. Therefore, in figure 6 we plot the maximum dose shadow that occurs within the region of the SOBP that receives greater than 98% of D_{SOBP}, as a function of the distance of the transponder from the point at the end of the SOBP where the dose has fallen to 98% of D_{SOBP}. We denote this distance d_{98}, with negative values meaning the transponder is positioned within the SOBP, upstream of the beam
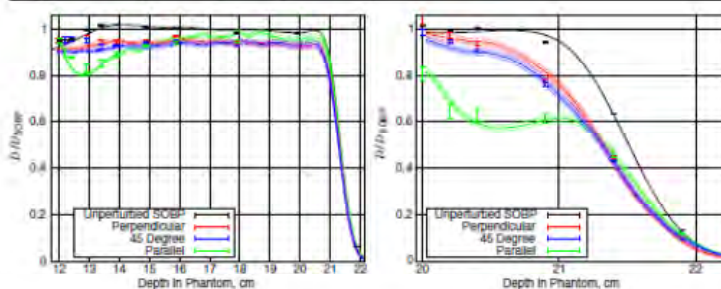
Figure 5. Validation of Geant4 simulation of transponders at 12 cm depth (left) and 20 cm depth (right) in the solid water and acrylic verification phantom. Dose is plotted relative to the dose at mid-SOBP. The error bars are 1σ and indicate dose measurements using Gafchromic EBT2 film and the lines are the simulation results. The width of the lines indicates the Monte Carlo statistical uncertainty.
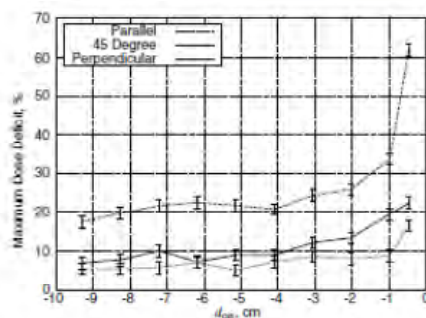

Figure 6. Maximum dose deficit that occurs within the spread-out Bragg peak (SOBP) downstream of a Beacon transponder as a function of the water-equivalent distance between the transponder and the distal end of the SOBP, d_{98}. The SOBP is defined to be the region between the two depths, proximal and distal, where the dose is 98% of the dose delivered at mid-SOBP. Three different orientations of transponder with respect to the beam direction are shown.

end of range. For transponders with d_{98} greater than 2 cm, the dose perturbation is less than 8% for transponders oriented perpendicularly, but still up to 25% for transponders oriented parallel. The dose shadow can become large when the transponder lies near the Bragg peak end of range: we observed up to 60% in the worst case for a parallel transponder located 5 mm upstream of R_{98}.

4. Discussion

Simulation and measurements of dose shadows downstream of transponders agree within the uncertainties of the film and Monte Carlo. A careful implementation of the components of

155

the transponder was necessary, with attention to the densities and chemical composition of the materials that comprise a transponder. The simulated capacitors are slightly underweight relative to the physical specification, but because the difference is only 0.6% of the total mass, we do not expect that to be significant. The mass difference could be due to the metal traces on the capacitor which we have not modeled in simulation. Note that the total mass of the physical and simulated transponders agree because the amount of silicone adhesive was chosen so that would be the case.

The dose deficit is larger for transponders positioned close to the Bragg peak end of range, similar to what has been observed in the studies of dose perturbations near implanted fiducial markers referenced above. At large d_{98}, protons passing through the transponder are sufficiently energetic that they do not stop in the transponder. Nevertheless, a situation of charged particle disequilibrium is created laterally because protons tend to experience more Coulomb scattering in the higher-Z materials of the transponder than in water, since the root-mean-square scattering angle due to multiple Coulomb scattering goes approximately as $\rho^{1/2} Z / A^{1/2}$ (Rossi and Greisen 1941). The disequilibrium produces a shadow region downstream of the transponder that, after reaching a minimum in dose, tends to restore to the unperturbed value as protons scatter laterally behind the transponder, i.e. as lateral charged particle equilibrium is re-established downstream of the perturbation. However, for smaller d_{98}, equilibrium may not be re-established downstream before the protons stop, or worse, at even smaller d_{98}, protons may actually stop in the transponder materials and the shadow will be larger. We can estimate under which conditions protons will stop in the transponder. The transponder coil represents the bulk of the material with a significantly higher relative stopping power. The coil is a little longer than 4 mm. A coil of this length would stop protons of energy below about 45 MeV. The range of 45 MeV protons in water is 1.8 cm. Indeed, it is at about this d_{98} that a change in the dose deficit for the parallel implant can be seen in figure 6: the deficit is 5% larger for the transponder at $d_{98} = 2$ cm compared with $d_{98} = 8$ cm, but there is a 10% difference between 2 and 1 cm, and 30% between 1 cm and 5 mm. The perpendicular water-equivalent thickness of the coil is only about 4 mm, and so the same stark increase in dose deficit is not observed in our data, though the start of an increase in the shadow magnitude can be identified between $d_{98} = 1$ cm and $d_{98} = 5$ mm.

Dose perturbations are expected to be highest in regions of steep dose gradients. Indeed, geometric rather than dose level measures are typically used for comparisons in high gradient regions. However, physicians set constraints on the amount of sub-prescription dose that is acceptable within the target volume, and a treatment plan with unacceptably low dose in the target, as judged by the treating physician, should be improved when possible. There are ways to minimize the dose shadowing effect through location and orientation of the transponders and the number of treatment fields and beam angles. For the case of multiple fields, in general the magnitude of the dose shadow is reduced by a factor equal to the number of fields, assuming that the fields are opposed or at least arranged so that the region of dose shadowing downstream of the transponders does not overlap. Our recommendation is that patients be treated with at least two opposed fields, that the transponders be located no closer than 2 cm to the beam end of range, and that transponders be oriented at most 45° with respect to the beam direction (preferably closer to perpendicular). Orientation of the transponder related to the beam direction is probably the most challenging of these recommendations. However, with common tumors and class solutions, this may be feasible. These guidelines ensure that the minimum dose deficit in the target caused by the transponder will be less than 7%. The goal of course is that the transponders be implanted within the tumor itself, in order that their locations directly indicate the position of the tumor. In practice the volume treated to prescription dose includes margins around the tumor, to account for treatment uncertainties, and so transponders

would tend to not be placed near the beam end of range. On the other hand, precise and consistent transponder implantation can be difficult to achieve, and transponders do migrate, and thus in practice, these guidelines may prove challenging to follow and reproduce for all three implanted transponders. We see no way around the fact that the final post-migration positions of the implanted transponders will need to be considered as part of the treatment planning process. The locations of typical transponders are easy to discern on the CT dataset of the patient. A similar study of dose perturbations in the vicinity of implanted radio-opaque fiducial markers supposed that dose perturbations at the level of 10% or less would not affect clinical outcomes (Newhauser et al 2007b) based on the Loma Linda University Medical Center prostate cancer experience (Slater et al 2004). If a Beacon electromagnetic transponder is not within 5 mm of R_{98}, and is at less than the 45° orientation with respect to the beam, then based on our findings the dose shadow within the target will not be greater than 10%.

Recent published studies (Giebeler et al 2009, Newhauser et al 2007b) concerning dose shadowing from implanted fiducial markers find comparable results for similarly-sized (0.9 mm diameter, 3.1 mm length) stainless steel fiducials (about 6% shadow at 2 cm for perpendicular) but note much larger shadowing from gold fiducials (20% shadow at 2 cm for perpendicular orientation) due to the higher atomic number of gold. There is also a slight dose enhancement effect, caused by charged particle disequilibrium near interfaces of different materials, but the effect is less than 5% to an even smaller region than the shadow. We follow others in disregarding this as a relatively minor perturbation given the dose shadow that develops further downstream of the implant. Our Geant4 implementation of electromagnetic transponders could be used to explore the effect of different transponder sizes or constructions.

The level of the dose shadow depends primarily on the (mean) residual range of protons at the depth of the transponder, as discussed by Newhauser et al (2007b). Therefore, the distance of the transponder from the beam end of range (d_{98} in our notation) can be measured as the distance to the target boundary, and is a variable that is easy to measure on a CT image and could be used to lookup the approximate level of expected dose shadow using figure 6. We have considered the dose shadow using a beam with range 22 cm to represent a depth similar to a typical prostate treatment field. There can be some difference in the level of dose shadow for different SOBP ranges. Since the dose gradient at the Bragg peak end of range is greater for shallower Bragg peaks, the equivalent of figure 6 for an SOBP of shorter range will have a steeper rise as d_{98} approaches zero. Similarly, as Newhauser et al (2007b) have argued, in patient there is also the range mixing produced by tissue heterogeneities that decreases the dose gradient relative to simulations and measurements in homogeneous phantom geometries. The results here are meant only to indicate the feasibility of using electromagnetic transponders with proton therapy. The dose shadow should be calculated in the anatomy of the patient with the transponders in the post-migration position and orientation. Ideally, the treatment planning system could be made to accurately calculate the dose near the transponders. Of course, the treatment planning procedure, or a Monte Carlo dose calculation, should be validated against dose measurements near transponders, and also in heterogeneous environments.

At last, we point out that it may be possible using modern IMPT delivery to offset the shadow by using pencil beams to selectively increase the dose in the region downstream of the transponder, assuming the treatment planning system can be made to calculate the dose in the shadow to a reasonable accuracy. A challenge for this technique will be the robustness of the plan to the usual treatment delivery errors: setup and motion errors are minimized by the transponders, but variations in patient anatomy causing heterogeneity misalignment with respect to the transponders needs to be considered carefully. We now have a validated simulation method which we are using to study these issues.

157

5. Conclusions

Beacon electromagnetic transponders could be used for patient setup and motion management for proton therapy provided some guidelines regarding their placement and orientation with respect to the beam can be met. If a transponder is implanted or migrates to within 5 mm of the PTV boundary, our findings indicate the possibility for greater than 10% dose shadow downstream of the transponder. Much larger shadowing has been observed downstream of implanted gold fiducial markers. In cases of difficult transponder positions, options to minimize the shadow include careful plan design with multiple beam angles to distribute the shadow over a larger volume, or possibly increasing the dose in the expected shadow region to offset the deficit, if the modality allows, though of course it would be necessary to consider the robustness of the technique to the delivery uncertainties.

Acknowledgments

References

Agostinelli S *et al* 2003 GEANT4–a simulation toolkit *Nucl. Instrum. Meth.* A **506** 250

Balter J M, Wright J N, Newell L J, Friemel B, Dimmer S, Cheng Y, Wong J, Vertatschitsch E and Mate T P 2005 Accuracy of a wireless localization system for radiotherapy *Int. J. Radiat. Oncol. Biol. Phys.* **61** 933–7

Cheung J, Kudchadker R J, Zhu X R, Lee A K and Newhauser W D 2010 Dose perturbations and image artifacts caused by carbon-coated ceramic and stainless steel fiducials used in proton therapy for prostate cancer *Phys. Med. Biol.* **55** 7135–47

Chow J C L and Grigorov G N 2005 Dose measurements near a non-radioactive gold seed using radiographic film *Phys. Med. Biol.* **50** N227–34

Chow J C L and Grigorov G N 2006 Monte Carlo simulations of dose near a nonradioactive gold seed *Med. Phys.* **33** 4614–21

Gez E, Cederbaum M, Yachia D, Bar-Deroma R and Kuten A 1997 Dose perturbation due to the presence of a prostatic urethral stent in patients receiving pelvic radiotherapy: an in vitro study *Med. Dosim.* **22** 117–20

Giebeler A, Fontenot J, Balter P, Ciangaru G, Zhu R and Newhauser W 2009 Dose perturbations from implanted gold markers in proton therapy of prostate cancer *J. App. Clin. Med. Phys.* **10** 63–70

Herrmann R, Carl J, Jäkel O, Bassler N and Petersen J B B 2010 Investigation of the dosimetric impact of a Ni-Ti fiducial marker in carbon ion and proton beams *Acta Oncol.* **49** 1160–4

Huang J Y, Newhauser W D, Zhu X R, Lee A K and Kudchadker R J 2011 Investigation of dose perturbations and the radiographic visibility of potential fiducials for proton radiation therapy of the prostate *Phys. Med. Biol.* **56** 5287–302

ICRU 2007 International Commission on Radiation Units Prescribing, recording, and reporting proton-beam therapy Technical Report 78 *ICRU* 7 Report 78

Jarlskog C Z and Paganetti H 2008 Physics settings for using the Geant4 toolkit in proton therapy *IEEE Trans. Nucl. Sci.* **55** 1018–25

Keall P J *et al* 2006 The management of respiratory motion in radiation oncology report of AAPM Task Group 76 *Med. Phys.* **33** 3874–900

Klassen N V, van der Zwan L and Cygler J 1997 GafChromic MD-55: investigated as a precision dosimeter *Med. Phys.* **24** 1924–34

Kupelian P *et al* 2007 Multi-institutional clinical experience with the Calypso system in localization and continuous, real-time monitoring of the prostate gland during external radiotherapy *Int. J. Radiat. Oncol. Biol. Phys.* **67** 1088–98

Langen K M, Willoughby T R, Meeks S L, Santhanam A, Cunningham A, Levine L and Kupelian P A 2008 Observations on real-time prostate gland motion using electromagnetic tracking *Int. J. Radiat. Oncol. Biol. Phys.* **71** 1084–90

Li H S, Chetty I J, Enke C A, Foster R D, Willoughby T R, Kupellian P A and Solberg T D 2008 Dosimetric consequences of intrafraction prostate motion *Int. J. Radiat. Oncol. Biol. Phys.* **71** 801–12

Li H S, Chetty I J and Solberg T D 2008 Quantifying the interplay effect in prostate IMRT delivery using a convolution-based method *Med. Phys.* **35** 1703–10

Lim Y K *et al* 2009 Microscopic gold particle-based fiducial markers for proton therapy of prostate cancer *Int. J. Radiat. Oncol. Biol. Phys.* **74** 1609–16

Lomax A J 2008a Intensity modulated proton therapy and its sensitivity to treatment uncertainties 1: the potential effects of calculational uncertainties *Phys. Med. Biol.* **53** 1027–42

Lomax A J 2008b Intensity modulated proton therapy and its sensitivity to treatment uncertainties 2: the potential effects of inter-fraction and inter-field motions *Phys. Med. Biol.* **53** 1043–56

Matsuura T *et al* 2012 Biological effect of dose distortion by fiducial markers in spot-scanning proton therapy with a limited number of fields: a simulation study *Med. Phys.* **39** 5584–91

Newhauser W D, Koch N C, Fontenot J D, Rosenthal S J, Gombos D S, Fitzek M M and Mohan R 2007a Dosimetric impact of tantalum markers used in the treatment of uveal melanoma with proton beam therapy *Phys. Med. Biol.* **52** 3979–90

Newhauser W, Fontenot J, Koch N, Dong L, Lee A, Zheng Y, Waters L and Mohan R 2007b Monte Carlo simulations of the dosimetric impact of radiopaque fiducial markers for proton radiotherapy of the prostate *Phys. Med. Biol.* **52** 2937–52

Niroomand-Rad A, Blackwell C R, Coursey B M, Gall K P, Galvin J M, McLaughlin W L, Meigooni A S, Nath R, Rodgers J E and Soares C G 1998 Radiochromic film dosimetry: recommendations of AAPM radiation therapy committee task group 55 *Med. Phys.* **25** 2093–115

Rajendran R R, Plastaras J P, Mick R, Kohler D M, Kassaee A and Vapiwala N 2010 Daily isocenter correction with electromagnetic-based localization improves target coverage and rectal sparing during prostate radiotherapy *Int. J. Radiat. Oncol. Biol. Phys.* **76** 1092–9

Rau A W, Nill S, Eidens R S and Oelfke U 2008 Synchronized tumour tracking with electromagnetic transponders and kV x-ray imaging: evaluation based on a thorax phantom *Phys. Med. Biol.* **53** 3789–805

Rossi B and Greisen K 1941 Cosmic-ray theory *Rev. Mod Phys.* **13** 240–309

Santanama L, Noel C, Willoughby T R, Esthappan J, Mutic S, Klein E E, Low D A and Parikh P J 2009 Quality assurance for clinical implementation of an electromagnetic tracking system *Med. Phys.* **36** 3477–86

Seiler P G, Blattmann H, Kirsch S, Muench R K and Schilling C 2000 A novel tracking technique for the continuous precise measurement of tumour positions in conformal radiotherapy *Phys. Med. Biol.* **45** N103–10

Shinohara E T, Kassaee A, Mitra N, Vapiwala N, Plastaras J P, Drebin J, Wan F and Metz J M 2012 Feasibility of electromagnetic transponder use to monitor inter- and intrafractional motion in locally advanced pancreatic cancer patients *Int. J. Radiat. Oncol. Biol. Phys.* **83** 566–73

Slater J D, Rossi C J, Yonemoto L T, Bush D A, Jabola R, Levy R P, Grove R I, Preston W and Slater J M 2004 Proton therapy for prostate cancer: the initial Loma Linda University experience *Int. J. Radiat. Oncol. Biol. Phys.* **59** 348–52

Smith A 2009 Vision 20/20: proton therapy *Med. Phys.* **36** 556–68

Su Z, Zhang L, Murphy M and Williamson J 2011 Analysis of prostate patient setup and tracking data: potential intervention strategies *Int. J. Radiat. Oncol. Biol. Phys.* **81** 880–7

Tanyi J A, He T, Summers P A, Mburu R G, Kato C M, Rhodes S M, Hung A Y and Fuss M 2010 Assessment of planning target volume margins for intensity-modulated radiotherapy of the prostate gland: role of daily inter-and intrafraction motion *Int. J. Radiat. Oncol. Biol. Phys.* **78** 1579–85

Vassiliev O N, Kudchadker R J, Kuban D A, Frank S J, Choi S, Nguyen Q and Lee A K 2012 Dosimetric impact of fiducial markers in patients undergoing photon beam radiation therapy *Phys. Med.* **28** 240–4

Willoughby T R *et al* 2006 Target localization and real-time tracking using the Calypso 4D localization system in patients with localized prostate cancer *Int. J. Radiat. Oncol. Biol. Phys.* **65** 528–34

Zhang P, Mah D, Happersett L, Cox B, Hunt M and Mageras G 2011 Determination of action thresholds for electromagnetic tracking system-guided hypofractionated prostate radiotherapy using volumetric modulated arc therapy *Med. Phys.* **38** 4001–8

159